

RV SONNE SO240

Cruise Report / Fahrtbericht

Manzanillo (Mexico): May 3rd, 2015

Manzanillo (Mexico): June 16th, 2015

SO240 – FLUM: Low-temperature fluid circulation at seamounts and hydrothermal pits: heat flow regime, impact on biogeochemical processes, and its potential influence on the occurrence and composition of manganese nodules in the equatorial eastern Pacific

Dr. Thomas Kuhn

Bundesanstalt für Geowissenschaften und
Rohstoffe (BGR)

Table of Contents

1 Cruise Summary	3
2 Cruise Participants	7
3 Narrative of the cruise	9
4 Aims of the cruise	13
5 Setting of the working area	16
6 Working and sampling progress during the cruise	17
6.1 SAMPLING STRATEGY	17
6.2 WORKING AREA 1	22
6.3 WORKING AREA 2	25
6.4 WORKING AREA 3	28
6.5 WORKING AREA 4	32
7 Work details and first results	37
7.1 GEOPHYSICS	37
7.1.1 General remarks	37
7.1.2 Working area 1	37
7.1.3 Working area 2	42
7.1.4 Working area 3	45
7.1.5 Working area 4	49
7.1.6 Conclusions	55
7.2 GEOPHYSICS BGR	58
7.2.1 BGR heat flow probe	58
7.2.1.1 Station work and preliminary results	60
7.2.2 The sea gravimeter system KSS32-M	62
7.2.2.1 Gravity ties to land stations	64
7.2.2.2 Gravity data process	67
7.2.2.3 Data quality	68
7.2.2.4 Gravity database	68
7.2.2.5 Comparison with gravity anomalies derived from satellite altimetry	69
7.2.2.6 Gravity anomaly maps	72
7.2.3 Magnetics	76
7.2.3.1 Shipborne MAGSON™ Fluxgate Magnetometer	76
7.2.3.2 Fluxgate Calibration	77
7.2.3.3 Magnetic vector data acquired during STROMER deployments	77
7.3 SEDIMENTOLOGY AND GEOCHEMISTRY	79
7.3.1 Methods	79
7.3.2 Manganese nodules – preliminary results	86
7.3.3 Sediments – preliminary results	95

7.4 PORE WATER AND SEDIMENT GEOCHEMISTRY	101
7.4.1 Research objectives	101
7.4.2 Methods	102
7.4.3 Preliminary/Shipboard results	110
7.5 OCEAN FLOOR VIDEO AND PHOTO MAPPING	115
7.5.1 Introduction and research objectives	115
7.5.2 Technical layout of the video sled STROMER	115
7.5.3 General deployment strategy	121
7.5.4 Shipboard results	124
7.5.4.1 Working area 1	124
7.5.4.2 Working area 2	132
7.6 BENTHIC BIODIVERSITY	140
7.6.1 Methods	140
7.6.2 Preliminary results	143
7.7 PHYSICAL OCEANOGRAPHY	152
7.7.1 Introduction and research objectives	152
7.7.2 Sea water properties	153
7.7.3 Long-term current profiling	162
7.7.4 Shipboard results: Preliminary analysis of long-term current and turbidity data	170
8 Acknowledgements	179
9 References	180
10 Abbreviations	183
11 Appendix	185

1 Cruise Summary

The research cruise SO-240 took place from May 3rd, 2015 until June 16th, 2015 at about 12°N and 118°W, approximately 900 nm offshore Mexico in the equatorial NE Pacific. This cruise started and ended in the port of Manzanillo on the west coast of Mexico. Scientists from the Federal Institute for Geosciences and Natural Resources (BGR), the University of Bremen, the Jacobs University Bremen, the Alfred Wegener Institute Helmholtz Center for Polar and Marine Research (AWI), Bremerhaven, Germany (AWI), and the German Centre for Marine Biodiversity Research Wilhelmshaven participated in the cruise.

The objective of this cruise was to investigate the regional pattern of seawater circulation within the basaltic seafloor underneath its sediment cover. Understanding such processes is important as hydrothermal fluids can withdraw significant amounts of heat from the oceanic lithosphere by lateral fluid flow through permeable basaltic crust having an age of up to 65 Ma. Basement outcrops in-between impermeable pelagic sediments permit recharge of oxic seawater and discharge of altered and slightly heated seawater. As the seawater migrates through the basaltic crust, it mines heat from the lithosphere, starts reacting with the basaltic rocks and feeds the microbial community with oxygen and nutrients.

Single-channel seismic surveys, heat flow measurements, pore-water, sediment and manganese nodule sampling as well as video mapping were carried out for these investigations.

The results of this cruise can be summarized as follows:

- The seismic surveys revealed low and variable sediment thickness between 0 and 100 m in the study area, with an average of about 40 m. The basaltic crust is characterized by intensive faulting with many faults cutting through the sediments up to the seafloor.
- Heat flow measurements revealed values below the lithospheric cooling model value of 103 mW/m² for 24 Ma year old crust in most cases. Heat flow profiles towards seamounts and at the base of seamounts confirm that all of these acts as recharge sites for cold seawater into the upper crust.
- Heat flow profiles across troughs or flat plains show that in numerous cases, faults in the upper basement appear to control the seafloor heat flow. This would suggest that they act as pathways for the interchange of fluids between the upper crust and the ocean.
- Deep-sea sediments consist of a mixture of deep-sea clay and siliceous ooze with variable manganese contents and increased input of Fe-rich clays deriving from basaltic weathering near seamounts. Two sediment cores demonstrate strong alteration of sediments, probably by hydrothermal fluids. These cores were taken at sites of increased heat flow.
- Pore water profiles show unusual oxygen enrichment at depth in many cores, indicating recharge of seawater at these sites. Such cores are not only situated close to seamounts but also at positions where fault structures occur far away from seamounts.
- Our results indicate that the fluid circulation system within the basaltic crust is not restricted to seamounts as potential recharge or discharge sites but rather that wide-spread circulation

occurs along faults that strip the basaltic basement. We suggest that a fault-controlled fluid circulation system in the working area has a distinct cooling effect on the 20 – 24 Mio. year old oceanic crust.

- Small-sized manganese nodules dominate the sediments at the bases of the investigated seamounts. Moreover, nodules frequently occur at different depths within the sediment cores. At some positions the metal contents of nodules divert significantly from the average metal concentrations in this area.

In addition to the work carried out within the SO-240 FLUM project, oceanographic investigations were carried out (recovery of moorings and landers, CTD yo-yo and CTD tow-yo deployment) as part of the project “EcoResponse” within the framework of the European “Joint Programming Initiative – Oceans” (JPI-O). This project deals with the potential ecological impacts of future manganese nodule mining. Amongst others, the data gathered during SO-240 will be used to model the hydrodynamic behavior of a sediment plume that may develop during manganese nodule mining.

Zusammenfassung

Die Forschungsfahrt SO-240 startete am 03. Mai und endete am 16. Juni 2015 jeweils in Manzanillo (Mexiko). Das Arbeitsgebiet befand sich bei 12° N und 118°W, ca. 900 Seemeilen vor der Westküste Mexikos im nordöstlichen äquatorialen Pazifik. An dieser Forschungsexpedition beteiligten sich Mitarbeiter der Bundesanstalt für Geowissenschaften und Rohstoffe (BGR) Hannover, der Universität Bremen und der Jacobs University Bremen (GeoB, IUP, JUB), des Helmholtz-Zentrums für Meeres- und Polarforschung Bremerhaven (Alfred-Wegener Institut – AWI) sowie des Deutschen Zentrums für Marine Biodiversitätsforschung in Wilhelmshaven (DZMB).

Im Mittelpunkt dieser Forschungsfahrt stand die Untersuchung der Meerwasserzirkulation innerhalb der 18 – 22 Millionen Jahre alten ozeanischen Kruste. An Ausbissen durchlässiger (permeabler) basaltischer Kruste zwischen undurchlässigen (impermeablen) pelagischen Sedimenten kann Meerwasser in den Meeresboden eindringen, in der basaltischen Kruste zirkulieren und an anderen Stellen, chemisch verändert und erwärmt, wieder austreten. Auf diese Weise werden der ozeanischen Lithosphäre signifikante Wärmemengen entzogen und im Rahmen von (bio)chemischen Reaktionen zwischen Fluid und Gestein kommt es zu Elementan- und/oder –abreicherungsprozessen, die das geochemische Budget des Porenwassers, der Sedimente und der Manganknollen verändern. Es ist das Ziel des Projektes, diese Prozesse qualitative und, wenn möglich, quantitativ zu erfassen.

Um dieses Projektziel zu realisieren wurden auf der SO240-Reise, Daten und Proben mittels geophysikalischer (Einkanalseismik, Wärmestrommessungen, Bathymetrie und Parasound), geologischer (Sediment- und Manganknollenprobenahme, optische Kartierung des Meeresbodens) und geochemischer Methoden (Porenwasserbeprobung, Vermessung und Beprobung des bodennahen Meerwassers) gewonnen.

Die prinzipiellen Ergebnisse dieser Fahrt können wie folgt zusammengefasst werden:

- Die seismischen Untersuchungen haben gezeigt, dass die Sedimentmächtigkeiten im Arbeitsgebiet mit 0 bis 100 m (im Durchschnitt 40 m) nicht nur deutlich geringer ausfallen als bisher angenommen, sondern dass sie auch sehr variabel sind. Darüber hinaus konnte gezeigt werden, dass die obere ozeanische Kruste durch zahlreiche Störungen verworfen wird, wobei viele Störungen nicht nur die basaltische Kruste, sondern auch die Sedimente versetzen und bis an oder nahe an den Meeresboden reichen.
- Die Wärmestromdichten liegen bei den allermeisten Messungen unter dem Modellwert von 103 mW/m² (für 24 Millionen Jahre alte ozeanische Kruste) für das ausschließlich konduktive Abkühlen. In der Umgebung von Seamounts deuten diese Ergebnisse darauf hin, dass dort kaltes Meerwasser in die basaltische Kruste eindringt.
- Die Wärmestromprofile, die in größerer Entfernung von Seamounts gemessen wurden, zeigen eine Korrelation von Wärmestromanomalien mit dem Auftreten von Störungen im Untergrund. Dieses Ergebnis lässt vermuten, dass die Störungen als Wegsamkeiten für die zirkulierenden Fluide fungieren können.
- Die beprobten Sedimente bestehen vorwiegend aus SiO₂-reichen Schalenresten und Tiefseeton mit variablen Mangangehalten und erhöhtem Anteil an tonigem Verwitterungsmaterial der

Basalte in der Nähe von Seamounts. In zwei Sedimentkernen treten deutliche Alterationen auf, die auf eine Reaktion mit hydrothermalen Fluiden hindeuten. Diese Kerne wurden an Lokationen mit erhöhten Wärmestromwerten entnommen.

- In vielen Sedimentkernen zeigen die Sauerstoffgehalte im Porenwasser einen Wiederanstieg mit der Sedimenttiefe, was auf nach oben diffundierenden Sauerstoff aus dem im basaltischen Untergrund zirkulierendem Meerwasser hinweist. Solche Kerne konnten nicht nur am Fuße von Seamounts genommen werden, sondern sie fanden sich auch an störungsgebundenen Lokationen.
- Unsere Ergebnisse belegen, dass Meerwasserzirkulation in der basaltischen Kruste unterhalb der Sedimente großflächig im gesamten Arbeitsgebiet stattfindet. Dabei ist besonders hervorzuheben, dass der Meerwasserein- und -austritt nicht nur an die Seamounts gebunden ist, sondern auch entlang von Störungen fernab der Seamounts erfolgen kann. Wir vermuten, dass es sich hierbei um eine Störungs- und Kluft-kontrollierte Fluidmigration handelt, die einen erheblichen Abkühlungseffekt auf die ca. 20 Millionen Jahre alte basaltische Kruste hat.
- Am Fuße der Seamounts dominieren vor allem kleine Manganknollen (Durchmesser < 4 cm). Darüber hinaus treten die Knollen nicht nur am Meeresboden auf, sondern finden sich auch in verschiedenen Tiefen innerhalb der Sedimentkerne. Erste geochemische Untersuchungen an Bord deuten an, dass der Metallgehalt dieser Knollen an einigen Lokationen deutlich von der durchschnittlichen Zusammensetzung der Knollen im gesamten Arbeitsgebiet abweicht.

Zusätzlich zu den Untersuchungen im Rahmen des SO240-Projektes wurden ozeanographische Arbeiten (Bergung und Aussetzen von Strömungsmessketten, CTD-Stationen) in einem Areal durchgeführt, indem zukünftig Manganknollenabbau stattfinden könnte. Diese Arbeiten sind Bestandteil des Projektes „EcoResponse“ im Rahmen der europäischen „Joint Programming Initiative – Oceans (JPI-O)“, für die die Expedition SO-240 um vier Arbeitstage verlängert wurde. Das Projekt „EcoResponse“ beschäftigt sich mit den möglichen ökologischen Auswirkungen eines zukünftigen Manganknollenabbaus. Die während der Expedition SO-240 gewonnenen Daten über die Strömungen gehen u.a. in hydrodynamische Modelle zum Verhalten einer „Suspensionswolke“ in den bodennahen Wasserschichten ein, die beim Abbau der Manganknollen entsteht.

2 Cruise Participants

Nr.	Participant	Task	Institution
1	Kuhn, Thomas, Dr.	Chief Scientist	BGR
2	Heller, Christina, Dr.	Nodules, sediments	BGR
3	Lückge, Andreas, Dr.	Nodules, sediments	BGR
4	Rühlemann, Carsten, Dr.	Nodules, sediments, Co-Chief Scientist	BGR
5	Stegger, Ulrich	Nodules, sediments, GIS	BGR
6	Vink, Anemiek, Dr.	Nodules, sediments, JPI-O	BGR
7	Wegorzewski, Anna, Dr.	Nodules, sediments	BGR
8	Heyde, Ingo, Dr.	Heat flow, gravimetry	BGR
9	Goergens, Rainer	Technician	BGR
10	Kevel, Oliver	Technician	BGR
11	Wedemeyer, Henning	Electronics engineer	BGR
12	Sturm, Simone	Logistics, lab. technician	BGR
13	Villinger, Heiner, Prof. Dr.	Heat flow, seismics	GeoB
14	Kaul, Norbert, Dr.	Heat flow, seismics	GeoB
15	Schwab, Arne	Heat flow, seismics	GeoB
16	Heesemann, Bernd	Technician	GeoB
17	Bösel, Janine	Bathymetry sediment echosounding	GeoB
18	Müller, Paulina	Bathymetry sediment echosounding	GeoB
19	Singh, Rasphal	Bathymetry sediment echosounding	GeoB
20	Kasten, Sabine, PD Dr.	Pore water, sediments	AWI
21	Dohrmann, Ingrid	Lab technician	AWI
22	Hartmann, Jan F.	Pore water, sediments	AWI
23	Fronzek, Julia	Pore water, sediments	AWI
24	Ritter, Simon	Pore water, sediments	AWI
25	Preuss, Inken-Marie, Dr.	Pore water, sediments	AWI / JUB
26	Filsmair, Christoph	Pore water, sediments	JUB
27	Kleint, Charlotte	Pore water, sediments	JUB
28	Gerken, Jan	Hydrodynamics JPI-O	IUP
29	Purkiani, Kaveh	Hydrodynamics JPI-O	IUP
30	Janssen, Annika	Marine biodiversity	DZMB
31	Uhlenkott, Katja	Marine biodiversity	DZMB

BGR: Bundesanstalt für Geowissenschaften und Rohstoffe, Hannover, Germany

JUB: Jacobs University Bremen, Germany

AWI: Alfred Wegener Institute Helmholtz Center for Polar and Marine Research (AWI), Bremerhaven, Germany

GeoB: Fachbereich Geowissenschaften, Universität Bremen, Germany

IUP: Institut für Umweltphysik, Ozeanographie, Universität Bremen, Germany

DZMB: Deutsches Zentrum für Marine Biodiversitätsforschung, Wilhelmshaven, Germany



Figure 2.1: Participants of cruise SO-240.

3 Narrative of the cruise

T. Kuhn

Cruise SO-240 started on May 3rd, 2015 with the embarkation of the scientific crew and the unloading of our containers in the port of Manzanillo, which is situated on the Pacific coast of Mexico. The new research vessel SONNE set sail on Monday afternoon, May 4th; the departure being delayed by half a day due to the late pickup of frozen samples from the previous cruise. During the 900-nm-long transit to the working area, which is situated to the southwest of Manzanillo (Fig. 3.1), our seismic gear was successfully tested and the scientists were busy installing their equipment in the laboratories. On May 5th, scientists were introduced to the hydro-acoustic systems onboard and were made familiar with security systems of the vessel. In a first science meeting, the scientific objectives and the technical approaches of this cruise were discussed. We arrived in working area 1 on May 7th at noon, starting with a first CTD for the calibration of the swath echo-sounding system EM 122.

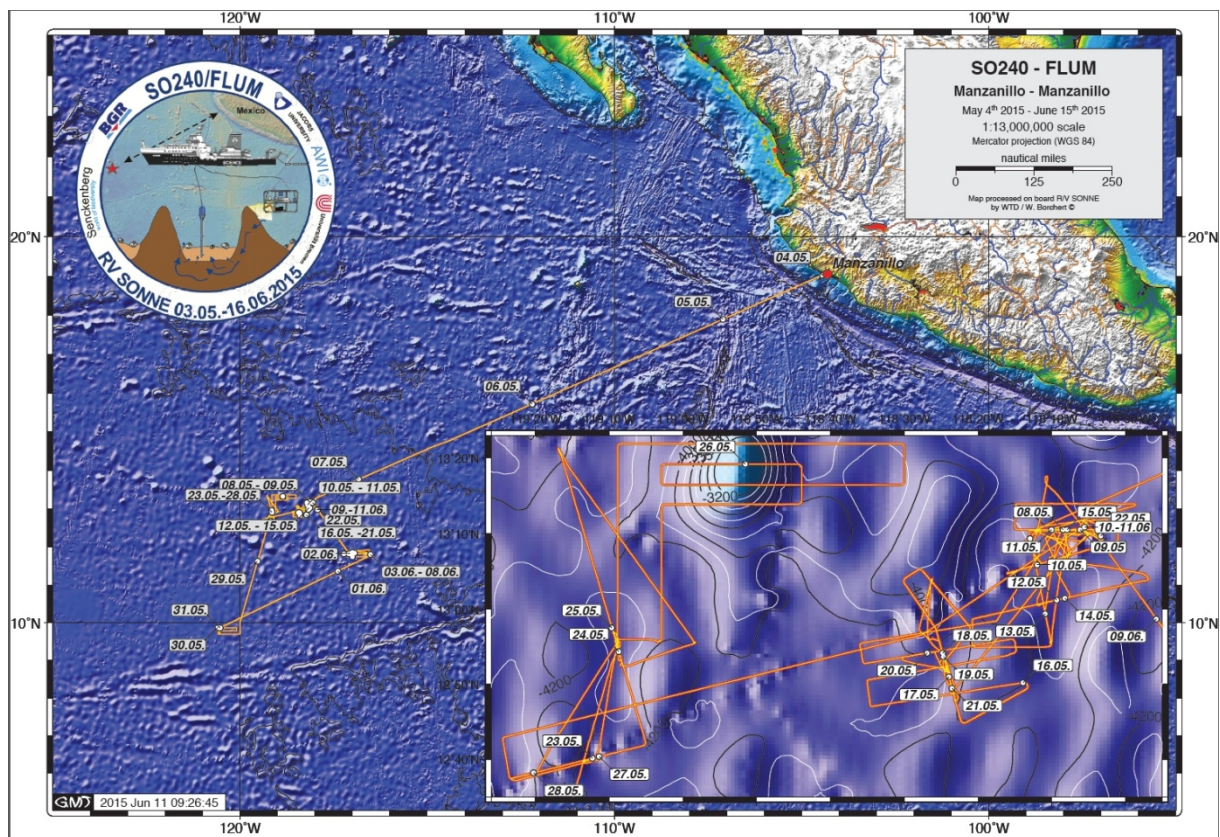


Figure 3.1. Cruise plot of SO-240 starting (on May 4th) and ending (on June 14th) in Manzanillo (Mexico). The inset indicates cruise plots in working areas 1, 2, and 3 (from east to west); working area 4 was investigated between June 1st and June 8th. The hurricane “Andres” forced us to move outside the working areas between May 29th and May 31st.

During SO-240, four working areas were investigated (Fig. 3.2), generally starting with a seismic and bathymetric survey in each area, and following up with heat flow profiles. The results of these geophysical measurements formed the basis for deciding on suitable locations for sediment sampling, which included taking long piston or gravity cores, multicores, and box cores. The long cores were split into 1 m segments immediately after recovery and stored in the cool room (at 4°C) for at least 12

hours so that the sediments could re-equilibrate to the temperature conditions prevailing at the seafloor. After 12 hours, the oxygen content of the pore water was measured along high-resolution profiles along all core segments using oxygen micro-electrodes. This procedure was followed up by pore water sampling, sedimentological description, and sub-sampling. One core from the multicorer was treated in the same way, the other 11 cores being used for biological and geochemical analyses. The near-bottom seawater was also sub-sampled from the multicorer. The box corer provides a seafloor sample with a pre-defined surface area (50 x 50 cm) and 40 to 50 cm sediment thickness. Manganese nodules were collected from the sediment surface and sub-samples from the sediments were taken at 3 cm intervals. Working areas were further investigated using a video sled equipped with video and photo cameras, Niskin bottles, a CTD, oxygen, chlorophyll, and turbidity sensors, a 5-function manipulator for rock sampling as well as three thrusters for enhancing the small-scale maneuverability of the sled.

Working areas 1 to 3 are situated to the east (WA-1), south (WA-2), and southwest (WA-3) of a large seamount complex. The center of WA-1 is a small seamount named Teddy Bare due to its topographic features, and we investigated the fluid flux in the vicinity of this and other seamounts until May 16th by carrying out three seismic surveys, six heat flow profiles, 15 sediment stations, two video stations and one dredge station.

WA-2 is characterized by a group of small seamounts to the north that rises up to 800 m above the surrounding seafloor with a basal radius of 1 to 2 km, and by NNW-SSE oriented basins and ridges to the south. We investigated this area with a size of 35 km x 30 km between May 17th and May 21st by carrying out three seismic surveys, three heat flow profiles, 12 sediment stations, and three video stations.

WA-3 is situated about 50 to 90 km to the southwest of the largest seamount in this area, a structure with a basal diameter of 25 km rising more than 3000 m above its surroundings. Between May 22nd and May 28th, we investigated small basins oriented parallel to the general basin and ridge structures of the seafloor and carried out heat flow profiles perpendicular to them. In the meantime, hurricane “Andres” developed a few hundred kilometers east-southeast of our position. As it started moving in our direction, we had to leave the working area early on May 29th and sailed to 10°N and 120°W.

We used the time in this refuge area (working area X; WA-X) to carry out heat flow measurements far away from the influence of seamounts. In order to do this, we had to map the area first, which took place between May 29th and 30th. One heat flow profile and a box core station were carried out on May 30th and 31st, after which we could transit to working area 4 (WA-4) on June 1st.

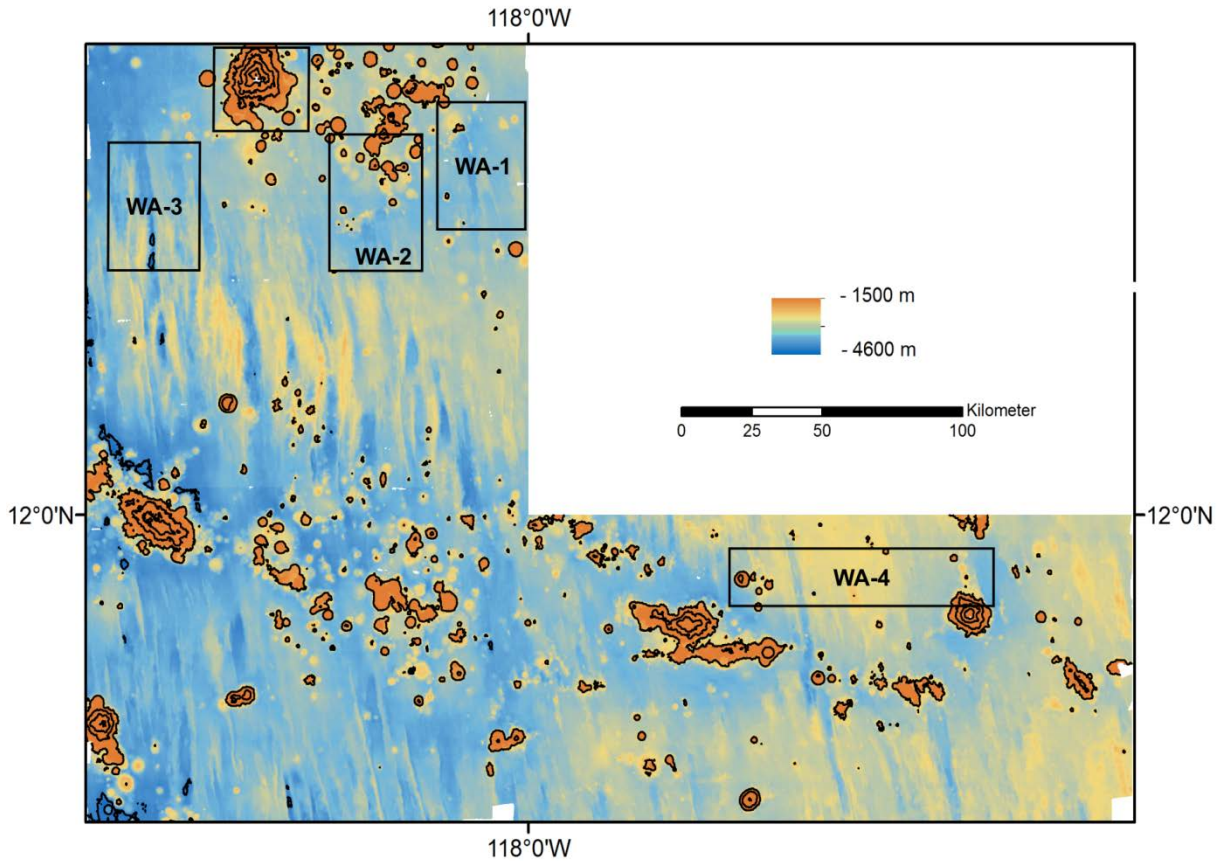


Figure 3.2. Working areas 1 – 4 of cruise SO-240 situated within the eastern part of the German license area for the exploration of polymetallic nodules. Bathymetric map from Ruehlemann et al. (2011).

WA-4 is located about 200 to 300 km to the southeast of WAs 1-3. The so-called “Prospective Area #1” of the BGR Manganese nodule exploration campaign forms the central part of WA-4. In the latter area, two lander systems (DOS, BoBo) equipped with oceanographic measuring devices and a 400 m long thermistor mooring were deployed during the previous cruise SO-239. These systems were successfully recovered on June 2nd and 3rd together with four BGR moorings. The latter moorings have measured near-bottom current strengths and directions for more than one year. All data were downloaded, the instruments maintained and the four BGR moorings were re-deployed on June 6th. In the meantime, one CTD tow-yo and two CTD yo-yo stations, each 14 hours long, were carried out. All this work (3.5 days) took place as part of the project “EcoResponse” within the framework of the European “Joint Programming Initiative – Oceans” (JPI-O), which deals with the potential ecological impacts of future Manganese nodule mining. Amongst others, the data gathered during SO-240 will be used to model the hydrodynamic behavior of a sediment plume that may develop during Manganese nodule mining.

In addition to the JPI-O work in this area, we investigated small depressions (about 200 m x 400 m) that occur within a 10 km wide (E-W), 35 km long (N-S), and 100 to 150 m deep basin which marks the eastern boundary of WA-4. The seafloor in these depressions is characterized by very low backscatter intensity, implying soft sediment that may be typical for water escape structures. Our investigations furthermore show that the basaltic crust under the sediment cover is heavily faulted and that many of these faults even reach to the seafloor and lead to an offset of the sediments, thus enabling fluid circulation in the basaltic crust far away from seamounts. Such conditions have also

been detected in the western part of WA-4. In total, we carried out 100 km of seismic and 200 km of bathymetric survey, three heat flow profiles, nine sediment stations, and one station for the *in-situ* shear strength measurement of deep-sea sediments between June 1st and 8th in WA-4.

Finally, on June 9th, we returned to WA-1 in order to investigate a temperature anomaly which we had found after the analysis of CTD data in the water column immediately above the Teddy Bare seamount. Between June 9th and June 11th, we carried out additional heat flow profiles, four sediment stations, one CTD cast and one dredge drag in this area.

As a new hurricane “Carlos” was shaping up to the southeast of Manzanillo, R/V SONNE had to start her transit back to Manzanillo in the late afternoon of June 11th, where she arrived safely on Sunday morning at 8:30 local time. On the transit back to Manzanillo, the labs were cleaned, containers were packed, and a first synthesis of the cruise was presented during a final science meeting.

4 Aims of the cruise

T. Kuhn

Hydrothermal fluids can withdraw significant amounts of heat from the oceanic lithosphere by lateral fluid flow through permeable basaltic crust of an age of up to 65 Ma. Basement outcrops in-between impermeable pelagic sediments permit seawater recharge and discharge of altered and slightly heated seawater. A recharge site was detected on the flank of one of the numerous seamounts in the working area in the equatorial eastern Pacific during earlier investigations. Moreover, successions of small basins typical for “hydrothermal pits” occur which could be interpreted as fossil discharge sites.

The objective of this project is to investigate the regional pattern of seawater circulation within the basaltic seafloor based on seismic surveys, heat flow measurements and pore-water geochemistry. Recharge of oxic seawater causes upward oxygen diffusion into the sediments overlying the permeable basalt in areas proximal to the recharge sites (seamounts or basalt outcrops). The prolonged oxygen exposure time is suggested to have a strong impact on biogeochemical processes in the sediments and the element inventory of Manganese nodules. Quantitative investigations of such processes and element enrichments and their range of influence around recharge sites thus form the second objective of this project. An additional goal is to investigate whether fluid circulation through the 20 Million years old crust can mobilize metals and affect metal flux rates into sediments and nodules at possible discharge sites.

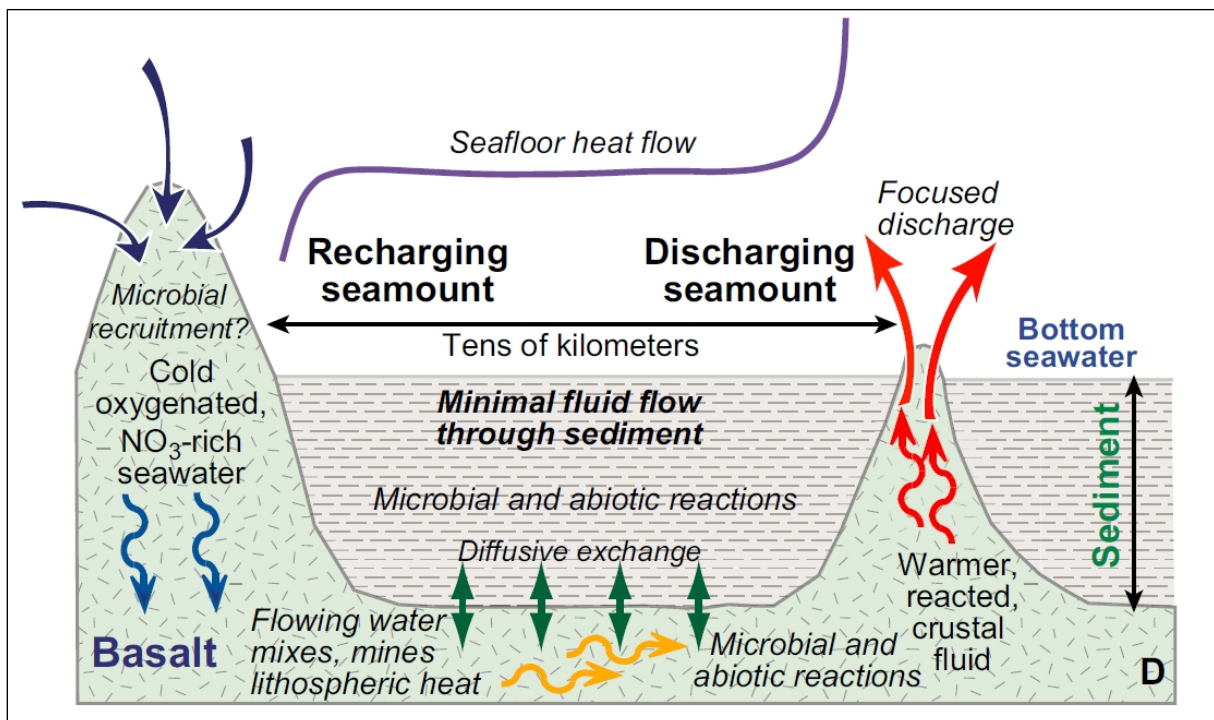


Figure 4.1. Sketch illustrating fluid circulation through permeable basaltic basement between seamounts that act as recharge and discharge sites. The primary driving force of the circulation system is the difference in fluid pressures at the recharge and discharge site. Seawater can move laterally through the basement, thus by-passing the sediment cover, mining lithospheric heat, and leading to biotic and abiotic reactions with the basaltic crust. Recharge and discharge sites can be several tens of kilometers apart. Figure from Fisher & Wheat (2010).

The following scientific questions were addressed on board and will be addressed further during the remainder of the SO-240 project:

1. What is the pattern and size of low-temperature fluid circulation systems in the working area?

It is the task of the project to investigate the circulation pattern in terms of recharge and discharge sites based on systematic heat flow measurements. Single-channel seismics were used to localize the sediment-basalt interface, a prerequisite to correctly interpret the regional heat flow. Based on the results of heat flow measurements, suitable locations for sediment, nodule and pore-water sampling as well as video transects were chosen. 4 different working areas were selected (see Fig. 3.2).

2. What is the impact of fluid circulation on element cycling and (bio)geochemical processes in the sediments overlying the permeable basaltic crust?

At recharge sites such as on basaltic outcrops, unaltered oxic seawater can entrain the basaltic crust. Sediments in the immediate vicinity of a recharge site may be subjected to upward oxygen diffusion from flowing water at the sediment-basement interface, inducing oxic conditions throughout the sediments. Increased oxygen content in pore water has implications for the microbial activity as well as the preservation of organic compounds and the mobilisation potential of elements sensitive to microbial turnover rates and redox processes (Mn, Cd, Cu, Li, V, etc. and isotopic systems of Sr, Li, Ca, O, H). As the seawater migrates through the basaltic crust, it mines heat from the lithosphere, starts reacting with the basaltic rocks and feeds the microbial community with oxygen and nutrients. Pore-waters at discharge sites should have detectable differences in composition compared to seawater (e.g. elevated Mn, Ca, Ba, B, Si) and detectable sedimentary precipitates (e.g. Mn oxides). Nothing is known about the mobility of trace and ultra-trace metals in such fluid circulation systems. This will be one focus of biogeochemical work. Based on this reasoning, we obtained long sediment cores and multicores along transects on the flanks of potential seamount recharge and discharge sites as well as in areas far away from seamount influence.

3. What is the potential influence of fluid circulation on the occurrence and composition of manganese nodules?

Manganese nodules consist of a succession of single layers which alternately form either from oxic pore- and seawater or from suboxic pore-water. Prolonged oxic conditions at recharge sites may lead to the enrichment of iron, cobalt, zirconium, tellurium, lead, and rare earth elements in nodules. Apart from the economic importance of these metals, the formation and enrichment processes under prolonged oxic pore-water conditions in a sedimentary environment are still poorly known. We investigated the influence of seamounts as well as off-seamount fluid recharge and discharge sites on the occurrence and composition of Mn nodules, either from low-temperature hydrothermal fluid flow or from the change in hydrography around large seamounts. Box core sampling and video mapping of the seafloor were carried out to realise this task.

4. What will be the hydrodynamic behaviour of a sediment plume during potential future Mn nodule mining?

At the end of SO-240, four days were dedicated to the recovery of bottom landers and four near-bottom current moorings in working area 4 (Fig. 3.2). The landers were deployed at the beginning of SO-239 and the recovery at the end of SO-240 provided a 9-week time series of high-resolution

oceanographic measurements. The four current moorings were deployed in May 2014 by the BGR and were recovered during this cruise. Data were downloaded, the moorings were serviced and then re-deployed at the same positions. The data will be used to establish models on the dilution and dispersion potential of mining-induced sediment plumes. This work was carried out as part of the European Joint Initiative - Oceans (JPI-O) “EcoResponse” Programme that sets out to analyse the potential ecological impacts of Mn-nodule mining.

5 Setting of the working area

T. Kuhn

The working area is part of the eastern German license area for the exploration of manganese nodules in the eastern equatorial Pacific (Fig. 5.1). Detailed bathymetric mapping of this area using an EM 120 mounted to R/V Kilo Moana as well as magnetic profiling was carried out in 2008 and 2009 (Wiedicke-Hombach et al., 2009; 2010). These studies reflect numerous seamounts in the working area, rising between a few hundred to more than 2000 m above the surrounding seafloor (Fig. 3.2). In-between the seamount chains the seafloor is characterized by NNW-SSE oriented ridge and graben structures rising about 100 m – 300 m above the surrounding seafloor at 4.200 m to 4.300 m water depth. Deep-sea sediments consist of a varying mixture of clay minerals and silt-sized radiolarian and diatom tests and are almost devoid of carbonate in the upper few meters. However, XRF scanning of long sediment cores and $^{10}\text{Be}/^9\text{Be}$ age dating has shown that carbonate-rich sediments do occur at about 15 Ma. or, alternatively, that carbonate sedimentation ceased about 15 million years ago when the working area moved out of the equatorial high bioproductivity zone. Manganese nodules occur on the sediment surface in variable densities (Kuhn et al., 2010; Rühlemann et al., 2011).

Indications for the recharge and discharge of seawater have been previously found on the flanks of a small seamount in working area 1 (Mewes et al., in review; see Fig. 3.2 for location). Moreover, the structural situation of the working area is very similar to the low-temperature fluid circulation end-member on the eastern flank of the East Pacific Rise (EPR) (Fig. 5.1). This end-member is characterized by low temperature (10 – 20°C) and slightly altered seawater with a rather high fluid flux of $1\text{--}20 \cdot 10^3 \text{ L s}^{-1}$ at the discharge site (Fisher & Wheat, 2010). Recharge and discharge locations are suggested to be 20 km apart. The discharge sites of both systems are small edifices rising 70 m and 250 m over the local bathymetry, respectively.

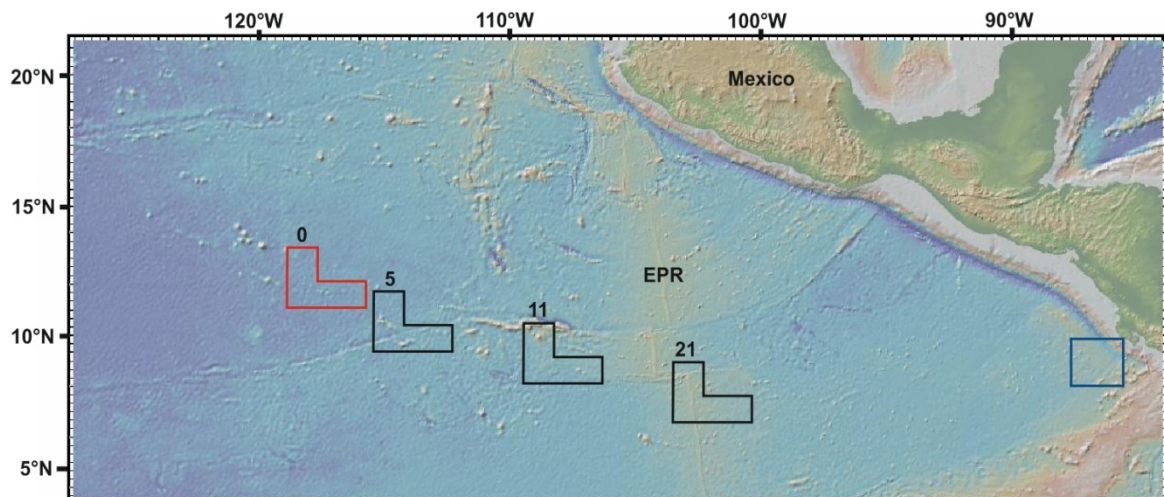


Figure 5.1. Location of the working area on the western East Pacific Rise (EPR) flank (red box) and position of the low-temperature fluid circulation end-member on the eastern EPR flank (blue box). The paleogeographic reconstruction represents the movement of the working area due to oceanic spreading during the last 21 million years. Both areas were formed 18-22 million years ago on the EPR. Therefore, we assume both areas have similar crustal structure and permeability. Figure after Rühlemann et al. (2009).

6 Work and sampling progress during the cruise

T. Kuhn

6.1 SAMPLING STRATEGY

Four different working areas were investigated during SO-240 (WA 1-4, Fig. 3.2), each of them representing different seamount configurations or basaltic outcrops on the seafloor. In each area we started with single-channel seismics, utilizing a 100 m long streamer chain for signal detection and one GI airgun, together with bathymetric mapping (with the swath echosounding system EM 122) and sediment echo-sounding (Parasound). The objective of this approach was to investigate the sediment-basalt interface, internal sediment structures as well as the local bathymetry in order to locate suitable positions for heat flow profiles. The following step was the deployment of a 5 m long heat flow lance in profiles over detected seafloor structures such as faults and/or in the surroundings of seamounts. Heat flow measurement points were about 1 km apart along the profiles. Based on the results of these geophysical investigations, suitable locations for porewater, sediment and manganese nodule sampling were chosen. Generally, sampling occurred at locations with unusual heat flow data. Optical seafloor mapping with the video sled and sampling of near-bottom water using Niskin bottles integrated in the sled complemented the station work.

In working area 4, two lander systems, a 400 m long thermistor chain and four ocean bottom current moorings were recovered (Fig. 3.2 and Figs. 6.27, 6.28). Whereas the lander systems and the thermistor chain stayed onboard, the current data of the moorings were downloaded, the instruments were serviced and the moorings were re-deployed at the same positions. Finally, two CTD/Rosette stations in yo-yo and one CTD/Rosette station in tow-yo style completed cruise SO-240.

The station list as well as some statistical data of cruise SO-240 are presented in Tables 6.1 and 6.2.

Table 6.1. Planned and realized stations during cruise SO-240 (without transit in-between stations)

Station	Planned	Realized
Seismics, bathymetry, parasound	10 profiles @ 220 hours	13 profiles @ 130 hours 5 seismic stations @ 83 hrs.
Heat flow stations	130 single point measurements @ 220 hours	116 single point measurements @ 204 hours
Multicorer	15 stations	17 stations
Gravity / Piston corer	15 Stations	18 stations with 171 m core length
Box corer	10 Stations	20 Stations
Video sled	7 Stations	7 Stations
CTD/Rosette	1 Station	5 Stations
Stations within JPI-O	96 hours	63.5 hours
Loss due to hurricane “Andres”		3.5 days (ca. 85 hours)

Table 6.2. List of stations during cruise SO-240. “UTC” indicates Universal Time Coordinated of bottom contact or max. depth of the respective device, affixes “B” and “E” after UTC for STROMER and dredge operations indicate beginning and end of bottom visibility or contact. Position and water depth refer to time of bottom contact or visibility, respectively. For mooring recovery the release position is given. Water depth is from EM 122 if not indicated otherwise.

Station SO240-	Date 2015	UTC			Position		Water depth [m]	Remarks
		start	bottom	end	latitude (N)	longitude (W)		
01CTD	07.05.	18:50		22:13	13° 10.52'	118° 12.19'	4262	24 bottles filled with water samples
02PS	07.05.	22:37			13° 10.359'	118° 11.673'	4272	Parasound profile with 8 knots
	08.05.			00:02	13° 11.872'	118° 02.544'	4255	
03HF	08.05.	01:03			13° 10.479'	118° 11.870'	4179	Six (6) heat flow stations along profile,
	08.05.			14:15	13° 10.512'	118° 07.855'	4284	each ca. 1 km apart
04KG	08.05.	14:51	16:12	17:48	13° 10.519'	118° 06.706'	4278	37 cm core length, 12.6 kg/m ² small nodules
05SL	08.05.	18:06	19:29	21:34	13° 10.525'	118° 06.705'	4287	756 cm core length
06STR	08.05.	22:20	00:51B		13° 10.060'	118° 04.858'	4024	Test of new video sledge STROMER
	09.05.		02:21E	03:50	13° 10.060'	118° 04.560'	4075	
07HF	09.05.	05:11			13° 10.525'	118° 07.862'	4313	Four (4) heat flow stations along profile,
	09.05.			13:35	13° 10.528'	118° 06.741'	4273	each ca. 1 km apart
08MUC	09.05.	13:53	15:36	17:30	13° 10.524'	118° 06.708'	4289	12/12 tubes filled, 29 cm core length
09KL	09.05.	18:11	19:53	22:01	13° 10.524'	118° 10.104'	4335	1187 cm core length
10KG	09.05.	22:13	23:31	01:00	13° 10.525'	118° 10.107'	4333	43 cm core length, 14.8 kg/m ² large nodules
11SCS	10.05.	02:16			13° 13.974'	117° 59.111'	4259	Three single-channel seismic profiles
				13:00	13° 04.672'	118° 15.913'	4288	Total length: 85 km
12HF	10.05.	13:43			13° 05.043'	118° 14.891'	4291	Seven (7) heat flow profiles, each ca. 1 km apart
	11.05.			02:08	13° 05.962'	118° 11.684'	4360	Posidonia transponder 100 m over HF lance
13STR	11.05.	03:01	04:19B		13° 09.441'	118° 12.985'	3725	Transect along NE slope of seamount
	11.05.		12:56E	14:23	13° 10.519'	118° 09.751'	4313	
14MUC	11.05.	15:13	16:51	18:46	13° 10.528'	118° 10.108'	4332	11/12 tubes filled, 35 cm core length
15KL	11.05.	19:23	21:04	22:55	13° 07.101'	118° 07.657'	4319	1161 cm core length
16KG	11.05.	23:21	00:43	02:14	13° 07.098'	118° 07.655'	4319	43 cm core length, no nodules
17SCS	12.05.	03:01			13° 01.080'	118° 13.031'	4140	Four single-channel seismic profiles
	12.05.			15:00	13° 03.610'	118° 57.992'	4241	Total length: 90 km
18MUC	12.05.	16:12	17:48	19:32	13° 07.109'	118° 07.657'	4318	12/12 tube filled, 36 cm core length
19KL	12.05.	20:10	21:46	23:32	13° 10.527'	118° 08.083'	4307	All steel pipes lost, only head weight recovered
20HF	13.05.	00:43			12° 55.688'	118° 09.971'	4599	Nine (9) heat flow stations along profile,
	13.05.			15:17	12° 59.862'	118° 10.946'	4375	each ca. 1 km apart
21KG	13.05.	16:48	18:07	19:37	13° 10.529'	118° 08.187'	4288	43 cm core length, 18.6 kg/m ² large nodules
22KL	13.05.	19:52	21:30	23:15	13° 10.527'	118° 08.184'	4302	1301 cm core length; repetition of 19KL
23MUC	13.05.	23:51	01:33	03:19	13° 10.526'	118° 08.186'	4305	10/12 tubes filled, 31 cm core length
24HF	14.05.	04:35			13° 00.743'	118° 11.175'	4374	Five (5) heat flow stations along profile,
	14.05.			14:44	13° 01.527'	118° 07.660'	4296	each ca. 1 km apart
25KG	14.05.	15:45	17:04	18:42	13° 07.013'	118° 09.845'	4331	43 cm core length, 18.2 kg/m ² large nodules
26KG	14.05.	19:11	20:33	22:09	13° 09.517'	118° 10.676'	4343	43 cm core length, 20.8 kg/m ² large nodules
27GDS	14.05.	22:47	00:03B		13° 09.227'	118° 05.594'	4251	Five Mn nodules, one indurated sediment with
	15.05.		01:51E	03:15	13° 09.630'	118° 05.240'	4122	2-cm-thick Fe-Mn crust
28STR	15.05.	03:42	05:14B		13° 10.007'	118° 04.869'	4035	Transect along west slope of Teddy Bare Smt.
			14:02E	15:50	13° 10.527'	118° 08.936'	4298	and E-W over sampling stations
29SCS	15.05.	17:20			12° 58.358'	118° 17.655'	4219	Five (5) seismic profiles over working area 2
	16.05.			17:15	12° 58.414'	118° 26.409'	4238	Total length: 200 km
30EM	16.05.	17:17			12° 58.540'	118° 26.490'	4186	Hydroacoustic mapping (EM 122) of seamounts
				19:46	12° 57.760'	118° 21.204'	4289	In the north of WA-2; length: 40 km
31KL	16.05.	20:31	22:02	23:55	12° 53.355'	118° 24.572'	4289	1174 cm core length; slump deposits?
32HF	17.05.	01:06			12° 48.015'	118° 23.136'	4292	Eight (8) heat flow stations along profile,
				14:38	12° 51.223'	118° 23.967'	4274	each ca. 1 km apart
33KG	17.05.	15:12	16:30	18:10	12° 53.365'	118° 25.576'	4292	37 cm core length, 12.6 kg/m ² small nodules
34MUC	17.05.	18:24	20:00	21:48	12° 53.358'	118° 24.569'	4287	11/12 tubes filled, 22 cm core length
35SL	17.05.	22:04	23:27	01:40	12° 54.128'	118° 24.791'	4319	982 cm core length
36HF	18.05.	01:56			12° 51.777'	118° 24.144'	4296	Continuation of 32HF; five heat flow stations
				10:54	12° 54.123'	118° 24.778'	4307	each ca. 1 km apart
37MUC	18.05.	10:57	12:32	14:20	12° 54.131'	118° 24.782'	4319	10/12 tubes filled, 28 cm core length

SO240 cruise report – Chapter 6 Work and sampling progress during the cruise

Table 6.2. continued

Station SO240-	Date 2015	UTC			Position		Water depth [m]	Remarks
		start	bottom	end	latitude (N)	longitude (W)		
39PS	18.05.	18:16			12° 57.344'	118° 27.966'	4296	Short profile over donut seamounts to map
				19:33	13° 03.891'	118° 26.244'	4188	sediment thickness in their craters
40STR	18.05.	18:05	22:05B		13° 02.020'	118° 26.744'	3712	Video mapping in seamount crater, 4 MAPRS at
			00:59E	02:22	13° 02.912'	118° 26.515'	3718	100, 200, 300, 400m; 2 water samples
41STR	19.05.	03:25	05:00B		12° 56.018'	118° 26.157'	3884	Video mapping of seamount flank and along
			14:00E	15:40	12° 51.978'	118° 24.180'	4275	32/36 HF profile
42SL	19.05.	16:09	17:38	19:20	12° 51.249'	118° 23.976'	4290	1036 cm core length
43MUC	19.05.	19:21	21:04	22:53	12° 51.247'	118° 23.980'	4289	12/12 tube filled, 33 cm core length
44KG	19.05.	23:01	00:22	02:03	12° 51.243'	118° 23.978'	4289	43 cm core length, 17.8 kg/m ² medium nodules
45HF	20.05.	02:57			12° 53.519'	118° 30.163'	4226	Seven (7) heat flow stations along profile,
				15:53	12° 54.266'	118° 26.008'	4290	each ca. 1 km apart; 1 station failed
46KG	20.05.	16:33	17:53	19:31	12° 52.266'	118° 24.271'	4275	39 cm core length, 18.4 kg/m ² small-med. nods
47KG	20.05.	19:59	21:15	22:53	12° 50.727'	118° 23.834'	4290	43 cm core length, 23.4 kg/m ² large nodules
48KG	20.05.	23:25	00:43	02:22	12° 48.749'	118° 23.295'	4313	42 cm core length, 23.0 kg/m ² med.-large nods
49STR	21.05.	03:00	04:40B		12° 51.980'	118° 24.170'	4273	Continuation of station 41STR
			13:04E		12° 49.056'	118° 23.374'	4292	
50CTD	21.05	17:21	19:30	21:14	13° 10.020'	118° 04.949'	4026	CTD profile & water samples at Teddy Bare Smt
51SL	21.05.	21:42	23:08	01:07	13° 10.526'	118° 06.584'	4286	537 cm core length
52HF	22.05.	01:13			13° 10.698'	118° 06.400'	4287	Nine (9) heat flow stations around Teddy Bare
				14:26	13° 09.367'	118° 03.230'	4283	each ca. 1 km apart
53SL	22.05.	15:09	16:33	18:30	13° 10.508'	118° 06.110'	4273	482 cm core length, closest to Teddy Bare Smt.
54SCS	22.05.	20:54			12° 56.437'	118° 28.025'	4327	Three (3) seismic profiles over working area 3
	23.05.			22:00	13° 20.258'	119° 16.466'	4407	Total length: 220 km
55CTD	24.05.	00:31	02:18	03:45	12° 55.596'	118° 58.433'	3870	CTD profile to calibrate EM 122
56HF	24.05.	05:09			12° 52.802'	119° 08.344'	4292	Seven (7) heat flow stations in pits of suspected
				14:39	12° 54.545'	119° 08.745'	4286	hydrothermal origin; each ca. 1 km apart
57KG	24.05.	15:19	16:41	18:12	12° 53.217'	119° 08.352'	4310	43 cm core length, no nodules
58SL	24.05.	18:19	19:39	21:30	12° 53.216'	119° 08.351'	4309	1244 cm core length
59MUC	24.05.	21:31	23:43	01:28	12° 53.216'	119° 08.344'	4306	12/12 tubes filled, 38 cm core length
60HF	25.05.	02:22			12° 55.007'	119° 08.965'	4280	Continuation of profile 56HF; five (5) heat flow
				13:10	12° 57.457'	119° 09.626'	4273	Stations, each ca. 1 km apart
61MUC	25.05	13:36	15:16	17:01	12° 56.109'	119° 08.871'	4293	12/12 tubes filled, 42 cm core length
62KG	25.05.	17:16	18:40	20:13	12° 56.107'	119° 08.870'	4294	44 cm core length, no nodules
63PS	25.05.	21:05			12° 55.635'	119° 08.998'	4294	Short profile over small depression to
				22:34	13° 02.965'	119° 08.829'	4348	identify sediment structures
64EM	25.05.	22:35			13° 02.440'	119° 08.820'	4360	EM 122 mapping of large, dominating seamount
	26.05.			18:11	12° 55.760'	119° 03.130'	4363	NW of working area 3
65SL	26.05.	19:07	20:29	22:19	12° 56.107'	119° 08.884'	4293	1275 m core length
66KG	27.05.	00:06	01:24	02:59	12° 40.311'	119° 11.520'	4406	41 cm core length, 4.1 kg/m ² small nodules
67HF	27.05.	03:37			12° 39.800'	119° 13.480'	4244	Seven (7) heat flow stations over tectonically
				14:21	12° 40.376'	119° 11.203'	4399	controlled basin structure; each ca. 1 km apart
68MUC	27.05.	14:50	16:33	18:29	12° 40.307'	119° 11.514'	4408	12/12 tubes filled, 36 cm core length
69SL	27.05.	18:54	20:16	22:00	12° 39.855'	119° 13.374'	4275	1265 cm core length
70MUC	27.05.	22:00	23:34	01:16	12° 39.857'	119° 13.385'	4270	12/12 tubes filled, 35 cm core length
71HF	28.05.	02:22			12° 37.460'	119° 23.158'	4283	Eight (8) heat flow stations over tectonically
				14:17	12° 38.219'	119° 20.085'	4207	controlled basin structure; each ca. 1 km apart
72SL	28.05.	18:51	20:15	22:00	12° 55.597'	119° 08.833'	4294	853 cm core length
73KG	28.05.	22:03	23:22	00:56	12° 55.601'	119° 08.829'	4295	41 cm core length, no nodules
74MUC	29.05.	01:07	02:44	04:25	12° 55.601'	119° 08.830'	4295	12/12 tubes filled, 37 cm core length
Leaving the working area due to hurricane "Andres", sail to 10° N / 120° W, principally to wait for the hurricane to pass by								
75EMPS	29.05.	20:39			09° 59.366'	119° 59.990'	4359	EM 122 mapping to select area without
	30.05.			11:45	09° 52.020'	120° 35.110'	4379	seamount for HF calibration
76HF-	30.05.	19:01			09° 52.027'	120° 32.098'	4420	Test of BGR-Heat Flow Lance; aborted due to
BGR				20:00	09° 52.036'	120° 32.101'	4420	technical problems
77HF	30.05.	20:37			09° 52.033'	120° 32.104'	4405	Four (4) heat flow stations for calibration
	31.05.			03:23	09° 52.034'	120° 31.197'	4360	without seamount influence; ea. ~ 0.5 km apart

SO240 cruise report – Chapter 6 Work and sampling progress during the cruise

Table 6.2. continued

Station SO-240	Date 2015	UTC			Position		Water depth [m]	Remarks
		start	bottom	end	latitude (N)	longitude (W)		
78KG	31.05.	13:41	15:08	16:51	09° 52.017'	120° 32.010'	4414	~20 cm indurated sediment, 1 crust, no nodules
Transit	31.05.	17:00			09° 52.017'	120° 32.010'		Transit to working area 4
	01.06			17:00	11° 45.997'	116° 32.005'		
79CTD	01.06.	17:26	18:26	19:09	11° 45.997'	116° 32.005'	4327	CTD to 2000 m for EM122 calibration
80EM	01.06.	19:34			11° 45.584'	116° 31.839'		EM 122 mapping of basin in WA-4 to identify
				22:38	11° 46.000'	116° 29.000'		small pits (black spots in side-scan sonar)
81SL	01.06.	23:21	00:45	02:13	11° 50.064'	116° 32.890'	4355	1346 cm core length
82SCS	02.06.	03:50			11° 42.977'	116° 26.596'		Three (3) seismic profiles over working area 4 &
				14:29	11° 49.285'	117° 17.284'		5, total length: 95 km
83TC	02.06.	17:59		20:27	11° 50.450'	116° 57.427'	4098	Recovery of thermistor chain of SO239 # 2
84OBM	02.06.	20:19		21:27	11° 51.355'	116° 58.704'	4093	Recovery of mooring KM14-037OBM
85OBM	02.06.	22:11		23:08	11° 49.245'	116° 56.837'	4112	Recovery of mooring KM14-035OBM
86OBM	02.06.	23:42		00:30	11° 54.064'	116° 57.842'	4107	Recovery of mooring KM14-034OBM
87HF	03.06.	02:36			11° 50.078'	116° 32.868'	4351	Six (6) heat flow stations over small basins with
				13:00	11° 48.063'	116° 31.135'	4313	with black spots; each ca. 1 km apart
88OBM	03.06.	15:27		16:29	11° 50.954'	117° 01.195'	4135	Recovery of mooring KM14-036OBM
89DOS	03.06.	17:00		18:53	11° 51.826'	116° 59.992'	4112	Recovery of SO239 # 44 DOS-2 lander
90BoBo	03.06.	19:18		21:30	11° 51.029'	116° 59.526'	4121	Recovery of SO239 # 4 BoBo lander
91KG	03.06.	22:04	23:18	00:54	11° 49.263'	117° 03.835'	4131	42 cm core length, 21.3 kg/m ² small-med. nod.
92HF	04.06.	01:15			11° 49.251'	117° 03.344'	4129	Six (6) heat flow stations over distinct fault
				12:31	11° 49.265'	117° 06.068'	4138	structures; each ca. 1 km apart
93CTD	04.06.	13:35			11° 53.850'	116° 57.783'	4101	CTD tow-yo station for JPI-O, tow yo between
Tow-Yo	05.06.			06:31	11° 49.089'	117° 02.971'	4132	50 and 500 m above bottom @ 0.5 m/s, 0.5 kn
94HF	05.06.	07:43			11° 49.262'	117° 12.673'	4153	Five (5) heat flow stations over distinct fault
				15:14	11° 49.277'	117° 14.288'	4157	structure near seamounts; each ca. 1 km apart
95MUC	05.06.	16:49	18:24	20:11	11° 49.262'	117° 13.197'	4150	12/12 tubes filled, 31 cm core length
96SL	05.06.	20:11	21:37	23:20	11° 49.260'	117° 13.195'	4145	980 cm core length
97CTD	06.06.	00:45			11° 51.490'	117° 00.233'	4118	JPI-O station, vessel at station, 4 cycles through
Yo-Yo	06.06.			14:34	11° 51.493'	117° 00.188'	4116	complete water column @ 0.7 m/s
98OBM	06.06.	15:13		15:16	11° 53.915'	116° 57.733'	4108	Redeployment of mooring KM14-034OBM
99OBM	06.06.	16:01		16:04	11° 48.987'	116° 56.669'	4120	Redeployment of mooring KM14-035OBM
100OBM	06.06.	17:12		17:16	11° 50.619'	117° 01.184'	4122	Redeployment of mooring KM14-036OBM
101OBM	06.06.	18:25		18:32	11° 50.447'	116° 58.317'	4088	Redeployment of mooring KM14-037OBM
102OBM	06.06.	19:03		22:21	11° 50.673'	116° 58.324'	4087	Triangulation of mooring positions
103SL	06.06.	23:08	00:26	02:14	11° 49.253'	117° 03.847'	4137	977 cm core length; for permeability analysis
104LIR	07.06.	02:22	03:52	10:18	11° 49.272'	117° 03.840'	4133	In situ shear strength of sediments @4 locations
105EM	07.06.	10:24			11° 49.332'	117° 04.546'	4134	EM 122 mapping of central working area 4
				15:11	11° 45.426'	116° 34.230'	4073	
106MUC	07.06.	15:49	17:27	19:18	11° 50.079'	116° 32.900'	4351	12/12 tubes filled, 40 cm core length
107KG	07.06.	19:20	20:49	22:20	11° 50.070'	116° 32.907'	4351	43 cm core length, nodule layers at 16, 36 cm
108SL	07.06.	22:57	00:20	02:04	11° 48.796'	116° 31.767'	4326	1038 cm core length
109MUC	08.06.	02:12	03:46	05:35	11° 48.791'	116° 31.760'	4327	12/12 tubes filled, 37 cm core length
110EM	08.06.	06:27			11° 55.723'	116° 33.200'	4017	EM 122 mapping of central working area 4
				09:22	11° 54.374'	116° 56.731'	4107	
111CTD	08.06.	09:57			11° 50.393'	116° 56.673'	4131	JPI-O station, vessel at station, 4 cycles through
Yo-yo	09.06.			02:10	11° 49.670'	116° 56.331'	4115	complete water column @ 0.7 m/s
112EM	09.06.	02:47			11° 54.370'	116° 56.500'	4100	EM 122 mapping of central working area 4
				04:16	11° 54.540'	117° 08.709'	4114	
Transit to working area 1 (Teddy Bare Seamount) at 13° 11.116' N / 118° 05.137' W								
113STR	09.06.	14:04	15:35B		13° 11.453'	118° 05.231'	4222	Video mapping along western basis of small
			19:43E	21:30	13° 10.723	118° 05.216'	4161	seamount north of Teddy Bare SMt.
114HF	09.06.	22:08			13° 11.092'	118° 06.004'	4266 m	Heat flow station at Teddy Bare Seamount;
-BGR				02:05	13° 11.106'	118° 05.772'	4258 m	aborted at first waypoint due to tech. problems
115HF	10.06.	02:44			13° 11.103'	118° 05.770'	4256	Eight(8) heat flow stations along foot of small
-BGR				15:30	13° 10.710'	118° 05.300'	4214	seamount north of Teddy Bare SMt.
116MUC	10.06.	15:58	17:40	19:21	13° 11.098'	118° 06.003'	4270	12/12 tubes filled, 31 cm core length

Table 6.2. continued

Station SO-240	Date 2015	UTC			Position		Water depth [m]	Remarks
		start	bottom	end	latitude (N)	longitude (W)		
117SL	10.06.	19:30	20:56	22:42	13° 11.103'	118° 05.992'	4271	Ca. 6 m core length, steel pipe bent
118KG	10.06.	22:52	00:12	01:46	13° 11.102'	118° 05.996'	4272	40 cm core length, 12.6 kg/m ² small nodules
119CTD	11.06.	02:45		05:25	13° 17.488°	118° 10.806°	3502	CTD station over larger seamount
120 GDS	11.06.	06:41	07:55B		13° 09.077°	118° 12.660	4010	Sampling at seamount in WA-1
			11:01E	12:27	13° 09.349°	118° 12.894°	3786	only Fe-Mn crusts sampled, no rocks
121MUC	11.06.	13:24	15:00	16:50	13° 11.235°	118° 03.624°	4268	12/12 tubes filled, 23 cm core length

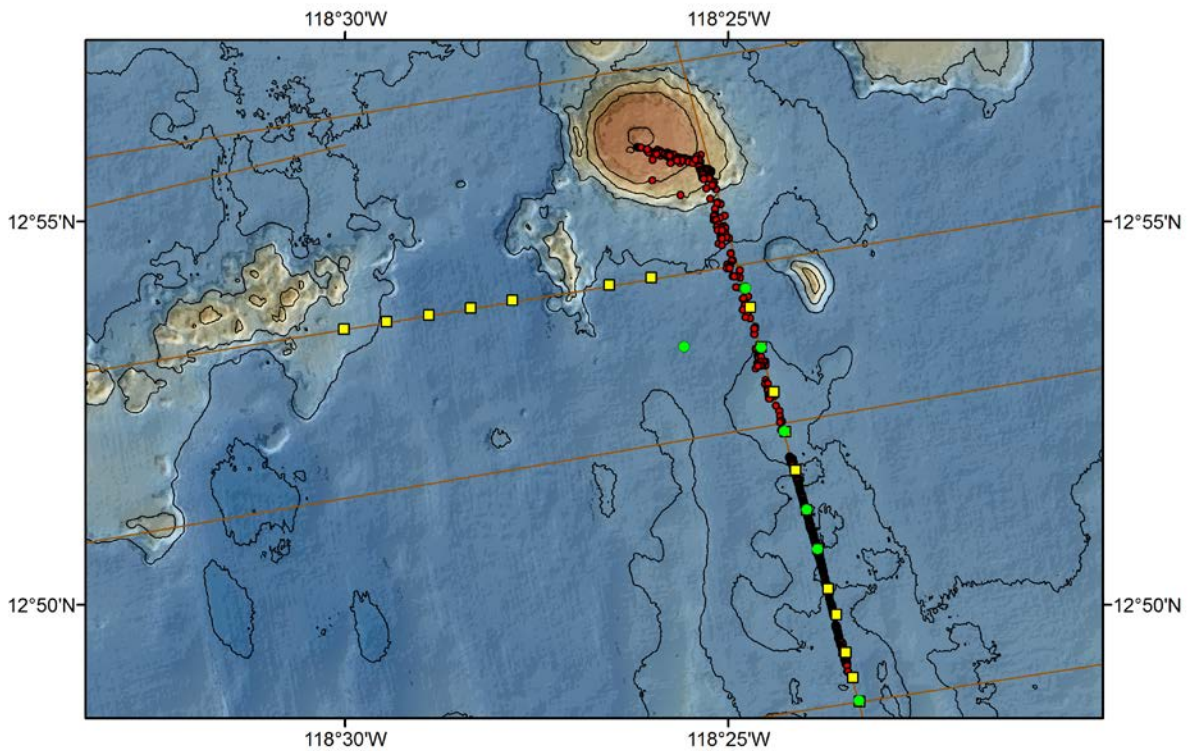


Figure 6.1. Example of the strategy of work in working area 2 (see Fig. 3.2 for the location of WA-2). The investigations started with a seismic-bathymetric survey (brown lines) followed by heat flow profiles along the seismic lines (yellow squares). Positions for sediment and pore water sampling were chosen based on the results of heat flow measurements (green dots). Visual seafloor observations were carried out over areas with combined information on geophysics and geology (red dots).

The following maps document the locations of the different types of stations in each working area.

6.2 WORKING AREA 1

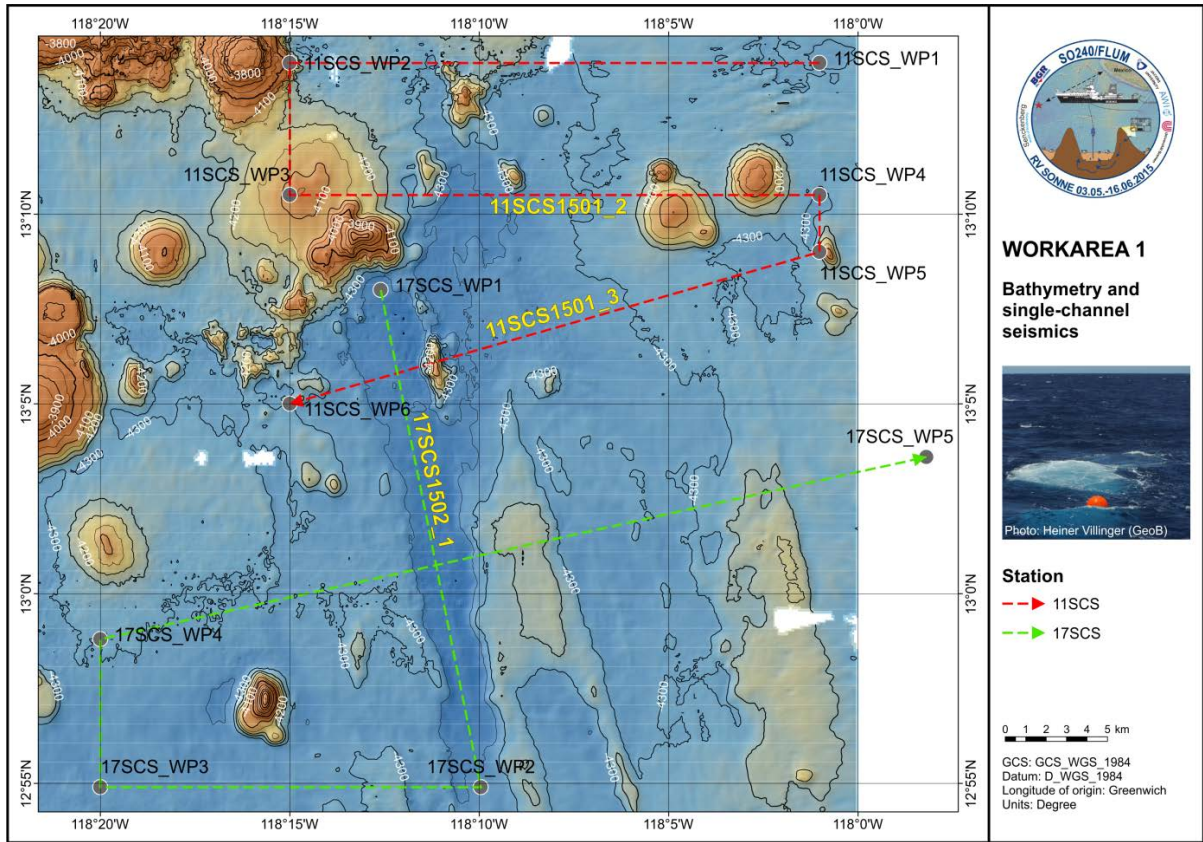


Figure 6.2. Bathymetry and seismic profiles (stations 11SCS and 17SCS) in working area 1.

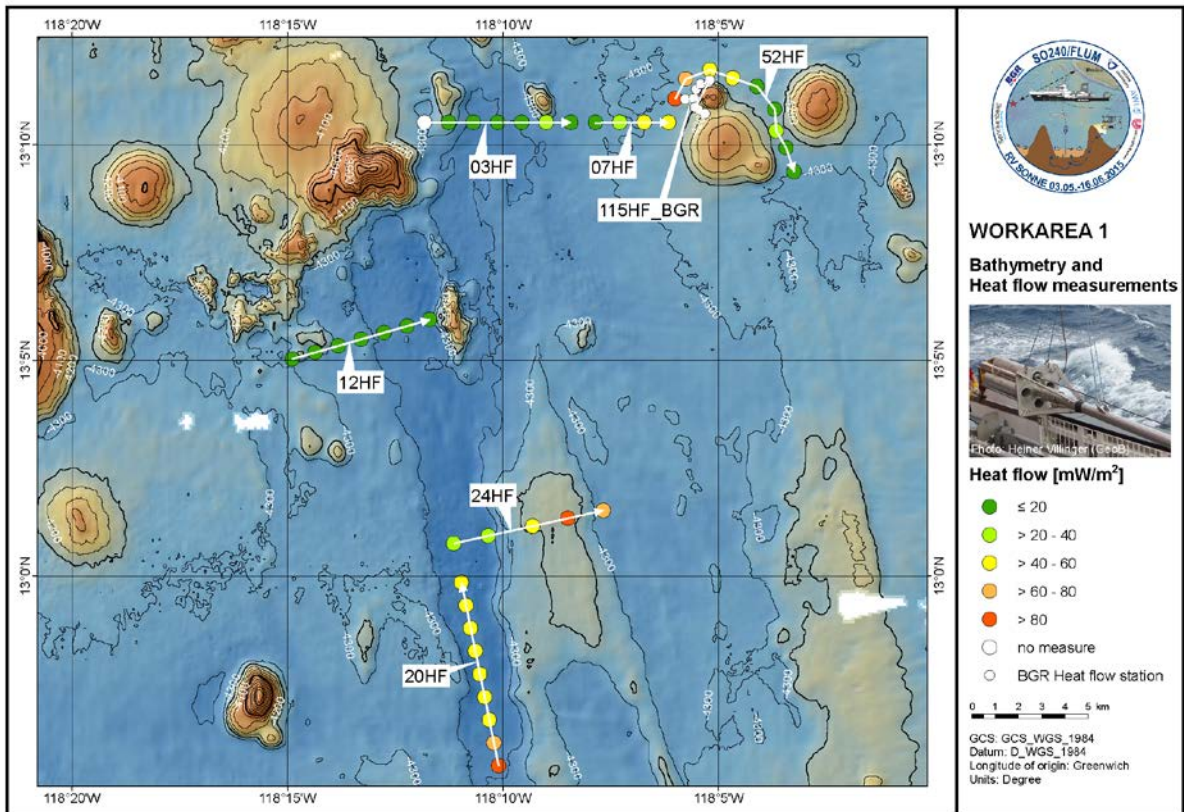


Figure 6.3. Heat flow (HF) stations in working area 1.

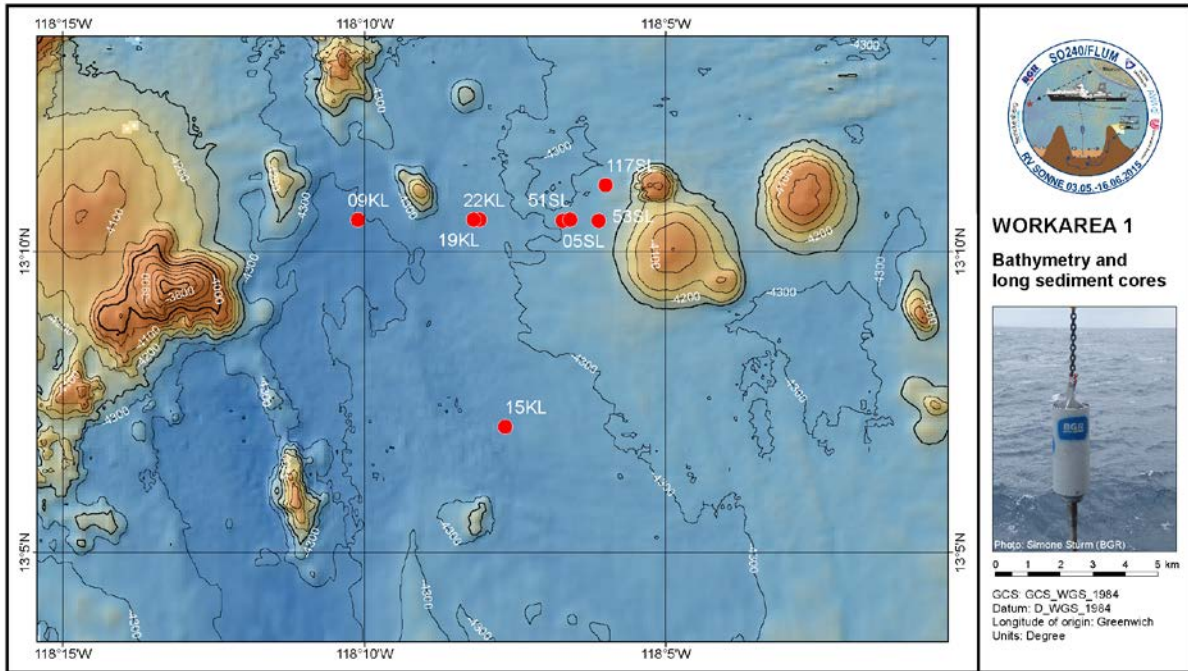


Figure 6.4. Long piston (KL) and gravity (SL) core stations in working area 1.

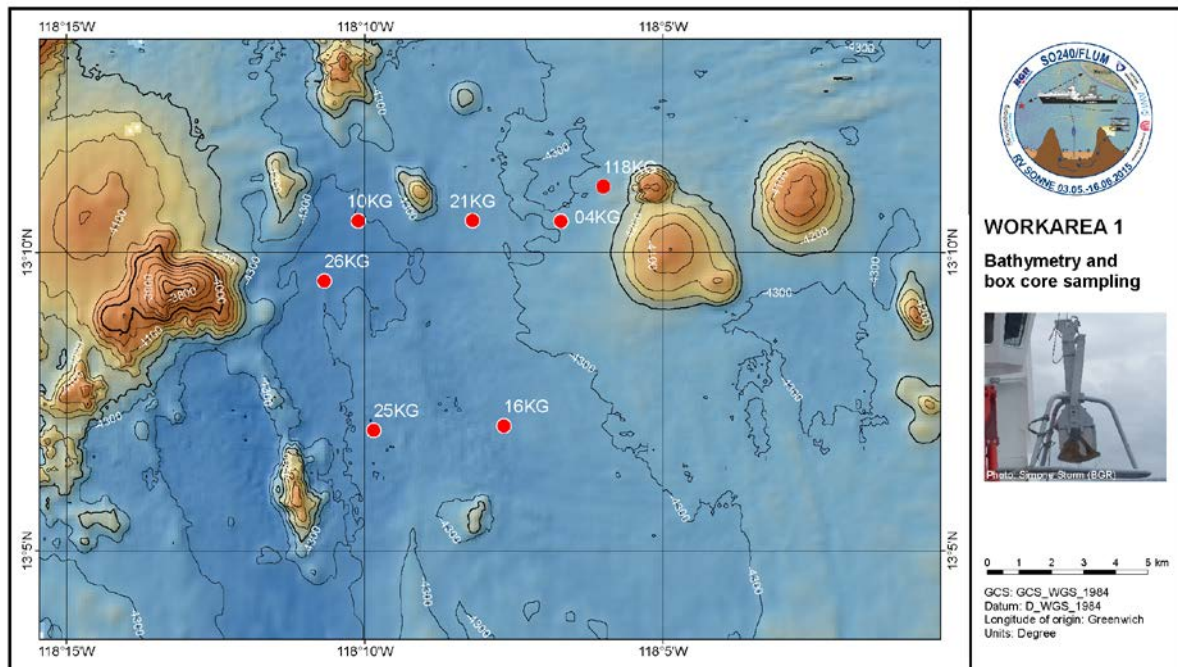


Figure 6.5. Box corer (KG) stations in working area 1.

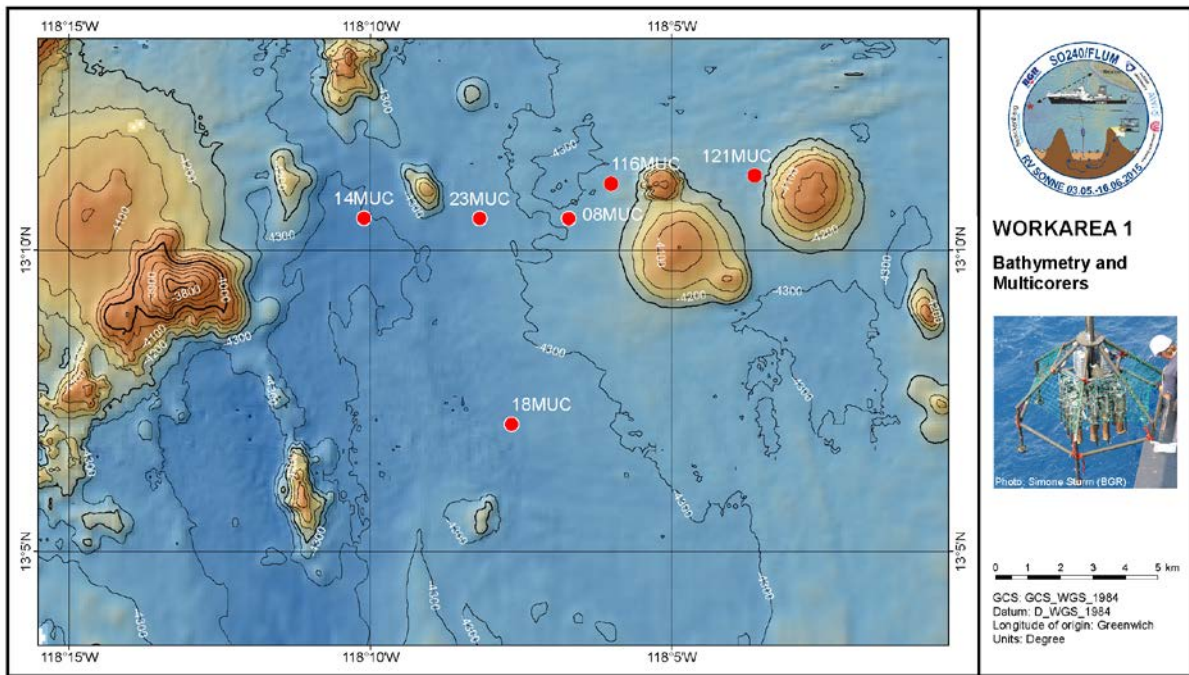


Figure 6.6. Multiple corer (MUC) stations in working area 1.

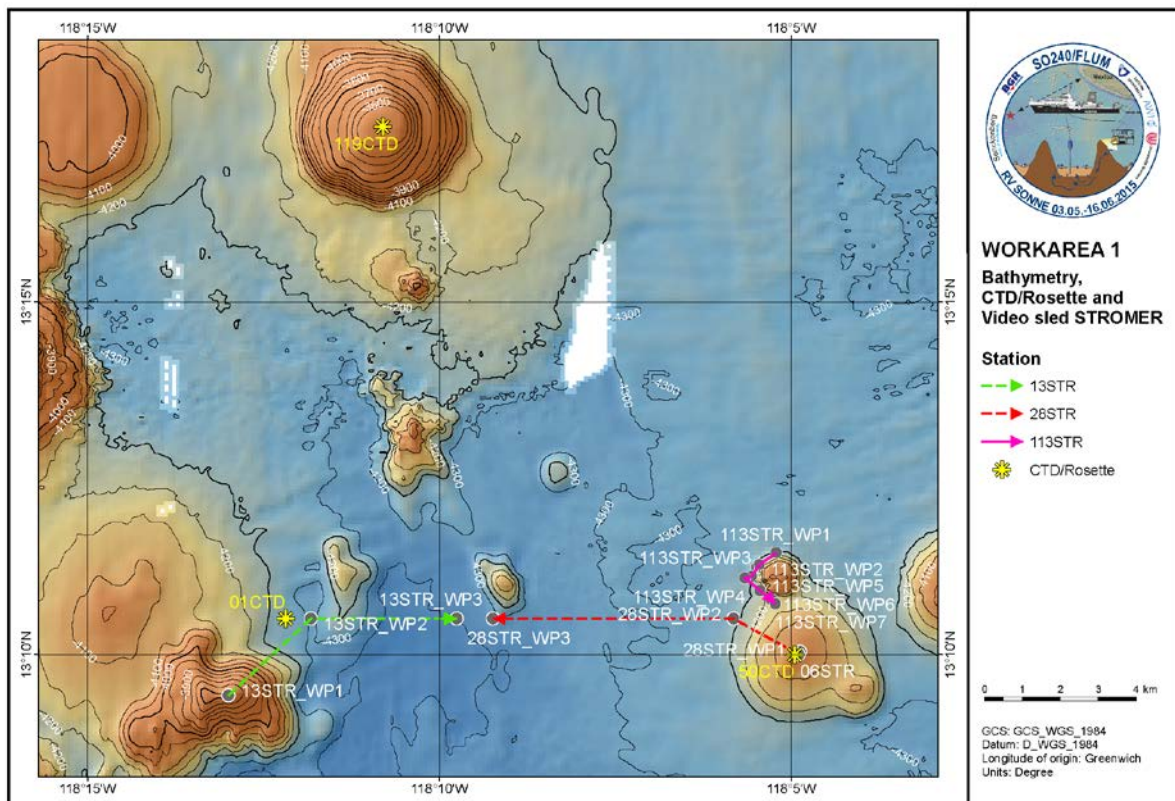


Figure 6.7. CTD/Rosette (CTD) and video (STR) stations in working area 1.

6.3 WORKING AREA 2

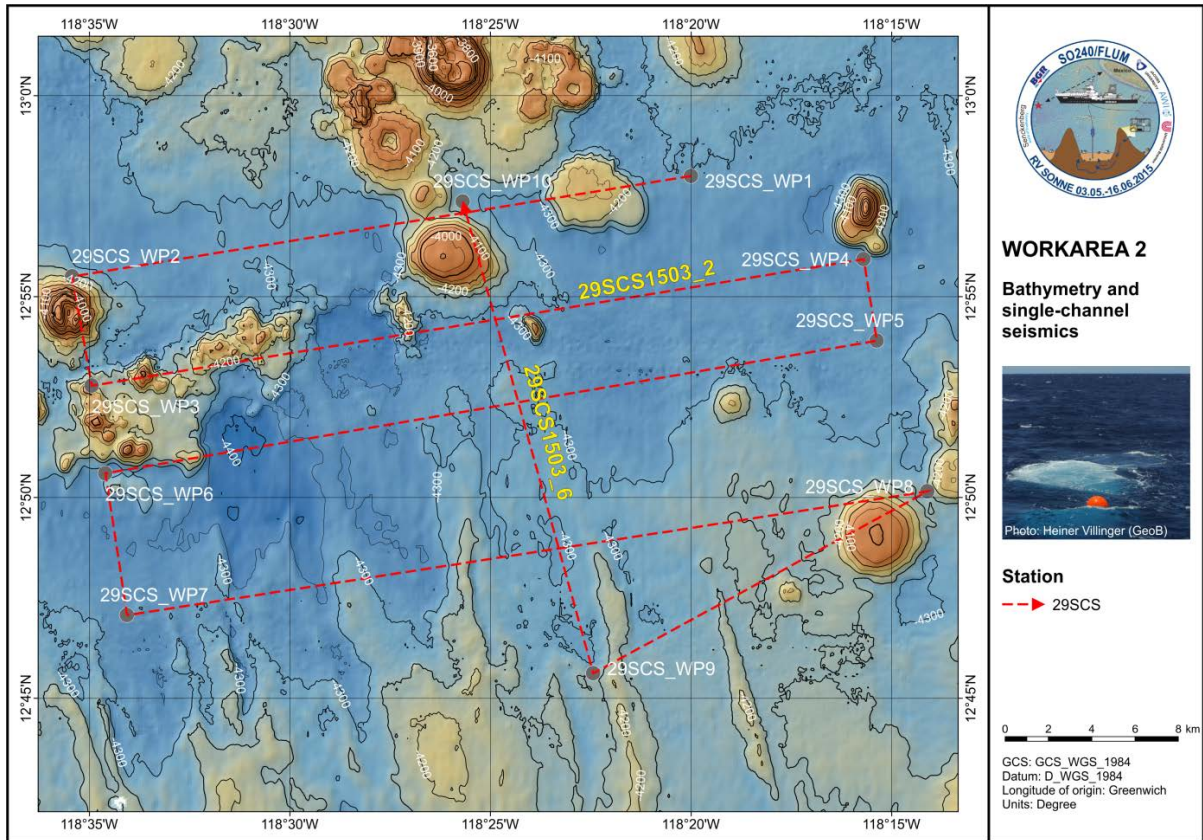


Figure 6.8. Bathymetry and seismic profiles (stations 29SCS) in working area 2.

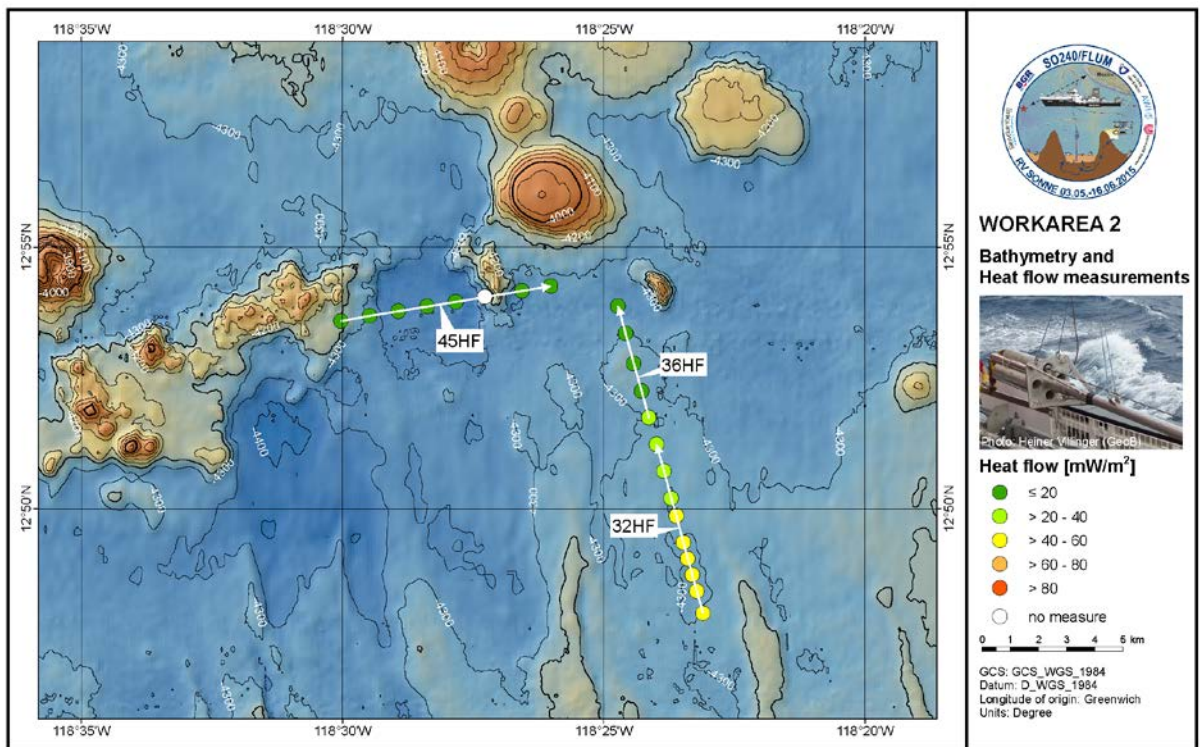


Figure 6.9. Heat flow (HF) stations in working area 2.

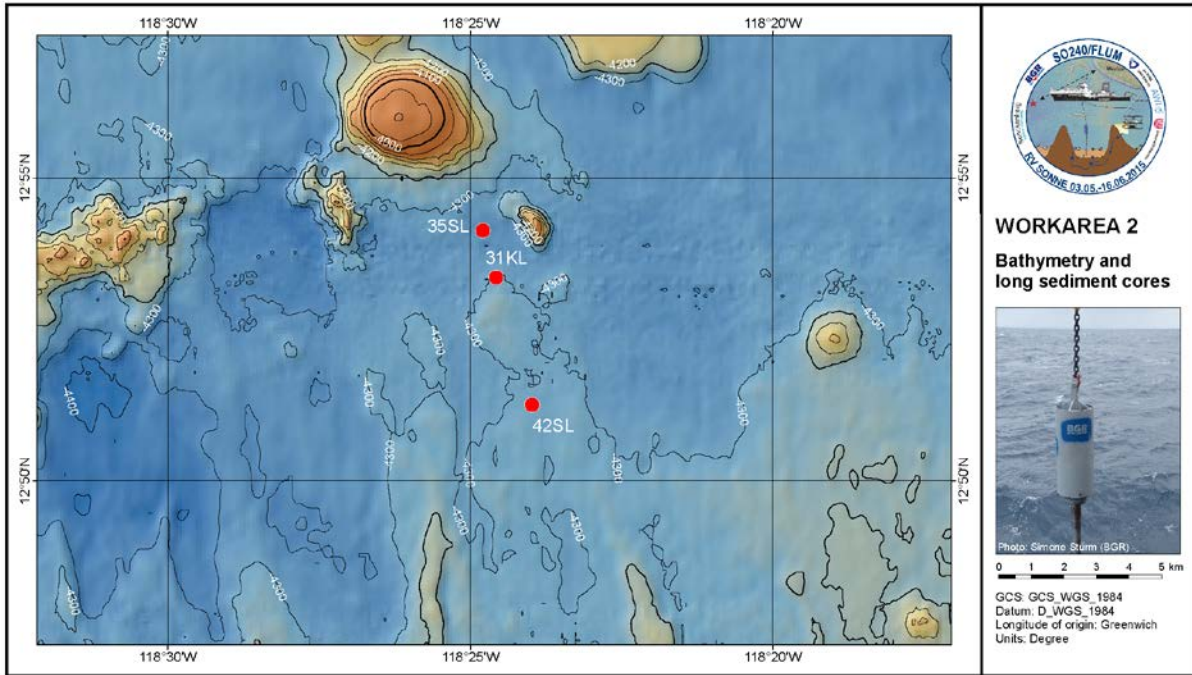


Figure 6.10. Long piston (KL) and gravity (SL) core stations in working area 2.

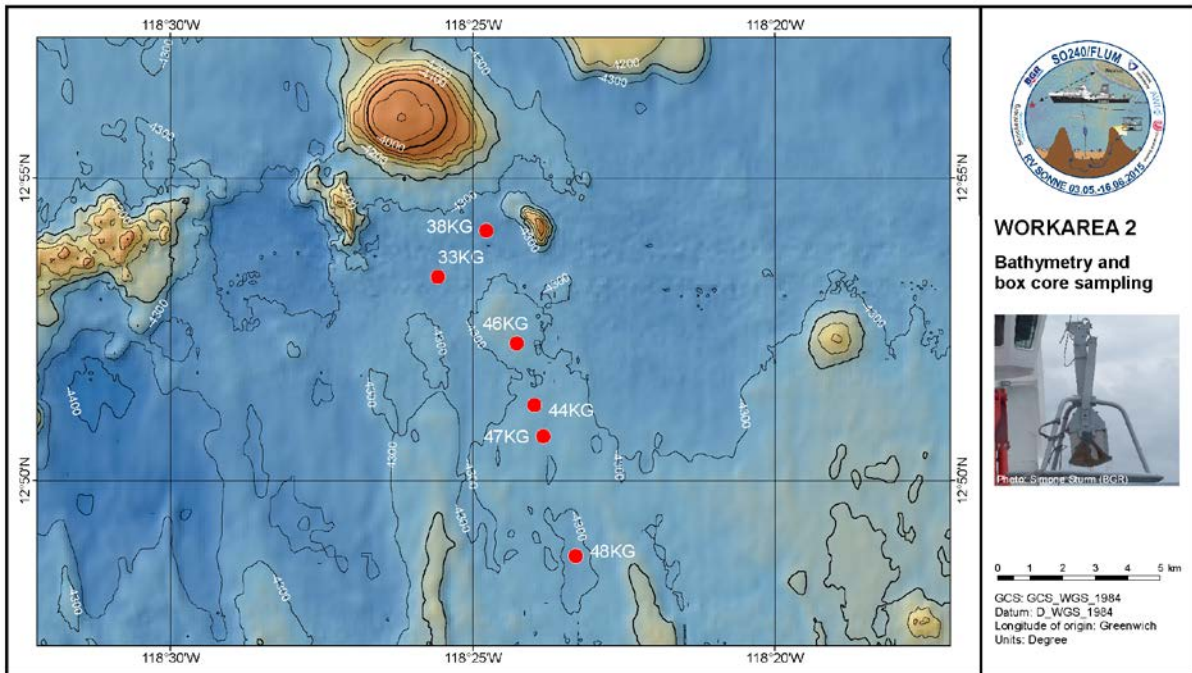


Figure 6.11. Box corer (KG) stations in working area 2.

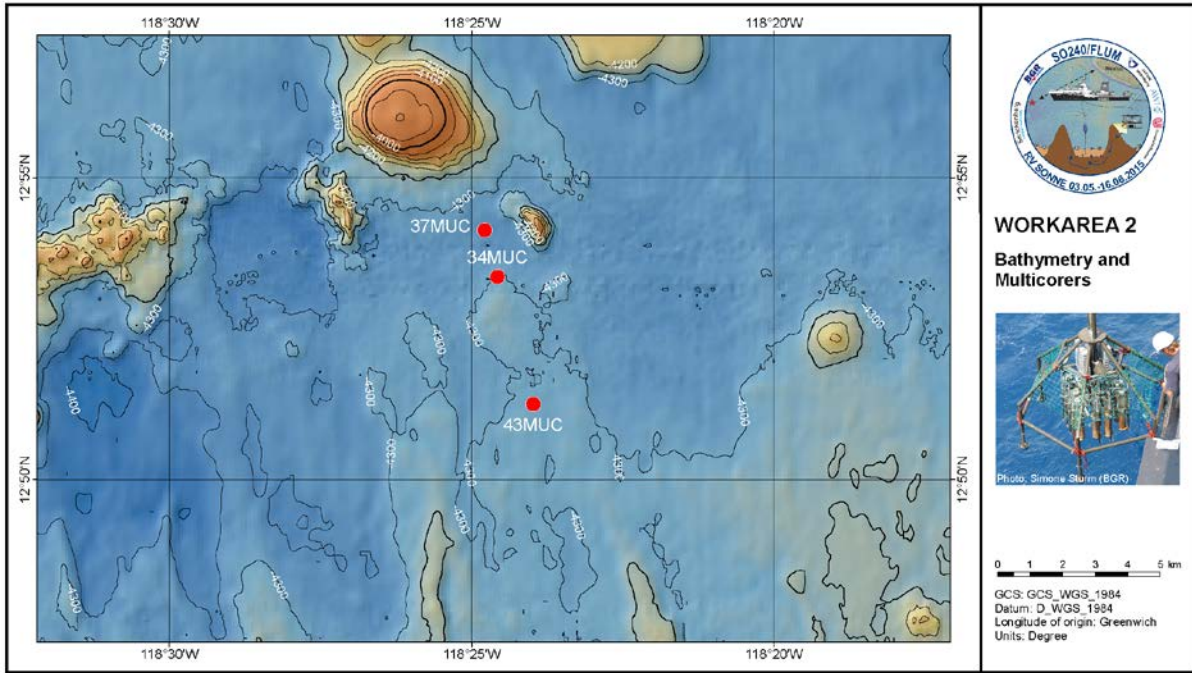


Figure 6.12. Multiple corer (MUC) stations in working area 2.

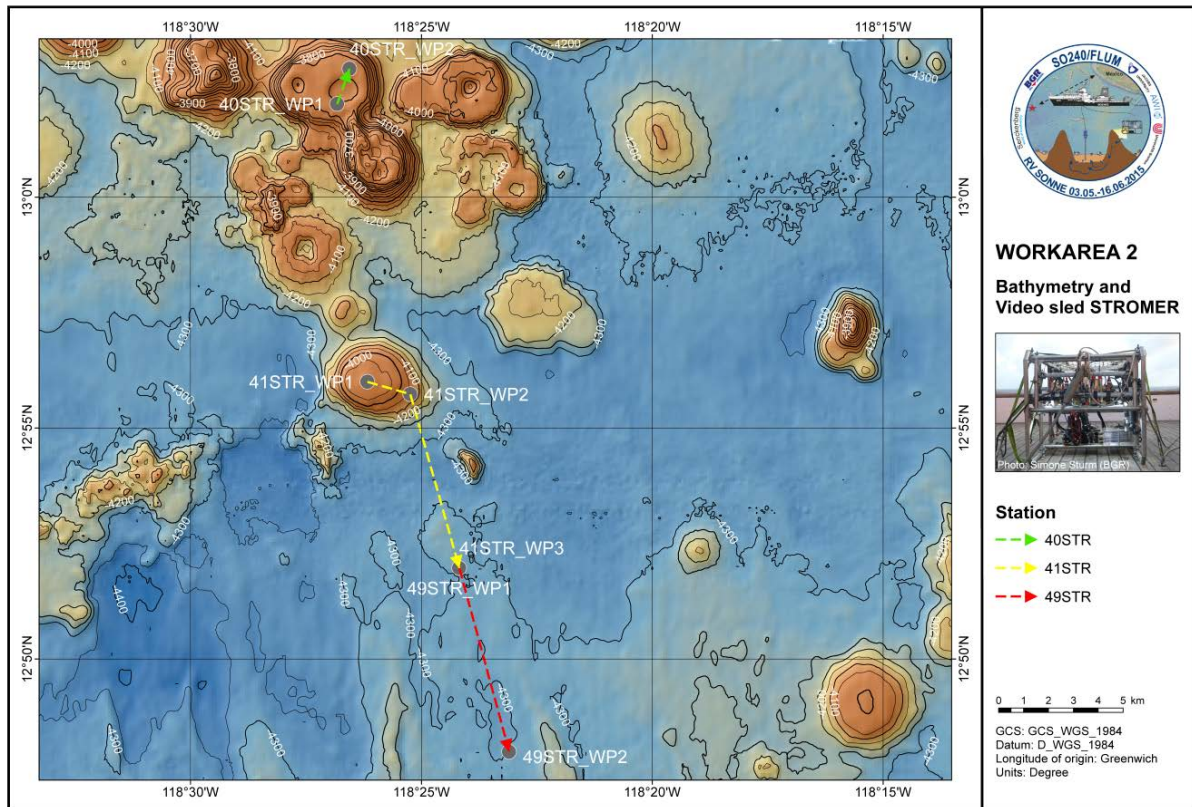


Figure 6.13. Video (STR) stations in working area 2.

6.4 WORKING AREA 3

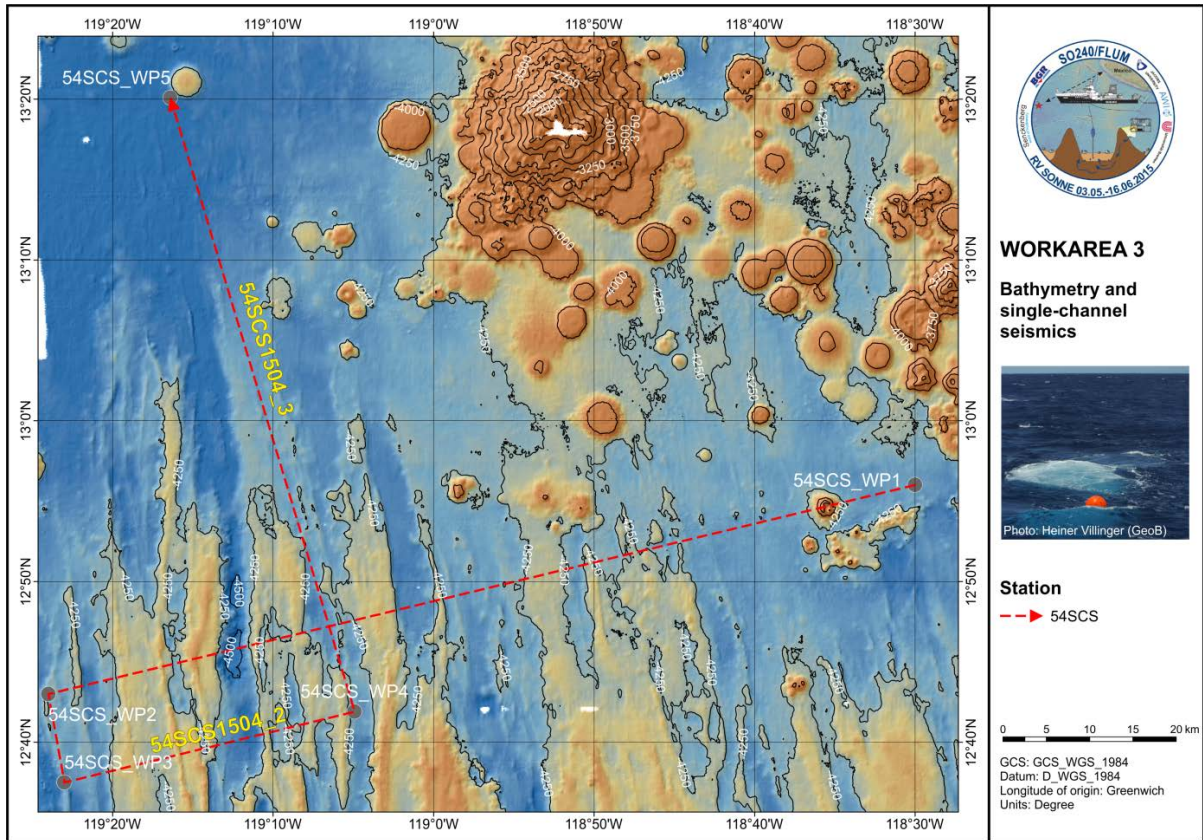


Figure 6.14. Bathymetry and seismic profiles (stations 54SCS) in working area 3.

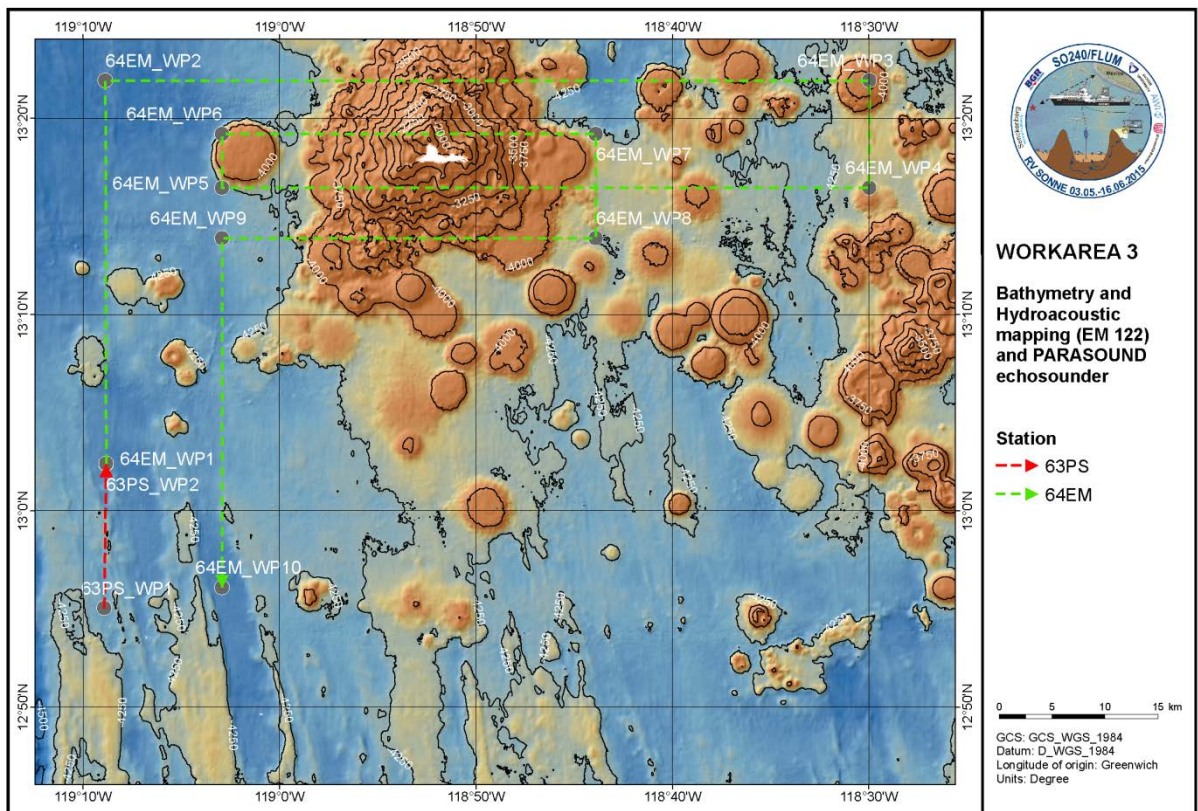


Figure 6.15. Bathymetric survey of a large seamount complex in working area 3.

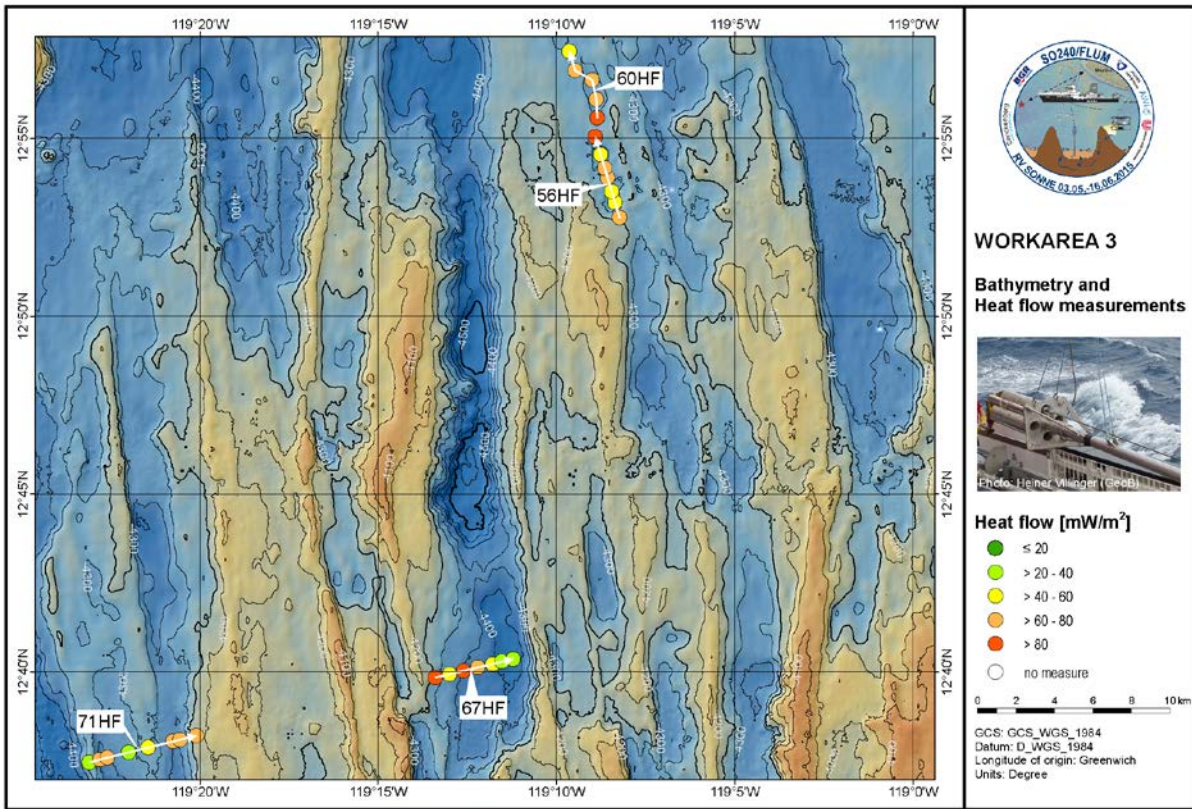


Figure 6.16. Heat flow (HF) stations in working area 3.

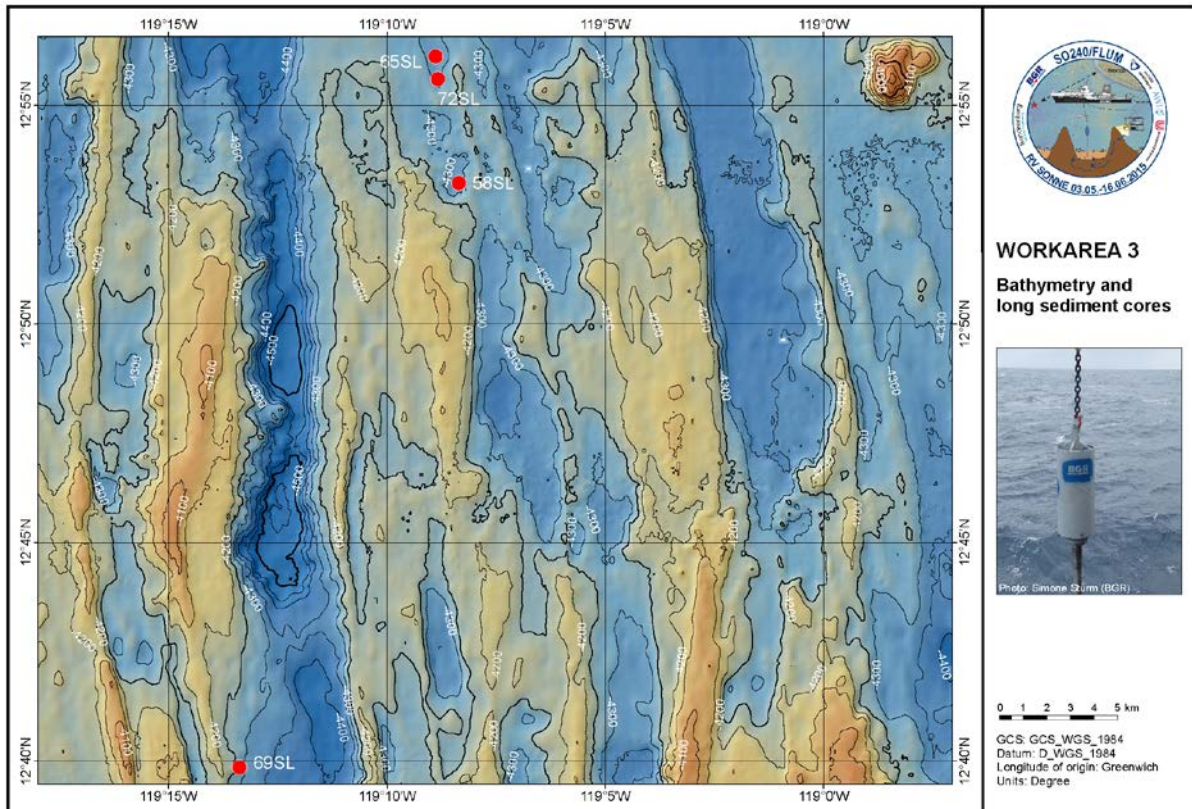


Figure 6.17. Long gravity (SL) core stations in working area 3.

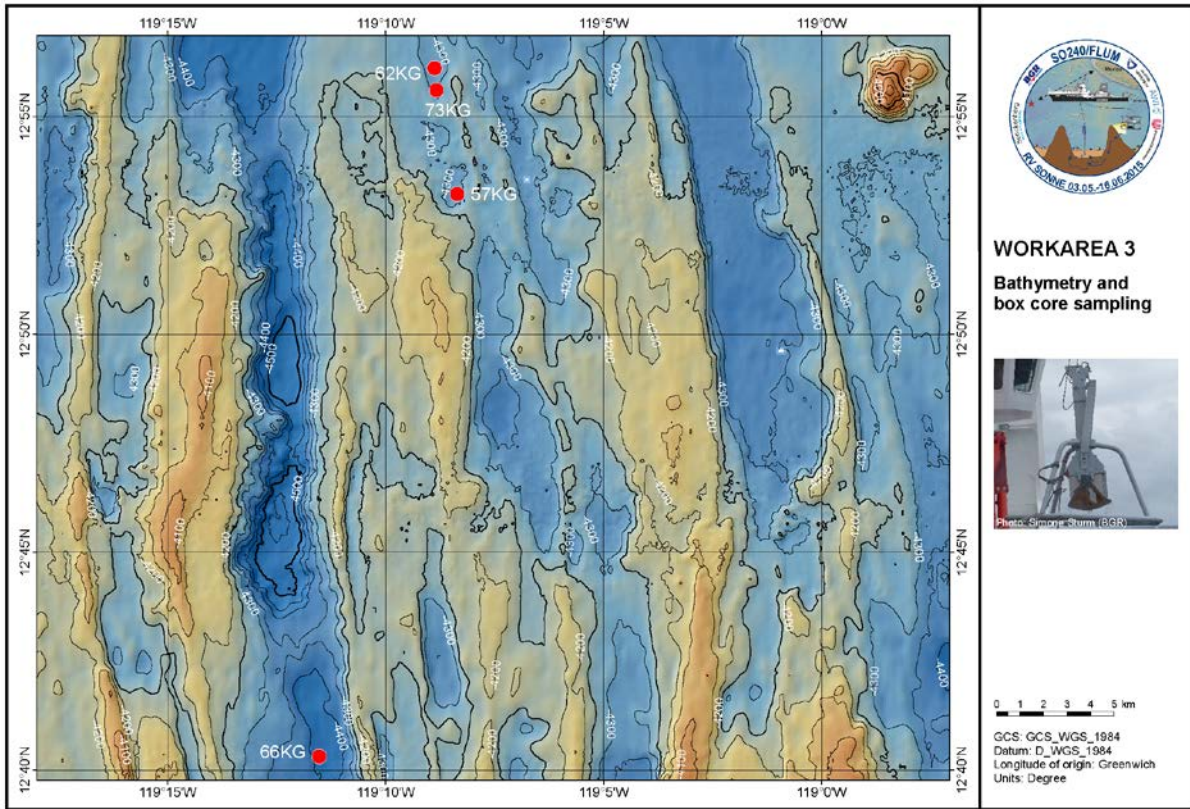


Figure 6.18. Box corer (KG) stations in working area 3.

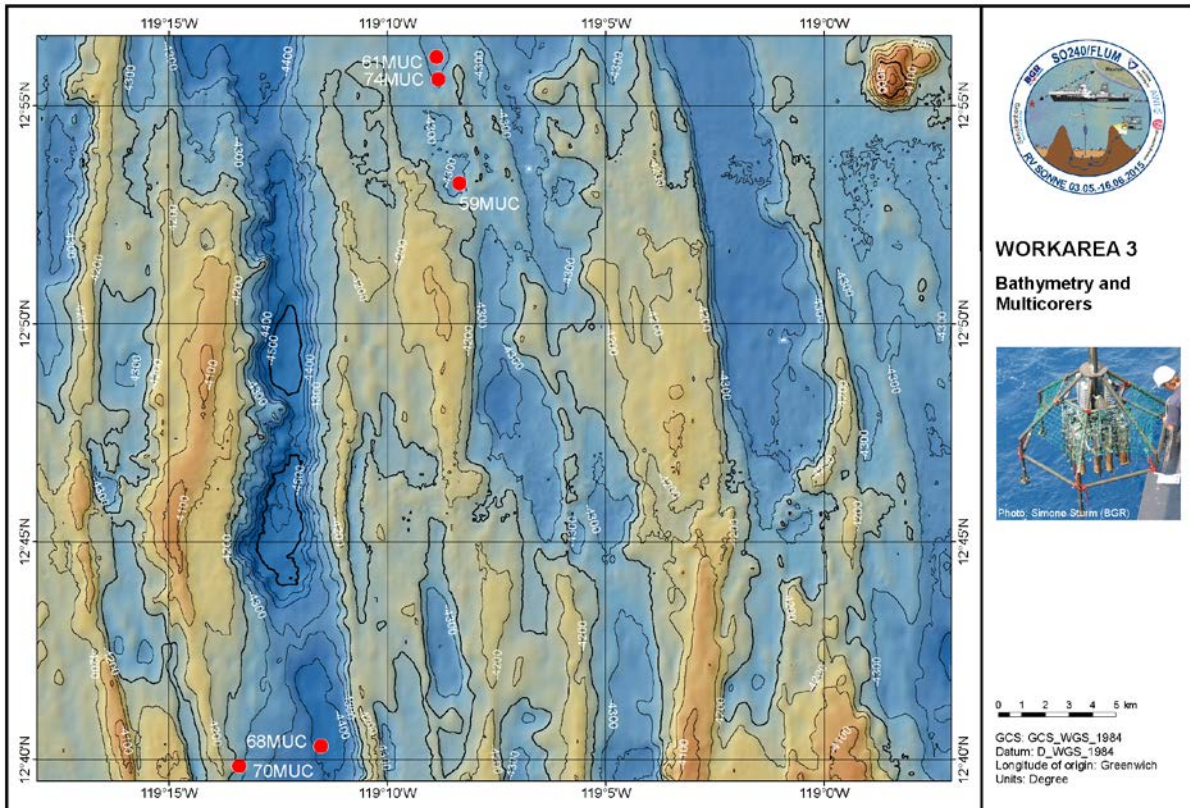


Figure 6.19. Multiple corer (MUC) stations in working area 3.

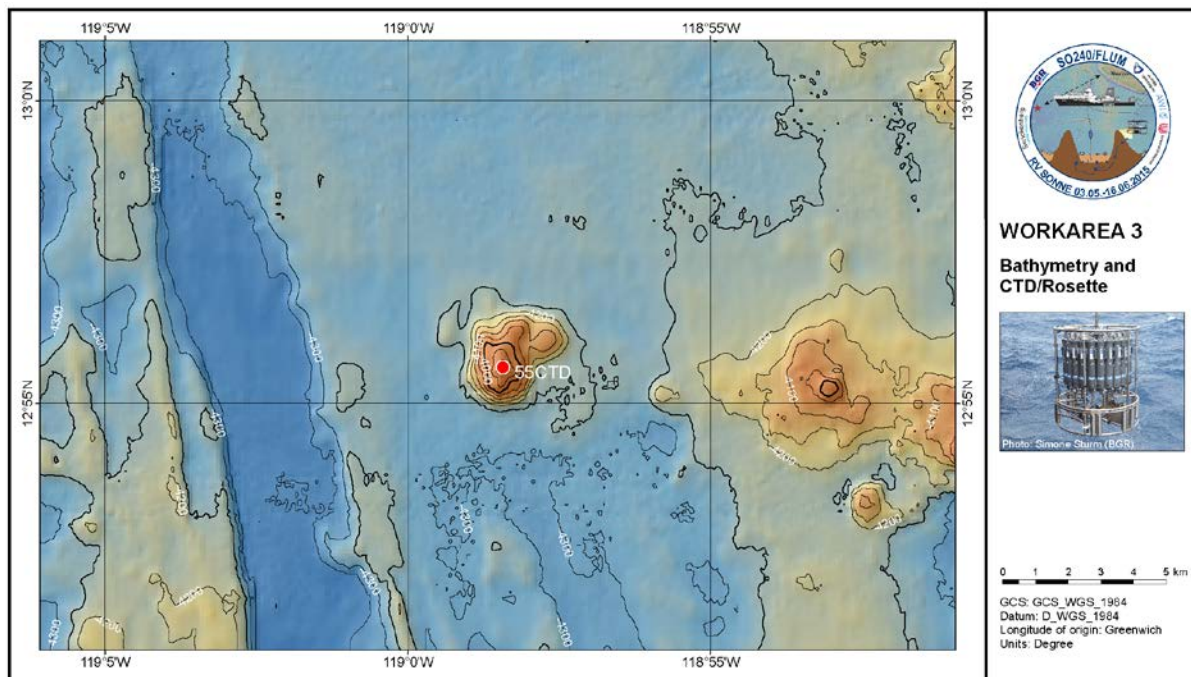


Figure 6.20. CTD/Rosette (CTD) station in working area 3.

6.5 WORKING AREA 4

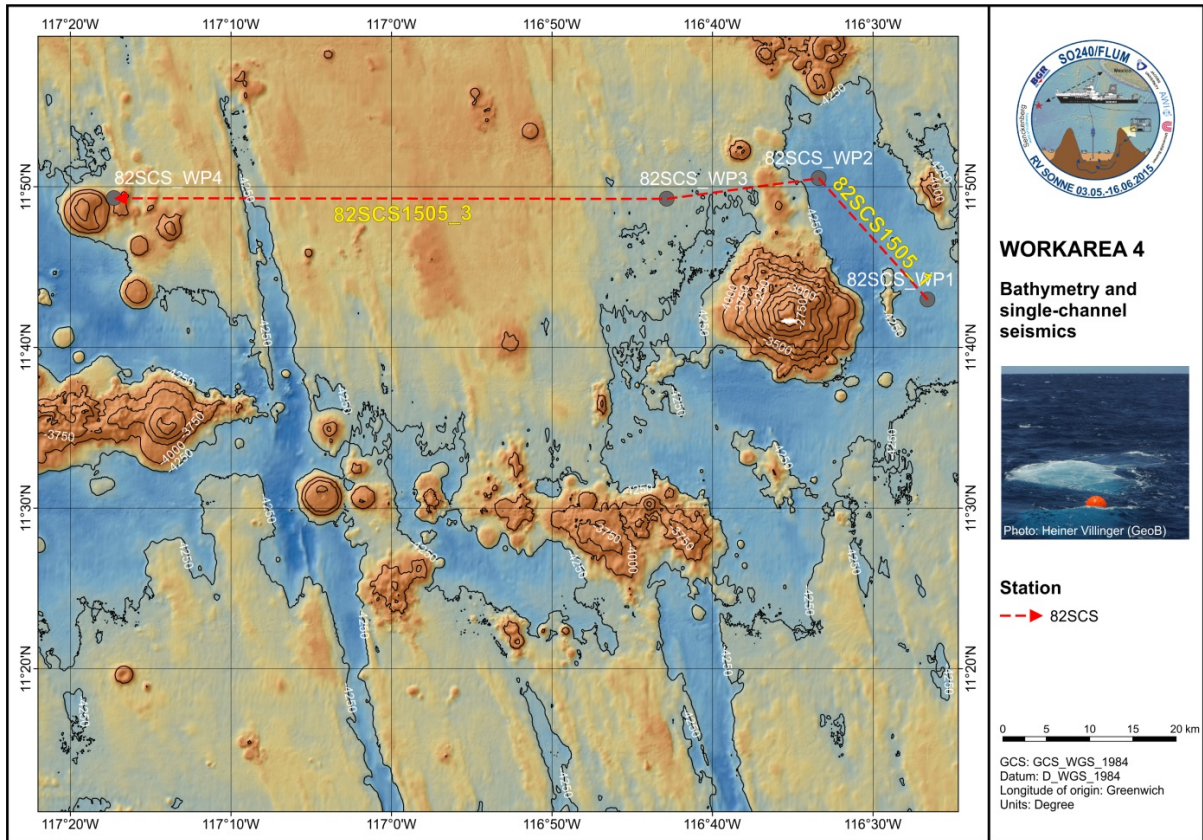


Figure 6.21. Bathymetry and seismic profiles (stations 82SCS) in working area 4.

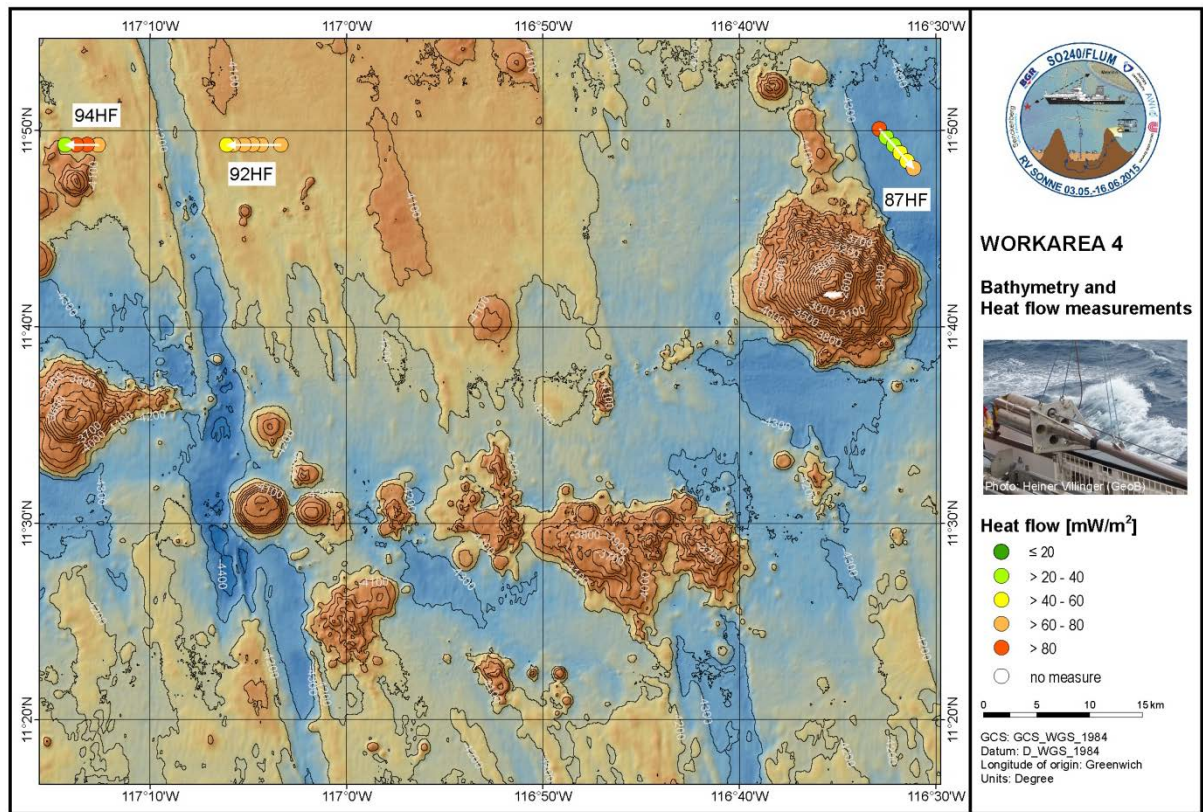


Figure 6.22. Heat flow (HF) stations in working area 4.

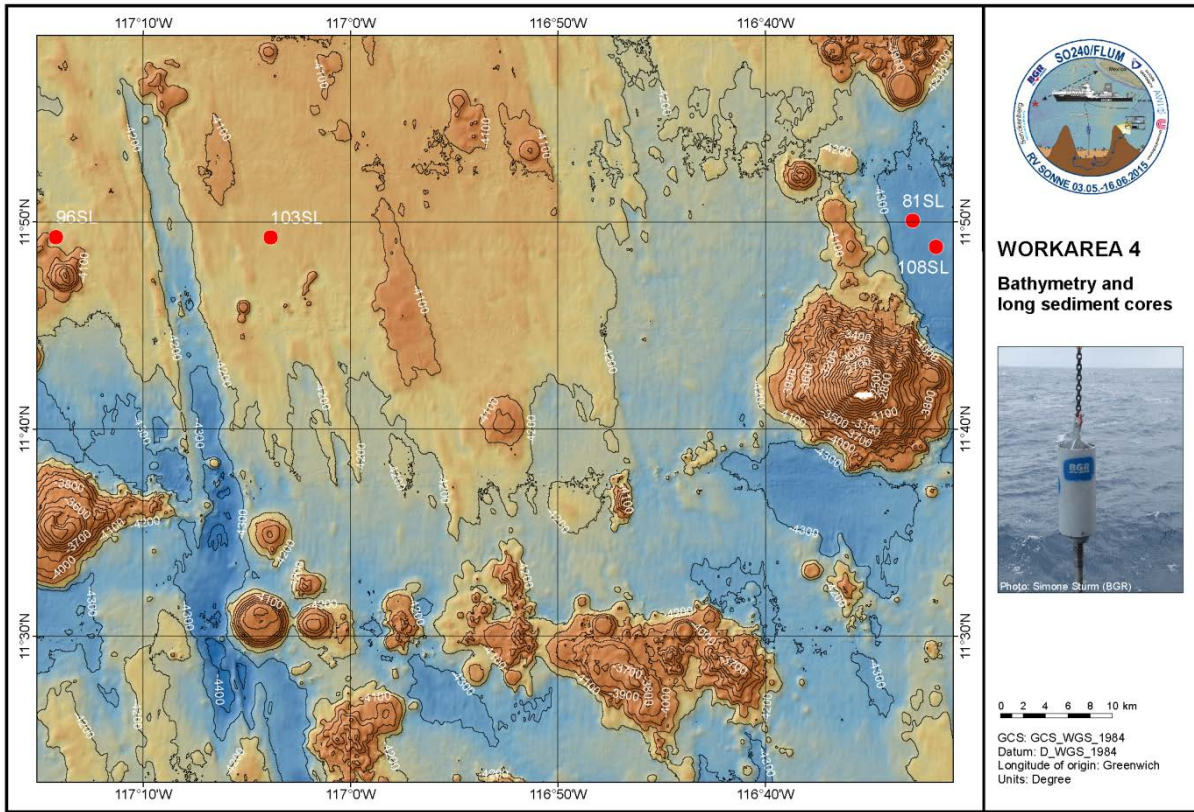


Figure 6.23. Long gravity (SL) core stations in working area 4.

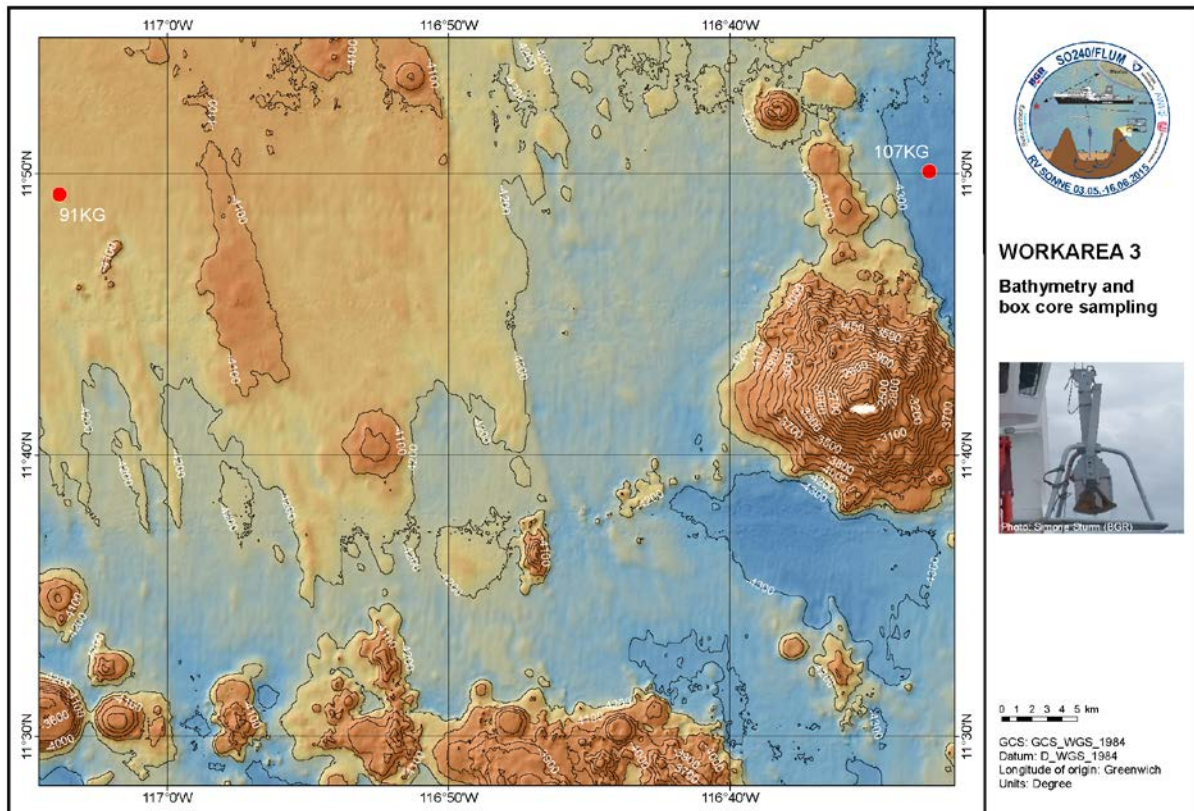


Figure 6.24. Box corer (KG) stations in working area 4.

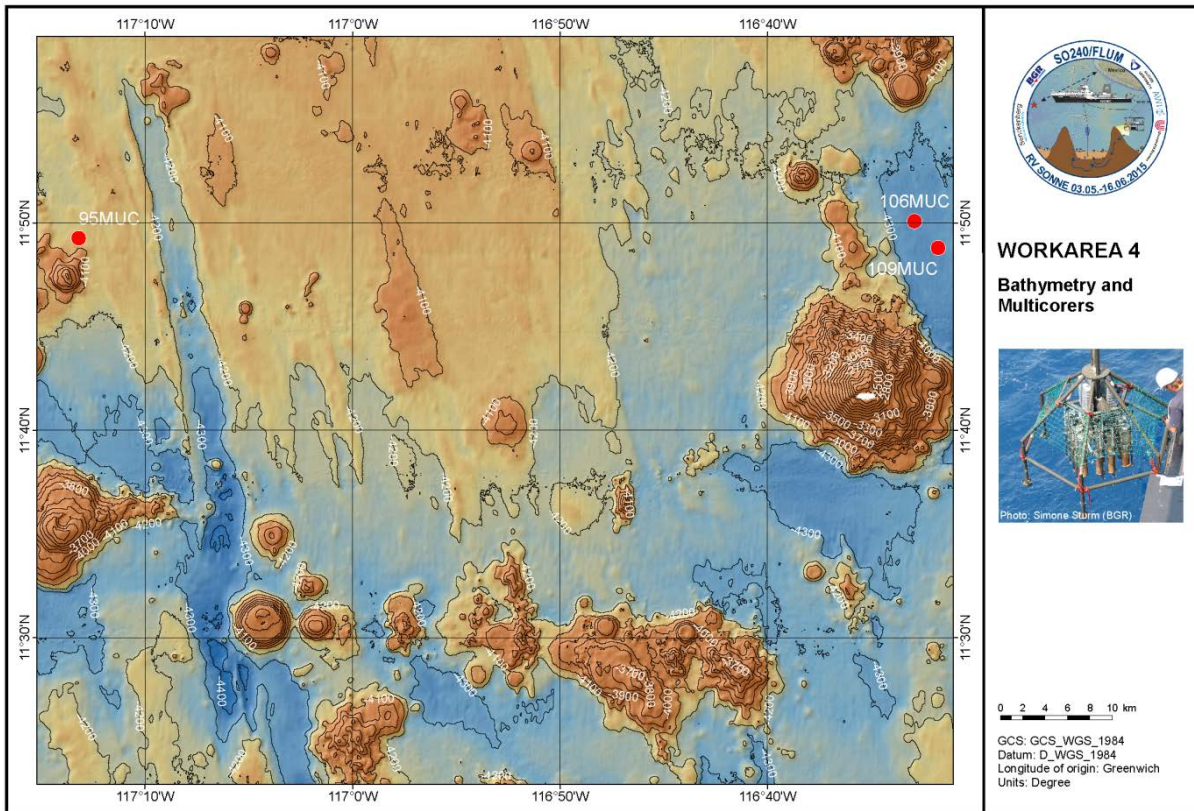


Figure 6.25. Multiple corer (MUC) stations in working area 4.

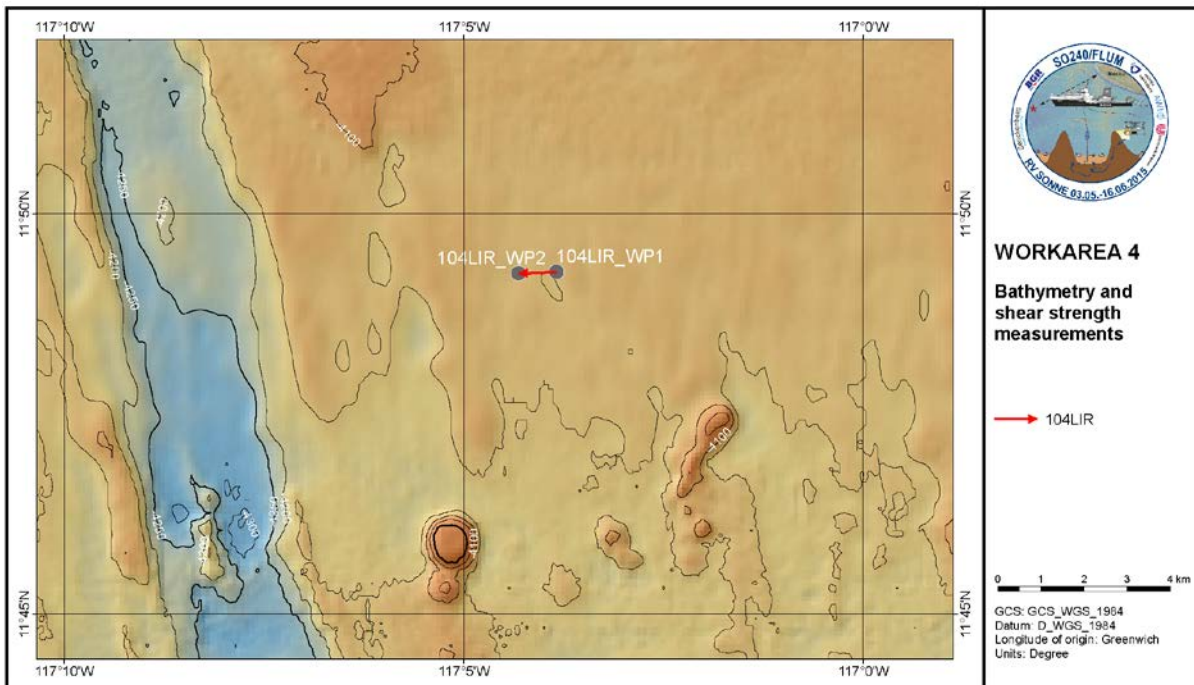


Figure 6.26. In-situ shear strength (LIR) station in working area 4.

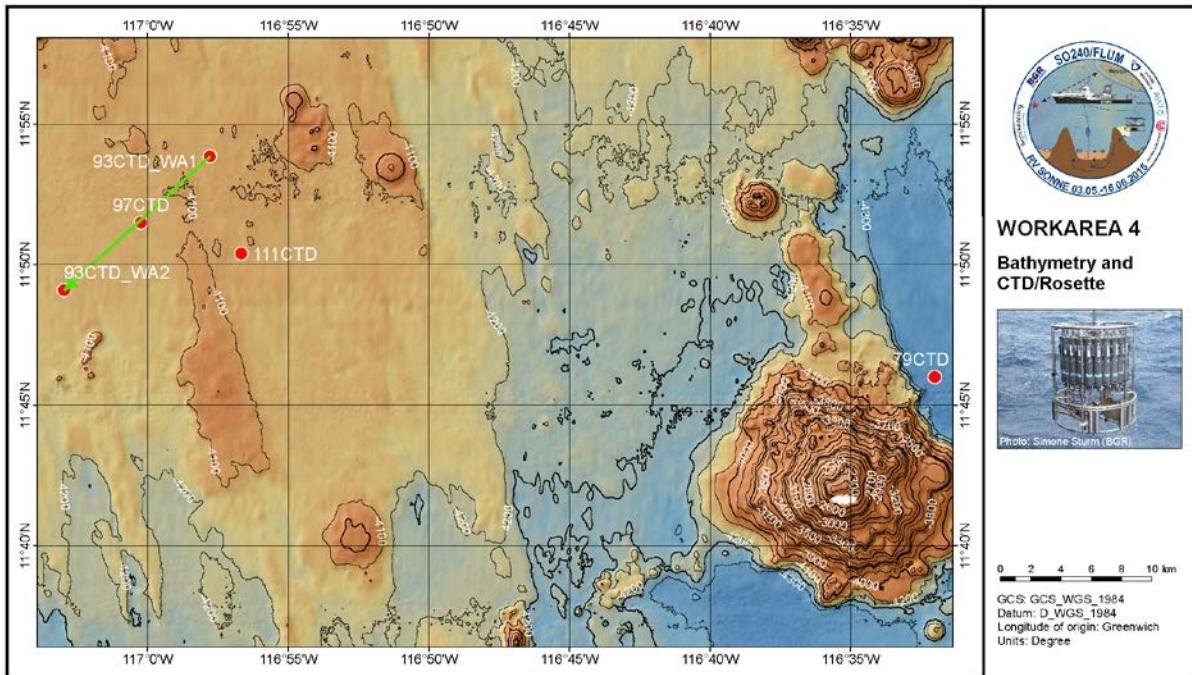


Figure 6.27. CTD/Rosette (CTD) stations in working area 4. Station 93CTD was carried out as tow-yo station, stations 97CTD and 111CTD as yo-yo station. Each station lasted about 13 hours. This work was carried out within the framework of the JPI-Ocean project “EcoResponse” as an add-on program to cruise SO-240.

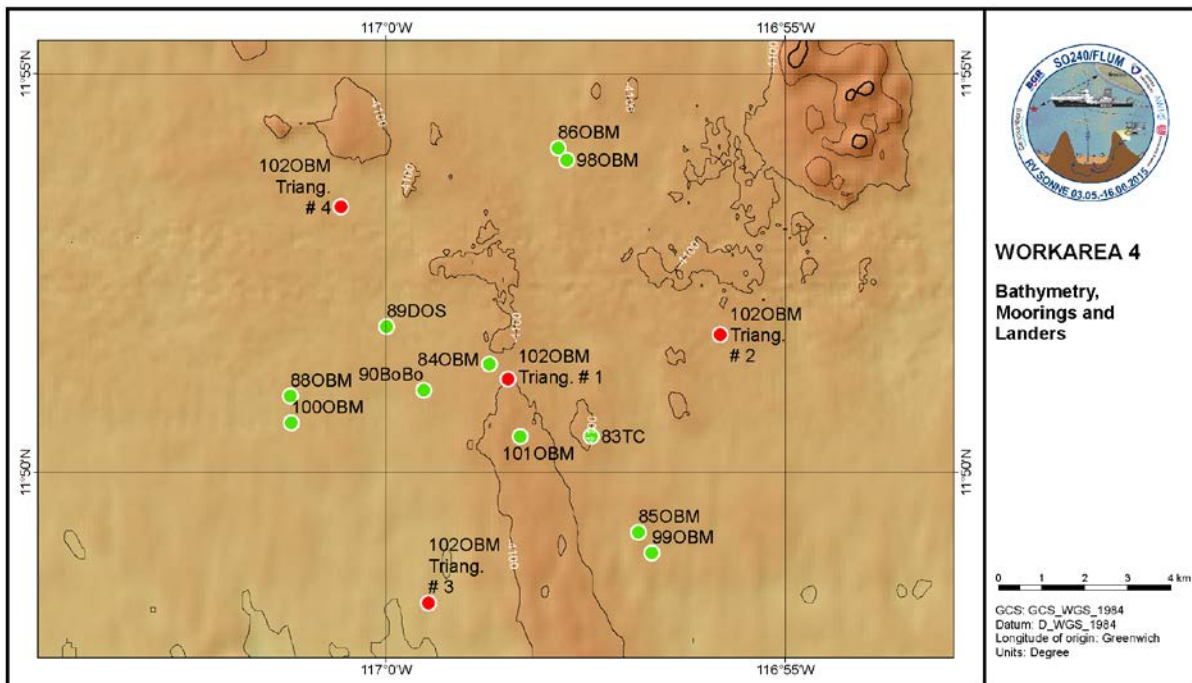


Figure 6.28. Locations of the ocean bottom moorings (OBM) recovered (stations 84, 85, 86, and 88OBM), and re-deployed (stations 98, 99, 100, 101OBM) during SO-240 in working area 4. The red points mark the positions for the triangulation of the re-deployed moorings in order to calculate their exact position on the seafloor (102OBM). Stations 89DOS, 90BoBo and 83TC indicate the recovery sites of these lander and thermistor chain systems. This work was carried out within the framework of the JPI-Ocean project “EcoResponse” as an add-on program to cruise SO-240.

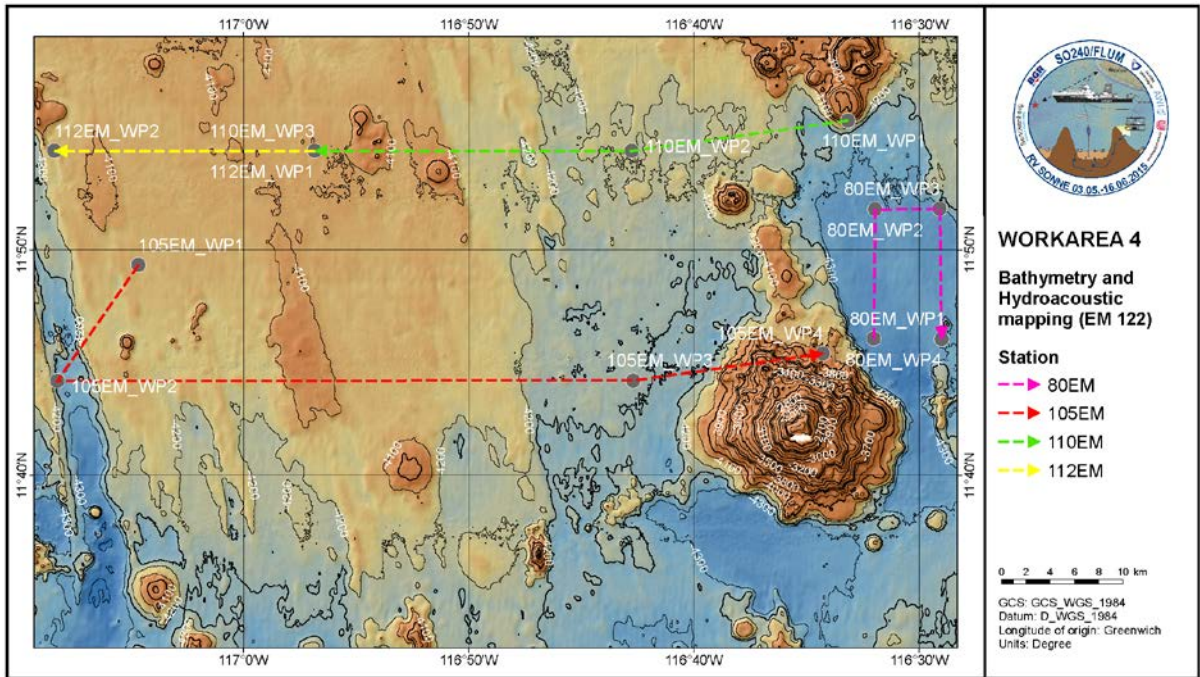


Figure 6.29. Bathymetric surveys with the swath echosounding system EM 122 in working area 4.

7 Work details and first results

7.1 GEOPHYSICS

H. Villinger, Norbert Kaul, Arne Schwab

7.1.1 General remarks

In the following short report we will show some examples of seismic and heat flow surveys in all four working areas. We intend to demonstrate the nature of the sedimentary cover as well as the heat flow regime with the examples shown and highlight the main preliminary results. The complete data set collected by the geophysics group of the University of Bremen can be found in the Appendix A1.

The presentation of the results of each working area contains an overview of seismic and heat flow profiles, a compilation of sediment thicknesses and heat flow results. Results of exclusively bathymetric surveys or bathymetric surveys combined with Parasound are only shown in the Appendix. During each seismic survey, Parasound data and multibeam bathymetry were always collected simultaneously, so each seismic profile has a corresponding Parasound profile. Each survey is subdivided into profiles which are sometimes split up into several parts for better readability. Table 1 and Table 2 summarize all profiles and help to locate the surveys on the track plots in the Appendix. The Parasound and seismic profiles shown in the Appendix are split into 12.5 km long pieces which in case of the seismic lines represent 500 CMPs with a spacing of 25 m. Sometimes the parts overlap. The vertical exaggeration of the seismic records is indicated on the seismograms, whereas the vertical exaggeration on Parasound records is always 54:1.

After completion of work in each working area, a compilation of heat flow results together with calculated estimates of temperatures at the sediment-basement interface was made. Detailed maps of each profile help to locate individual measurements. All heat flow values have to be compared to the lithospheric cooling model value of 103 mW/m² for 24 Ma year old oceanic crust (Hasterok, 2013).

Data collected during the days that were spent outside of the working areas to avoid the hurricane Andres can be found in the Appendix as well.

7.1.2 Working area 1

In working area 1 (WA-1), two seismic surveys were run in combination with Parasound and multi-beam mapping (see Fig. 6.2 for location). Heat flow measurement positions and results are shown in Figure 6.3. Details of the individual profiles as well as all the Parasound and seismic records can be found in the Appendix A1.

In WA-1 the first survey concentrated on the northern part of the area around the Teddy Bare seamount, as this seamount was already planned to be one of the targets for detailed heat flow mapping and sediment sampling during the preparations for the cruise. The Parasound profile 11PS1502_2 (Fig. 7.1.1) towards Teddy Bare shows features we see in almost all Parasound profiles in all working areas. In most cases the seafloor reflector is very strong and we see no or very little internal structure within the thin sediment cover. The dark cloudy band in the subsurface is the top of

the oceanic crust, which is quite pronounced in this profile but fairly weak in others where the sediment cover is thicker.

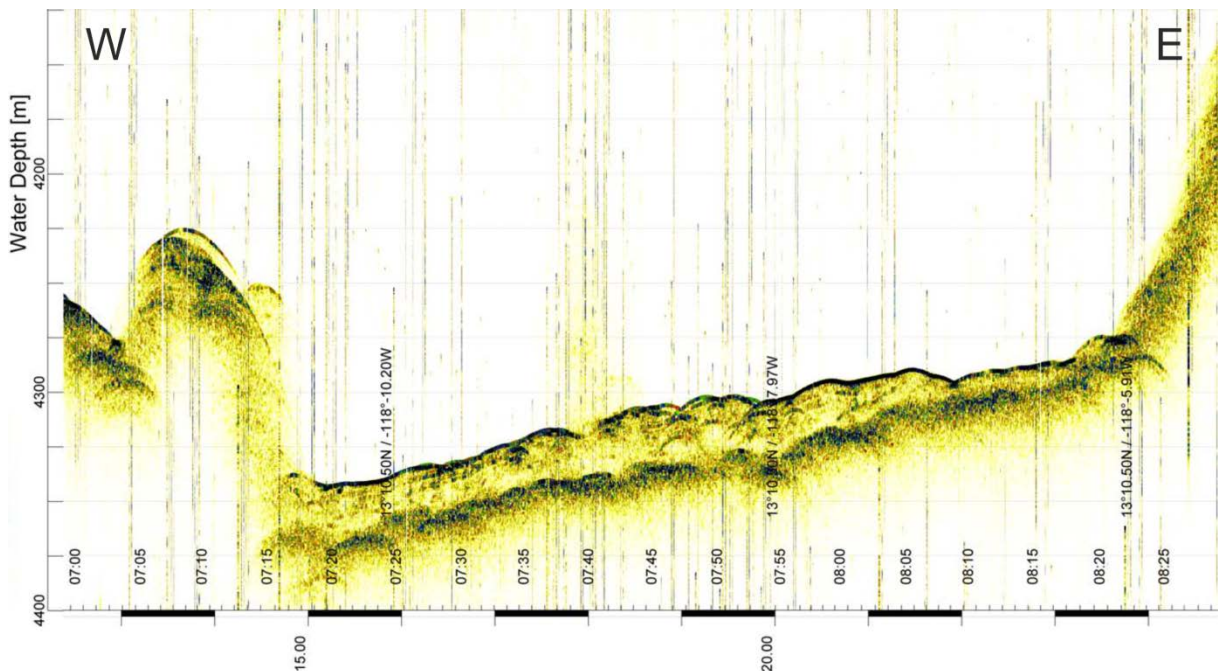


Figure 7.1.1. Example of a Parasound record. Parasound profile 11PS1502_2 (co-located with seismic profile 11SCS1501_2), runs from west to east towards the Teddy Bare seamount on the right. For location see Fig. 6.2.

In each working area, we produced figures like Figure 7.1.2 which are used to create an overview map of sediment thickness (Fig. 7.1.3). The basis for these data is the seismic record, on which the seafloor and basement reflector have been picked and the travel time difference is converted to sediment thickness using a constant velocity of 1500 m/s for the sediments. Magenta triangles on top of the seafloor reflector mark locations where heat flow measurements were carried out. In some cases it is difficult to pick either seafloor or basement or both reflectors. If the sediment thickness is below ~10 m it cannot be resolved in the seismogram due to the low frequency of the air gun signal. The compilation of sediment thickness in WA-1 (Fig. 7.1.3) shows that the sedimentary cover is fairly thin, which is in good agreement with the latest worldwide sediment thickness compilation (Whittaker et al., 2013). The highly variable thickness over short distances is remarkable but enigmatic.

Results of a heat flow profile 03-07HF1501 (Fig. 7.1.4) running east-west towards Teddy Bare are superimposed on seismic profile 11SCS1501_2 which coincides with the Parasound profile shown in Figure 7.1.1. The top of the crust is clearly identifiable and fairly smooth with the exception of a few small faults in the basement. Heat flow at the western end of the profile starts off with values about one fifth of the expected value of 103 mW/m² and increases toward the foot of the Teddy Bare seamount to nearly 60 mW/m². Parallel to that, sediment thickness decreases substantially to a value of probably less than 10 m close to Teddy Bare. Therefore, the increase of heat flow could just reflect a heat flow refraction effect caused by the different thermal conductivities of sediment and basement.

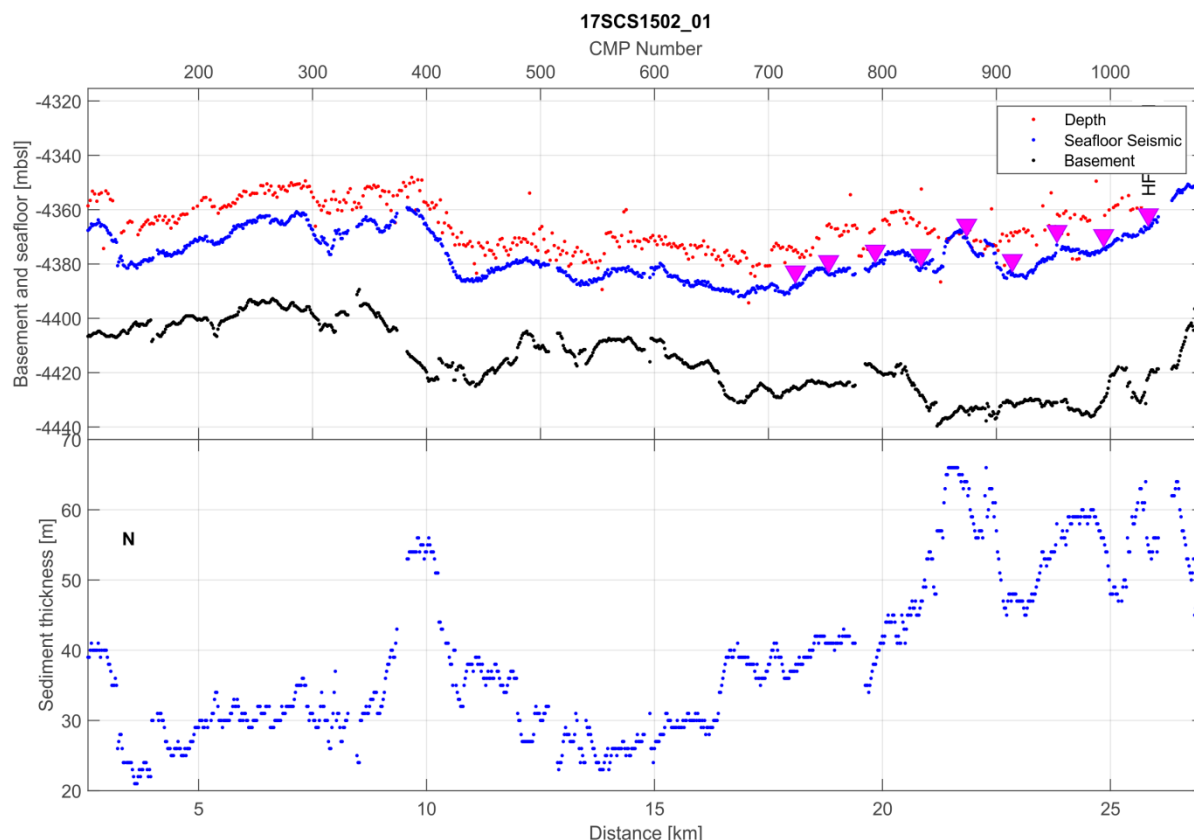


Figure 7.1.2. Basement and water depth on seismic profile 17SCS1502_1. For location of the seismic profile and heat flow measurements see Figs. 6.2 and 6.3. Top: Red dots: water depth from ship's systems; blue: water depth picked from seismic profile (seafloor seismic); black: basement depth. The magenta triangles on top of seafloor seismic mark positions of heat flow measurements with the first one annotated to refer to the heat flow profile name. If the triangles are not on top of the seismically identified seafloor, no sediment and basement pick was possible. Bottom: Sediment thickness. Calculations of water depth from seismic profiles (top blue) as well as sediment thickness are based on a constant velocity of 1500 m/s. Seismic data are not corrected for air gun depth and gun delay.

The seismic profile 11SCS1501_3 (Fig. 7.1.5; for location see Fig. 6.2) across a small basin south of a seamount shows a few significant faults in the basement reaching up to the sediment surface. Heat flow (profile 12HF15002) at the western end is extremely low and rises to relatively higher but still low values at the eastern end. The sudden increase between 2 and 3 km may be associated with the fault in the basement.

The seismic survey 17SCS1502 (see Figs. 6.2 and 7.1.6) starts at the foot of a seamount, runs SSE along a pronounced bathymetric trough (17PS1502_01) bounded by basement ridges and is crossed by the east-west seismic line 17PS1502_03. The sediment cover is very thin at the start of the profile close to a seamount (Fig. 7.1.6), probably due to erosional effects (moat) around the seamount. Sediment thickness increases towards the south to 40 to 60 m. In general, the top of the basement is quite smooth. Further to the south it is broken up by numerous small-scale faults. Heat flow decreases in a very systematic way from ~ 80 mW/m² to values as low as 30 mW/m². This is clearly a result of the massive recharge of cold seawater through the seamount at the end of the profile. The heat flow increase at the end of the profile may be associated with a thinning sediment cover. However, looking at the compilation of all data (Fig. 7.1.7), heat flow decreases to values ~ 10 mW/m² close to the seamount base.

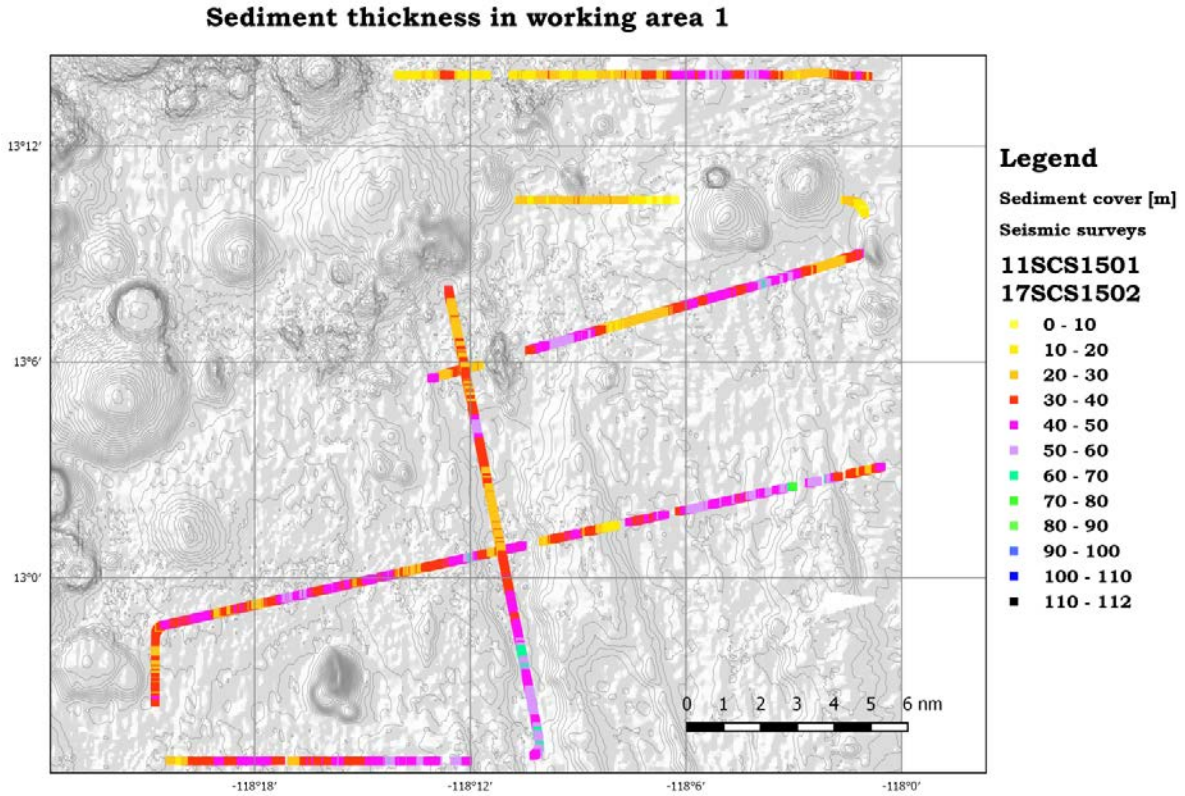


Figure 7.1.3. Sediment thickness in WA-1, based on seismic surveys 11SCS1501 and 17SCS1502. Calculations of sediment thickness are based on a constant velocity of 1500 m/s.

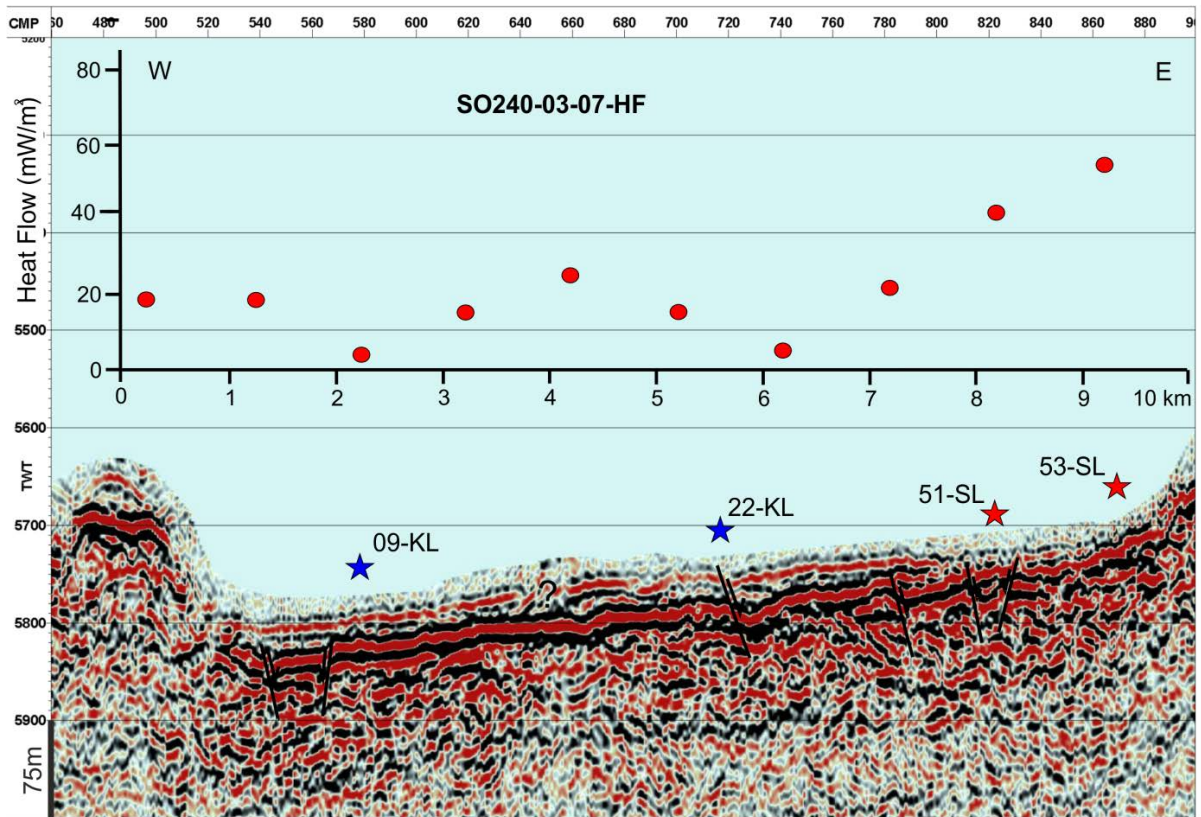


Figure 7.1.4. Heat flow profile along seismic profile 11SCS1501_2. Teddy Bare can be seen at the right-hand side of the profile. Stars mark locations where piston cores (KL) or gravity cores (SL) were taken. For location see Figs. 6.2 and 7.1.7.

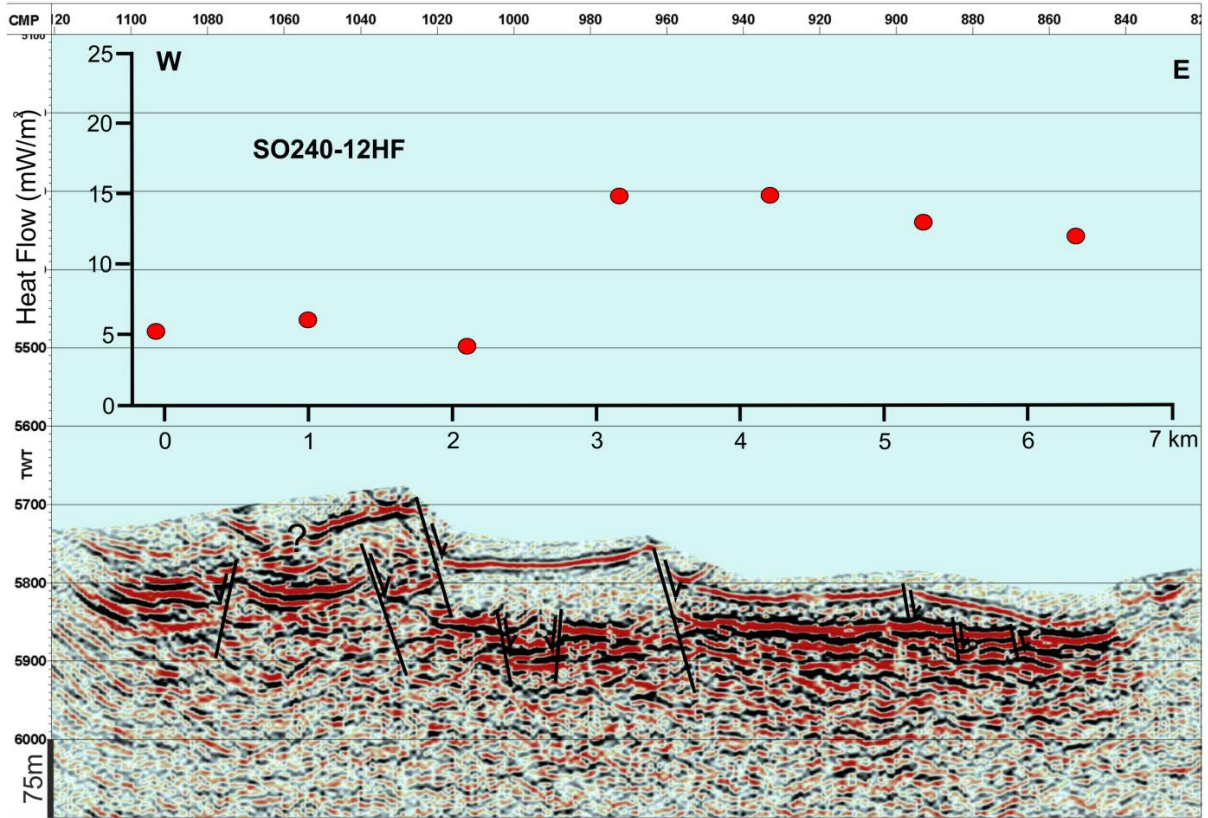


Figure 7.1.5. Heat flow profile 12HF1025 along seismic profile 11SCS1501_3. For location see Figs. 6.2 and 7.1.7.

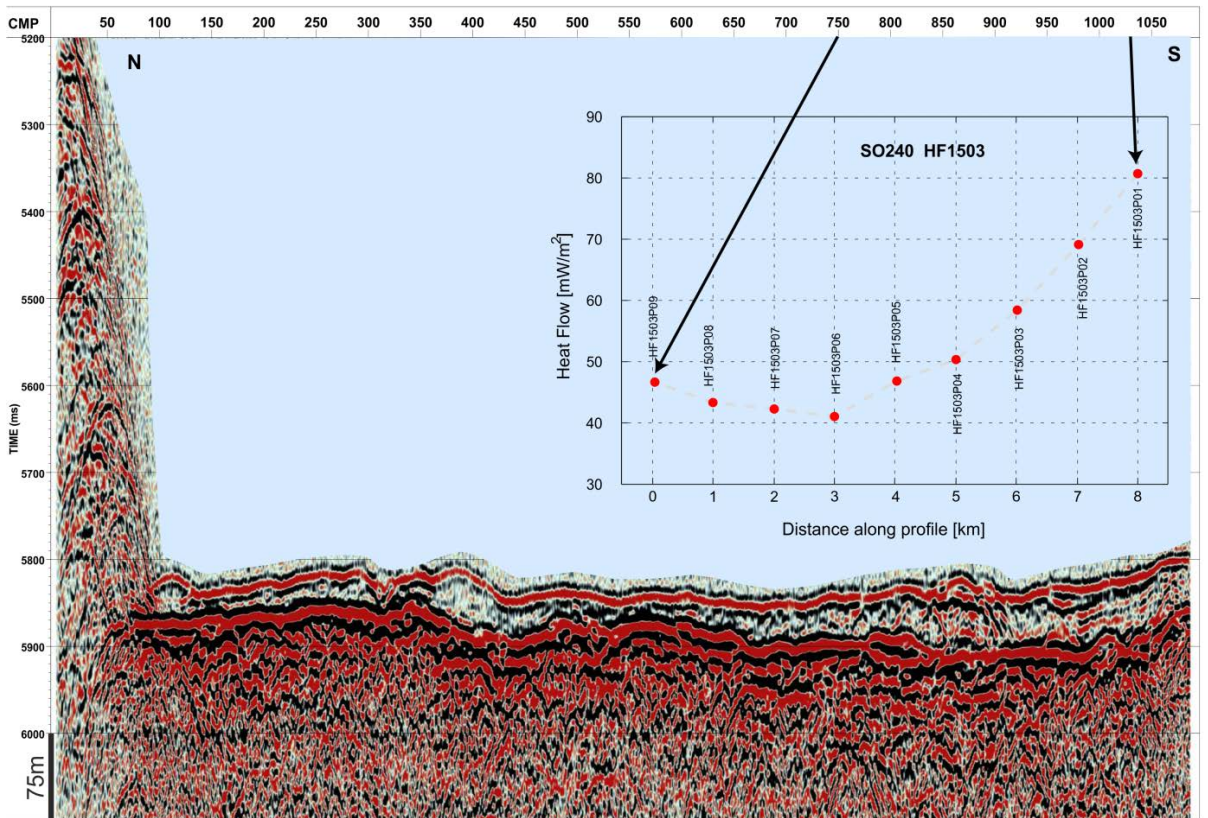


Figure 7.1.6. Heat flow profile 20HF1503 along seismic profile 17SCS1502_01. For location see Figs. 6.2 and 7.1.7.

Figure 7.1.7 displays all heat flow values in WA-1 in an overview and in detail. The numbers on the detailed maps close to the measurement locations are estimated temperatures at the sediment-basement interface, calculated with the Bullard-formula:

$$T(z) = T_0 + q \int_{z=0}^z \frac{dz'}{k(z')}$$

where T_0 is the bottom water temperature, q is the measured heat flow, $k(z)$ is the thermal conductivity profile and z is the depth. In all cases we used a bottom water temperature of 1.48°C and a constant thermal conductivity of 0.82 W/km.

Heatflow in working area 1

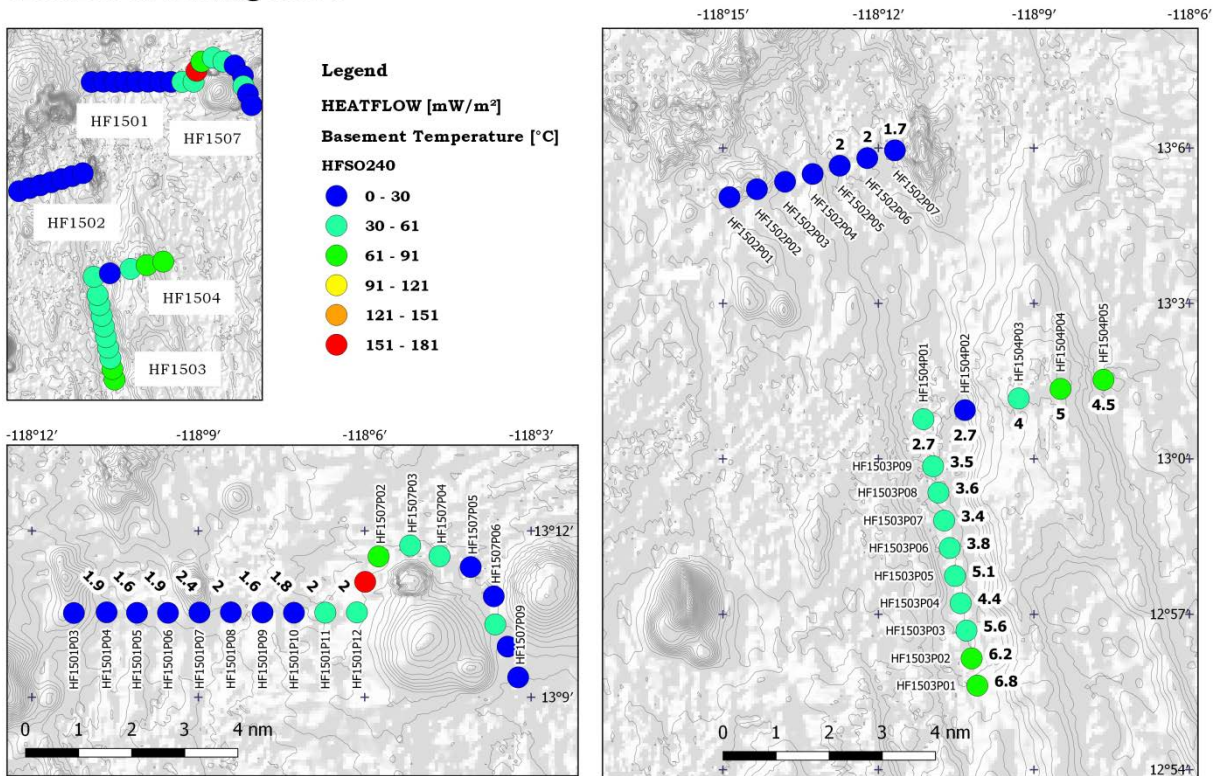


Figure 7.1.7. Overview of heat flow results in WA-1. The numbers at the location of heat flow measurements are estimates of temperature at the sediment-basement boundary, based on measured heat flow. See text for details.

7.1.3 Working area 2

In working area 2 (WA-2) one long seismic survey was run in combination with Parasound and multibeam mapping (see Fig. 6.8 for location). Heat flow measurements and results are shown in Figure 6.9. Figure 7.1.8 shows the highly variable sediment thickness in WA-2. Details of the individual profiles as well as all the Parasound and seismic records can be found in the Appendix XX.

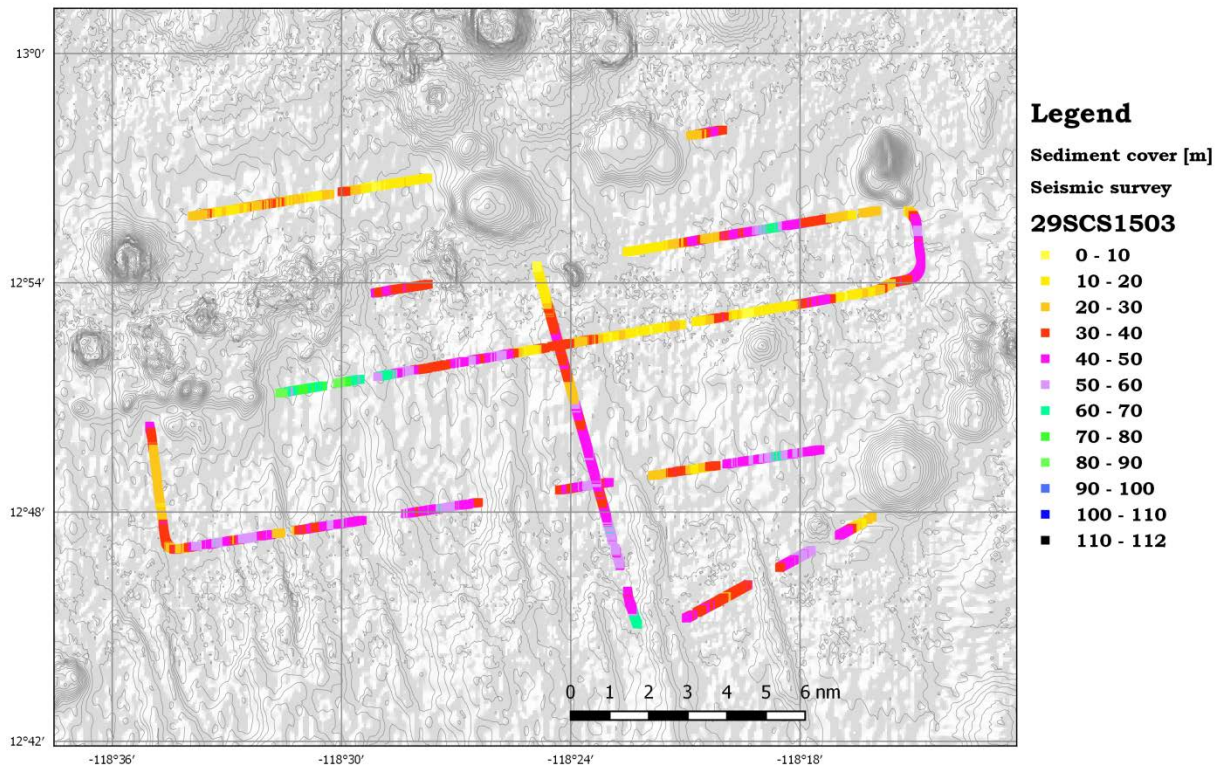
Sediment thickness in working area 2

Figure 7.1.8. Overview of sediment thickness in WA-2.

In WA-2, one profile (29SCS1503_6 and 32-36-HF1505; see Figs. 6.8 and 6.9) follows a basement ridge from the south towards a seamount complex in the north. Its orientation is parallel to the general strike direction (170°) of the ridge as seen in the bathymetry. On top of the ridge a number of small-scale depressions can be identified which might be relics of hydrothermal circulation ('hydrothermal pits'; Bekins et al., 2007). Figure 7.1.9 shows the seismogram of this profile together with heat flow values. Superimposed on the overall trend of a decreasing heat flow towards the seamount are small-scale positive anomalies which may be associated with the depressions in the sedimentary cover. Alternatively, it seems to be more likely that these anomalies are connected to faults in the basement which may act as pathways for fluids. The effect of a recharging seamount on heat flow is again clearly documented.

Seismic line 29SCS1503_2 (Fig. 7.1.10) runs across a deep depression southwest of the seamount complex. The basement contains a few small faults. Apart from these offsets it is fairly smooth. Sediment cover is on the order of 50 m within the basin and decreases towards the seamount (Fig. 7.1.8). Basement is hardly visible in the Parasound records of this line (29PS1504_2; see Appendix A1). Bathymetry and thinning of the sediments towards the seamount suggest that this is an erosional effect caused by bottom water currents around the seamounts. Heat flow on this profile (45HF1506, Fig. 7.1.10) across the two small basins revealed the lowest values of heat flow measured during the cruise, i.e. the vertical temperature gradient is close to zero. The seismic section also shows very thin sediment cover on top of the basement around CMP 820 to CMP 840. It is highly unlikely that this low temperature gradient is caused by erosion as erosional events would increase the gradient.

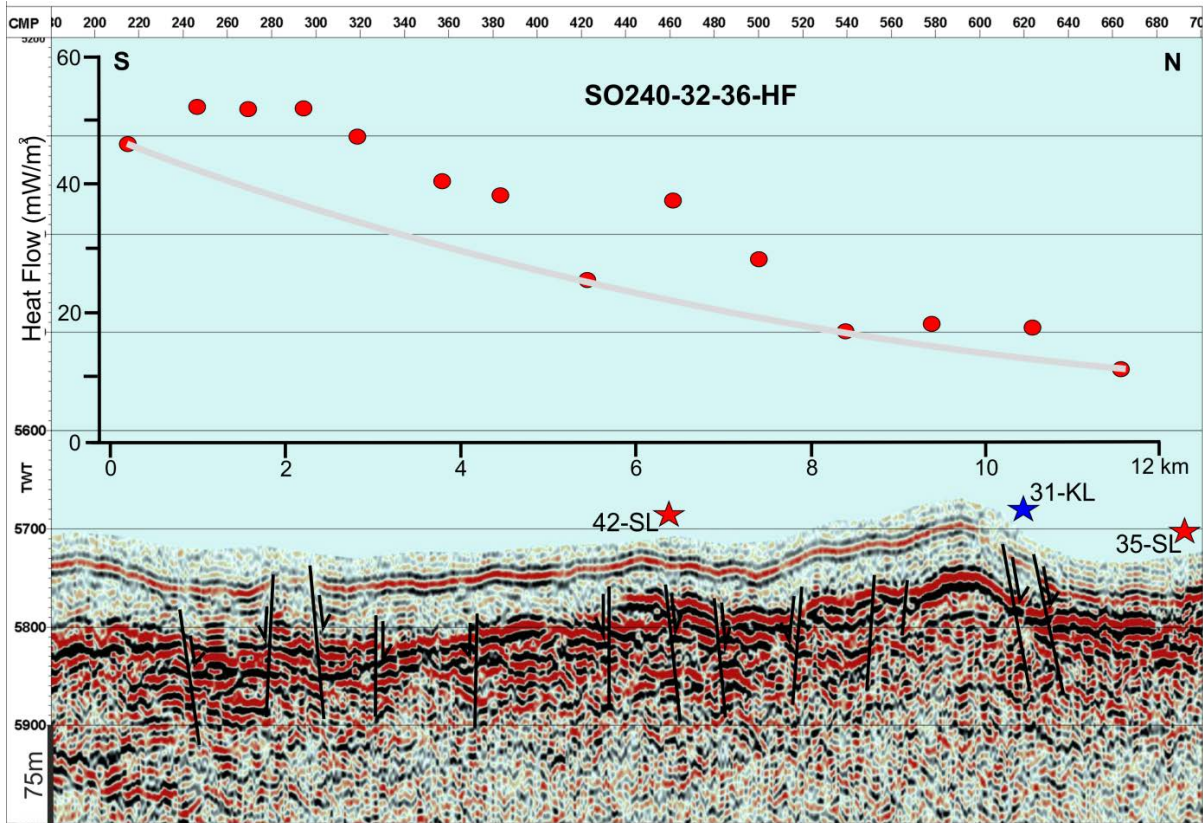


Figure 7.1.9. Heat flow profile 32-36HF1505 (co-located on seismic line 29SCS1503_6) (see Fig. 6.8).

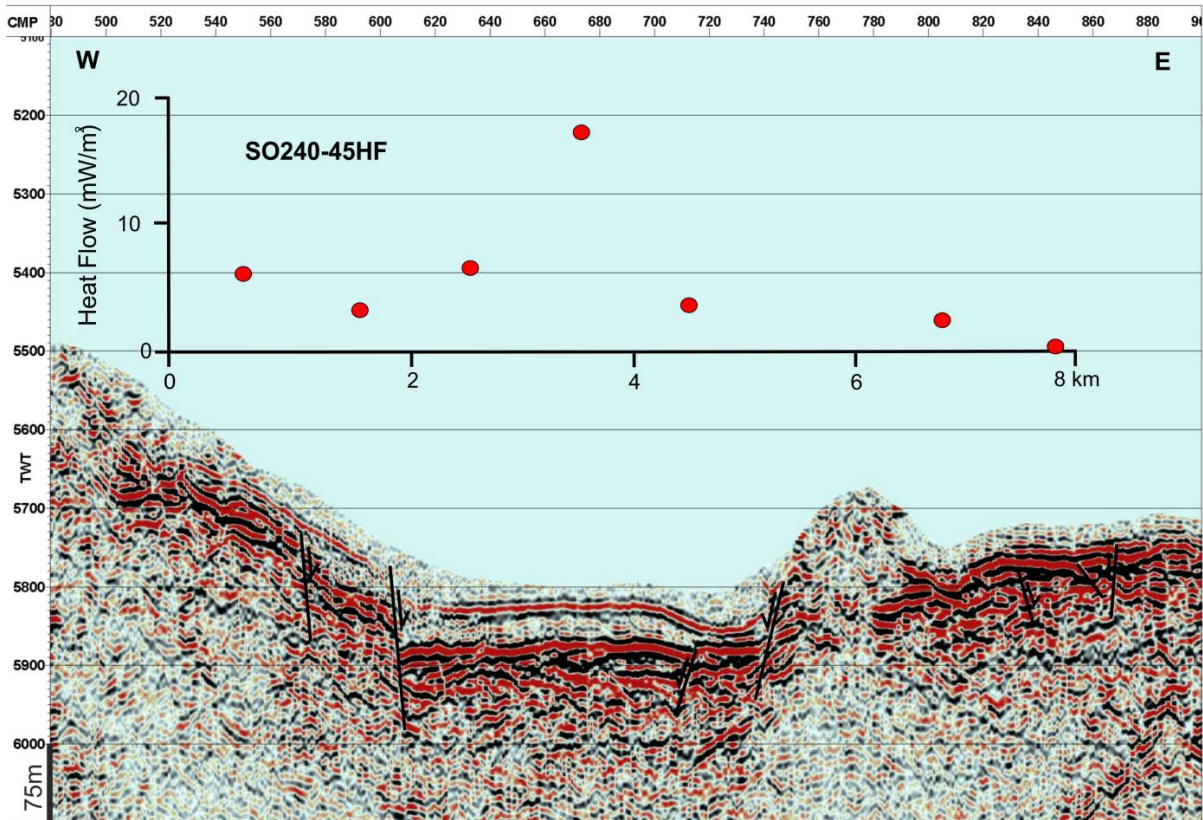


Figure 7.1.10. Heat flow profile 45HF1506 co-located on seismic profile 29SCS1503_2 (see Fig. 6.8)

It can clearly be seen that in the whole area heat flow is lower than predicted by lithospheric cooling models by a factor of 2 to 20. A compilation (Fig. 7.1.11) of all heat flow values and calculated temperatures at the sediment-basement boundary indicates that temperatures within the upper part of the oceanic crust (Layer 2A) are only slightly to moderately above those of the bottom waters.

Heatflow in working area 2

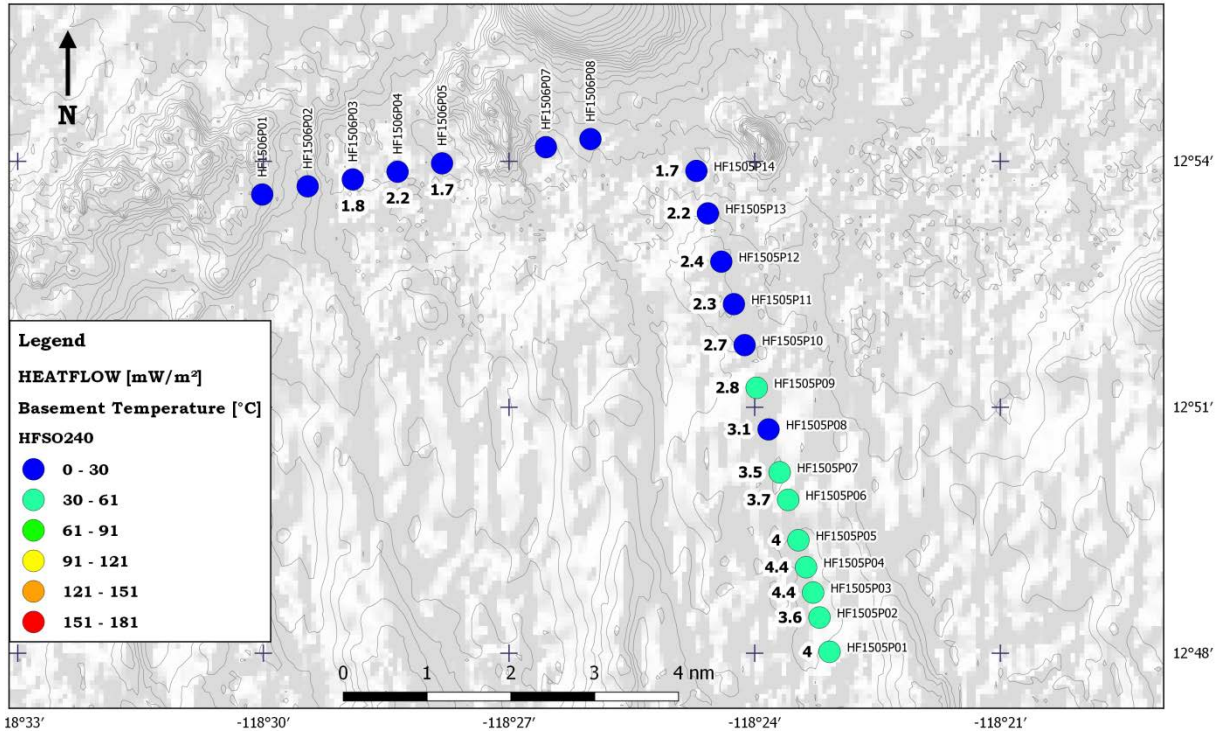


Figure 7.1.11. Overview of heat flow results in WA-2. The numbers at the location of heat flow measurements are estimates of temperature at the sediment-basement boundary, based on measured heat flow.

7.1.4 Working area 3

Working area 3 (WA-3) is the westernmost of all working areas. It is dominated in the south by parallel striking ridges at an angle of about 170° and in the north by a large seamount complex. Our seismic profile starts on the eastern edge of WA-3 with a general orientation perpendicular to the strike of the ridges, crossing them in two places, continuing north along the top of one of the basement ridges and further north switching over to a basement trough. Figures 6.14 and 6.15 present the locations of the profiles while Figure 7.1.12 illustrates the inferred sediment thickness.

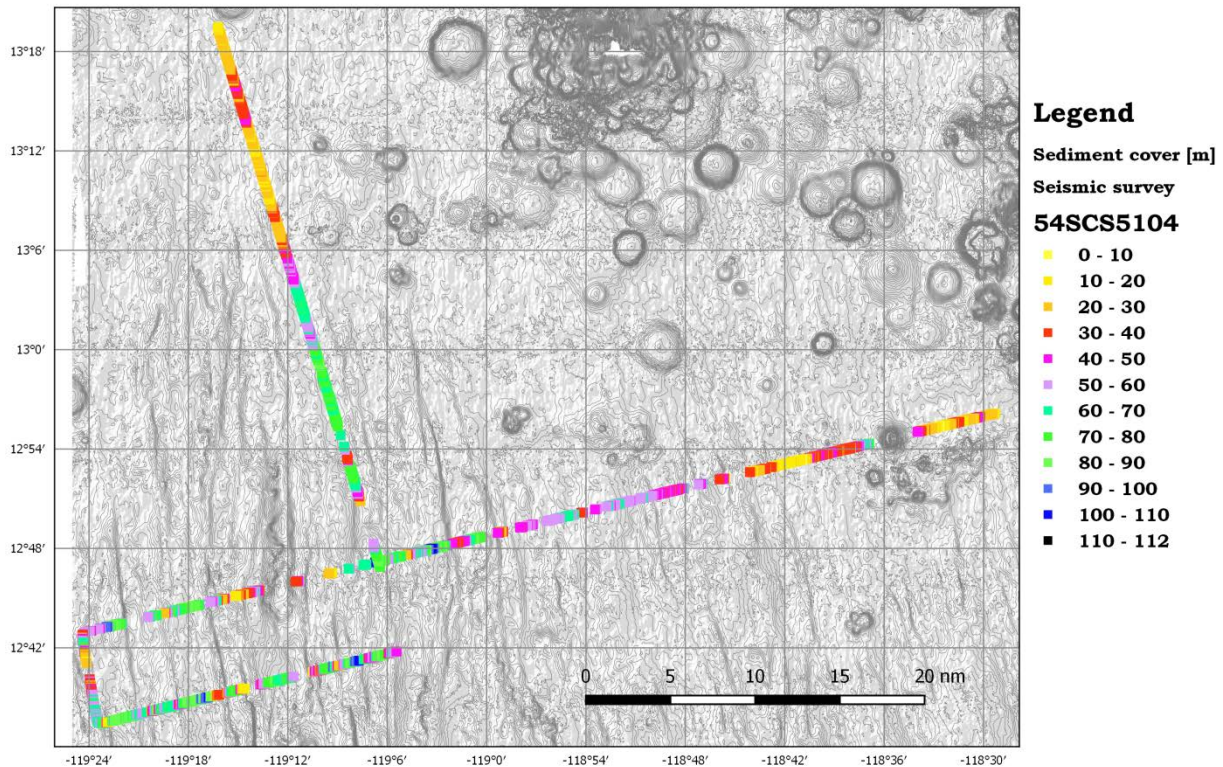
Sediment thickness in working area 3

Figure 7.1.12. Overview of sediment thickness in WA3.

The ridge-parallel seismic profile (54SCS1504_3) crosses some depressions in the sedimentary cover. On the basis of the bathymetry only they could be identified as hydrothermal pits. However, a closer look at the seismic record (Fig. 7.1.13) does not confirm this, as there is not a characteristic lack of sediments which generally characterizes such pits. Heat flow along this profile varies around 60 mW/m^2 with a distinctive positive anomaly of $\sim 140 \text{ mW/m}^2$ at CMP 1010 (5 km). It is most likely associated with a fault in the basement in combination with a change of sediment thickness. Detailed measurements across one sedimentary depression mapped with Parasound (see Appendix A1) reveal no indications for (anomalously) high heat flow. Therefore, the depressions are most likely not hydrothermal pits.

Two profiles in the south of the working area across troughs between basement ridges show a distinctive graben-type pattern of faults in the basement reaching up to the surface in most cases. Heat flow on profile 67HF1509 (see Fig7.1.14 and for location Fig. 6.16) varies by an order of magnitude. The variations seem to reflect the faults within the basement. A similar pattern emerges on heat flow profile 71HF1510 (see Fig. 7.1.15). Both heat flow profiles suggest that the faults are hydrologically active and may act either as sites of recharge or discharge. A compilation of heat flow values and sediment-basement temperatures is shown in Figure 7.1.16. Temperatures in the upper oceanic crust are significantly higher than in WA-1 and WA-2, generally reflecting greater heat flow and thicker sediment cover in WA-3.

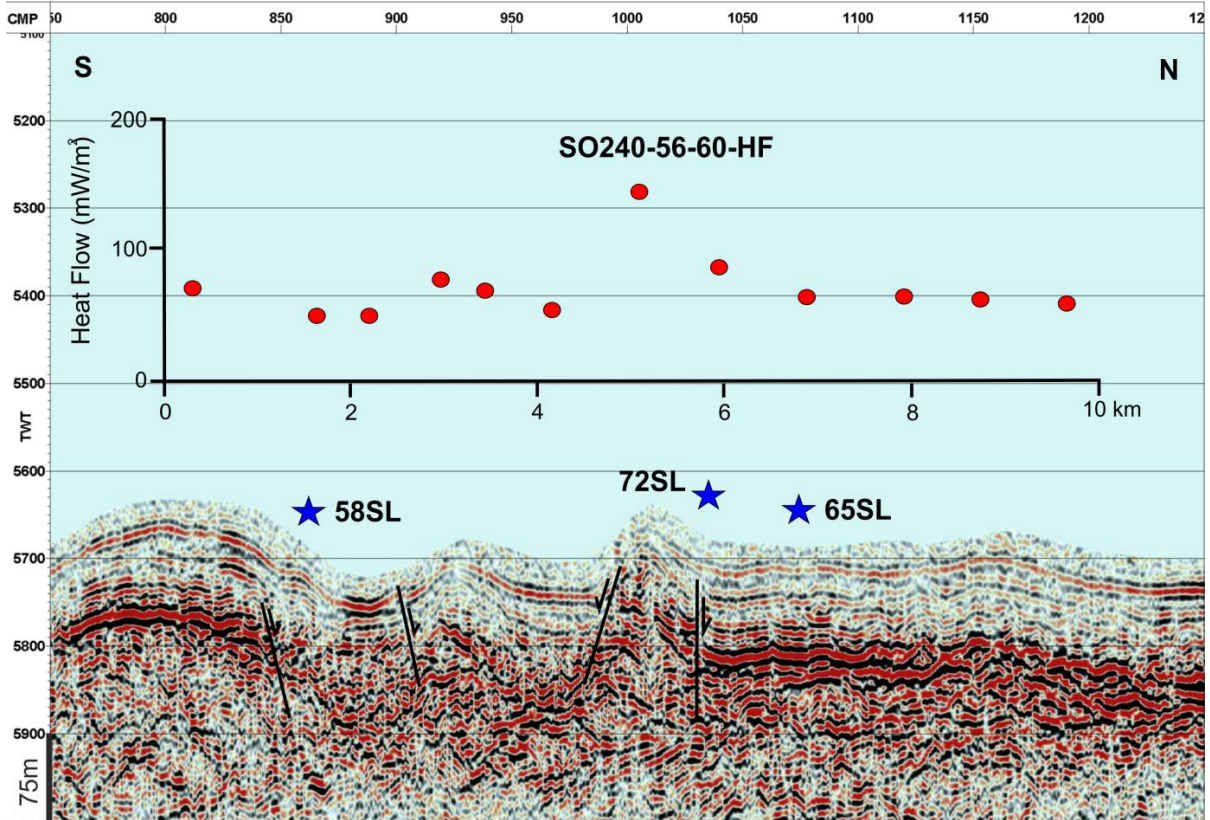


Figure 7.1.13. Heat flow profile 56HF1508, located on seismic line 54SCS1504_3 (see Figs. 6.14 and 6.16 for locations).

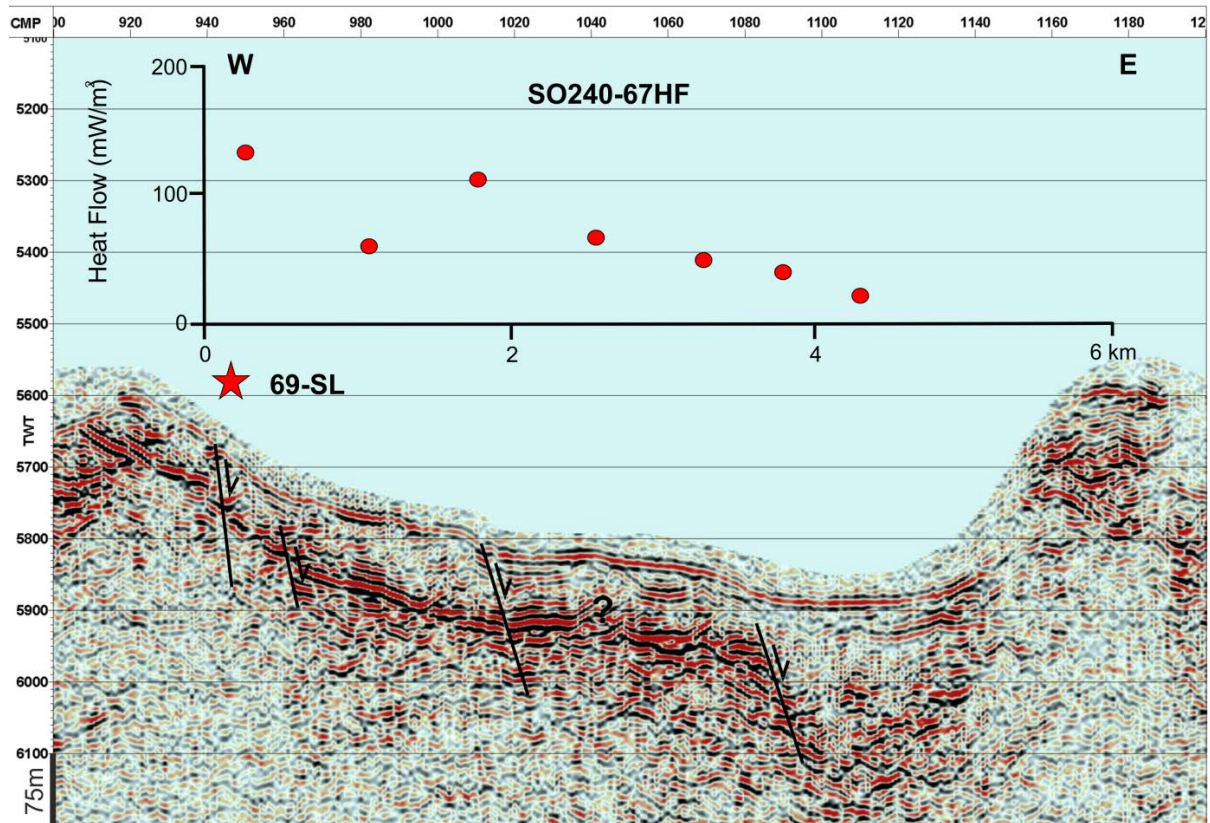


Figure 7.1.14. Heat flow profile 67HF1509, located on seismic line 54SCS1504_2 (see Figs. 6.14 and 6.16 for locations).

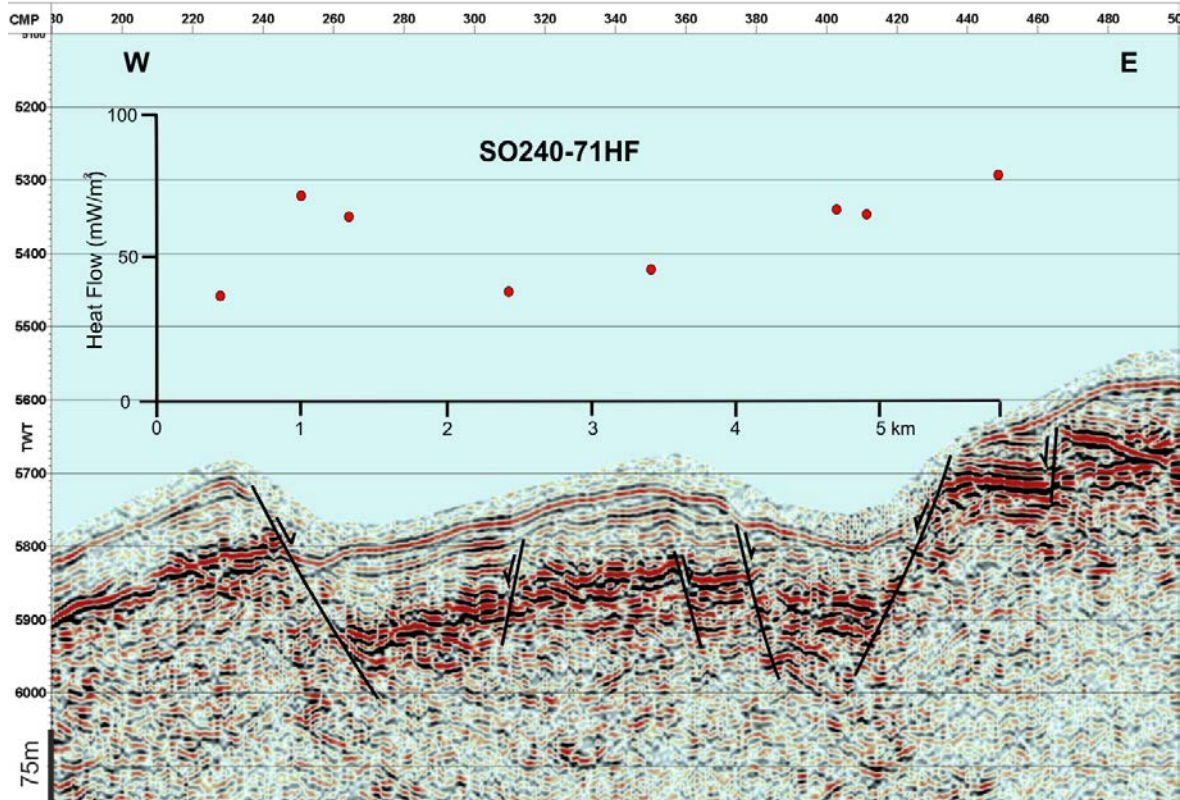


Figure 7.1.15. Heat flow profile 71HF15010, located on seismic line 54SCS1504_2 (see Figs. 6.14 and 6.16 for locations).

Heatflow in working area 3

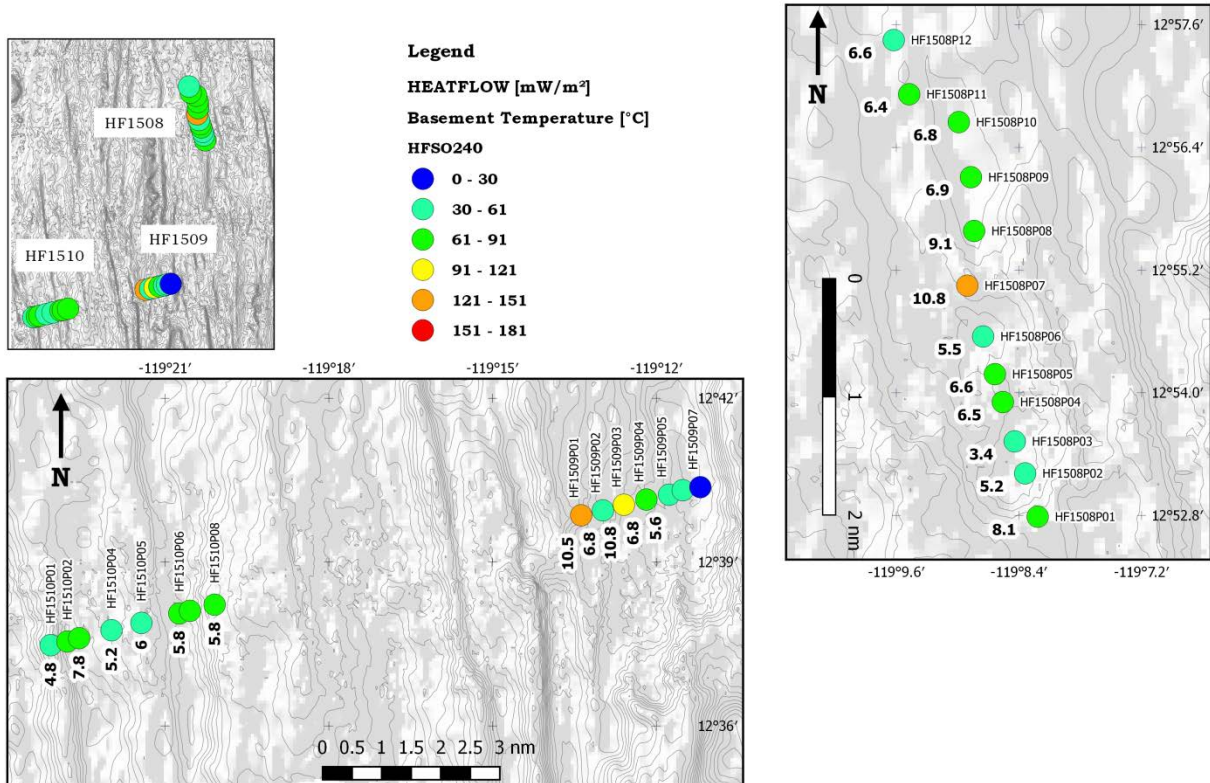


Figure 7.1.16. Overview of heat flow results in WA-3. The numbers at the location of heat flow measurements are estimates of temperature at the sediment-basement boundary, based on measured heat flow.

7.1.5 Working area 4

Working area 4 (WA-4; see Fig. 6.21) is a prime area within the German manganese nodule license area for potential future mining of manganese nodules. It is bounded to the south by a chain of smaller and larger seamounts and to the east by one large single seamount rising about 1500 m above the surrounding seafloor. This seamount is bounded to the east and south by a large basin with very little internal relief. To the west the seafloor is rather flat and only interrupted by a deep trough striking at an angle of about 170° (~ parallel to the ridge orientation). We shot a seismic line through the basin at the easternmost seamount and continued on an east-west profile across the flat plain to the western edge of the working area at the foot of a seamount. Heat flow sites are concentrated on three short profiles, one in the eastern basin northeast of the large seamount, one east of the trough and one at the foot of the seamount at the far western end of the seismic profile (see Fig. 6.22).

WA-4 was the first working area where we observed a strong internal reflector within the sedimentary sequence at a depth of ~7 to 10 m (see Fig. 7.1.17). Most likely it marks a sudden change of sedimentation from carbonate-rich to siliceous ooze which occurred when the location shifted out of the equatorial high-productivity area. Therefore, this reflector can be used as a time mark when it is visible. This horizon is barely visible on the seismic record (see Fig. 7.1.18), although optimized processing might help to increase its visibility. It is also remarkable that we see internal structures in the Parasound record at the eastern end of the profile as shown in Figure 7.1.17. This is also true for the seismic record from CMP 950 to 1150 as shown in Figure 7.1.18. The sediment thickness around the eastern seamount with 10 to 30 m is surprisingly small but increases towards the west to a thickness of up to ~100 m (Fig. 7.1.19).

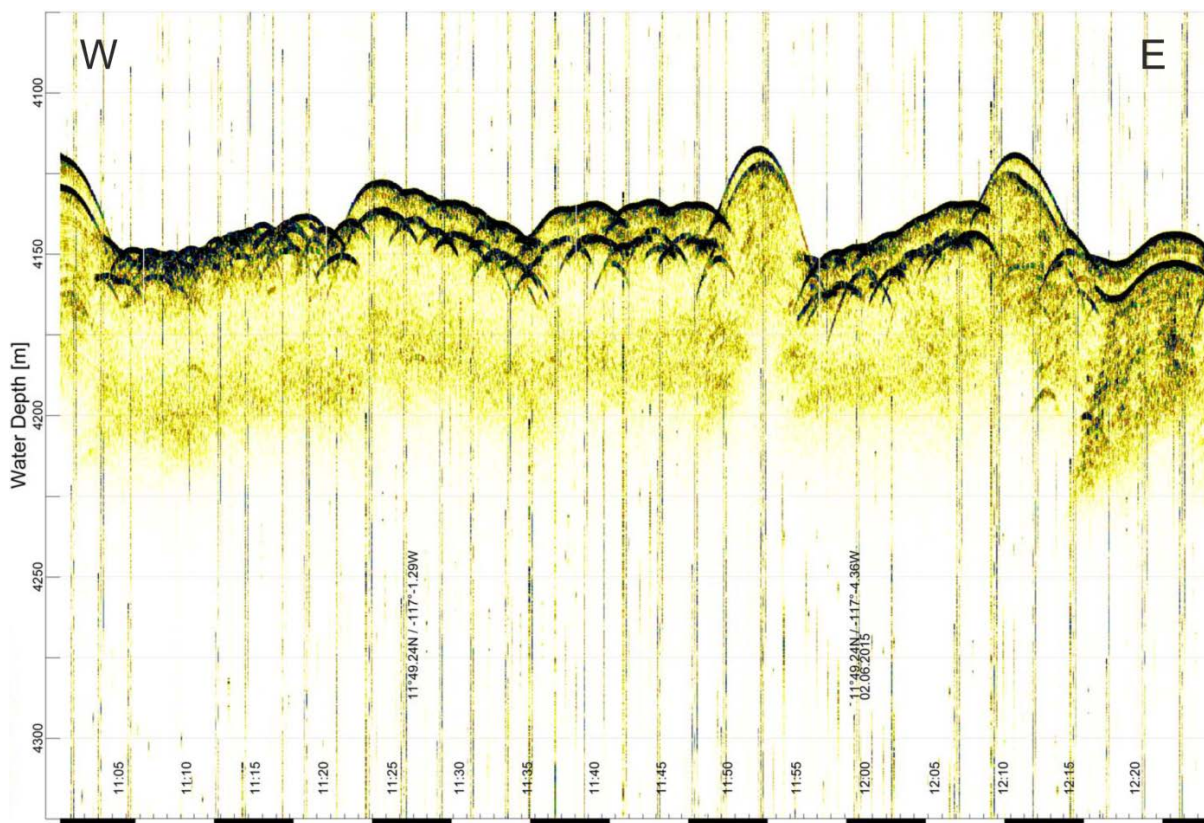


Figure 7.1.17. Parasound profile along seismic profile 82SCS1505_3, part 3 of 5 (see Fig. 6.21 for location).

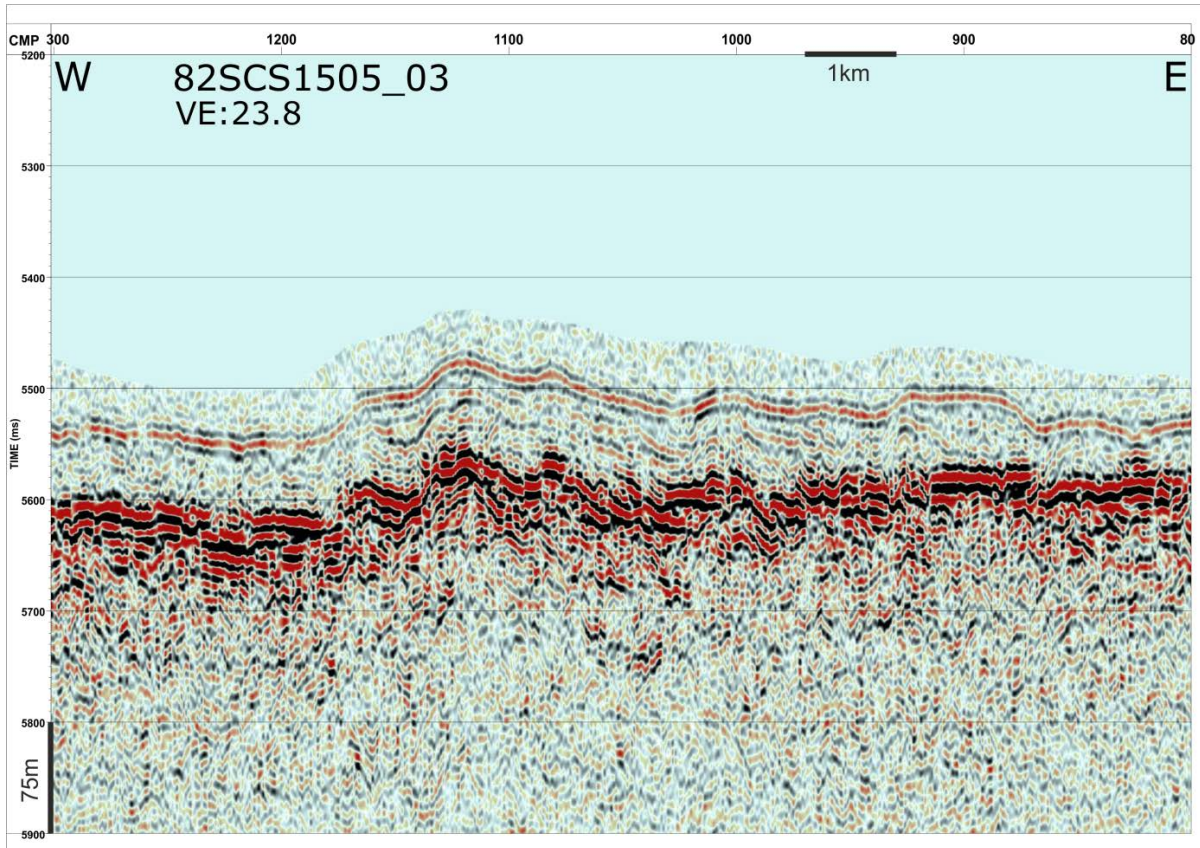


Figure 7.1.18. Part of seismic profile 82SCS1505_3 (for location see Fig. 4.1).

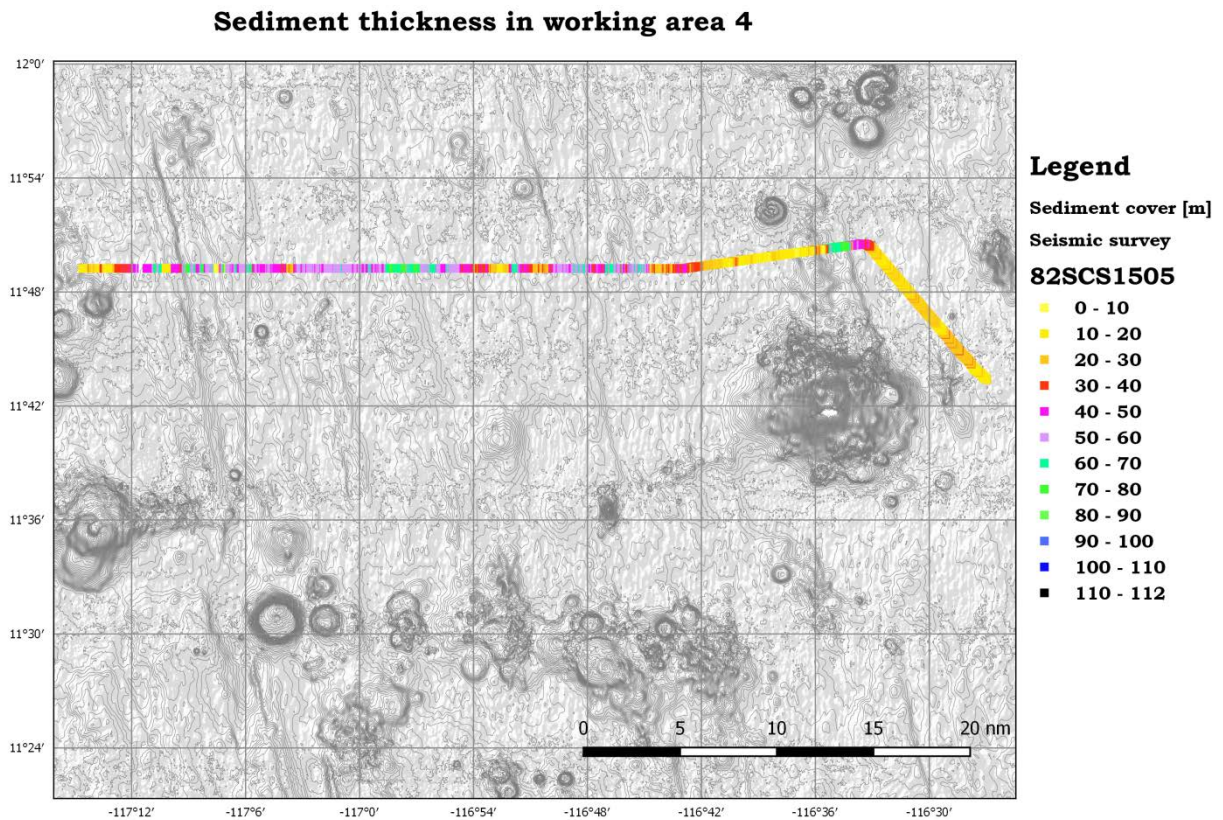


Figure 7.1.19. Overview of sediment thickness in WA-4.

Heat flow profile 87HF1512 (Fig. 7.1.20) to the east of the seamount in the featureless basin with a very thin sediment cover shows highly variable values from $\sim 90 \text{ mW/m}^2$ to $\sim 10 \text{ mW/m}^2$. The changes seem to correlate with faults in the basement. Further west on seismic profile 82SCS1505_3 but still east of the trough, basement is broken up by numerous small faults which appear to affect the seafloor heat flow (see Fig. 7.1.21). The heat flow profile close to the seamount at the western end of seismic profile 82SCS1505_3 covers in its central part a horst-like structure with a maximum of $\sim 110 \text{ mW/m}^2$ (see Fig. 7.1.22). Heat flow values drop to 20 mW/m^2 at the foot of the seamount. Figure 7.1.23 summarizes again all heat flow results in WA4 including estimates of sediment-basement interface temperatures.

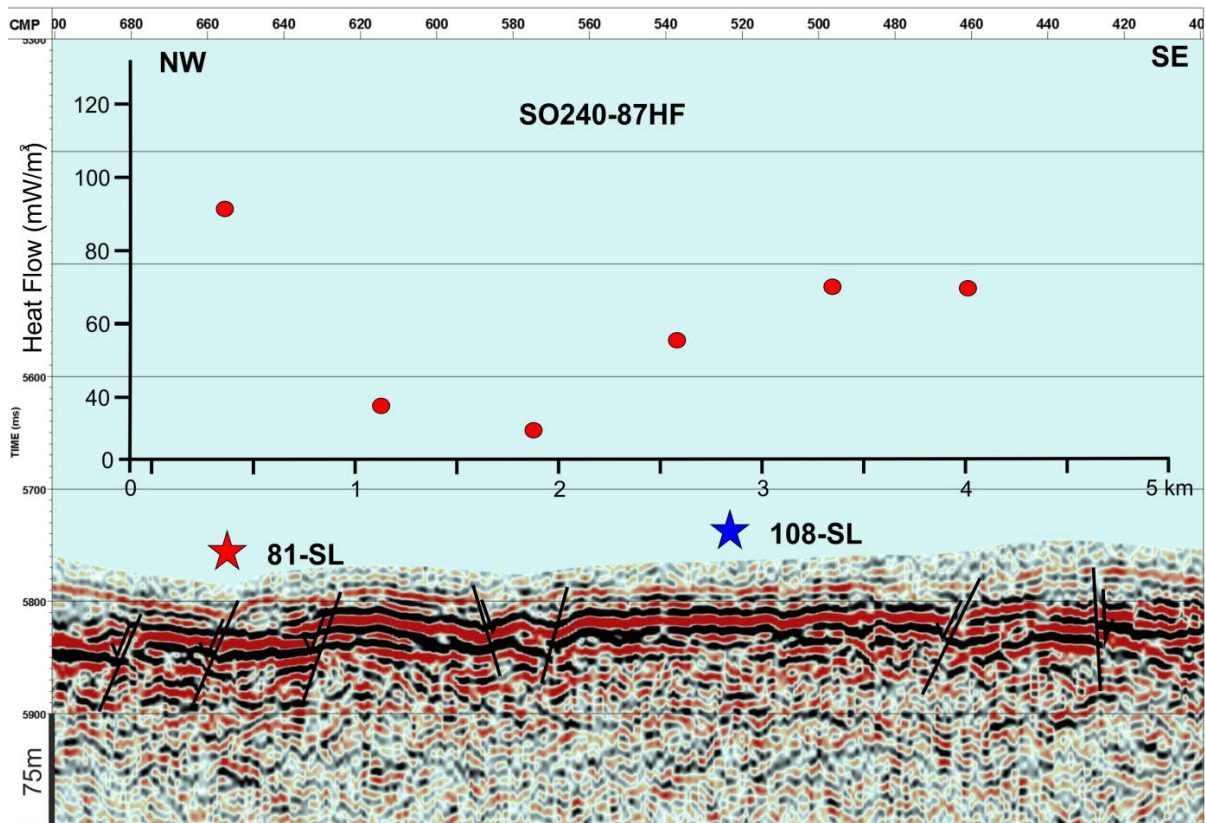


Figure 7.1.20. Heat flow profile 87HF1512 on seismic profile 82SCS1505_1. The stars mark locations where gravity cores were taken. For location see Figs. 6.21 and 6.22.

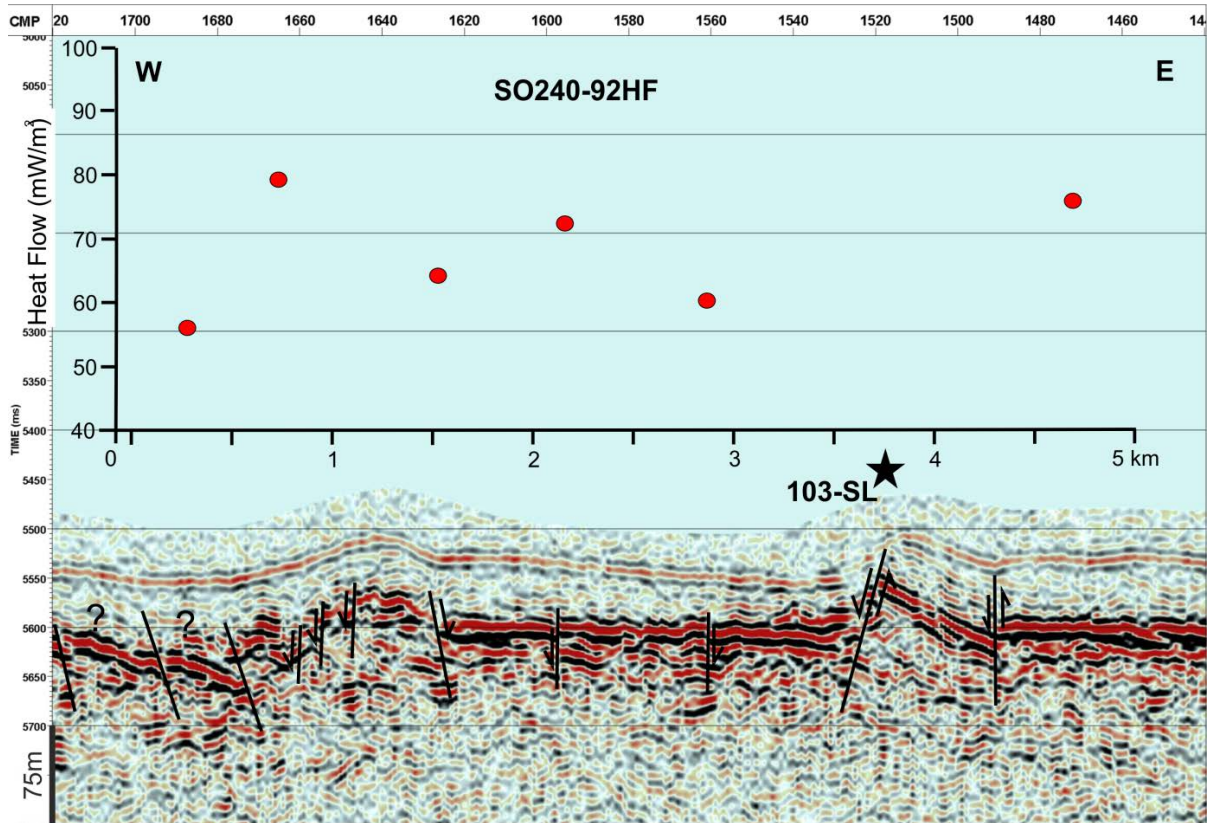


Figure 7.1.21. Heat flow profile 92HF1513 on seismic profile 82SCS1505_3. The star marks the location where a gravity core was taken. For location see Figs.6.21 and 6.22.

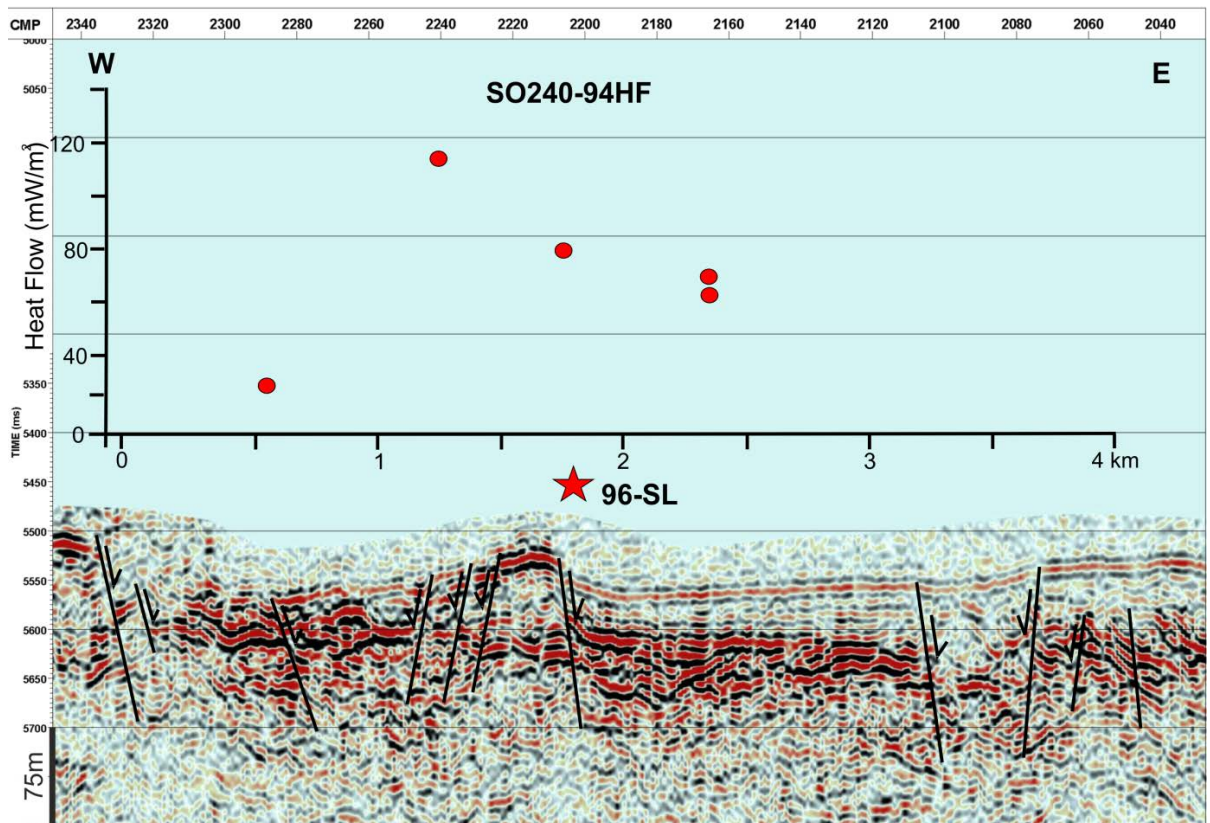


Figure 7.1.22. Heat flow profile 94HF1514 on seismic profile 82SCS1510_3. The star marks the location where a gravity core was taken. For location see Figs. 6.21 and 6.22.

Heatflow in working area 4

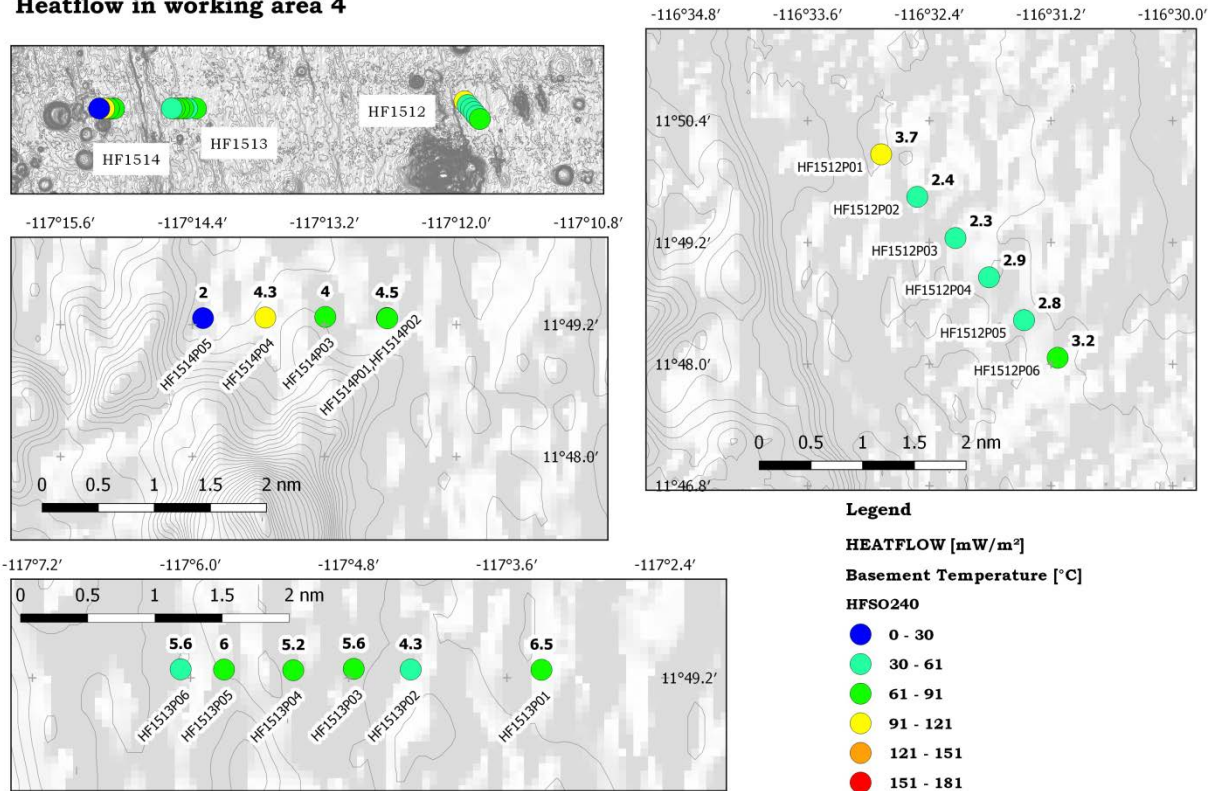


Figure 7.1.23. Overview of heat flow results in WA-4. The numbers at the location of heat flow measurements are estimates of temperature at the sediment-basement boundary, based on measured heat flow.

Test measurements along one short profile were made with the LIRmeter (**L**ance **I**nsertion **R**etardation **m**eter) in order to derive the shear strength of the sediments (see Fig. 7.1.24). At each measurement location, three penetrations were made in order to test the repeatability of the results. One of the measurements is shown in Figure 7.1.25. The main problem with the interpretation of the results is the fact that the exact moment that the lance enters the sediments is not easy to determine as the sediments are very soft. Further processing will be needed to evaluate the data further.

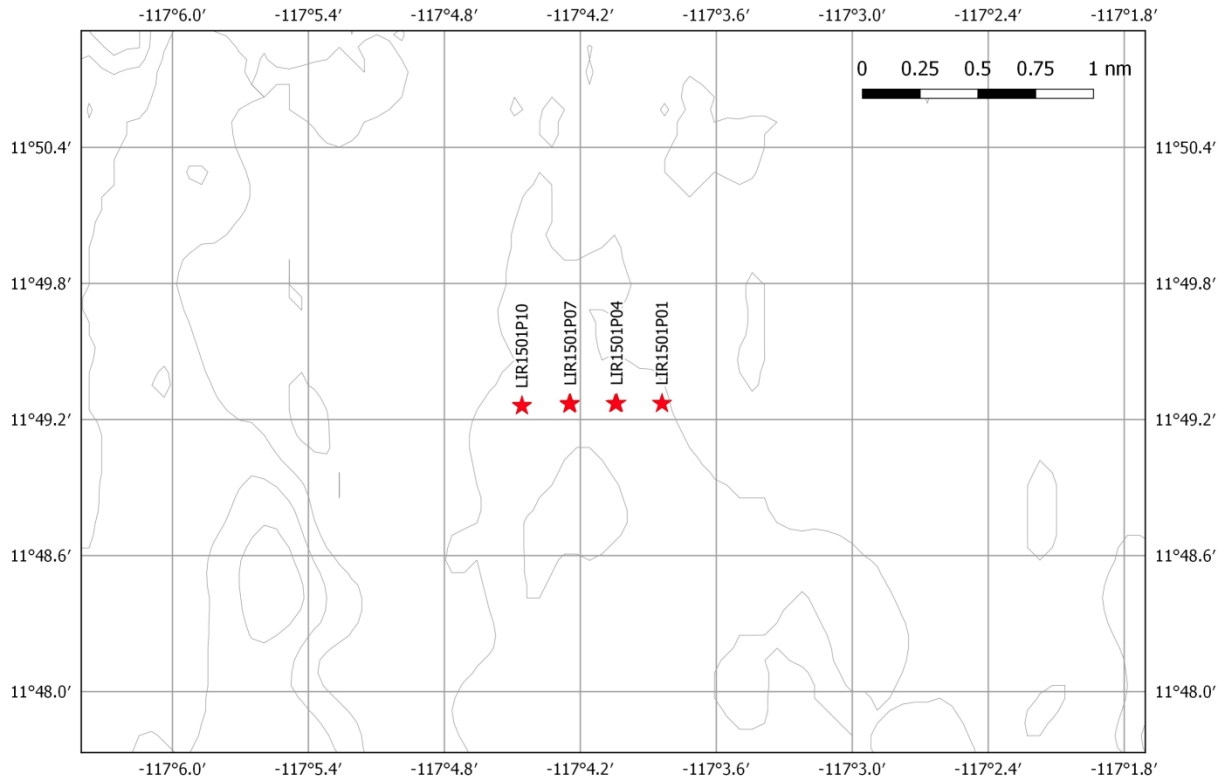


Figure 7.1.24. Locations on seismic profile 82SCS1510_3 where in-situ shear strength measurements (LIRmeter) were made.

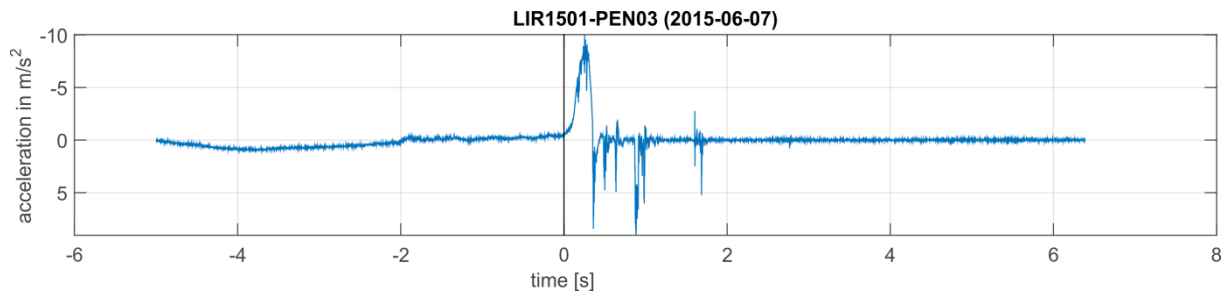


Figure 7.1.25. Example of a LIRmeter measurement at location LIR1501P01. For location see Fig. 7.1.24.

7.1.6 Conclusions

Overall the geophysical surveys carried out within the four working areas were very successful. All instruments worked without any problems, especially the Bremen heat probe. Our results can be summarized as follows:

Acoustic measurements

The Parasound record helps to determine whether sediments are present. It is surprising that in most cases we do not see internal reflectors within the sediment package, nor do we see a clear reflection from the top of the oceanic crust. We speculate that the latter is a consequence of the rough surface topography of the pillows which creates a diffuse reflection pattern at the frequency of the Parasound signal, whereas the seismic records show a clear reflection.

The seismic records suffer from the fact that at a number of locations the sediment cover is so thin that we are not able to resolve sediment thickness. This is mainly due to the fact that the air gun's main signal frequency is well below 100 Hz, resulting in a wave length of the signal in the order of a couple of tens of meters that makes sediment thicknesses of less than 20 m difficult or impossible to resolve. At a water depth of well above 4300 m the use of an air gun with a higher signal frequency is not possible due to the higher signal amplitude losses (absorption) at high frequencies. In addition, a ship-generated 50 Hz signal was present which is right in the middle of our source frequency band and therefore, could not be removed during the preliminary processing done on board. Despite these shortcomings, the seismic records proved to be absolutely essential for identifying tectonic structures in the upper crust, which in turn are needed to interpret the heat flow results.

Heat flow

Heat flow profiles towards seamounts or at the foot of seamounts confirm that all of these acts as recharge sites for cold seawater into the upper crust. We found only one location to the northwest and right at the base of the Teddy Bare seamount (WA-1; see Fig. 7.1.17) with an abnormally high heat flow value of ~ 180 mW/m². This value was confirmed by an even higher value measured with the BGR heat probe. Either thin sediment cover or the nature of the sediments (volcano-clastics) prevented both probes from penetrating completely. Due to time constraints we could not investigate this area more closely in order to pinpoint the anomaly precisely and possibly detect a seafloor discharge site.

Heat flow profiles across troughs or on flat plains show that in numerous cases faults in the upper basement appear to control the seafloor heat flow. This would suggest as a consequence that they act as pathways for the interchange of fluids between the upper crust and the ocean. According to Spinelli et al. (2004) a thin sediment cover of siliceous ooze does not prevent an advective exchange with fluid velocities below about 10 mm/a. Such a small Darcy velocity is hard to detect based on thermal measurements, but hopefully can be done with the help of pore water geochemistry. A plot of heat flow versus sediment thickness (Fig. 7.1.26) demonstrates very clearly that variation in heat flow at locations with less than ~ 40 m of sedimentary cover is much higher than at locations with a greater sedimentary cover. This evidence suggests that at locations with thin sediments, energy (heat) and mass (fluids) are exchanged between the ocean and the upper crust either by recharge and/or discharge of fluids.

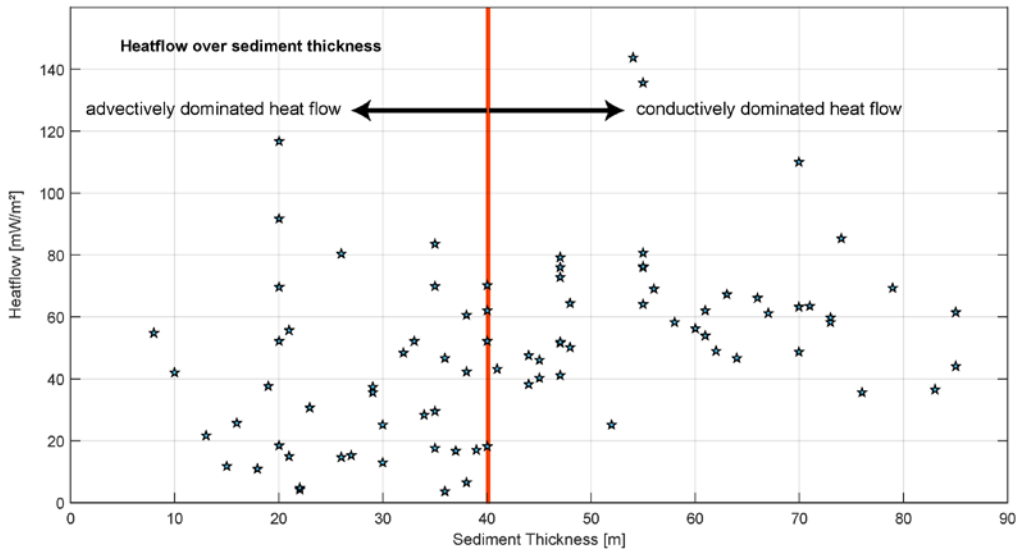


Figure 7.1.26. Heat flow versus sediment thickness within the FLUM working area.

In-situ thermal conductivities are presented in Figure 7.1.27. The very uniform thermal conductivity of (0.82 ± 0.02) W/Km reflects the fact that the sediments in all working areas are fairly uniform. Conductivity measurements on recovered cores with a KD2Pro needle probe (<http://www.decagon.com/products/thermal/instruments/KD-2-Pro-Thermal-Properties-Analyzer/>) basically show the same with the exception of gravity cores SO240-69SL and SO240-117SL (see Fig. 7.1.28). The discrepancy between the mean values produced by in-situ measurements and ex-situ measurements on cores is enigmatic and will need further investigation.

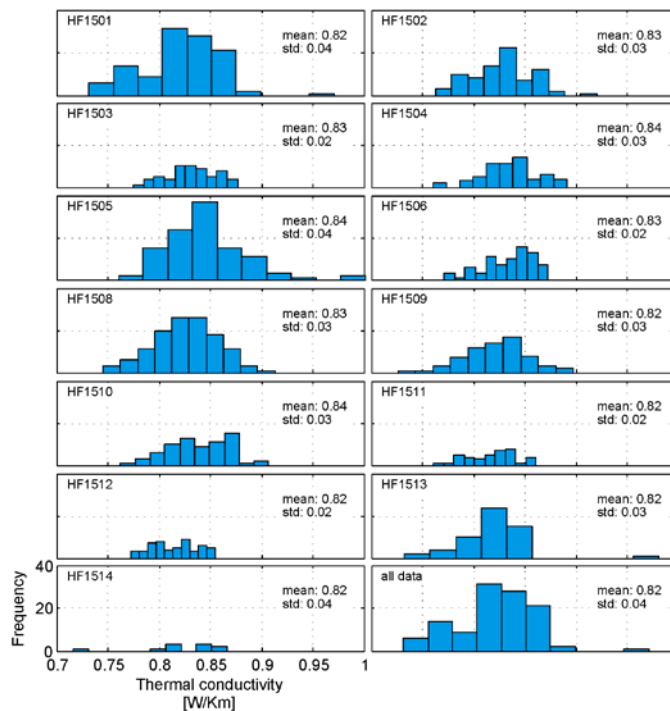


Figure 7.1.27. Compilation and statistics of all in-situ measured thermal conductivities.

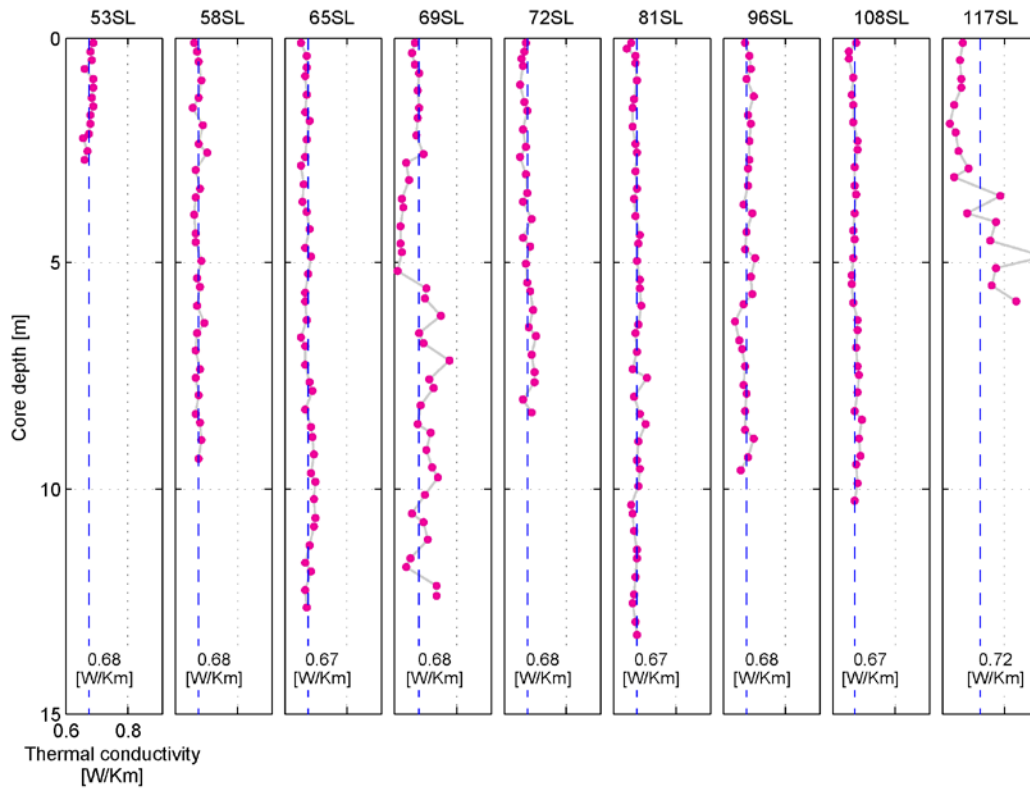


Figure 7.1.28. Thermal conductivities measured on recovered gravity cores. The data are not corrected for in-situ temperature conditions.

7.2 GEOPHYSICS BGR

Ingo Heyde

7.2.1 BGR Heat flow Probe

BGR currently deploys two different types of marine heat flow probes – a conventional probe, built according to the so-called violin-bow concept and a second probe that has been specially designed for deployment in hard ground situations. During cruise planning it was agreed upon that the GEOB group would routinely deploy their heat flow probe following the violin-bow concept, whereas the BGR “hard ground” heat flow probe (Fig. 7.2.1) would be used for stations with steeper terrain and less sediment coverage, e. g. closer to seamounts. The “hard ground” heat flow probe features a 2.2 m long sensor rod made of steel with a diameter of 2 cm mounted along the long axis of a cage and held in position by a special mechanism to prevent bending during penetration of hard ground sediments. It contains 7 thermistors with a spacing of 28 cm. The necessary force to press the sensor rod into the sediments is provided by a cylinder, which houses lead plates with a total weight of 600 kg and an electronic unit within a pressure vessel with a total weight of an additional 144 kg. The purpose of the electronic unit housed in the pressure vessel is to control the data transfer and the measurements. All measured data are transferred via the ship’s coax cable in real time online to a laptop PC on board.

All measured data are recorded, stored, digitized and monitored by so-called “intelligent sensor modules” (ISM) installed in the pressure vessel. This technology relies on immediate digitization and downloads of measured values in the memory and enables us to improve the accuracy of measurement to ~ 0.002 K. All recorded values are sent to an analogue-multiplexer and then to a 16bit-A/D-converter. The high accuracy and linearity during A/D-transformation is achieved by the application of the sigma delta method. To further improve the accuracy of the measurements, an arithmetic mean of 20 consecutive measurements per sensor is formed and then accepted as one single measured value. All specific modules that control the configuration, linearization and scaling data in the ISM-module are stored in an EPROM. Storage and display of the measured data is carried out via a special computer code, stored on the PC. A patent has been issued for this particular design.

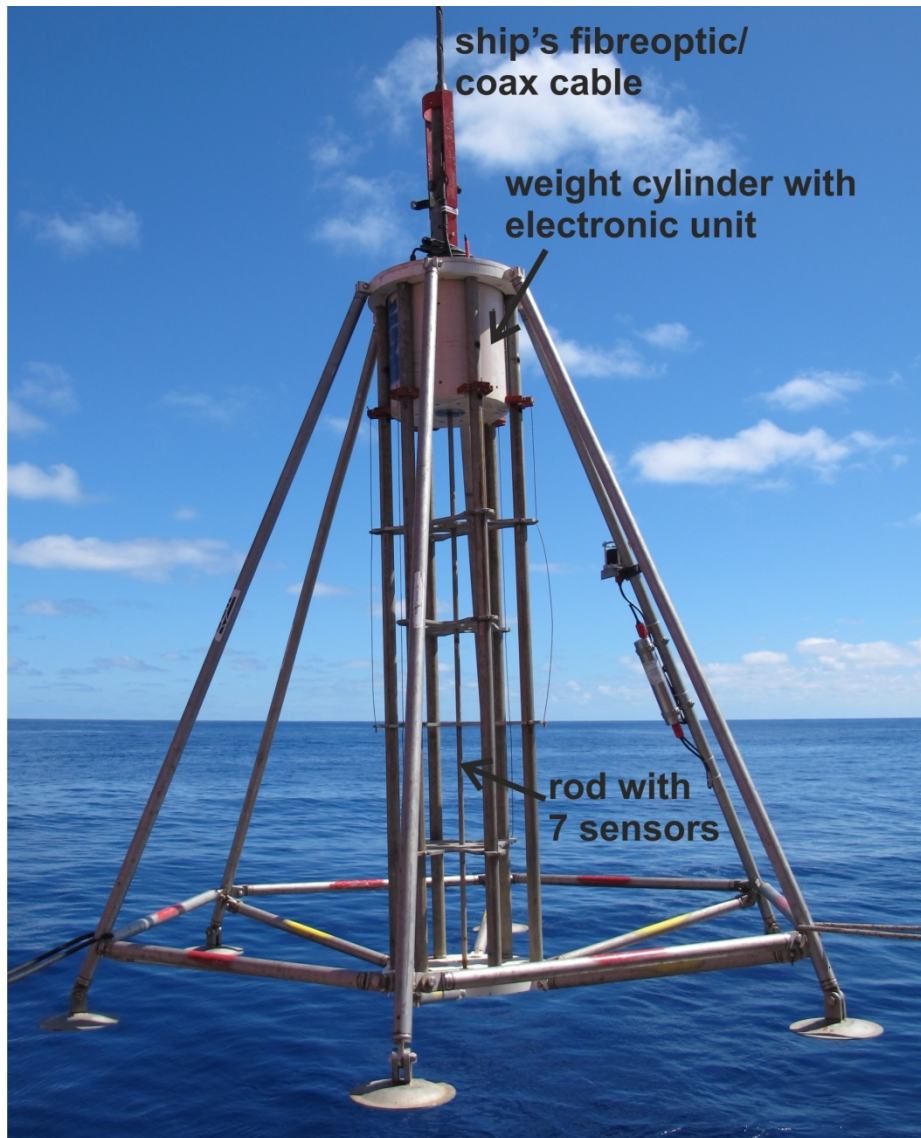


Figure 7.2.1. BGR - hard ground heat flow probe.

Figure 7.2.2 shows a typical heat flow measurement indicating the temperature graphs of 7 sensors from the time of reaching the seafloor to the time that the probe is hoisted back through the water column. To achieve optimal thermistor calibration, the heat flow probe is stopped slightly above the seafloor during lowering. A horizontal tilt meter in the recording device (in two perpendicular directions) allows verification of the moment when the probe has stopped swinging. After a time period of typically less than 2 minutes, thermal stabilization within ~ 0.001 K is obtained by all thermistors. It is assumed that the thermistors measure identical seawater temperatures. Recalibration of all thermistors is achieved by using one thermistor as the master sensor, whose measured value is used to calibrate the data measured by the other thermistors.

Following this procedure, the probe is lowered with a velocity of 0.1 m/s until penetration of the seafloor by the sensor rod is achieved. The tilt meter provides information on the inclination of the probe. The thermal gradient in the sediments is measured continuously for a time period of about 7 minutes. After this period, the frictional heat component caused by the penetration of the rod into the sediments has decayed to negligible values. Thereafter, a constant electric current of about 1 A (@ 10 V) is sent through the heating wire (about 4 m long) for the measurement of in-situ thermal

conductivity (λ). The temperature increase in the metallic rod is inversely proportional to the in-situ thermal conductivity of the adjacent sediments. We have measured the linear T-increase after initial heat-up of the assemblage and derived λ from this curve at all stations.

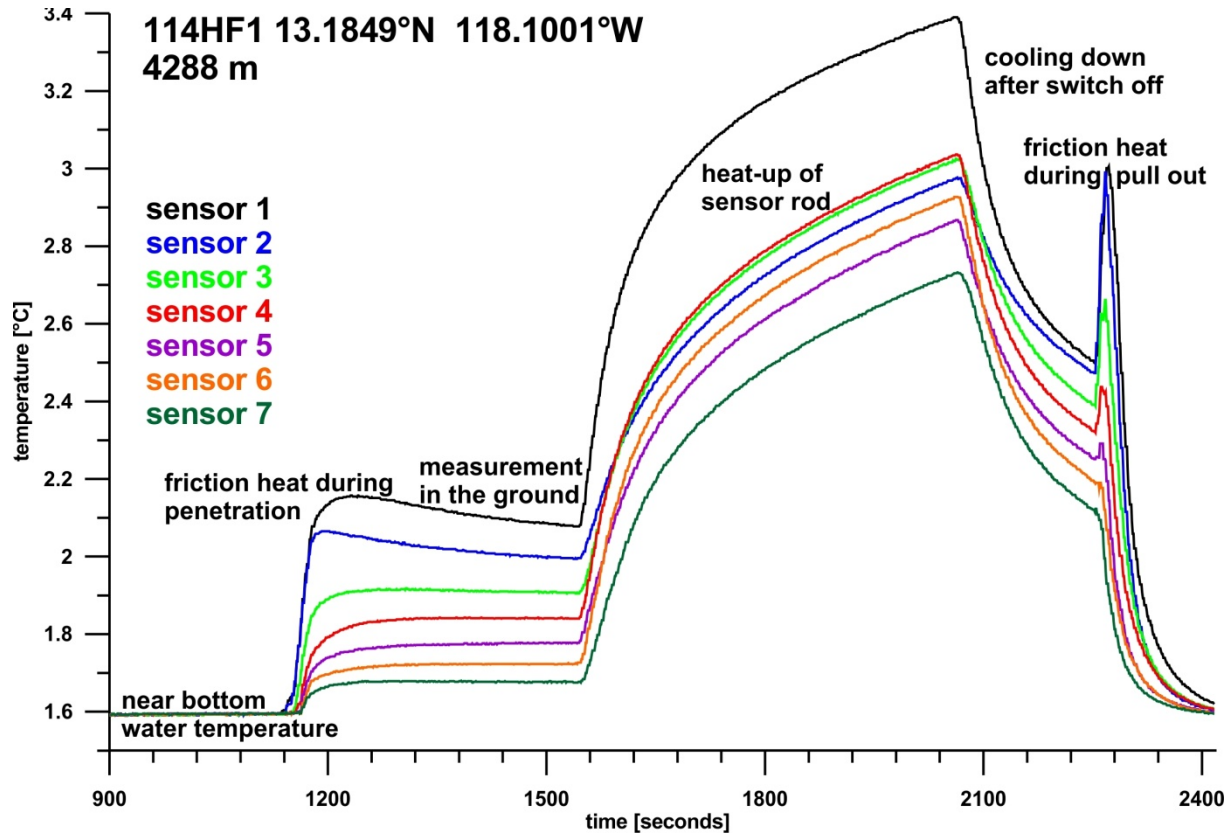


Figure 7.2.2. Heat flow measurement 114HF1 indicating the temperatures of the 7 sensors from the time of reaching the seafloor to penetration into the ground, heating and to the start of hoisting back through the water column.

7.2.1.1 Station work and preliminary results

The measurements with the BGR heat flow probe were conducted towards the end of the cruise in the area of the Teddy Bare seamount (WA-1). Earlier measurements with the GEOB probe showed a high heat flow value to the west of the seamount (see Chapter 7.1.2). With the BGR hard ground probe it was possible to take measurements closer to the seamount due to its capability to measure in areas of up to 5° inclination and/or covered with thin sediments of 2.5 m thickness only. Altogether heat flow measurements were conducted at 8 stations (Tab. 7.2.1). Figure 7.2.3 shows an example of the heat conductivities derived from the heat-up experiment at 2 stations. The mean value of 0.96 W/mK is considerably higher than the average value of the GEOB measurements (0.83 W/mK). Detailed investigations to explain this difference will be performed after the cruise.

The results are discussed together with the GEOB results in Chapter 7.1. Unfortunately the probe tumbled down at station 115HF-BGR5, presumably due to the steep terrain. Although the probe was heaved immediately after the tilting was recognized, the sensor rod was probably already somewhat bent, so that at station 115HF-BGR8 the sensor rod was deformed and twisted so strongly that it could not penetrate into the ground. Back on the vessel the twisted sensor rod had to be cut off before the probe could be set on the deck. For upcoming measurements the hard ground probe will be

complemented by an underwater camera system so that it will be possible to recognize visually steep terrain and insufficient sediment coverage before lowering the probe.

Table 7.2.1. List of heat flow stations with position, water depth, temperature gradient and heat flow values (assuming a heat conductivity of 0.83 W/mK).

Station	Date/Time	Latitude	Longitude	Depth [m]	Inclination Comments	Heatflow [mW/m ²] Temp. Gradient [mK/m]
114HF-BGR	09.06.-10.06.15 22:10-02:05	13.18487°N	118.10007°W	4288	0.9° / 0.3°	169.8 204.6
115HF-BGR1	10.06.15 02:44-04:40	13.18412°N	118.09617°W	4270	0.2° / 3.2°	143.1 172.4
115HF-BGR2	10.06.15 05:32-05:50	13.18442°N	118.0929°W	4272	0.4° / 4.6°	108.0 130.1
115HF-BGR3	10.06.15 06:46-07:09	13.18802°N	118.0920°W	4275	4.1° / 1.1°	53.8 64.8
115HF-BGR4	10.06.15 08:01-08:14	13.19000°N	118.09028°W	4272	1.0° / 2.8°	80.2 96.7
115HF-BGR5	10.06.15 09:07-09:10	13.19068°N	118.08705°W	4248	Probe tumbled down due to steep terrain	No penetration
115HF-BGR6	10.06.15 09:26-09:52	13.19147°N	118.08678°W	4272	5.0° / 2.9°	71.9 86.6
115HF-BGR7	10.06.15 12:18-12:42	13.18097°N	118.09232°W	4243	0.1° / 4.9° no Posidonia position	51.1 61.6
115HF-BGR8	10.06.15 13:23-13:40	13.17853°N	118.08848°W	4214	5.8° / 1.9° no Posidonia position	No Penetration due to bent rod

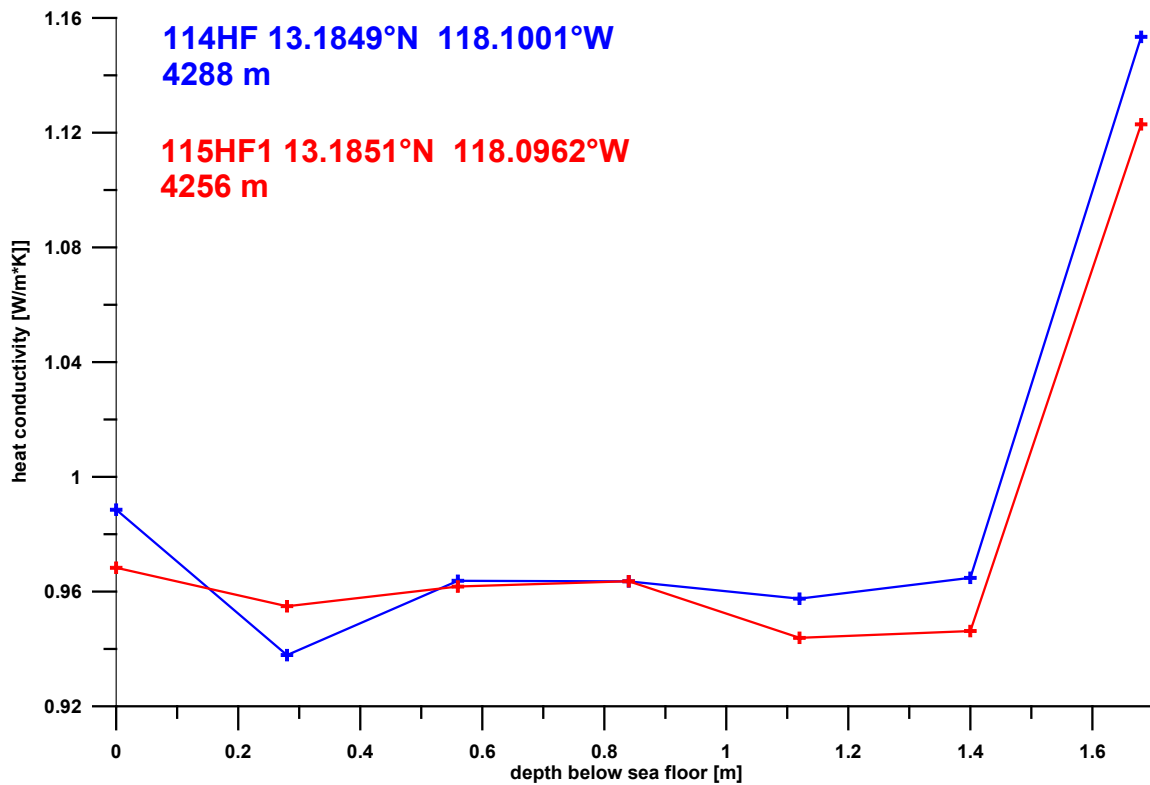


Figure 7.2.3. Derived heat conductivities at the contiguous stations 114HF-BGR and 115HF-BGR1. The mean value for the upper 6 sensors amounts to 0.96 W/mK.

7.2.2 The sea gravimeter system KSS32-M

During cruise SO-240, the BGR-owned sea gravimeter system KSS32-M was installed in the Gravimeter Lab on deck 02 one level below the main deck (Figs. 7.2.4 and 7.2.5). The gravimeter sensor was located approximately 1 m above in the vessel’s nominal water line, 1.5 m to portside from the centerline, and about 61 m from the ship’s stern.

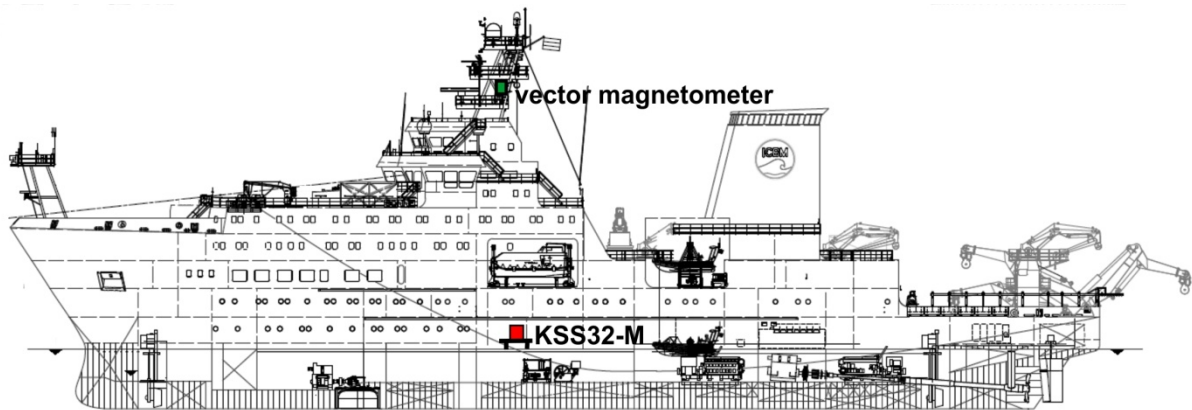


Figure 7.2.4. Sketch of RV SONNE with the location of the gravimeter (red) and the vector magnetometers (green).

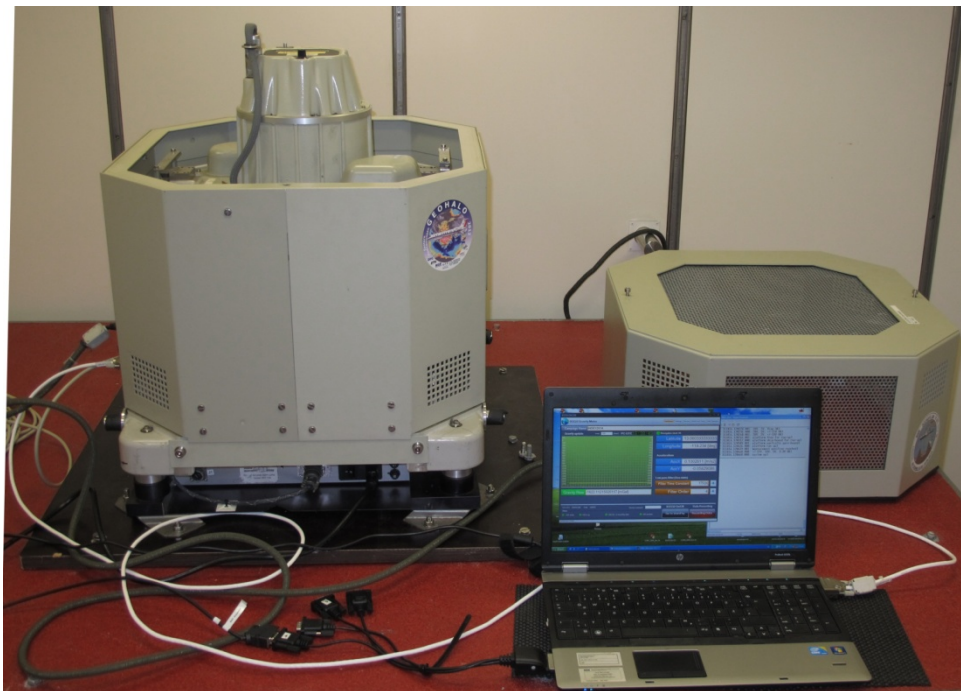


Figure 7.2.5. KSS32-M gravimeter system in the Gravimeter Lab on RV SONNE.

The gravimeter system KSS32-M is a high performance instrument for marine gravity measurements, manufactured by the Bodenseewerk Geosystem GmbH. While the sensor is based on the Askania type GSS3 sea gravimeter designed by Prof. Graf in the 60ties, the development of the horizontal platform and the corresponding electronic devices took place at Bodenseewerk Geosystem in the beginning of the 1980ties. The system was completely modernized and modified in 2011 by the successor company BGGS (Bodensee Gravimeter Geosystem GmbH, Meersburg). Before, the system consisted of two main assemblies: the gyro-stabilized platform with the gravity sensor and a rack containing the control

electronics, the data handling subsystem and the power supply. After the modernization, the system electronics and the power supply were integrated into the platform. The system is controlled by a notebook (HP ProBook 6550B).

The main software to operate the KSS32-M is DACQS developed by BGG. It is possible to change a number of settings (e.g. parameters of the Bessel Filter applied to the measured data) and the software provides detailed information on the status of the system. Data acquisition is also managed by DACQS, whereby a wide range of values, not only for gravity but also e.g. for the attitude and horizontal accelerations of the platform, can be recorded.

The gravity sensor GSS30 (Fig. 7.2.6) was not affected by the modernization. It consists of a tube-shaped mass that is suspended on a metal spring and guided frictionless by 5 threads. It is non-astatized and particularly designed to be insensitive to horizontal accelerations. This is achieved by limiting the motion of the mass to the vertical direction. Thus, it is a straight line gravity meter avoiding cross-coupling effects of beam type gravity meters. The main part of the total gravity acceleration is compensated by the mechanical spring, but gravity changes are compensated and detected by an electromagnetic system. The displacement of the spring-mass assembly with respect to the outer casing of the instrument is measured using a capacitance transducer.

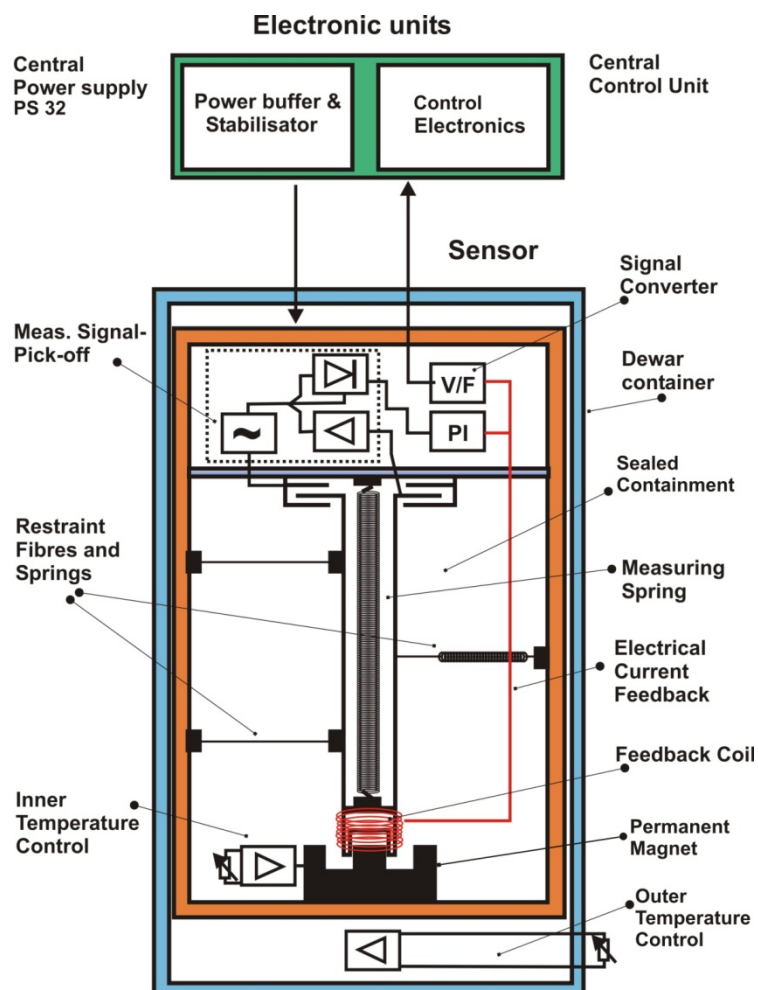


Figure 7.2.6. Principle sketch of the gravity sensor GSS30 of the gravimeter system KSS32-M.

The leveling subsystem consists of a platform stabilized in two axes by a vertical, electrically erected gyro. The stabilization during course changes can be improved by providing the system with online navigation data. The stabilized platform keeps the sensor in an upright position with an accuracy of leveling in the order of 0.5 arc-minutes. This is particularly important as the sensor is very sensitive to tilting and the corresponding effects of horizontal accelerations. Vertical accelerations, however, cannot be eliminated. Luckily on a ship the vertical acceleration oscillates symmetrically with the ship's motion. The period of the oscillation is in the order of several seconds. This signal can be eliminated easily by means of low-pass filtering.

The data were transmitted via the notebook to the BGR data acquisition and processing system in Dry Lab II and online navigation data from this system were sent with a rate of 1 Hz to support the stabilizing platform. The support is realized as follows: The horizontal position of the gyro-stabilized platform is controlled by two orthogonal horizontal accelerometers. The platform is leveled in such a manner that the horizontal accelerations are zero. If the ship describes a curve, the additional horizontal acceleration will cause the platform to be leveled according to the resulting apparent vertical axis. This axis may differ substantially from the true vertical axis and will result in reduced gravity values and additionally in an effect of horizontal accelerations on the measured gravity. This error, named Harrison effect, is eliminated by supplying the KSS32-M system with online navigation data. A microprocessor calculates the leveling errors from this input and enters them into the platform electronics which corrects the platform accordingly.

7.2.2.1. Gravity ties to land stations

To compare the results of different gravity surveys with each other, the measured data have to be tied to a world-wide accepted reference system. This system is represented by the International Gravity Standardization Net IGSN71 (Morelli, 1974). Furthermore, the instrumental drift of the KSS32-M can be derived from the tie measurements at the beginning and the end of each cruise. The marine geophysical group of BGR uses a LaCoste&Romberg gravity meter, model G, no. 480 (LCR G480) for the gravity connections. Descriptions and absolute gravity values for reference stations near Manzanillo were provided by Dr. Ernesto Torres Orozco from the Facultad de Ciencias Marinas, Universidad de Colima. Reliable and accessible reference stations are located at the Naranjo Campus of the University of Colima in Manzanillo. Especially the station Manzanillo AA is very reliable, as it is marked clearly and located inside an institute building.

RV SONNE moored at the southern part of the main quay (point A) in the harbour of Manzanillo (Fig. 7.2.7). Unfortunately, it was not possible to carry out tie measurements on May 4th as we did not receive a short-time permission from the harbour and customs authorities to leave the harbour with the LCR G480. Thus, the tie measurements had to be postponed until RV SONNE returned to Manzanillo at the end of the cruise. A preliminary absolute gravity value to tie into our gravity data was taken from the summary of cruise MGL0812 of the Lamont-Doherty Earth Observatory, Columbia University, in 2008. Although the exact mooring site of RV LANGSETH is not provided, it should have been relatively close to our mooring site. The absolute gravity value was assumed to be 978583.54 mGal. The sensor was located 1 m above the water level, resulting in an absolute gravity value of 978583.83 mGal (with water level -2.1 m, IGSN71). The reading of the KSS32-M during

departure from port (May 4th 2015, 20:45 UTC) with the same water level was -1343.18 mGal. The draught of the vessel was 6.4 m.

At the end of the cruise, RV SONNE moored at the cruise passenger jetty in Manzanillo. On June 14th tie measurements on the pier opposite the gravity lab on RV SONNE were made. However, it was impossible to get a stable reading on the jetty due to the movement of this light construction. Stable measurements could only be taken about 200 m to the SW at the northern tip of the main pier (**B**) (Fig. 7.2.7). The connection measurements resulted in an average absolute gravity value of 978583.75 mGal (reduced to water level -2.0 m, IGSN71) for point **B**. The draught of RV SONNE was about the same (6.3 m) as during the departure time on May 4th. Thus, the absolute gravity value for point **B** at the height of the KSS32-M sensor was 978583.48 mGal. The reading of the KSS32-M at the same time (June 14th 2015, 13:00 UTC) was -1344.75 mGal. Unfortunately, it was not possible to measure directly at the departure quay site from May, 4th as it again was not possible to obtain permission from the harbour and customs authorities to enter the harbour. In order to control the assumed absolute gravity for this quay location, we carried out a measurement at point **C**, just outside the harbour and at the same latitude to the best of knowledge (Fig. 7.2.7). The absolute gravity at **C** was determined to be 978583.105 mGal. This value is in good agreement with the assumed value for the departure quayside. Thus, we retained the absolute value assumed after leaving Manzanillo on May 4th 2015.

The instrumental drift for cruise SO-240 can be derived from the readings in Manzanillo to -1.22 mGal / 40.68 days or -0.03 mGal/day. This drift rate is quite low and a proof for the good quality and condition of the gravity sensor. The gravity data were corrected for this instrumental drift.

Table 8.1.1. Observation report of the gravity tie measurements in Manzanillo, Mexico.

Station	Observer	Date	Time UTC	Reading units	Gravity value [mGal]
B	H	14.06.15	14:30	2181.68	2214.524
01	H	14.06.15	15:45	2193.22	2226.251
02	H	14.06.15	15:50	2193.41	2226.444
C	H	14.06.15	16:30	2181.54	2214.382
B	H	14.06.15	16:45	2181.70	2214.544
Observer: H = Heyde. Gravity in mGal using LCR G 480 scaling table.					

Reference Stations:

- 01:** Manzanillo CA, University of Colima, FACIMAR 978594.841 mGal (IGSN71)
(National Imagery and Mapping Agency station no. 5844-3,
19.1246°N, 104.4009°W, 18 m above MSL)
- 02:** Manzanillo AA, University of Colima, FACIMAR 978595.125 mGal (IGSN71)
(National Imagery and Mapping Agency station no. 5844-2,
19.1243°N, 104.4012°W, 18 m above MSL)

Gravity stations:

- A:** Manzanillo Harbor, Main Quay, bollard C16
- B:** Manzanillo Harbor, Cruise Passenger Pier, southern end
- C:** Manzanillo, Corner Niños Heroes/Dolores Hidalgo Roads, Outside Manzanillo Harbor

Differences between reference and gravity stations:

$$02 - 01 = 0.193 \text{ mGal (0.284 mGal expected)}$$

$$02 - C = 12.02 \text{ mGal}$$

Absolute gravity at C: 978583.105 mGal

Absolute gravity for C (reduced to water level –2.0 m) 978583.637 mGal (IGSN71).

Reading of sea gravimeter KSS32M at departure time 04.05.15 (20:45 UTC): -1343.18 mGal.

$$02 - B = 11.91 \text{ mGal}$$

Absolute gravity at B: 978583.215 mGal

Absolute gravity for B (reduced to water level -2.0 m) 978583.747 mGal (IGSN71) used for the gravity tie on 14.06.2015 (13:00 UTC). Reading of sea gravimeter KSS32-M at that time: -1344.75 mGal.

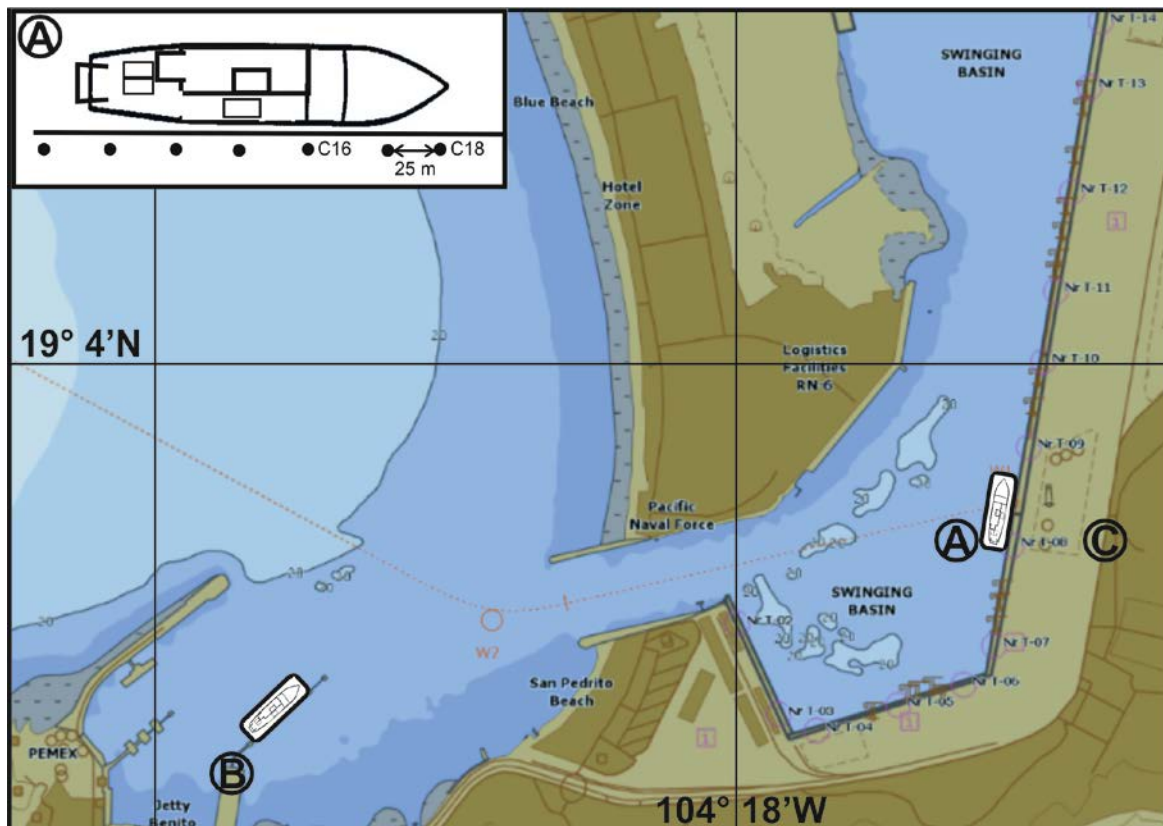


Figure 7.2.7. Location of the mooring sites of RV SONNE at the Main Quay in the harbour of Manzanillo.

7.2.2.2 Gravity data processing

Processing of the gravity data consists essentially of the following steps:

- a time shift of 76 seconds due to the overcritical damping of the sensor,
- conversion of the output from measured voltage to mGal by applying a conversion factor of 4.7271 mGal/mV. This was carried out directly during data acquisition in the DACQS software from BGGs.
- connection of the harbour gravity value to the world gravity net IGSN 71,
- correction for the Eötvös effect using the navigation data,
- subtraction of the normal gravity (GRS80),
- correction for the instrumental drift (performed after completion of the cruise).

As a result, we obtain the so-called free-air gravity anomaly (FAA) which in the case of marine gravity simply is the Eötvös-corrected, observed absolute gravity minus the normal gravity. Gravity values were recorded with a data rate of 1 Hz. This data rate was retained during data processing. The KSS32-M anomalies show short-wavelength oscillations in the order of 1-2 mGal especially while cruising at higher ship velocities (Fig. 7.2.8). Therefore, a median filter with a length of 300 s was applied to the data. Infrequent outliers were removed manually in advance. Additionally, data recorded during sharp turns and rapid speed changes of the vessel show affected values and were removed manually.

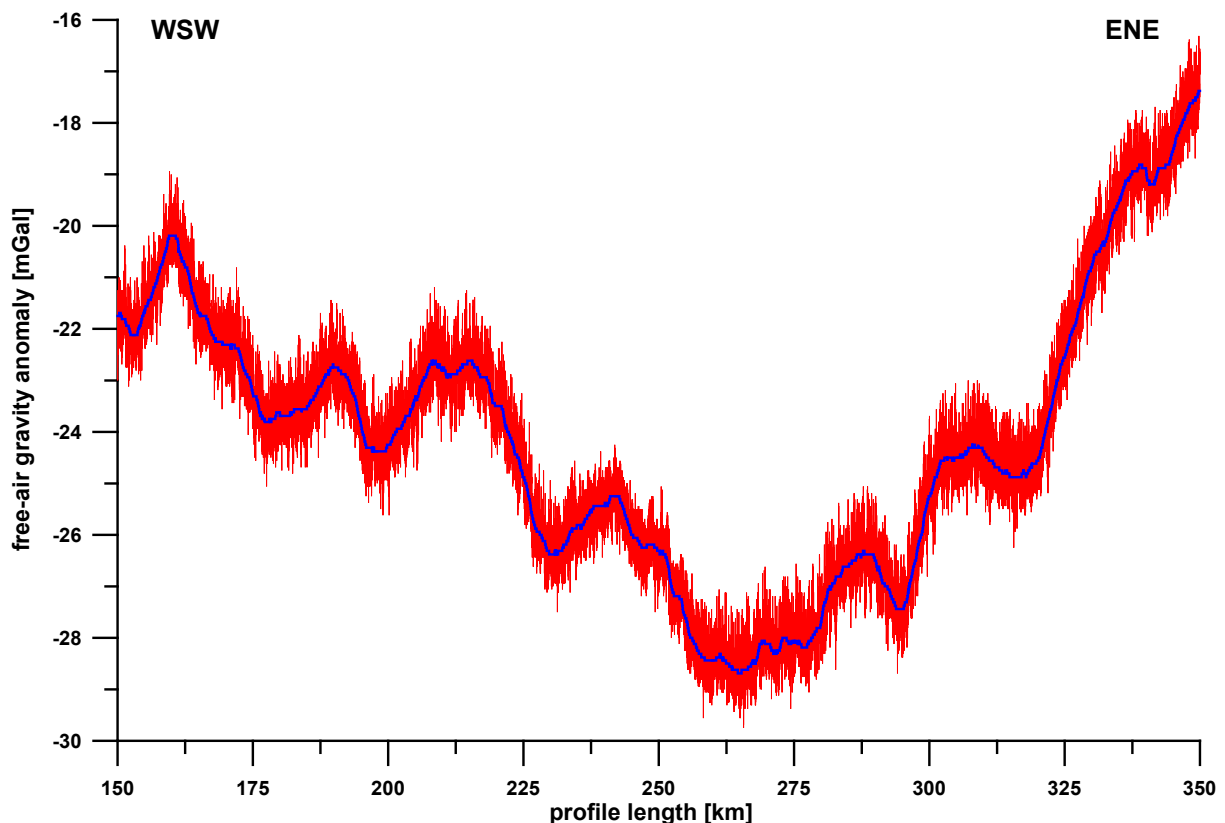


Figure 7.2.8. Free-air gravity anomalies along a part of profile BGR15-101 approaching the working area before and after applying a 300 s median filter.

7.2.2.3 Data quality

The gravity data observed obtained during the cruise were of high quality and only showed long-wavelength noisy behavior whilst entering sharp curves or during rapid speed changes of the vessel. In order to check the accuracy of the data quantitatively, the values of gravity profiles at crossovers were compared. However, whereas there are a lot of crossovers during transits between stations, there are only a few crossovers during dedicated survey profiles. The average COE in the free-air gravity anomalies for 11 crossovers is 0.42 mGal ($1\sigma = 0.69$ mGal).

7.2.2.4 Gravity database

Gravity measurements were carried out continuously during the complete cruise. However, data acquisition did not start before the EEZ of Mexico was left, and was respectively stopped on re-entering the EEZ. Thus, gravity data along all survey and transit profiles with a total length of about 4750 km were obtained (Fig. 7.2.9). The details of the survey profiles including the numeration and location are listed in Appendix **XX**.

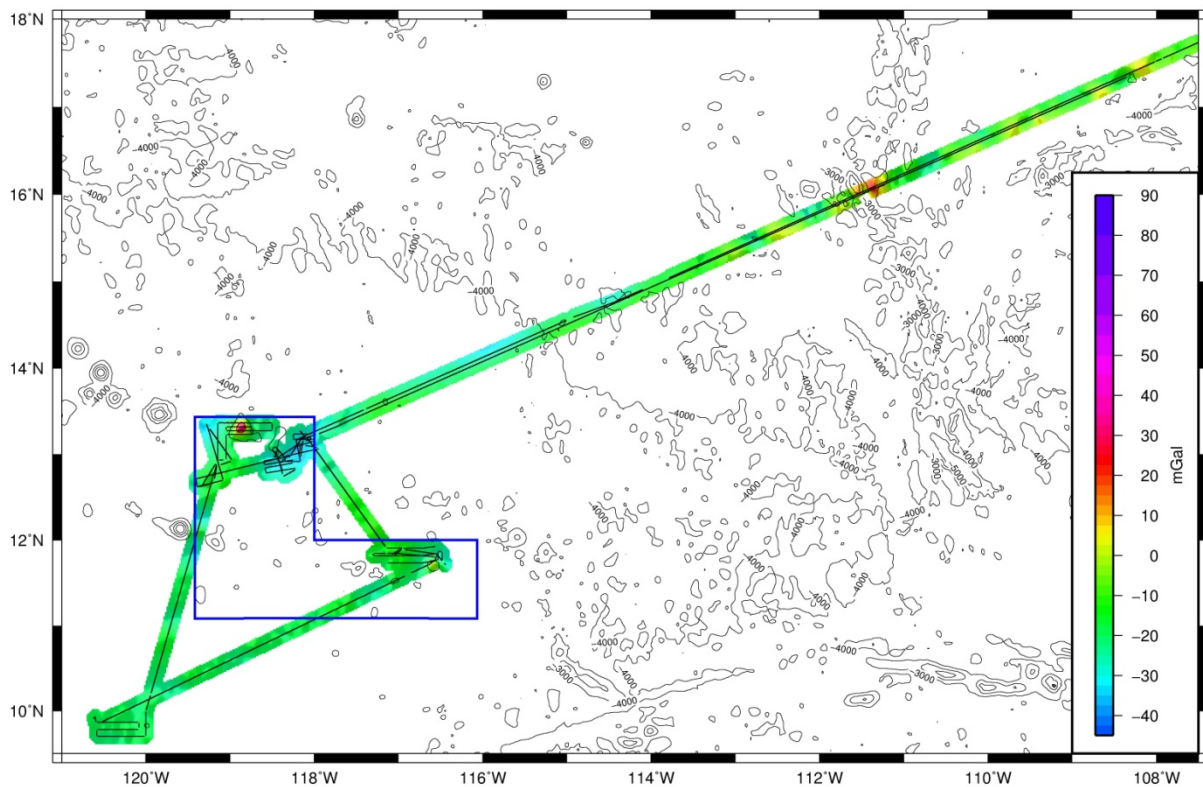


Figure 7.2.9. Map of the free-air gravity anomalies acquired during cruise SO-240 FLUM. The map is drawn up to a distance of 10 kilometers from the tracks. The map is based on a 1 x 1 (arc-)minutes grid and is underlain by the bathymetry of Sandwell and Smith (2009, version 18.1).

7.2.2.5 Comparison with gravity anomalies derived from satellite altimetry

The analysis of crossover errors shows that our gravity measurements are far more precise than those from alternate methods to measure the marine gravity field, such as the calculation of free-air gravity anomalies from satellite altimeter measurements. A satellite altimeter uses pulse-limited radar to measure the altitude of the satellite above the closest point to the sea surface. Global precise tracking coupled with dynamic orbit calculations provide an independent measurement of the height of the satellite above the ellipsoid. The difference between these two measurements is equal to the geoid height. In marine areas the free-air anomaly can be calculated from the slope of the geoid. Closely spaced satellite altimeter profiles collected during the GEOSAT Geodetic Mission (~ 6 km) and the ERS 1 Geodetic phase (~ 8 km) were used by different groups to calculate grids of the free-air gravity anomalies. Our data set can serve as a reference for the comparison of two different satellite gravity data compilations. The first is the one from Sandwell and Smith (2009), version 23.1, referred to as SDW23.1 in the following. The second data set is from the DTU Space Center, Copenhagen (Andersen, 2010) referred to as DTU10 here.

Subtracting the 1 x 1 minute grid of the SDW23.1 and DTU10 data from the 1 x 1 minute grid of the shipboard data, one obtains maps showing the differences within our working area (Fig. 7.2.10). The maps are masked beyond a distance of 2 kilometers from the SO-240 tracks. The differences between both datasets range between +16 and -8 mGal, but the differences are below ± 4 mGal along most tracks. There is no pronounced areal distribution of the differences. It is remarkable, however, that the greatest differences were found above the seamount at 13.3°N/118.9°W. Satellite gravity anomalies along the complete track were additionally calculated with bicubic interpolation out of the 1 x 1 minute grids and subtracted from the shipboard data (Fig. 7.2.11). The mean differences are smaller for the DTU10 data (0.35 mGal vs. 0.64 mGal). However, the standard deviation is lower for the SDW23.1 data (1.73 mGal vs. 2.49 mGal). Considering the standard deviation as the main criteria, the above statistical results helped us to decide on using the SDW23.1 data set for further gravity map compilations in areas where no SO-240 shipboard data were measured.

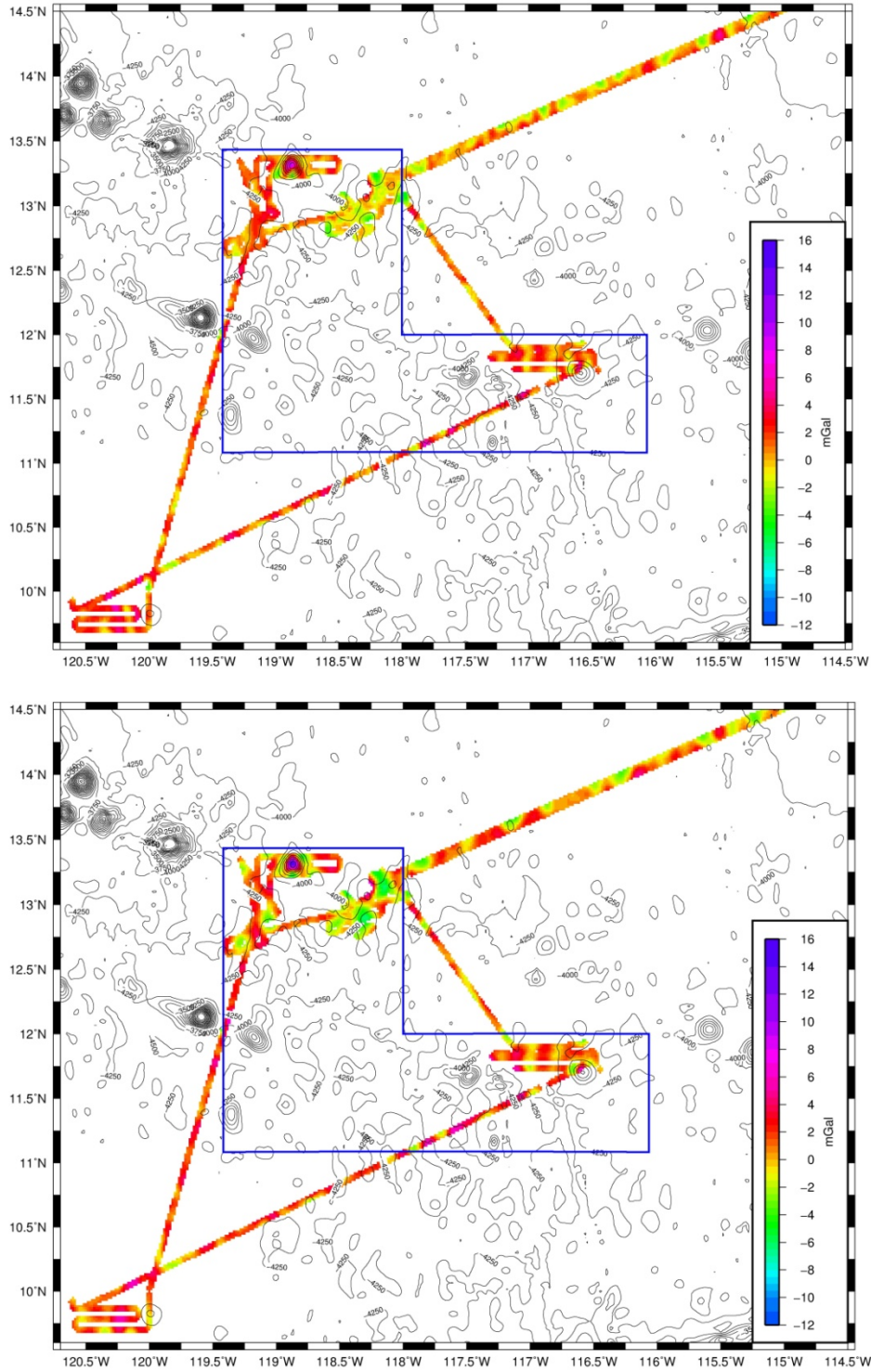


Figure 7.2.10. Differences between the shipboard free-air gravity data and the gravity datasets derived from satellite altimetry (above: SDW23.1 Sandwell and Smith (2009), version 23.1.; below: DTU10, Andersen (2010)). The maps are underlain by the bathymetry of Sandwell and Smith (2009, version 18.1).

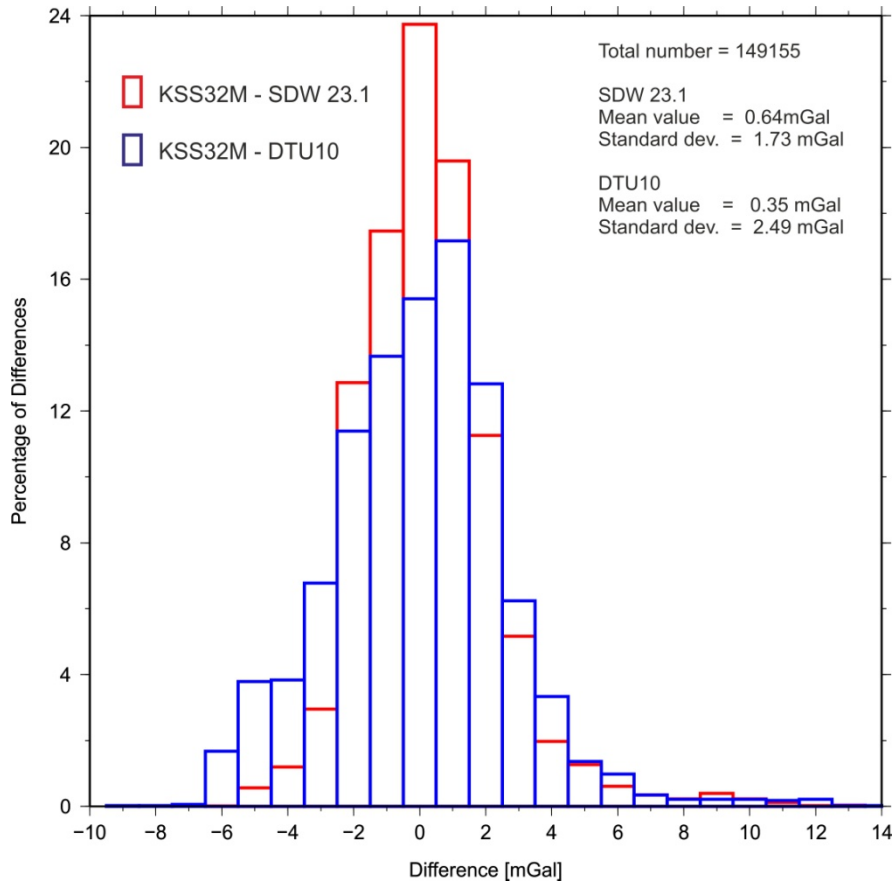


Figure 7.2.11. Histogram of differences between shipboard KSS32-M free-air gravity anomalies and the corresponding gravity datasets derived from satellite altimetry.

To illustrate the differences between the data sets in detail, Fig. 7.1.12 exemplary shows a comparison along a part of the transit profile BGR15-101 to the working area. The resolution of the shipboard anomalies is higher and the positions of maxima and minima of satellite-derived anomalies are also shifted by several kilometres. This shows the significance of shipboard gravity for the actual survey. The free-air gravity anomalies derived from satellite altimetry are only of importance to obtain an overview of the gravity field within an oceanic area. For detailed investigations, however, shipboard gravity measurements are indispensable.

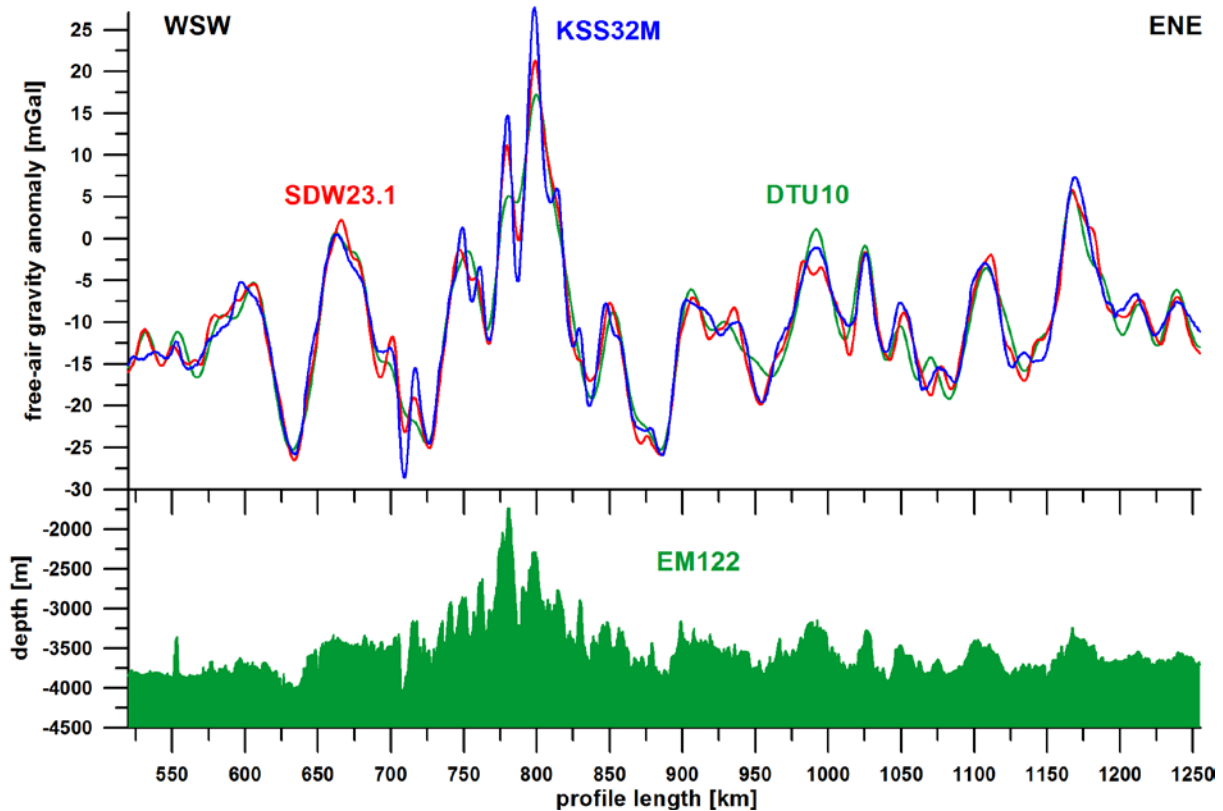


Figure 7.2.12. Comparison between the ship-based KSS32-M and satellite (SDW23.1 and DTU10) free-air gravity anomalies along a part of the transit profile to the working area (above). The shipboard-measured bathymetry is shown below.

7.2.2.6 Gravity anomaly maps

Figure 7.2.13 shows the free-air gravity anomaly map of working areas 1 to 3. The map is based on shipboard data only and is drawn up to a distance of 4 km from the ship tracks. The gravity values in the East generally show low values of -40 to -25 mGal. This reflects the large mean water depth of about 4350 m in this area. Topographic elevations of the oceanic crust cause only small increases of the gravity values. It is not possible to resolve individual topographic features due to the water depth and their limited height and extent. In WA-3 the gravity values amount to -20 to -10 mGal, reflecting the lower mean water depth of about 4200 m. Again it is not possible to resolve smaller topographic features. The strongly positive anomaly at 13.3°N/118.9°W with gravity values of up to +45 mGal reflects a seamount with an elevation of nearly 2 km above the surrounding crust. The seamount is not surrounded by a gravity low and thus shows no signs of subsidence in the gravity map. Low gravity values in the NW reflect the increased water depth in that area.

For the determination of the Bouguer gravity anomalies, water depth values were taken from the shipboard swath echo-sounding data. The reduction density was 1.64 g/cm³ (rock density: 2.67 g/cm³ - sea water density: 1.03 g/cm³) and an infinite horizontal slab was assumed. A topographic reduction was not performed. Figure 7.2.14 shows the map of the Bouguer gravity anomalies in working areas 1 to 3. Topographic features of smaller scale are better resolved in this map. For example, in WA1 the Teddy Bare seamount (13.18°N/118.08°W) is represented by low Bouguer gravity anomaly values of +240 mGal compared to +260 to +270 mGal in the surroundings.

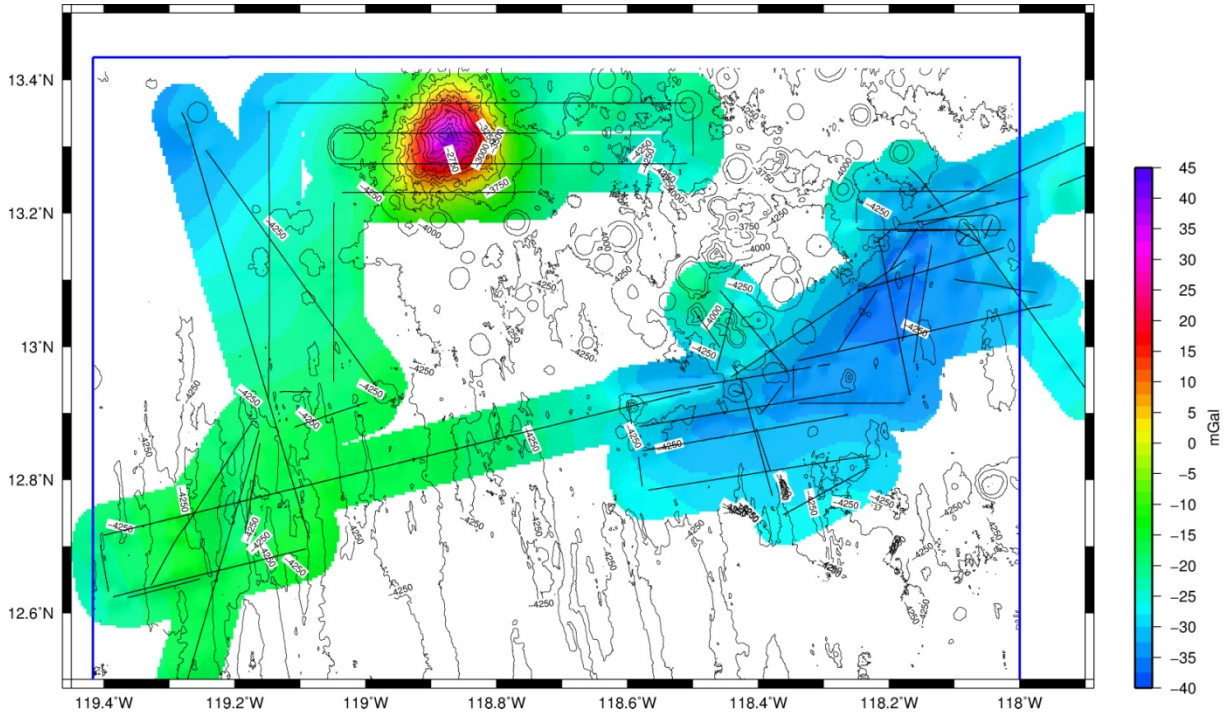


Figure 7.2.13. Free-air gravity anomaly map of working areas 1 to 3. The map is based on a 0.25 x 0.25 (arc-) minutes grid and is drawn up to a distance of 4 kilometers from the ship track. It is underlain by the bathymetry measured during previous MANGAN cruises.

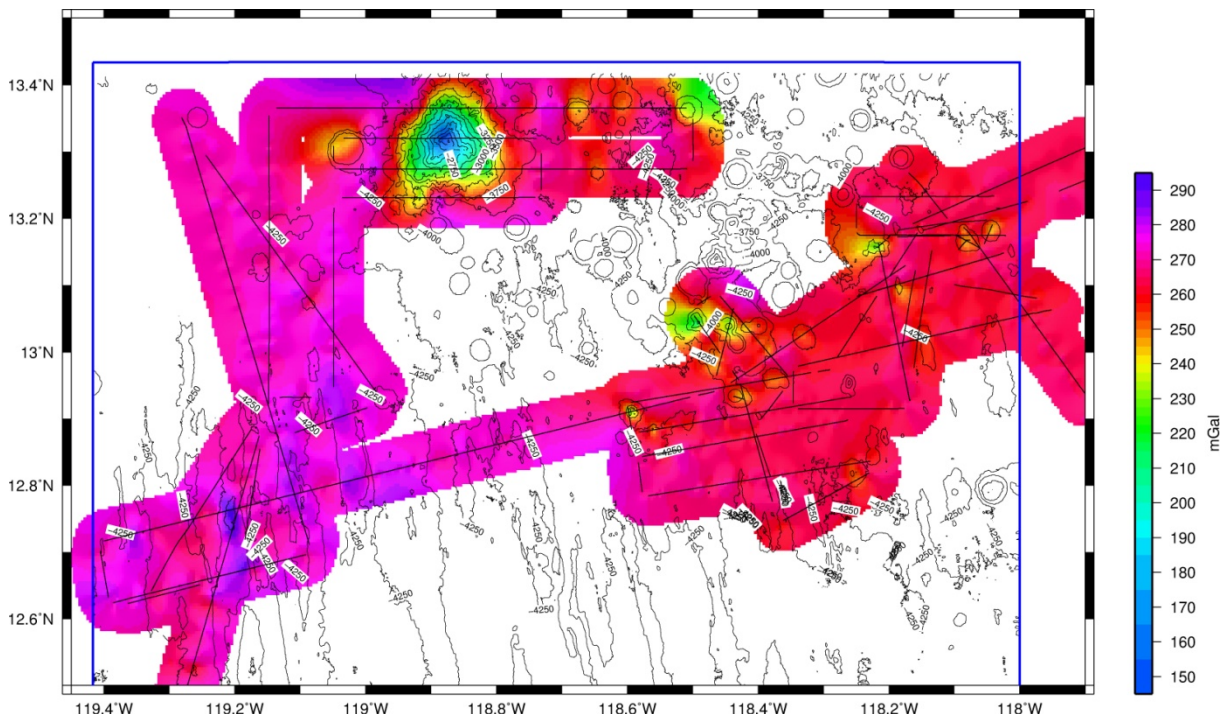


Figure 7.2.14. Map of Bouguer gravity anomalies in working areas 1 to 3. The reduction density was 1.64 g/cm³. The map is based on a 0.25 x 0.25 (arc-)minutes grid and is drawn up to a distance of 4 kilometers from the ship track. It is underlain by the bathymetry measured during previous MANGAN cruises.

Figure 7.2.15 shows the free-air gravity anomaly map of WA4. The map again is based on the shipboard data only and is drawn up to a distance of 4 km from the ship tracks. The gravity values in the East show low values of -30 to -20 mGal compared to the West with values of -20 to -10 mGal.

This reflects the slightly greater water depth in the eastern part of the area. Topographic elevations of the oceanic crust mostly cause small increases gravity values. However, the seamount at 11.7°N/116.6°W causes a positive gravity anomaly. The low gravity values in its immediate surroundings indicate that the seamount has probably subsided into the crust. It is again not possible to resolve smaller individual topographic features due to the water depth and their limited height and extent.

Figure 7.2.16 shows a map of the Bouguer gravity anomalies in WA4. On this map some topographic features of smaller scale, such as the seamount at 11.51°N/117.08°W, are resolved.

Figure 7.2.17 shows the free-air gravity anomaly map of the evasion area. The map is again based on shipboard data only and is drawn up to a distance of 4 km from the ship tracks. It is underlain by the bathymetry of Sandwell and Smith (2009, version 18.1). The free-air gravity values only vary between -25 and -15 mGal, reflecting the homogeneous water depth of around 4200 m. The presence of a seamount at 9.8°N/120°W as predicted in the bathymetry derived from satellite altimetry could not be verified by the shipboard echo-sounder data. Hence also the gravity data show no anomalies in that area. This illustrates and confirms again that free-air gravity anomalies and bathymetry derived from satellite altimetry should not be trusted blindly but should be checked by shipboard measurements.

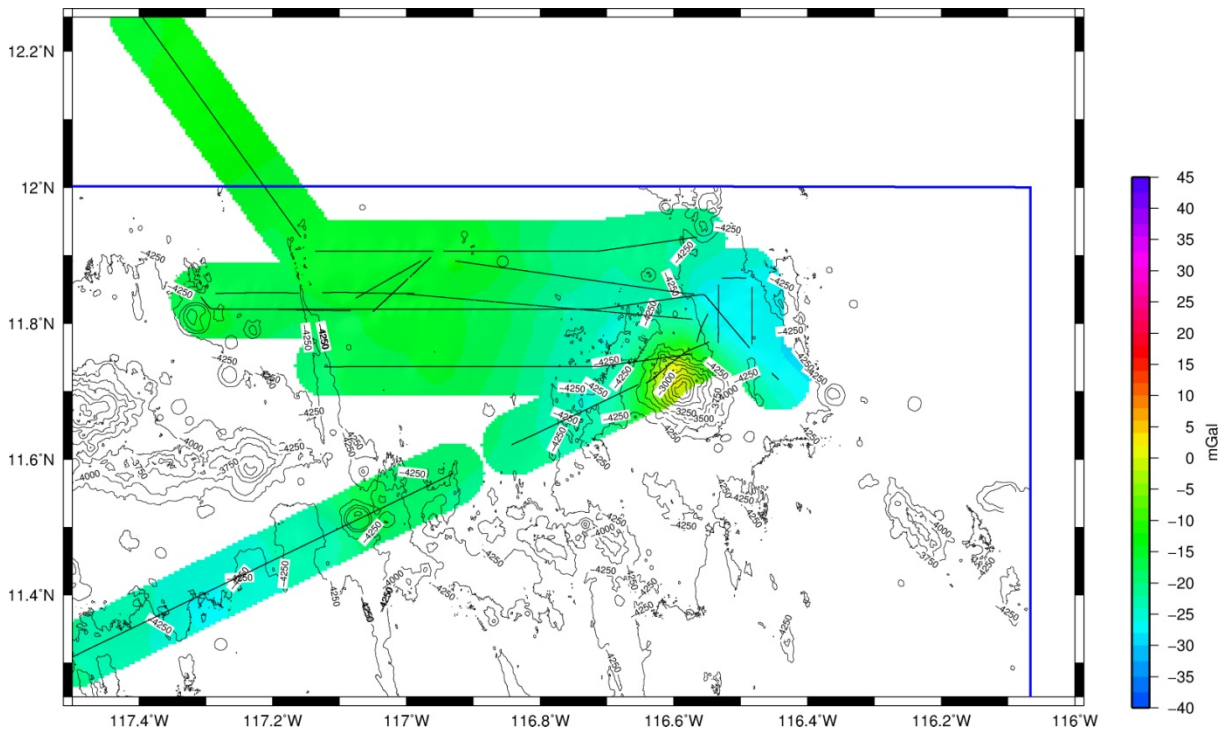


Figure 7.2.15. Free-air gravity anomaly map of working area 4. The map is based on a 0.25 x 0.25 (arc-) minutes grid and is drawn up to a distance of 4 kilometers from the ship track. It is underlain by the bathymetry measured during previous MANGAN cruises.

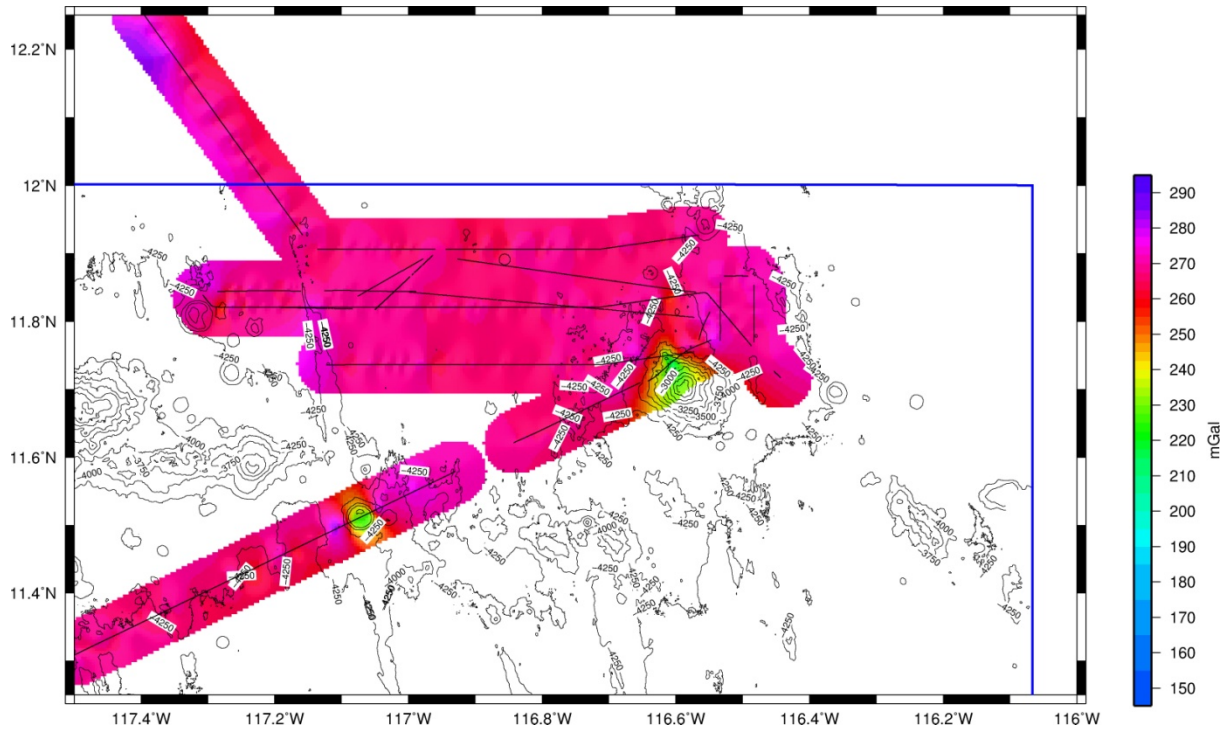


Figure 7.2.16. Map of Bouguer gravity anomalies in working area 4. The reduction density was 1.64 g/cm^3 . The map is based on a 0.25×0.25 (arc-)minutes grid and is drawn up to a distance of 4 kilometers from the ship track. It is underlain by the bathymetry measured during previous MANGAN cruises.

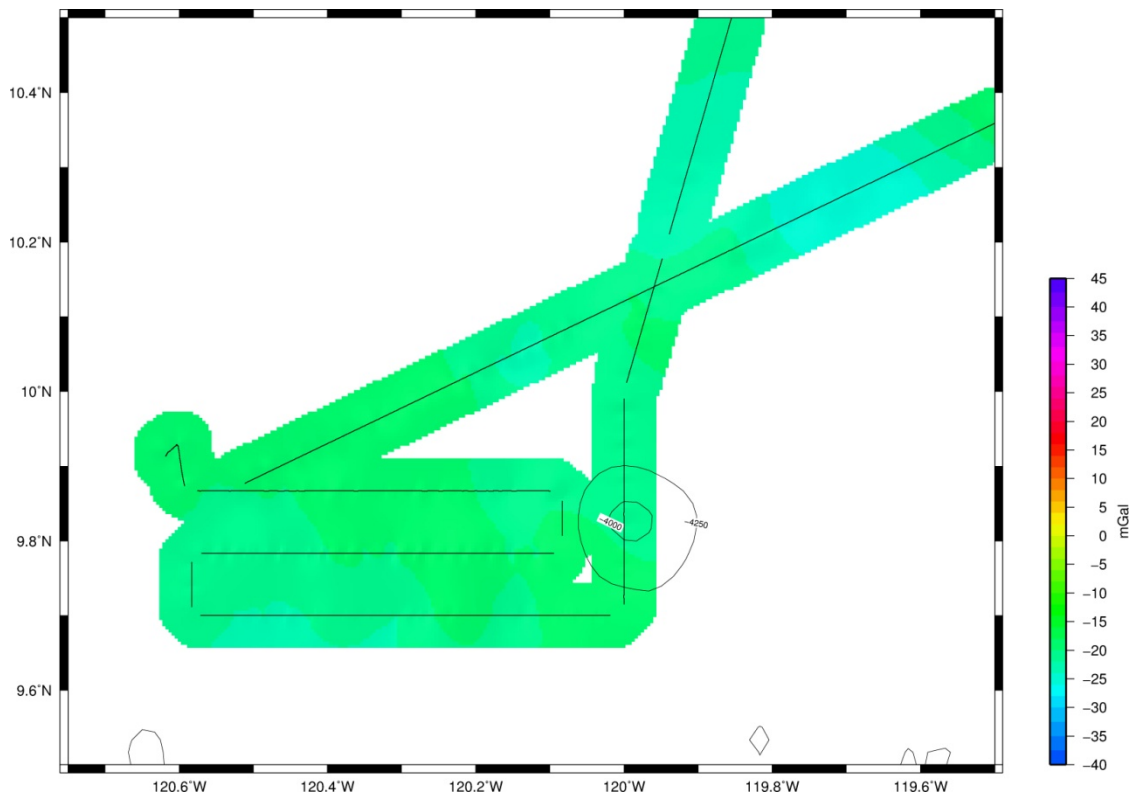


Figure 7.2.17. Free-air gravity anomaly map of the evasion area. The map is based on a 0.25×0.25 (arc-)minutes grid and is drawn up to a distance of 4 kilometers from the ship track. It is underlain by the bathymetry measured during previous MANGAN cruises.

7.2.3 Magnetics

During cruise SO-240 the following fluxgate magnetometers were operated on different platforms:

1. Two MAGSON fluxgate sensors were mounted onto both sides of the first platform of the main mast and recorded magnetic data permanently from departure of the Mexican EEZ on May 5th 2015, until re-entering the EEZ on June 12th 2015.
2. Two oriented MAGSON fluxgate sensors were mounted together onto the STROMER deep tow vehicle on one platform in a pressure housing with 6000 m depth rating.

7.2.3.1 Shipborne MAGSON™ Fluxgate Magnetometer

A shipborne vector magnetometer system was installed above the observation room on the first platform of the main mast. It consists of two separate waterproof housings that contain orthogonal digital ring core fluxgate sensors and two-axis inclinometers, a data acquisition box and a GPS mouse. The system was built by MAGSON GmbH in Berlin for the BGR and delivered in January 2010 as an onboard system for research vessels. The sensors have a dynamic range of +/- 100000 nT and a long-term stability of <10 nT/year, and were fixed to the railing on the port and starboard sides of the platform (Fig. 7.2.18). The data acquisition box and the power supply were installed in the observation room. The data are recorded internally on a CF memory card and optionally online on a laptop. Two different types of data files are stored separately for each hour. The first file type (file extension M60) contains the values of the three orthogonal vector components and the inclination values together with UTC time marks. The sampling rate can be chosen between 1 and 20 Hz. On this cruise, we used 10 Hz. The second file type (file extension S60) contains time marks and latitude and longitude from the GPS receiver and temperature values for both sensors. The sensors are internally heated to a selectable temperature, on our cruise to 35°C.



Figure 7.2.18. Shipborne dual vector magnetometers (marked by arrows) installed on the first platform of the main mast (left: starboard; right: portside).

Additionally we also recorded the values from the ship's motion reference units (heave, roll, pitch and azimuth). Experience shows that roll and pitch values from the vessel sensors are much more reliable than the inclinometer values from the fluxgate sensors that are less precise due to dynamic accelerations.

7.2.3.2 Fluxgate Calibration

A fluxgate magnetometer has to be calibrated regularly against a precisely known reference field in order to estimate the calibration parameters (1) offset, (2) scale factor, and (3) a non orthogonal angle for each axis - thus a total of nine parameters for a three-axis vector magnetometer. During a scalar calibration, the fluxgate sensor is rotated around all axes and the total field reading is adjusted to the reference field. This optimization of calibration parameters is done by a least squares fit of the measurements (here: downhill simplex method; one variant keeping the non-orthogonality angles fixed, which are regarded stable; calibration software by Jeff Gee, SIO). Using this procedure, one combination of calibration parameters is obtained which minimizes deviations from the reference field for all attitudes of the sensor.

Calibration parameters drift slowly with time, and changes may also occur after long-distance transportation to different latitudes. Furthermore, calibration parameters are temperature dependent, which means that laboratory calibrations have to be repeated at different temperatures. In addition to a laboratory calibration, where the sensor is rotated around all axes at different temperatures, a calibration loop is required in the survey area waters, which provide a fine adjustment to the local magnetic field conditions and water temperatures. Therefore, calibration parameters should be estimated at the beginning and end of each survey in order to account for possible drift.

The measured vector components are heavily influenced by the induced and remanent magnetization of the ship, which may also be time dependent. The three components of the remanent magnetic field of the ship and the nine matrix elements of the susceptibility tensor can be determined by a least squares fit of the measured magnetic field components against the values of a magnetic reference field during a calibration loop (Isezaki, 1986, König, 2006). After the determination of all 12 parameters that describe the magnetic field of the ship for all azimuthal directions, the measured vector components of the ship-based magnetometers can be corrected for the field of the vessel. Several calibration maneuvers, consisting of a full loop over starboard followed directly by a full loop over portside, were performed during cruise SO-240. However, the vessel compensation is part of the post-cruise processing.

7.2.3. Magnetic vector data acquired during STROMER deployments

The dual vector magnetometer sensors in one pressure vessel rated for 6000 m are of the same type as the shipborne vector magnetometer sensors. They were built by MAGSON in 2012 for the BGR and successfully mounted onto BGR's MFT deep tow vehicle during the INDEX cruises in 2012 and 2013. During SO-240, the magnetometer (Fig. 7.2.19) was installed after the first three STROMER deployments and worked very well during the last four deployments (40STR, 41STR, 49STR and 113STR). However, the magnetic field caused by the steel frame of the sledge and probably also some of the other instruments mounted onto the platform turned out to be higher than expected and needs to

be compensated for in a numerical approach (similar to the compensation of the vessel's magnetic field for the onboard fluxgates). This requires further post-cruise processing and was carried out successfully by Uta Engels for the first MFT deployments on cruise INDEX 2012 with newly written codes. However, the magnetic data acquired during the STROMER deployments have only been processed in a very preliminary way during the cruise. The data format and the merging of the magnetic data with the positions of the STROMER acquired with a POSIDONIA system require major changes in the existing processing codes for vector magnetic data and this could not be completed during the cruise. A lucky incident seems to be the fact that the STROMER slowly rotates several times while being heaved up to the sea surface. This should allow the determination of the 12 parameters of the induced and remanent magnetization of the deep tow vehicle.

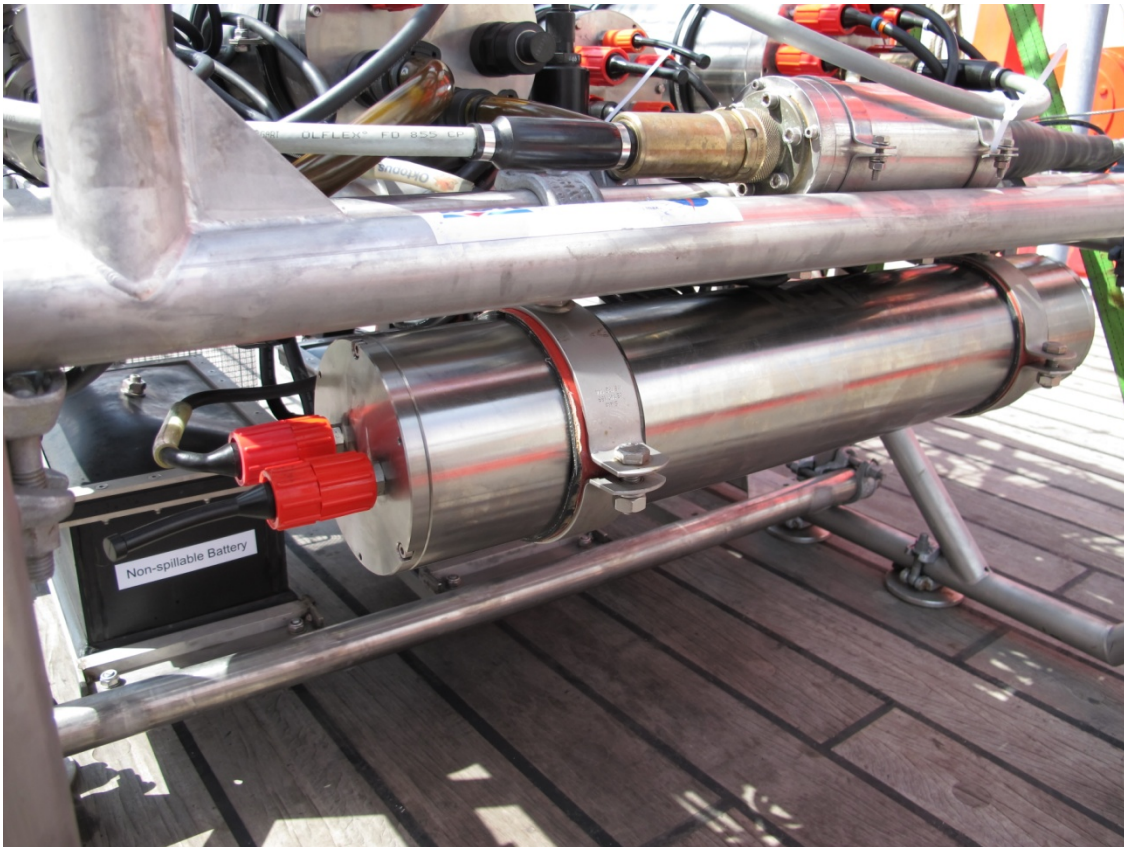


Figure 7.2.19. Deep-towed double vector magnetometer installed on the frame of the STROMER.

7.3 SEDIMENTOLOGY AND GEOCHEMISTRY

C. Heller, A. Wegorzewski, T. Kuhn, A. Lückge, C. Rühlemann, S. Sturm, A. Vink,

The aim of the sedimentology and geochemistry studies carried out during the FLUM S0-240 cruise was to analyze the influence of the processes of fluid fluxes between seamounts on the sediments and the occurrence and composition of manganese nodules.

7.3.1 Methods

Box corer

The box corer was deployed at 20 stations, of which 15 could be used for concurrent sampling of manganese nodules and 19 for sampling of the upper undisturbed ~40 cm of sediment (Tab. 6.2). The box corer is composed of a steel frame and a central piston with a sampling box of 50 x 50 cm size (48 cm height) at its lower end (Fig. 7.3.1). During descent, insertion and sampling, the cover flaps on top of the sampling box remain open, allowing for a free flow of water to prevent pressure build-up and disturbance of the sediment surface. After landing on the seabed, an automatic mechanism releases the closing shovel. On withdrawal from the seabed, the sampling box is closed by drawing the shovel beneath the sampling box and closing the top of the box with the cover flaps. The box corer was usually lowered with an average speed of 1 m/s until it reached about 50 m above the seafloor, where the corer was stopped for 1 min and then lowered with a speed of 0.7 m/s until contact with the seafloor as monitored through the cable tension. The box corer was pulled out of the bottom sediment with a speed of ~0.3 m/s and finally heaved back to the surface with a speed of 1.0 m/s.



Figure 7.3.1. BGR box corer.

Immediately after recovery of the box corer, supernatant water was removed using flexible plastic tubes and passed through a 300 μm mesh sieve to sample the macrobenthic fauna. After that, photos were taken to document the distribution and original position of the nodules on top of the sediment. Subsequently, sessile organisms were sampled, nodules and sediment were described and the upper faces of the nodules (according to their position on the seafloor) were marked with a yellow point of a signal marker gel. The nodules were then collected and washed with seawater pumped through the ship's clean seawater intake. Afterwards, one short sediment core per box corer was taken using a plastic liner (length: 39–45 cm; \O : 117.6 mm), which was split along core. The core was photographed, described sedimentologically with respect to color, structure and bioturbation, used for the measurement of shear strengths and stored for further sampling. Moreover, 100 cm^2 of the surface layer of box corer sediments (0-1 cm) were sampled for measurements of (1) physical properties (dry bulk density, porosity) and geochemistry, (2) microfossils and (3) grain size (Fig. 7.3.2, left panel). Five series of 10 cm^3 syringes were taken at 3 cm spacing from top to bottom for physical properties, geochemistry and grain size analyses (Fig. 7.3.2, left panel). Sampling of the benthic organisms is described in chapter 7.6. Photos were taken of the washed nodules deriving from the actual surface of the sediment, which were sorted according to their size into a metal frame with an area of 50 x 50 cm (equal to the size of the box corer). Nodules deriving from 1–10 cm and 10–20 cm sediment depth and those found even deeper were collected separately in order to investigate their mass and size ratios. Finally, the wet weight of the total nodule mass was determined (Tab. 6.2). The further treatment of the collected nodules is described in chapter X-ray fluorescence analyzer (XRF) below.

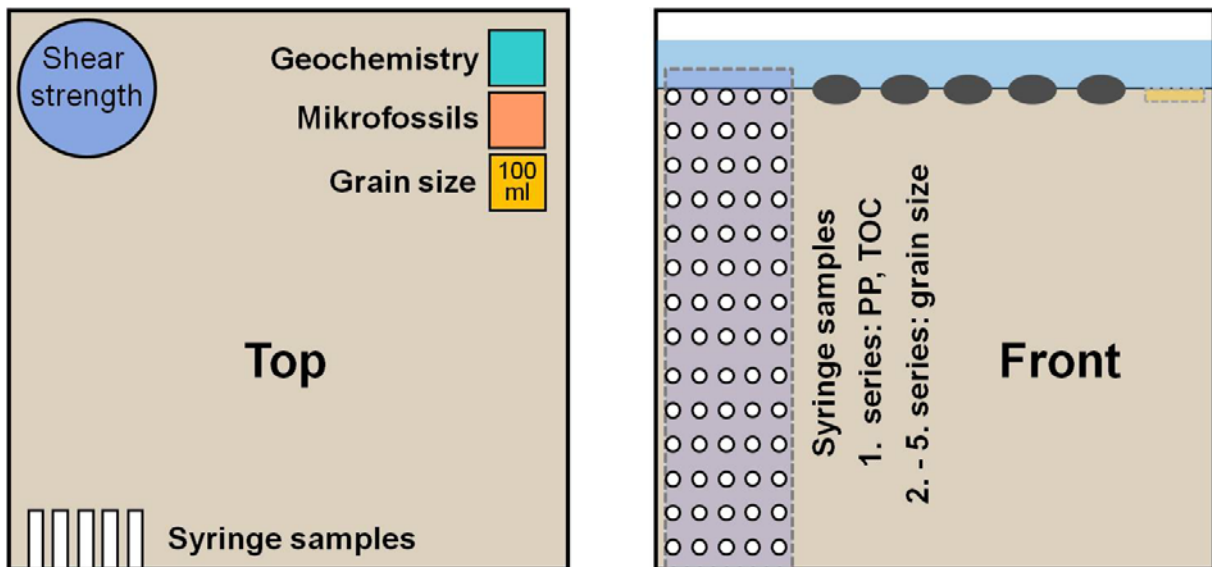


Figure 7.3.2. Sampling scheme of the box corer. Left: panel for surface sampling. Right: panel for down-core sediment sampling.

Piston corer (KL) and gravity corer (SL)

A piston corer (Fig. 7.3.3) with a steel pipe of 15 m length, equipped with a plastic liner of 12 cm in diameter, and a weight of 2 tons on top was used for obtaining long sediment cores at 6 stations and the gravity corer with a variable pipe length of 5, 10 or 15 m (depending on the nature of the bottom sediments and the proximity to seamounts) was used at 13 stations (see Tab. 6.2 and Tab. 7.3.1). Both corer were lowered with an average speed of 0.5 m/s within the uppermost 100 m water depth and then with an average speed of 1.0 m/s, stopped at 50 m above the seafloor for 1 min and then lowered with 0.3 m/s. After penetration into the sediment, the corer was heaved with 0.1 m/s until it was free from the bottom. The corer was then heaved with 1 m/s to the sea surface. The plastic liner was immediately cut into 1 m segments and cooled for at least 12 hours for oxygen analysis (see chapter 7.4). Subsequently, the liner was labeled and cut along core into a work and an archive half. The work halves were used for the sampling at ca. 10 cm spacing of pore waters and sediments. In addition, several subsamples per core were taken to analyze the geochemistry directly on board using the handheld XRF. The archive halves were used for photographing and for measurements of shear strength and reflectivity (lightness) in the upper 2 m of each core.

Table 7.3.1. List of piston and gravity corer deployments during the SO240 cruise.

Core #	Station SO240-	Work area #	Position		Water depth [m]	Corer length [m]	Recovery [cm]	O ₂ at base	Sediment cover [m]	Fault	Dark brown sediment at base	Heat flow [mW/m ²]
			latitude (N)	longitude (W)								
1	05SL	1	13° 10.525'	118° 06.705'	4287	10	756	yes	< 10	yes	yes	n.d.
2	09KL	1	13° 10.524'	118° 10.104'	4335	15	1187	no	23	no	no	4.1
3	15KL	1	13° 07.101'	118° 07.657'	4319	15	1161	no	22	?	no	n.d.
4	19KL	1	13° 10.527'	118° 08.083'	4307	15	steel pipe of corer lost during deployment					
5	22KL	1	13° 10.527'	118° 08.184'	4302	15	1301	no	< 20	yes	no	~10
6	31KL	2	12° 53.355'	118° 24.572'	4289	15	1174	no	36	yes	no	17.7
7	35SL	2	12° 54.128'	118° 24.791'	4319	10	982	yes	18	no	yes	< 11
8	42SL	2	12° 51.249'	118° 23.976'	4290	15	1036	yes	29	yes	yes	37.4
9	51SL	1	13° 10.526'	118° 06.584'	4286	15	537	yes	10	yes	yes	42.0
10	53SL	1	13° 10.508'	118° 06.110'	4273	5	482	yes	< 10	no	yes	54.8
11	58SL	3	12° 53.216'	119° 08.351'	4309	15	1244	no	73	no	no	48.9
12	65SL	3	12° 56.107'	119° 08.884'	4293	15	1275	no	72	no	no	63.4
13	69SL	3	12° 39.855'	119° 13.374'	4275	15	1265	yes	51	yes	yes	135.5
14	72SL	3	12° 55.597'	119° 08.833'	4294	15	853	no	73	yes	no	85.3
15	81SL	4	11° 50.064'	116° 32.890'	4355	15	1346	yes	20	yes	yes	91.7
16	96SL	4	11° 49.260'	117° 13.195'	4145	10	980	yes	21	yes	yes	80.4
17	103SL	4	11° 49.253'	117° 03.847'	4137	15	977	n.d.	37	yes	yes	~68
18	108SL	4	11° 48.796'	116° 31.767'	4326	15	1038	no	20	no	no	~54
19	117SL	1	13° 11.103'	118° 05.992'	4271	15	600	yes	< 10	no	yes	181.1

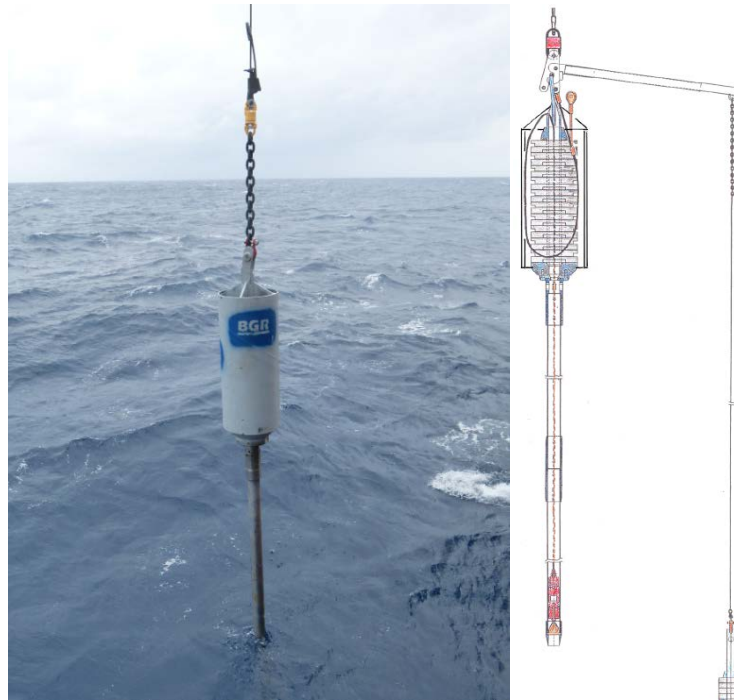


Figure 7.3.3. Piston corer (KL), right and gravity corer (SL), left, used for sediment core sampling during the SO240 cruise in the eastern German license area.

Chain-bag dredge (GDS)

The BGR-owned chain-bag dredge was deployed at 2 stations (27GDS and 120GDS; see Tab. 6.2) in order to collect Mn-nodules, Fe-Mn crusts and basaltic rocks from seamounts. The dredge is composed of a steel framework (2.50 m x 1.20 m x 0.50 m) and a metal chain bag attached to the framework (length 2.70 m; Fig. 7.3.4). During deployment, the dredge was lowered to the seafloor at 0.5 m/s. Starting 100 m before bottom contact, 1000 m of extra wire was paid out at 0.5 m/s while the vessel moved straight ahead along the planned track of 0.53 nm length at a speed of 1.0 knots. At the end of the track, the vessel stopped and the dredge was pulled over the seafloor at 0.5 m/s until it left the bottom. Finally, the dredge was heaved on board at a speed of 0.3 m/s and the samples (nodules, crusts and basaltic rock fragments) were emptied onto the deck and stored for later analyses in the home laboratories.



Figure 7.3.4. Chain bag dredge (GDS) used for the recovery of manganese crust, nodules and basaltic rock fragments.

Sediment shear strength measurements

Short sediment cores obtained from the box corer were split into two equal halves, and the undrained shear strength of the predominantly cohesive clayey sediments in one half of the core was measured at ca. 3 cm sampling intervals using a "Strassentest Baustoff-Prüfungssysteme" fallcone penetrometer type 318-D with a digital display (Fig. 7.3.5). In addition, the undrained shear strength was measured at ca. 5 cm sampling intervals in the upper 2 m of the archive half of the long sediment cores recovered by piston or gravity corer. The cone and vertical sliding rod of the penetrometer have a total weight "GK" of 79.9 g (= 0.78 N), and the apex angle of the cone is 30°. The tip of the cone was positioned to just touch the surface of the sediment to be measured. The cone was then released so that it could penetrate into the surface of the sediment, and was fixed after 5 sec. The undrained shear strength " τ_u " of the sediments (in N/m² or Pa) was determined from the penetration depth "s" (in m) according to the following equation (Hansbo, 1957):

$$\tau_u = \frac{k \cdot G_K}{s^2}$$

The dimensionless factor "k" depends on the cone angle and, to a lesser extent, on the sensitivity to adhesion. Its value is 0.85 for undisturbed, cohesive marine clayey samples and a cone apex angle of 30° (Houlsby, 1982). In total, ca. 1000 measurements were performed (38 cores, 19 short box cores and 19 long cores).



Figure 7.3.5. Fall cone penetrometer used for shear strength measurements.

X-ray fluorescence analyzer (XRF)

After nodules and sediments were sampled from the box cores, the nodules were visually inspected, described in detail and the lengths of their three axes were measured. After that, a few representative nodules of different sizes and types were selected for chemical analyses using an energy dispersive handheld XRF analyzer (Delta DS 6000 by Innov-X Company; Fig. 7.3.6 B) on board of the research vessel as well as for further analyses in the home laboratory. Additionally, subsamples of sediments collected from the gravity and piston cores were also used for chemical analyses on board. The selected samples (nodules and sediments) were dried at 40°C for 48 h and then ground to a particle size $< 0.25 \mu\text{m}$ in a single-station planetary sphere mill (type “PM 100 CM” by Retsch; Fig. 7.3.6 A). A fraction of the powder was separated and additionally dried for 48 h at 100°C for chemical analyses using the handheld XRF. The powder samples were transferred to plastic vials, of which the bottoms were covered with a 2.5- μm -thick mylar foil. The nodule powder was analyzed for its Mn, Fe, Cu, Ni, Zn, Zr, Ti, and V content and the sediment samples for Si, Fe, Mn, Ca, Al, Ti, P, Ni, Cr, S, K, Cu, Zn, Zr and Pb.

With this method, high-energy primary X-ray photons are emitted from an X-ray tube (4 watt, 8-40 keV, 5-200 μA). The emitted X-ray photons strike the sample and because of their high energy, they knock electrons out of the innermost *K* or *L*-orbital. An electron from a higher energy level (outer orbital *L* or *M*) can move into the inner orbital to occupy the vacant position, thereby emitting energy as secondary x-ray photons. The amount of energy is characteristic for specific elements. The beam used has a diameter of 8 mm. Before analyzing the nodule samples, the XRF-Analyzer was calibrated with a certified reference Mn-oxide material (Manganese Nodule standard; Kriete, C. 2014). The accuracy and reproducibility was checked against the Mn-standard and by repetition of analyses. The measurement accuracy of Mn, Fe, Ni, Cu, and V was better than 5%. However, the accuracy for Ti, Zr and Zn was lower with 40%, 10% and 6%, respectively. Reproducibility for Mn, Fe, Ni, Cu and Zn was better than 7% and for Ti, V and Zr better than 30%.



Figure 7.3.6. Instruments used for nodule grinding and the chemical analyses. A: planetary sphere mill "Retsch PM 11 CM". B: Innov-X tube-based portable XRF analyzer "Delta DS 6000" with workstation for lab use.

Measurement settings

The manganese nodule samples were analyzed with the XRF-Analyzer using the setting "Erze" and the sediment samples with the setting "Erze plus" (Tab. 7.3.2). All samples were analyzed three times to check for reproducibility, afterwards an average was calculated afterwards.

Table 7.3.2. Measurement settings for XRF-Analyzer "Delta DS 6000".

Mode	Beam	Elements	Energy [kV]	Counting time [s]	Measurements per sample
Erze	1	Ti, V, Cr, Mn, Fe, Ni, Cu, Zn, Zr, Mo	40	30	3
Erze Plus	1	Ti, V, Cr, Mn, Fe, Ni, Cu, Zn, Zr, Mo	40	30	3
		40	30	3	

7.3.2 Manganese nodules – preliminary results

Manganese nodules collected with the box corer and the chain bag dredge were analyzed in order to investigate the potential influence of fluid circulation on nodule type, distribution and chemistry. In this chapter, only Mn/Fe ratios and the Ni+Cu contents of the analyzed nodules are discussed to illustrate the major differences between the individual nodules and to relate these to the potential influence of seamounts and fluids. Analyses of further trace elements (e.g. rare earth element contents) will be carried out in the home laboratory to obtain a better characterization and discrimination of nodules and the influence of fluid circulation through the oceanic crust on nodule formation.

Working Area 1

In working area 1 (WA1) six box corers and one chain-bag dredge were deployed at different distances from the „Teddy-Bare“ seamount (Fig. 6.5). The Fe-Mn crust (Fig. 7.3.7) sampled directly on seamount with the chain bag-dredge (27GDS) shows a Mn/Fe ratio of 0.36 ± 0.01 , whereas the Ni+Cu content is below the detection limit (Fig. 7.3.9, Tab. 7.3.3). The Fe-Mn crust grew on basaltic substrate and consolidated sediment. They also have exceptionally high Ti contents of 1.2% (Tab. 7.3.3)



Figure 7.3.7. Iron manganese crust from the “Teddy Bare” seamount (WA1).

In addition to the Fe-Mn crust, a few large Mn-nodules were sampled on the seamount. These nodules are large (>8 cm) and discoidal to oval-shaped with a slightly botryoidal rim (HH-type; Fig. 7.3.8C, D). The Mn/Fe ratio of this nodule is 3.27 ± 0.28 and the Ni+Cu content is 2.04 ± 0.05 wt.% (Fig. 7.3.9; Tab. 7.3.3).

The Mn-nodules from the box corer 04KG were sampled near the seamount (Fig. 6.5). These nodules are predominantly small-sized with a spheroidal to discoidal shape and are generally smooth on all sides (Fig. 7.3.8E, F; Appendix A2, A3). The Mn/Fe ratios ranges from 3.85 to 4.32 and the Ni+Cu contents from 2.60 to 2.81 wt.% (Fig. 7.3.9; Tab. 7.3.3).

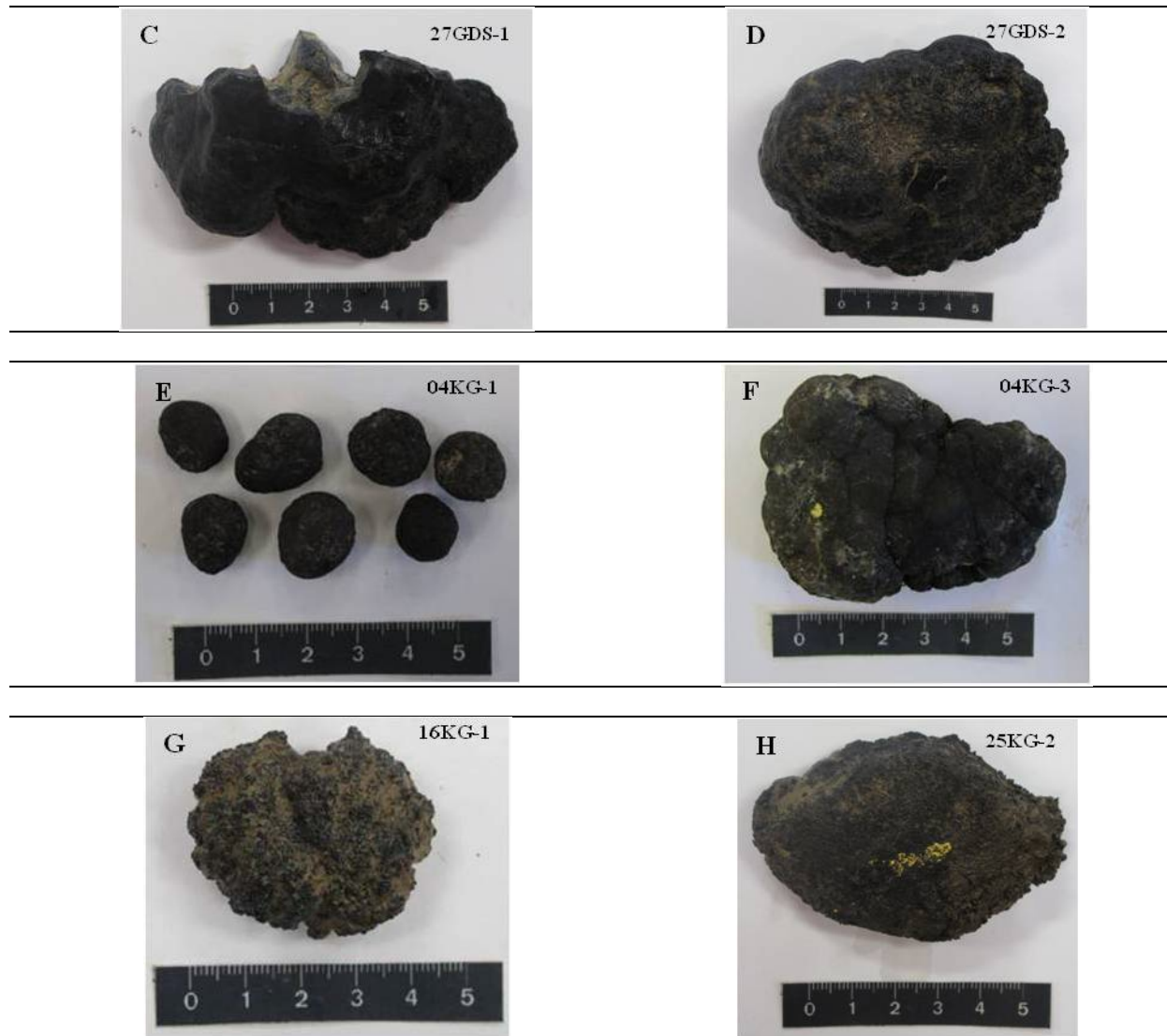


Figure 7.3.8. Manganese nodules recovered by chain bag dredge and the box corer in working area 1 (WAI).

Box corer 16KG and 25KG are located in the abyssal basin (~4300 m) at the greatest distance from the “Teddy-Bare” seamount. Nodules from the box corer 16KG are small, discoidal and rough on all sides (Fig.7.3.8G) with a Mn/Fe ratio of 6.09 ± 0.04 and a Ni+Cu content of 2.42 ± 0.01 wt.% (Fig. 7.3.9; Table 7.3.3; Appendix A2, A3). In contrast, Mn-nodules from the box core station 25KG are medium to large-sized with a discoidal shape. In most cases, the nodule surface is smooth and the bottom side is rough (Fig.7.3.8H; Appendix A2, A3). The average Mn/Fe ratio of these nodules is 5.85 ± 0.31 and the Ni+Cu content is 2.47 ± 0.10 wt.%. Mn-nodules from the box corer stations 10KG and 26KG were also sampled in the abyssal basin in water depth of ~4400 m. Those nodules are predominantly medium to large-sized sized with a spheroidal to discoidal shape and with one smooth and one rough side (see Appendix A2, A3). Nodules from the box corer 10KG show Mn/Fe ratios between 5.51 and 5.99 and Ni+Cu contents of 2.64 ± 0.12 wt.%. Nodules from the box corer 26KG reveal Mn/Fe ratio of 5.20 ± 0.16 and a Ni+Cu content of 2.60 ± 0.05 wt.% (Fig. 7.3.9, Tab. 7.3.3).

These results show that nodules found in the abyssal basin show the highest Mn/Fe ratios as well as the highest metal contents (Ni+Cu) and therefore, the greatest diagenetic influence. In contrast, nodules which were formed near the seamounts are smaller and show lower Mn/Fe ratios as well as

lower metal content (e.g., Ni, Cu) due to higher influence of hydrogenetic growth. Nodules from the box corer 21KG are an exception. Mainly large-sized nodules were found which are discoidal with a botryoidal rim (HH-type) and which have rough surfaces on all sides. The Mn/Fe ratios is high with 6.28 ± 0.02 , but simultaneously the lowest Ni+Cu concentrations of 1.37 ± 0.02 wt.% are observed, which is mainly due to the absence of Cu in these nodules (Fig. 7.3.9, Tab. 7.3.3).

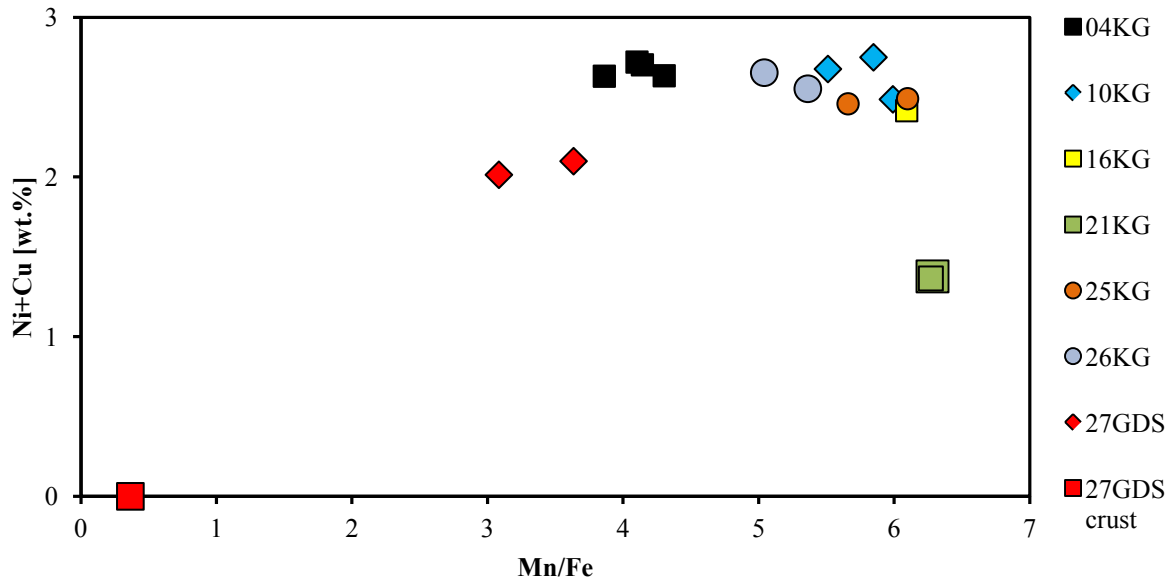


Figure 7.3.9. Mn/Fe ratios vs. Ni+Cu contents of Mn-nodules from different box cores (KG) and chain bag dredge (GDS) of working area 1.

Table 7.3.3. Contents of major and minor metals (in wt.%) of nodules and in a crust deriving from working area 1.

sample (WA 1)		Fe	Mn	Ti	Ni	V	Cu	Zn	Zr	Pb	Mn/Fe	Ni+Cu
SO240-04KG-1	MEAN	7.91	30.5	0.33	1.52	0.48	1.11	0.04	0.05	0.06	3.86	2.63
	STD. DEV.	0.04	0.19	0.01	0.01	0.00	0.02	0.00	0.00	0.00	0.01	0.02
SO240-04KG-2	MEAN	7.65	31.7	0.34	1.64	0.49	1.07	0.04	0.05	0.06	4.14	2.70
	STD. DEV.	0.02	0.14	0.01	0.02	0.01	0.02	0.00	0.00	0.00	0.01	0.03
SO240-04KG-3	MEAN	7.80	32.0	0.34	1.59	0.49	1.13	0.04	0.05	0.06	4.10	2.72
	STD. DEV.	0.08	0.24	0.01	0.04	0.00	0.03	0.00	0.00	0.00	0.02	0.06
SO240-04KG-4	MEAN	7.41	31.9	0.34	1.53	0.49	1.11	0.16	0.04	0.06	4.30	2.63
	STD. DEV.	0.02	0.13	0.01	0.02	0.00	0.01	0.01	0.00	0.00	0.01	0.02
SO240-10KG-1	MEAN	5.44	31.8	0.28	1.49	0.50	1.26	0.17	0.01	0.04	5.85	2.75
	STD. DEV.	0.03	0.14	0.01	0.02	0.01	0.02	0.00	0.00	0.00	0.03	0.03
SO240-10KG-2	MEAN	5.76	31.7	0.33	1.49	0.52	1.19	0.14	0.02	0.04	5.51	2.68
	STD. DEV.	0.04	0.23	0.01	0.02	0.01	0.03	0.04	0.00	0.00	0.02	0.05
SO240-10KG-3	MEAN	5.36	32.1	0.35	1.26	0.52	1.23	0.04	0.02	0.04	5.99	2.49
	STD. DEV.	0.02	0.20	0.01	0.02	0.01	0.02	0.00	0.00	0.00	0.03	0.03
SO240-16KG-1	MEAN	5.15	31.4	0.33	1.16	0.53	1.26	0.18	0.01	0.04	6.09	2.42
	STD. DEV.	0.02	0.13	0.01	0.01	0.01	0.01	0.00	0.00	0.00	0.04	0.01
SO240-21KG-2	MEAN	5.14	32.2	0.32	1.35	0.19	0.01	b.d.l.* ¹	b.d.l.* ¹	b.d.l.* ¹	6.27	1.36
	STD. DEV.	0.05	0.14	0.01	0.02	0.00	0.00	b.d.l.* ¹	b.d.l.* ¹	b.d.l.* ¹	0.03	0.02
SO240-21KG-3	MEAN	4.97	31.3	0.29	1.36	0.20	0.01	b.d.l.* ¹	b.d.l.* ¹	b.d.l.* ¹	6.28	1.38
	STD. DEV.	0.03	0.16	0.01	0.03	0.00	0.00	b.d.l.* ¹	b.d.l.* ¹	b.d.l.* ¹	0.01	0.03
SO240-25KG-1	MEAN	5.62	31.7	0.32	1.38	0.51	1.08	0.10	0.02	0.04	5.66	2.46
	STD. DEV.	0.36	0.59	0.01	0.07	0.01	0.04	0.06	0.00	0.00	0.29	0.11
SO240-25KG-2	MEAN	5.35	32.6	0.33	1.37	0.52	1.13	0.17	0.02	0.04	6.10	2.49
	STD. DEV.	0.06	0.08	0.00	0.01	0.00	0.01	0.00	0.00	0.00	0.06	0.00
SO240-26KG-1	MEAN	6.17	31.1	0.33	1.52	0.50	1.14	0.17	0.02	0.04	5.04	2.65
	STD. DEV.	0.03	0.16	0.02	0.01	0.01	0.01	0.00	0.00	0.00	0.02	0.01
SO240-26KG-2	MEAN	5.94	31.8	0.33	1.42	0.51	1.13	0.12	0.02	0.04	5.36	2.55
	STD. DEV.	0.08	0.11	0.01	0.01	0.00	0.00	0.07	0.00	0.00	0.06	0.01
SO240-27GDS-1	MEAN	8.70	31.6	0.44	1.19	0.51	0.91	0.04	0.05	0.06	3.63	2.10
	STD. DEV.	0.02	0.08	0.01	0.01	0.00	0.00	0.00	0.00	0.00	0.01	0.01
SO240-27GDS-2	MEAN	9.83	30.3	0.46	1.14	0.51	0.87	0.03	0.06	0.07	3.08	2.01
	STD. DEV.	0.06	0.17	0.01	0.01	0.01	0.02	0.00	0.00	0.00	0.02	0.03
SO240-27GDS crust	MEAN	8.64	3.14	1.21	b.d.l.* ¹	0.43	b.d.l.* ¹	0.01	0.04	0.03	0.36	b.d.l.* ¹
	STD. DEV.	0.09	0.03	0.01	b.d.l.* ¹	0.01	b.d.l.* ¹	0.00	0.00	0.00	0.01	b.d.l.* ¹

*¹ below detection limit

Working Area 2

In working area 2 (WA2), six box corers were taken (Fig.6.11). The box corers 33KG and 38KG are located in the vicinity of a seamount (Fig.6.11). The nodules obtained are predominantly small and discoidal to spheroidal and slightly rough on all sides (Fig. 7.3.10A-C; Appendix A2, A3). The Mn/Fe ratios are relatively low ranging from 2.5 to 4.74 and the Ni+Cu concentrations range from 1.88 to 2.73 wt.% (Fig. 7.3.11; Tab. 7.3.4). There is one exception in the box corer 33KG. The sample contains very small intergrown spheroidal concretions (micronodules) similar to polytype nodules (Fig. 7.3.10C). These concretions have high Mn/Fe ratio (5.78 ± 0.01) with Ni+Cu concentration of 2.40 ± 0.40 wt.% (Fig. 7.3.11; Tab. 7.3.4).

With increasing distance from the seamount, the Mn/Fe ratios as well as Ni+Cu contents increase. Nodules from the box corer 46KG are either small and spheroidal with rough surfaces or medium-sized and discoidal with smooth surface and rough bottom sides (Fig. 7.3.10D; Appendix A2, A3). The Mn/Fe ratios range from 3.99 to 6.09, increase with the nodule size. The Ni+Cu contents range from 2.55 to 2.74 wt.% (Fig. 7.3.11; Table 7.3.4).

Box corer 44KG contained nodules that are small and medium-sized and discoidal with a botryoidal rim (HH-type). The surfaces are smooth and the bottom sides are rough (Fig. 7.3.10E; Appendix A2, A3). The Mn/Fe ratio is ~ 5.09 and Ni+Cu content of 2.51 wt.% (Fig. 7.3.11; Tab. 7.3.4).

Nodules of box corer 47KG are small, medium and large-sized with a discoidal shape, botryoidal rim (HH-type) and a smooth surface and a rough bottom side (Appendix A2, A3). These nodules have Mn/Fe ratios ranging from 4.87 to 5.64 and Ni+Cu contents between 2.59 and 2.78 wt.% (Fig. 7.3.11; Tab. 7.3.4).

The box corer 48KG predominantly contained small to medium-sized, discoidal nodules with a botryoidal rim (HH-type) and a smooth surface and rough bottom side (Fig. 7.3.10F; Appendix A2, A3). These nodules show Mn/Fe ratios ranging from 4.13 to 5.84 and Ni+Cu content vary from 2.46 to 2.58 wt.% (Fig. 7.3.11; Tab. 7.3.4).

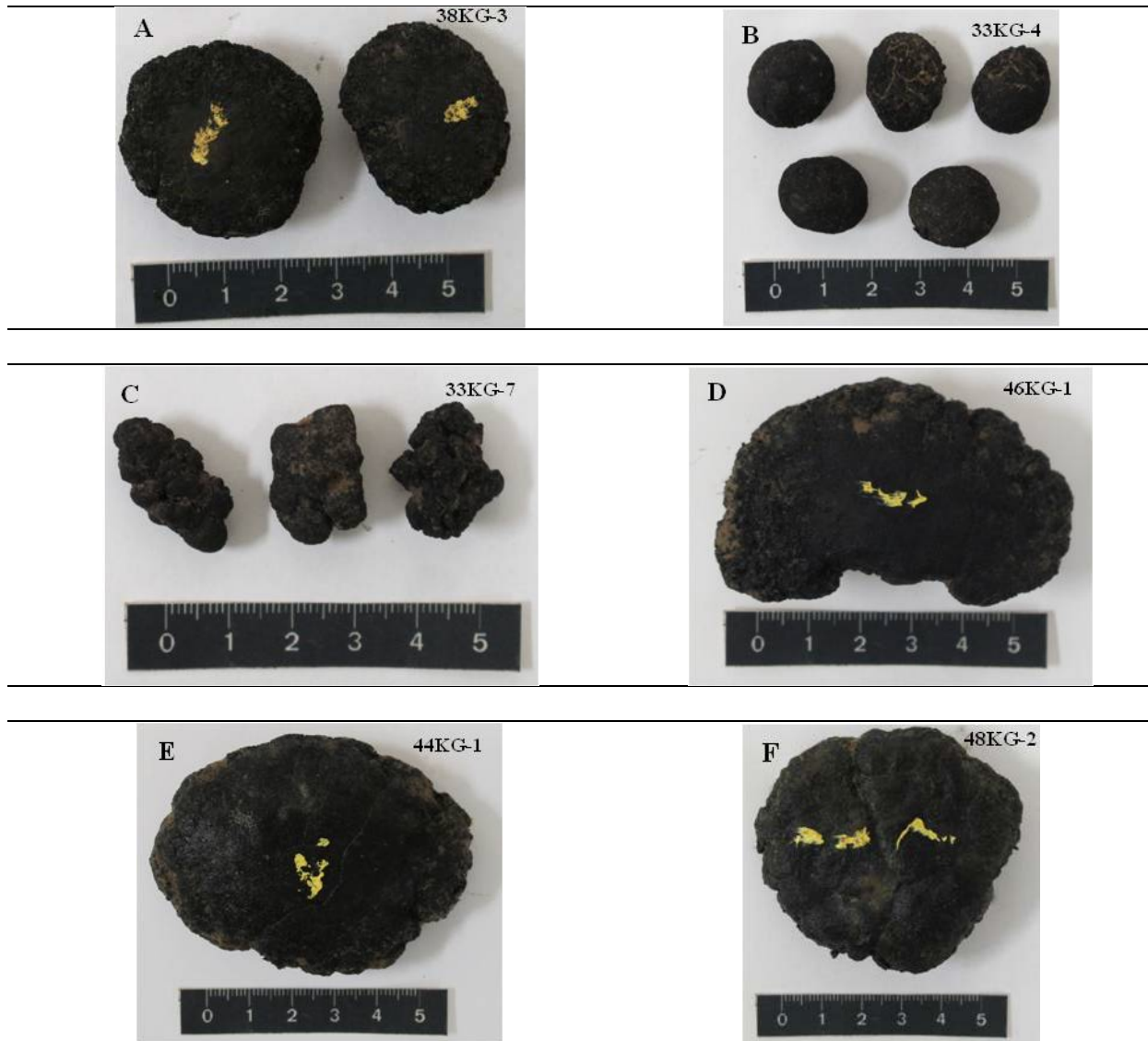


Figure 7.3.10. Manganese nodules recovered by box corer in working area 2 (WA2.)

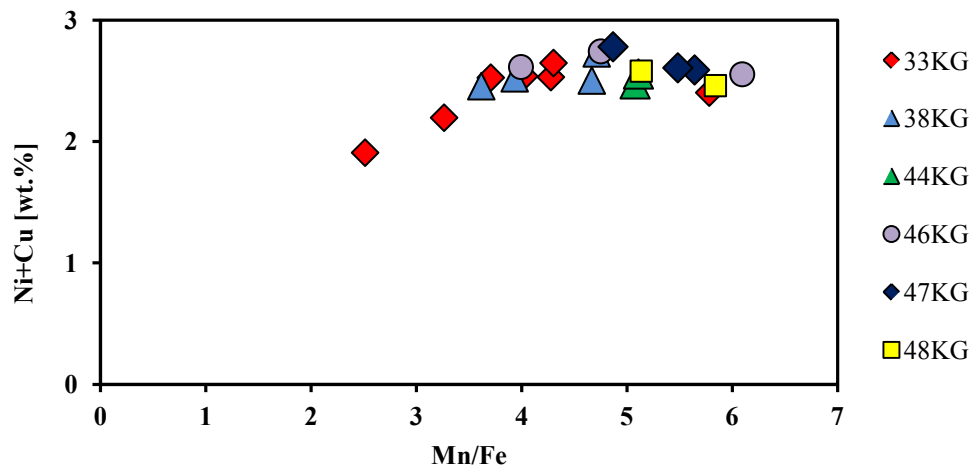


Figure 7.3.11. Mn/Fe ratios vs. Ni+Cu contents of Mn-nodules deriving from different box cores (KG) of working area 2.

Table 7.3.4 Contents of major and minor metals (in wt.%) in nodules deriving from working area 2.

Sample (WA 2)		Fe	Mn	Ti	Ni	V	Cu	Zn	Zr	Pb	Mn/Fe	Ni+Cu
SO240-33KG-1	MEAN	10.9	27.5	0.42	1.18	0.50	0.72	0.04	0.07	0.06	2.51	1.91
	STD. DEV.	0.08	0.12	0.01	0.02	0.00	0.01	0.00	0.00	0.00	0.01	0.02
SO240-33KG-2	MEAN	7.00	30.0	0.35	1.45	0.50	1.08	0.05	0.04	0.06	4.28	2.53
	STD. DEV.	0.02	0.17	0.01	0.00	0.00	0.03	0.00	0.00	0.00	0.01	0.03
SO240-33KG-3	MEAN	7.28	31.3	0.33	1.53	0.48	1.12	0.04	0.04	0.06	4.30	2.65
	STD. DEV.	0.04	0.20	0.00	0.02	0.01	0.01	0.00	0.00	0.00	0.02	0.03
SO240-33KG-4	MEAN	7.50	30.2	0.31	1.47	0.48	1.06	0.04	0.04	0.06	4.02	2.54
	STD. DEV.	0.07	0.20	0.02	0.01	0.01	0.01	0.00	0.00	0.00	2.78	0.02
SO240-33KG-5	MEAN	8.07	29.9	0.32	1.40	0.48	1.12	0.03	0.04	0.06	3.71	2.52
	STD. DEV.	0.10	0.26	0.01	0.04	0.01	0.02	0.01	0.02	0.01	0.01	0.06
SO240-33KG-6	MEAN	8.49	27.7	0.37	1.20	0.49	0.99	0.03	0.05	0.07	3.26	2.19
	STD. DEV.	0.06	0.30	0.01	0.03	0.00	0.02	0.00	0.00	0.00	0.01	0.04
SO240-33KG-7	MEAN	5.73	33.1	0.28	1.38	0.48	1.02	0.04	0.02	0.04	5.78	2.40
	STD. DEV.	0.03	0.19	0.01	0.03	0.00	0.01	0.00	0.00	0.00	0.01	0.04
SO240-38KG-1	MEAN	6.21	29.0	0.32	1.41	0.51	1.09	0.08	0.03	0.04	4.67	2.50
	STD. DEV.	0.08	0.20	0.01	0.04	0.00	0.02	0.06	0.01	0.00	0.02	0.05
SO240-38KG-2	MEAN	8.30	30.0	0.41	1.45	0.50	1.00	0.04	0.05	0.06	3.62	2.45
	STD. DEV.	0.04	0.21	0.01	0.01	0.01	0.02	0.00	0.00	0.00	0.02	0.03
SO240-38KG-3	MEAN	6.64	31.3	0.30	1.54	0.49	1.18	0.16	0.02	0.04	4.71	2.72
	STD. DEV.	0.04	0.08	0.01	0.01	0.01	0.00	0.00	0.00	0.00	0.03	0.01
SO240-38KG-4	MEAN	7.55	29.7	0.33	1.45	0.48	1.07	0.04	0.04	0.06	3.93	2.52
	STD. DEV.	0.01	0.12	0.00	0.02	0.00	0.02	0.00	0.00	0.00	0.01	0.03
SO240-44KG-1	MEAN	6.22	31.6	0.33	1.43	0.49	1.05	0.16	0.02	0.04	5.08	2.47
	STD. DEV.	0.07	0.28	0.01	0.03	0.00	0.02	0.00	0.00	0.00	0.05	0.04
SO240-44KG-2	MEAN	6.30	32.2	0.31	1.47	0.50	1.08	0.16	0.02	0.04	5.11	2.55
	STD. DEV.	0.03	0.21	0.02	0.04	0.01	0.02	0.00	0.00	0.00	0.02	0.06
SO240-46KG-1	MEAN	5.48	33.4	0.30	1.42	0.49	1.13	0.19	0.02	0.04	6.09	2.55
	STD. DEV.	0.03	0.05	0.01	0.03	0.01	0.01	0.00	0.00	0.00	0.03	0.03
SO240-46KG-2	MEAN	6.64	31.5	0.33	1.62	0.51	1.13	0.04	0.03	0.05	4.75	2.74
	STD. DEV.	0.06	0.23	0.01	0.04	0.00	0.02	0.00	0.01	0.01	0.03	0.05
SO240-46KG-3	MEAN	7.44	29.7	0.31	1.53	0.48	1.08	0.04	0.05	0.06	3.99	2.61
	STD. DEV.	0.07	0.18	0.01	0.03	0.00	0.01	0.00	0.00	0.00	0.01	0.04
SO240-47KG-1	MEAN	5.65	31.9	0.32	1.46	0.51	1.12	0.17	0.02	0.04	5.64	2.59
	STD. DEV.	0.10	0.39	0.00	0.04	0.01	0.03	0.00	0.00	0.00	0.03	0.07
SO240-47KG-2	MEAN	5.87	32.2	0.35	1.45	0.51	1.16	0.16	0.02	0.04	5.48	2.61
	STD. DEV.	0.00	0.20	0.01	0.00	0.01	0.01	0.01	0.00	0.00	0.03	0.02
SO240-47KG-3	MEAN	6.39	31.1	0.29	1.55	0.49	1.23	0.08	0.02	0.04	4.87	2.78
	STD. DEV.	0.06	0.27	0.01	0.03	0.00	0.04	0.06	0.00	0.00	0.03	0.07
SO240-48KG-2	MEAN	6.19	31.8	0.34	1.44	0.52	1.14	0.04	0.02	0.04	5.13	2.58
	STD. DEV.	0.01	0.05	0.02	0.01	0.01	0.01	0.00	0.00	0.00	0.00	0.00
SO240-48KG-1	MEAN	5.58	32.6	0.30	1.38	0.49	1.08	0.16	0.02	0.04	5.84	2.46
	STD. DEV.	0.02	0.21	0.01	0.02	0.01	0.01	0.01	0.00	0.00	0.03	0.03

Working Area 3

In working area 3 (WA3), four box corers were obtained (57KG, 62KG, 66KG, 73KG; see Fig. 6.18; Appendix A2, A3). Box cores 57KG and 62KG were barren of nodules. Box core 66KG contained a few small and medium-sized whole and broken, rough discoidal hamburger-type nodules. The chemistry of these nodules was not determined. Similarly, box core 73KG only contained a few small spheroidal nodules with rough surfaces (Fig. 7.3.12). The nodule sample from this box core has a Mn/Fe ratio of 5.50 ± 0.04 and a Ni+Cu content of 2.63 ± 0.043 wt% (Tab. 7.3.4).



Figure 7.3.12. Manganese nodules recovered by box corer in WA3.

Working Area 4

Two box corers were taken in working area 4 (91KG and 107KG; Fig. 6.24; Appendix A2, A3); whereby only box corer 91KG had nodules on the surface. Box corer 107KG had no nodules at the surface but contained two distinct layers of nodules at 16 cm and 36 cm sediment depth.

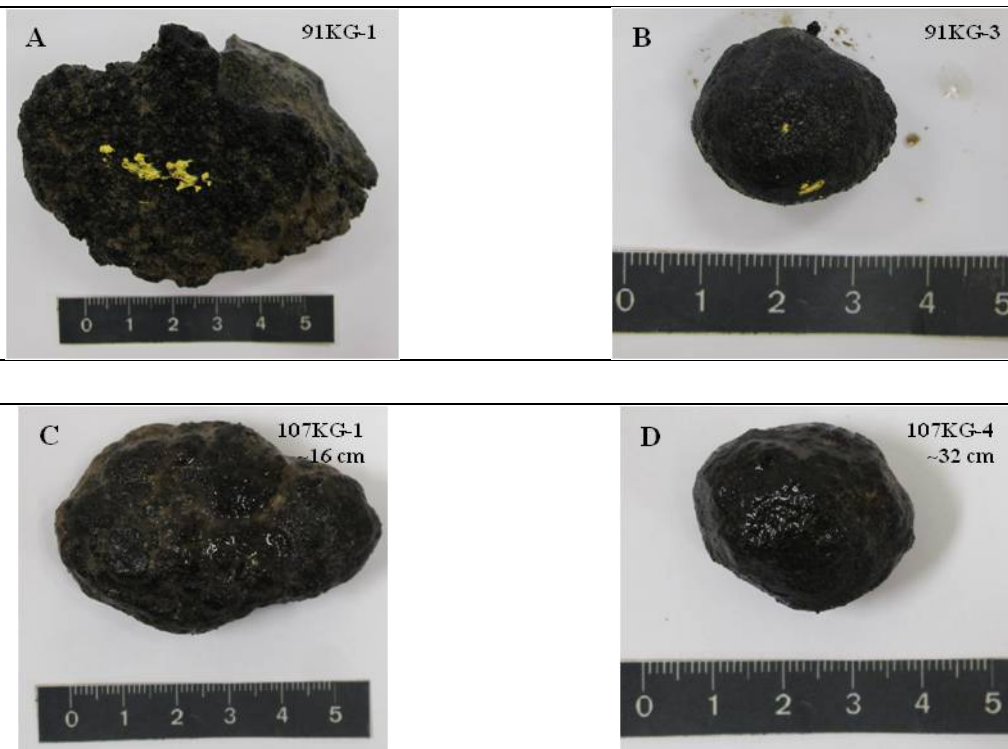


Figure 7.3.13. Manganese nodules recovered by box corer in WA4.

Nodules of the box corer 91KG are small to medium sized, have a discoidal shape and a smooth and a rough side (Fig. 7.3.13A, B). These nodules have a Mn/Fe ratio of 5.51 ± 0.62 and Ni+Cu contents of 2.65 ± 0.04 wt.%. Furthermore, small spheroidal nodules, which are rough on all sides, were found within this box core. The Mn/Fe ratio is 4.10 ± 0.01 and Ni+Cu content of 2.62 ± 0.10 (Fig. 7.3.14; Tab. 7.3.5).

The nodules found at depth in box core 107KG are generally small-sized with a spheroidal shape as polytype nodules with slightly rough surfaces. Medium-sized, discoidal nodules occur subordinated within this box corer (7.3.13C, D). Most of the nodules from 16 cm sediment depth show a yellowish to brown coating, which is probably Fe-rich. The Mn/Fe ratio of these nodules is ~ 2.63 and the Ni+Cu content is ~ 2.19 wt.% (Fig. 7.3.14; Tab. 7.3.5). Additionally, a crust like concretion was found in 16 cm sediment depth. The crust sample show a Mn/Fe ratio of 0.41 and a Ni+Cu content of 0.65 wt.% (Tab. 7.3.5). Nodules from ~ 36 cm sediment depth are predominantly small, spheroidal and intergrown as polytype nodules. The Mn/Fe ratio is 2.39 ± 0.18 and the Ni+Cu content is 2.27 ± 0.17 wt.% (Fig. 7.3.14; Tab. 7.3.5). The lower Cu+Ni contents of nodules from station 107KG are due to decreased Ni concentrations compared to most of the other nodules sampled during this cruise. This reduced Ni content is in contrast to nodules from station 21KG (WA1) which have constant Ni amounts but very low Cu contents. It is not clear yet what causes these different metal contents.

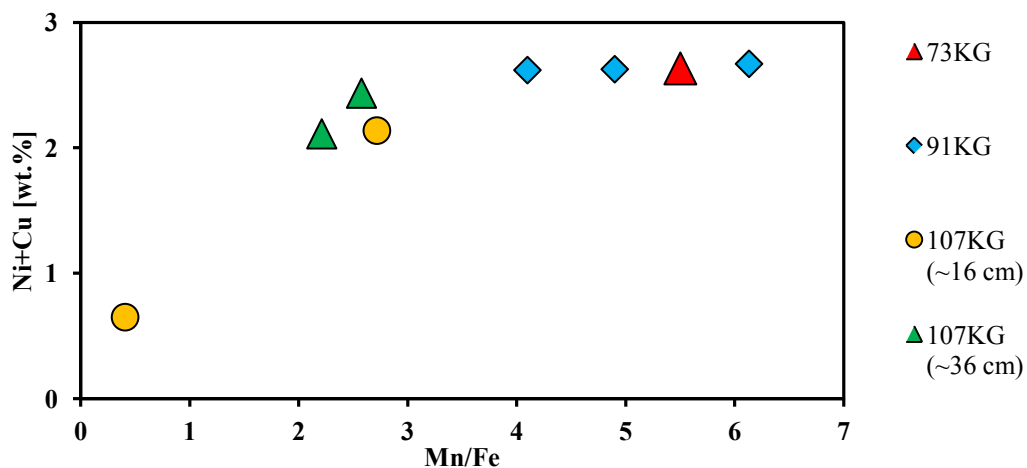


Figure 7.3.14. Mn/Fe ratios vs. Ni+Cu contents of Mn-nodules deriving from different box cores (KG) of working area 3 and 4.

Table 7.3.5. Contents of major and minor metals (in wt.%) of nodules from the working area (WA) 3 and 4.

sample (WA 3)		Fe	Mn	Ti	Ni	V	Cu	Zn	Zr	Pb	Mn/Fe	Ni+Cu
SO240-73KG-1	MEAN	5.51	30.3	0.29	1.26	0.51	1.38	0.17	0.02	0.04	5.50	2.63
	STD. DEV.	0.02	0.28	0.01	0.02	0.00	0.03	0.00	0.00	0.00	0.04	0.04
Sample (WA 4)												
SO240-91KG-1	MEAN	5.62	34.4	0.30	1.51	0.49	1.16	0.19	0.02	0.04	6.13	2.67
	STD. DEV.	0.03	0.14	0.01	0.03	0.00	0.02	0.00	0.00	0.00	0.02	0.05
SO240-91KG-2	MEAN	6.59	32.3	0.31	1.50	0.50	1.13	0.17	0.02	0.04	4.90	2.63
	STD. DEV.	0.04	0.18	0.01	0.02	0.01	0.02	0.00	0.00	0.00	0.03	0.02
SO240-91KG-3	MEAN	7.47	30.6	0.30	1.46	0.48	1.16	0.04	0.04	0.05	4.10	2.62
	STD. DEV.	0.08	0.45	0.00	0.05	0.01	0.05	0.00	0.00	0.01	0.01	0.10
SO240-107KG-1 ~16 cm	MEAN	9.50	24.1	0.31	0.81	0.52	1.43	0.02	0.04	0.04	2.54	2.24
	STD. DEV.	0.06	0.15	0.01	0.02	0.00	0.02	0.00	0.00	0.00	0.01	0.03
SO240-107KG-2 ~16 cm	MEAN	9.05	24.6	0.27	0.74	0.51	1.40	0.02	0.02	0.04	2.72	2.14
	STD. DEV.	0.03	0.07	0.02	0.01	0.00	0.00	0.00	0.00	0.00	0.00	0.02
SO240-107KG-3 ~16 cm crust	MEAN	16.5	6.70	0.34	0.24	0.47	0.41	0.02	0.06	0.07	0.41	0.65
	STD. DEV.	0.13	0.01	0.00	0.01	0.00	0.01	0.00	0.00	0.00	0.00	0.01
SO240-107KG-4 ~36 cm	MEAN	10.2	22.6	0.25	0.75	0.49	1.37	0.02	0.02	0.04	2.21	2.11
	STD. DEV.	0.10	0.21	0.01	0.02	0.00	0.04	0.00	0.00	0.00	0.00	0.05
SO240-107KG-5 ~36 cm	MEAN	9.28	23.9	0.25	0.85	0.49	1.59	0.02	0.02	0.04	2.57	2.44
	STD. DEV.	0.06	0.17	0.01	0.02	0.00	0.04	0.00	0.00	0.00	0.00	0.05

In general, medium (4 – 8 cm) to large-sized nodules (>8 cm) with Mn/Fe ratios ranging from 3 to 10 and with Ni+Cu contents around 2.5 wt.% are typically formed mainly under oxic diagenetic conditions (Halbach et al., 1988). Smaller nodules (< 4 cm) show low Mn/Fe ratios (< 3) as well as low Ni+Cu contents (< 1.5 wt.%). These nodules contain a greater portion of hydrogenetic material (Halbach et al., 1988). Tables 7.3.2 – 7.3.5 show the average metal contents (in wt.%) of the analyzed nodules from the WA1 – WA4. The concentrations of Zn, V, Zr and Pb are quite similar in all nodules (Tab. 7.3.2 – 7.3.5). Interestingly, Ti concentrations are slightly different between nodules. Smaller nodules as well as the Fe-Mn crust (WA 1) show higher Ti concentrations (~0.4 wt.%) than medium and large nodules, which is due to greater hydrogenetic influence on the formation of smaller nodules and crusts.

7.3.3 Sediments – Preliminary results

Long sediment cores were mainly recovered to determine the pore-water and solid-phase geochemistry in order to investigate the possible influence of hydrothermal fluids diffusing from the basaltic crust to the overlying pelagic sediments. After opening, all cores were visually described and sediment samples from selected depths were taken and analyzed for their metal contents.

Working area 1

Figure 7.3.15 summarizes the preliminary results determined on board for working area 1. The sediment cores can be divided into two groups. Cores 05SL, 51SL, 53SL and 117SL were recovered from the western flank of the Teddy Bare seamount where the thickness of the sediment cover overlying the basaltic crust is about 10 m. All four sediment cores are characterized by stiff and compact dark brown clays. The color is caused by weathering products from the basaltic crust of the

seamount. Due to the high cohesiveness of the sediments (shear strength: 10–40 kPa), the gravity corer could only penetrate 5 to 8 m into the seafloor deposits, irrespective of the total length of the corer pipe (5–15 m) used for recovery. The two cores located closest to the seamount (53SL and 117SL) contain the remains of debris flows in their lower parts. The other three sediment cores (09KL, 15KL and 22KL) were recovered from areas located 4 to 6 km away from seamounts. At these distant locations the total sediment thickness is about 20 m. Cores 09KL, 15KL and 22KL are 12–13 m long and are characterized by light brown sediments of low cohesiveness (shear strength: 1–8 kPa). These sediments regularly contain buried nodules at various depths. In the lower part of the cores the color changes from lighter to darker brown and accordingly the Mn contents increase from 0.1 to 0.7 or 1.3 wt.%. The elevated Mn contents suggest an influence of low-temperature hydrothermal fluids circulating through the basaltic crust of the seafloor and diffusing upward through the overlying sediments.

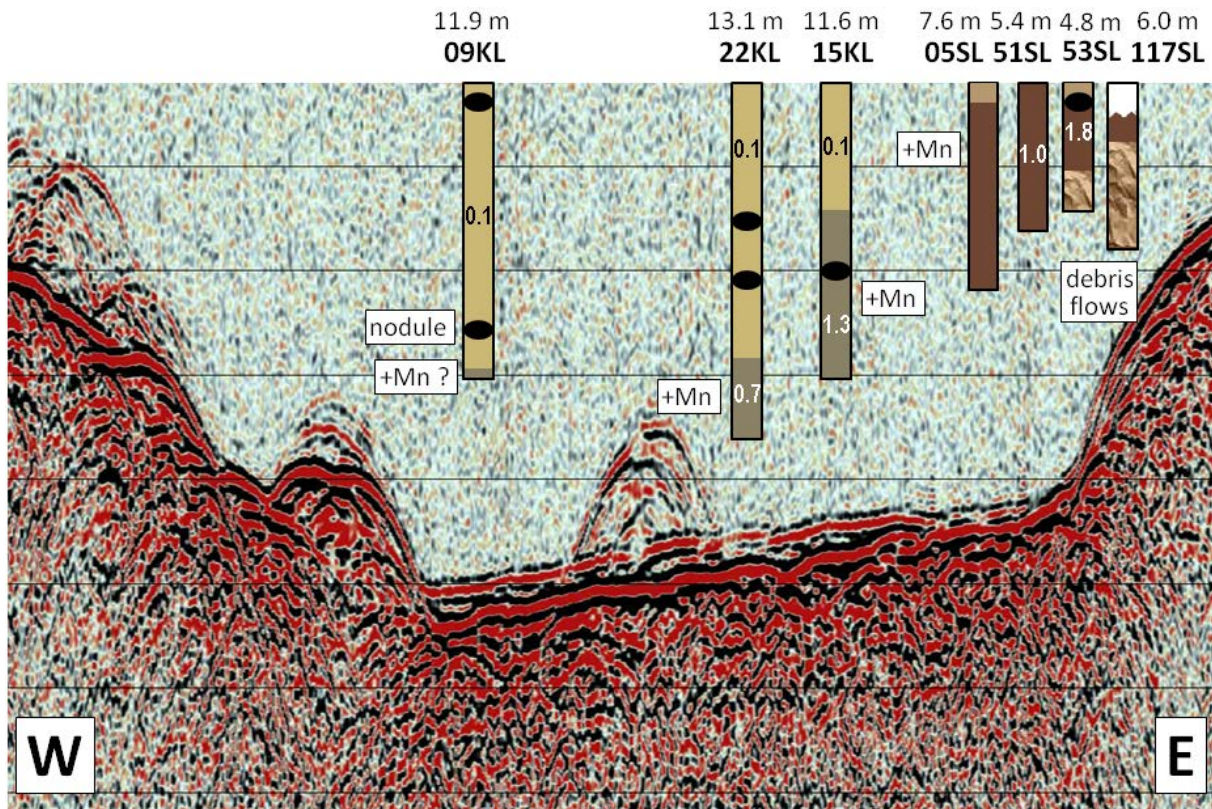


Fig. 7.3.15. West-East transect along seismic profile 11SCS1501_2 in working area 1 (cf. Figs. 6.2 and 6.4 and Chapter 7.1) with schematic representations of sediment core characteristics. The numbers shown above core labels signify the total length of each sediment core. The colors represent the average color of the sediment sections and the numbers inside the cores reflect the manganese contents of the sediments. Black ovals represent buried nodules.

Working area 2

The sediment cores in working area 2 exhibit a similar pattern as those in working area 1. The cores 31KL and 35KL located close to the seamount in the north (Fig. 7.3.16) are characterized by stiff dark brown sediments and contain debris flows in their lower parts, whereas core 42SL, located in a potential hydrothermal pit, consists of light brown soft sediments in the top two thirds and dark brown stiff sediment in the bottom third of the core. The Mn contents of the sediments are generally enriched in the dark brown sections of the three cores. Cores 31KL and 42KL are located above faults that run

through the basement and the sediment coverage. Core 35KL is located within an erosion channel that exhibits lower sediment thickness.

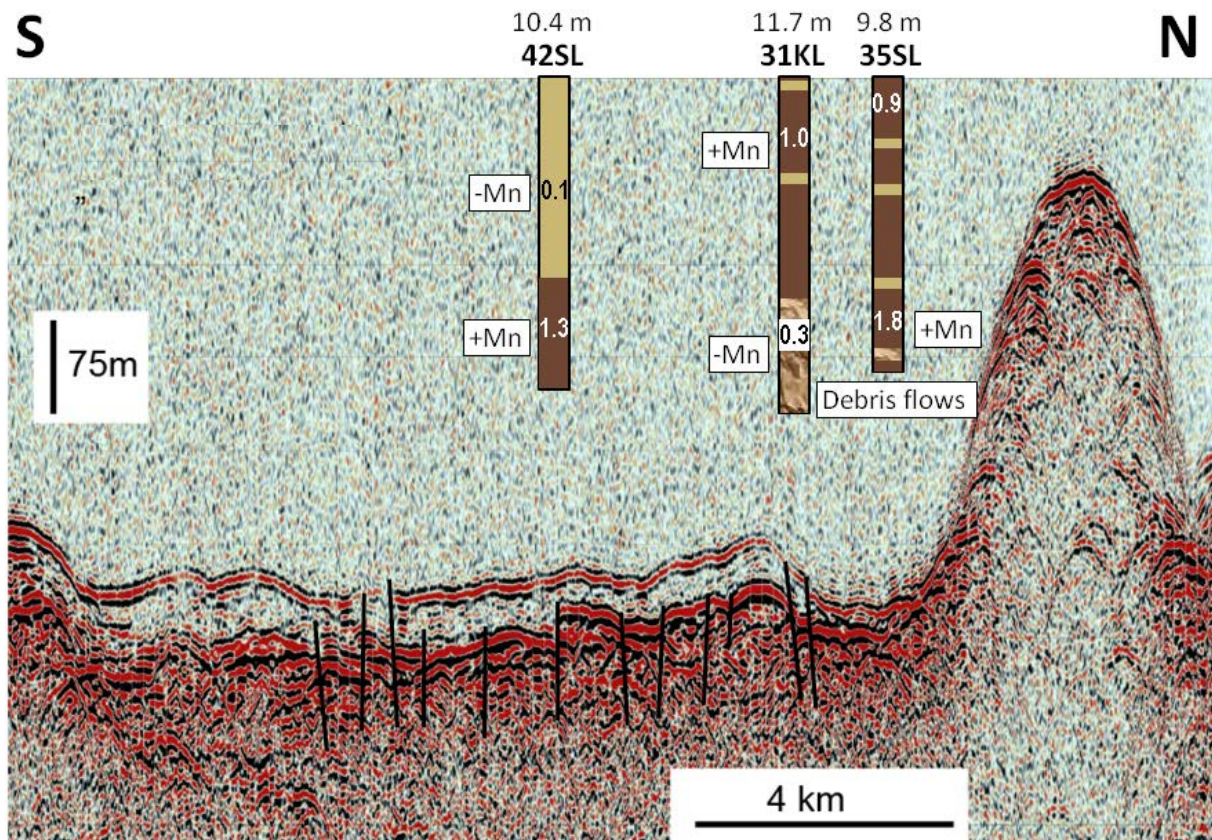


Fig. 7.3.16. North-South transect along seismic profile 29SCS1503_6 in working area 2 (cf. Figs. 6.8 and 6.10 and Chapter 7.1) with schematic representations of sediment core characteristics. The numbers shown above the core labels signify the total length of each sediment core. The colors represent the average color of the sediment sections and the numbers inside the cores reflect the manganese contents of the sediments.

Working area 3

Cores 58SL, 65SL and 72SL were obtained from tectonic depressions with a relatively high sediment cover of ~ 70 m (Fig. 7.3.17). All three cores mainly consist of soft light brown clay in the upper parts and greyish brown to dark brown sediments in the bottom sections, where the Mn contents are significantly enriched. Core 69SL was recovered from a location above a basement fault with elevated heat flow values of 136 mW/m² (Fig. 7.3.18). This core mainly consists of dark brown stiff sediment. The Mn content of 4.7 wt.% at the base of the sediment core is by far the highest value measured during cruise SO-240.

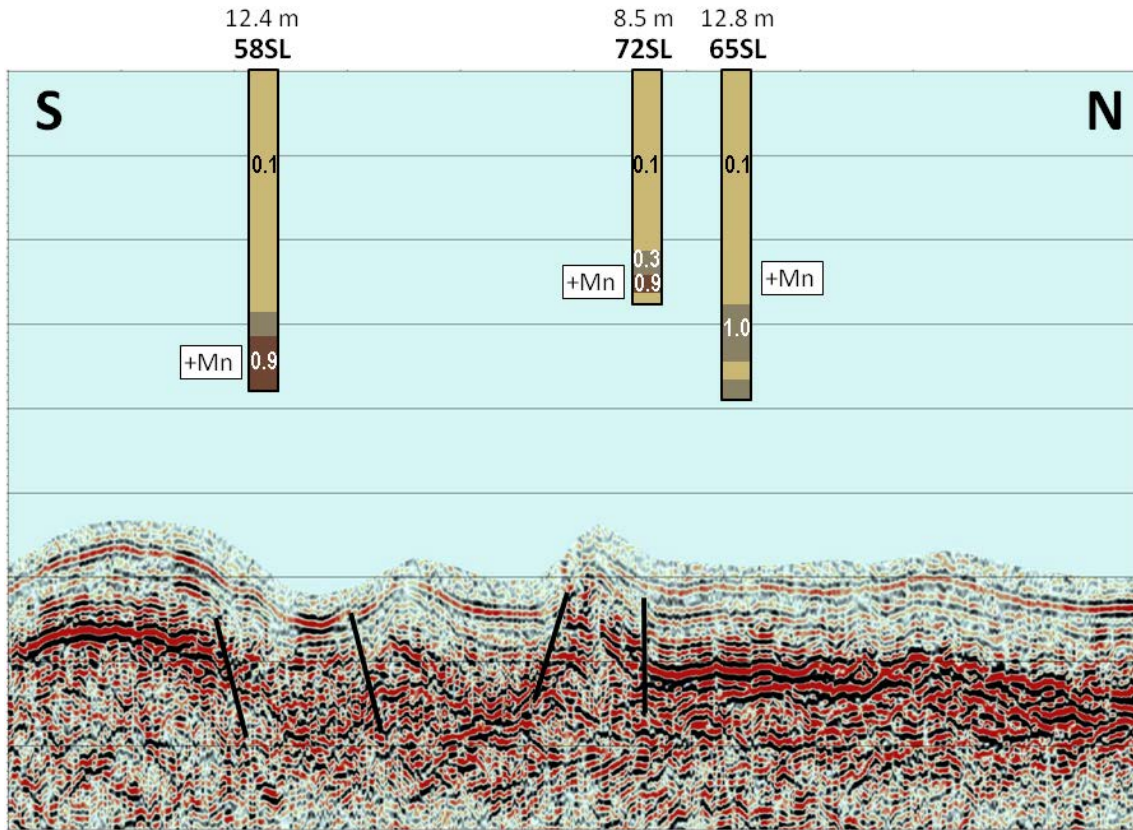


Fig. 7.3.17. North-South transect along seismic profile 54SCS1504_3 in working area 3 (cf. Figs. 6.14 and 6.16 and Chapter 7.1) with schematic representations of sediment core characteristics. The numbers shown above the core labels signify the total length of each sediment core. The colors represent the average color of the sediment sections and the numbers inside the cores reflect the manganese contents of the sediments.

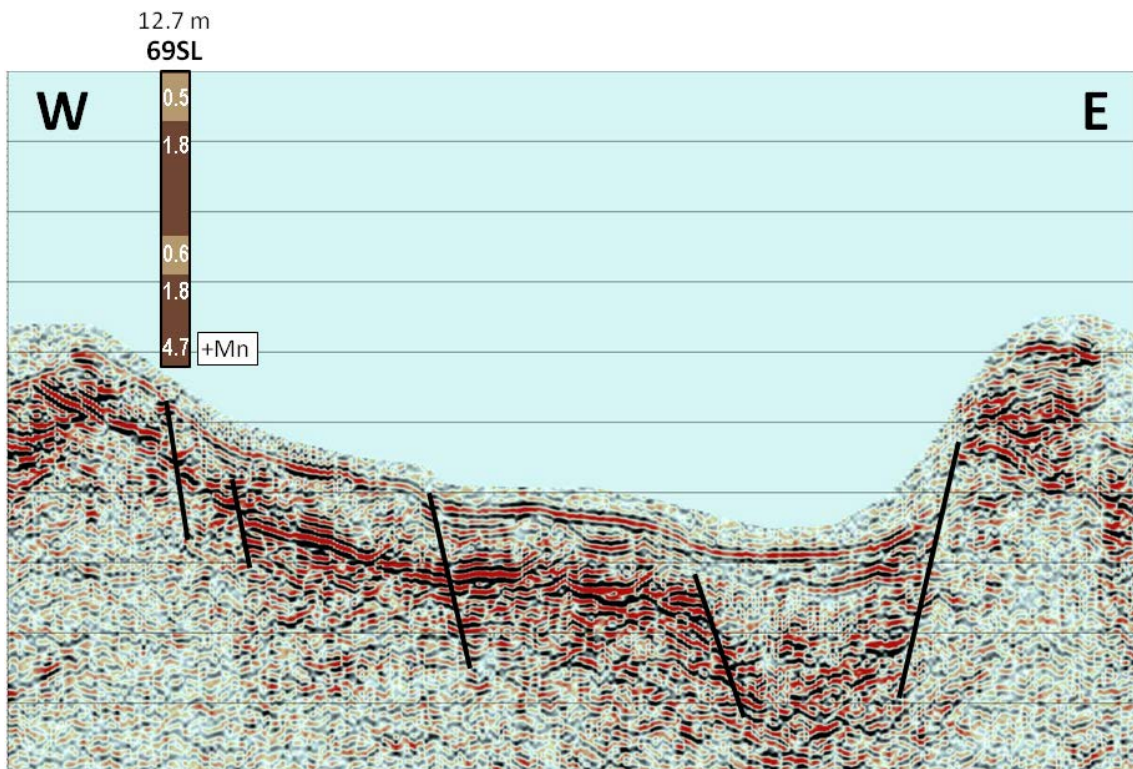


Fig. 7.3.18. West-East transect along seismic profile 54SCS1504_2 in working area 3 (cf. Figs. 6.14 and 6.16 and Chapter 7.1) with schematic representations of sediment core characteristics. The numbers shown above the core labels signify the total length of each sediment core. The colors represent the average color of the sediment sections and the numbers inside the cores reflect the manganese contents of the sediments.

Working area 4

Core 81SL was recovered above a fault within a small basin with a low sediment cover of only 20 m and heat flow values of 92 mW/m^2 (Fig. 7.3.19), indicating the potential influence of hydrothermal fluids. The EM120 multibeam backscatter values of this area are very low, implying a coverage of soft sediments without nodules. The upper three quarters of core 81SL consist of light brown and greyish brown clay with Mn contents of 0.6 to 1.6 wt.%, whereas the bottom quarter consists of dark brown clay and Mn contents of about 2.4 wt.%. Core 108SL was taken from an area with average backscatter values, with the aim of using it as a reference against which 81SL can be evaluated. The core mainly consists of light brown sediment. Core 96SL was recovered close to a seamount above a distinct fault running through the basement and the entire sediment layer (Fig. 7.3.20). Heat flow is slightly elevated with values of 80 mW/m^2 . Sediment core 103SL was also taken above a fault with lower heat flow values of $\sim 68 \text{ mW/m}^2$ (Fig. 7.3.21). This core mainly consists of light brown sediment and was sampled for permeability analyses from every single meter.

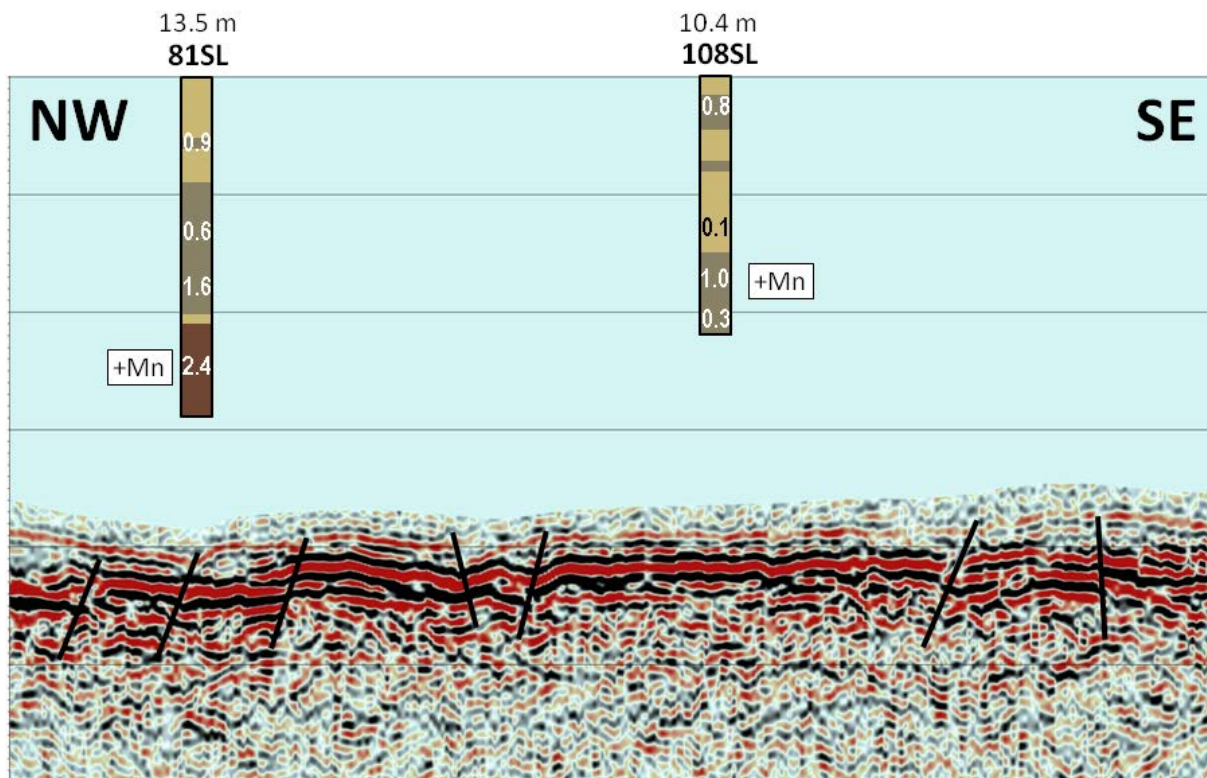


Fig. 7.3.19. West-East transect along seismic profile 82SCS1505_1 in working area 4 (cf. Figs. 6.21 and 6.22 and Chapter 7.1) with schematic representations of sediment core characteristics. The numbers shown above the core labels signify the total length of each sediment core. The colors represent the average color of the sediment sections and the numbers inside the cores reflect the manganese contents of the sediments.

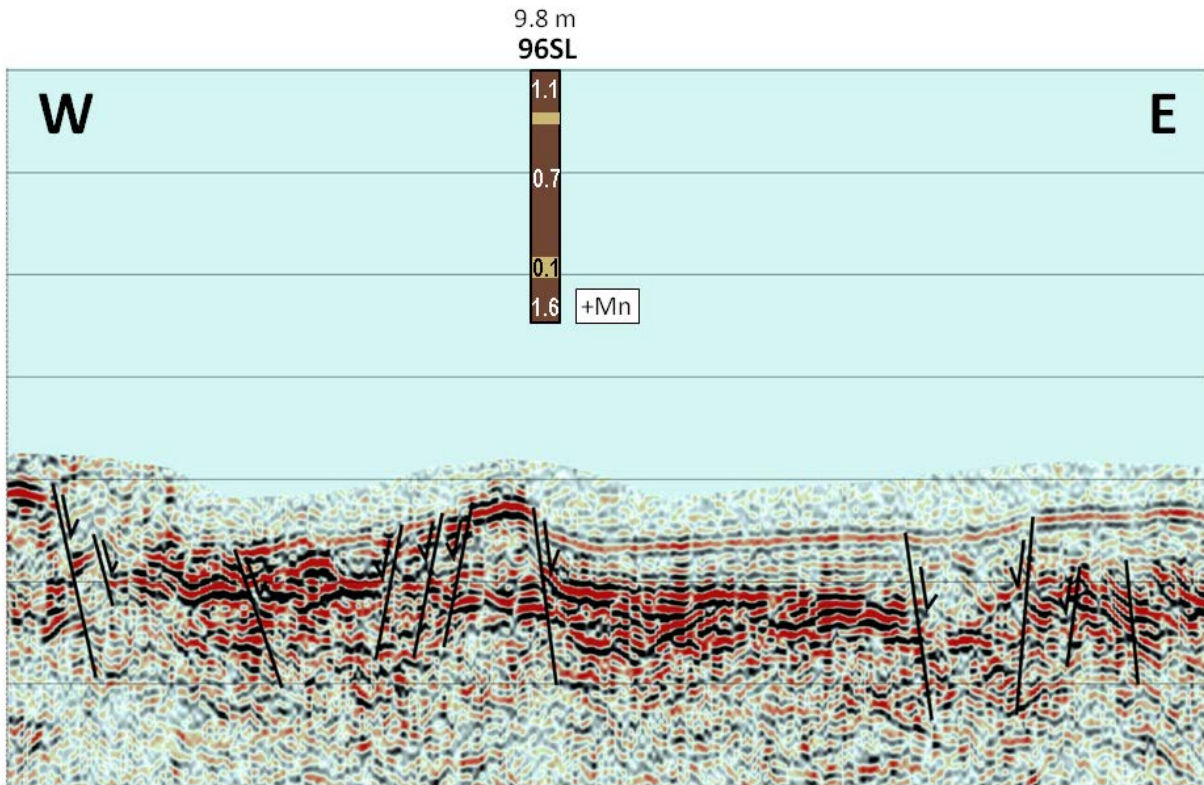


Fig. 7.3.20. West-East transect along seismic profile 82SCS1510_3 in working area 4 (cf. Figs. 6.21 and 6.22 and Chapter 7.1) with schematic representations of sediment core characteristics. The numbers shown above the core labels signify the total length of each sediment core. The colors represent the average color of the sediment sections and the numbers inside the cores reflect the manganese contents of the sediments.

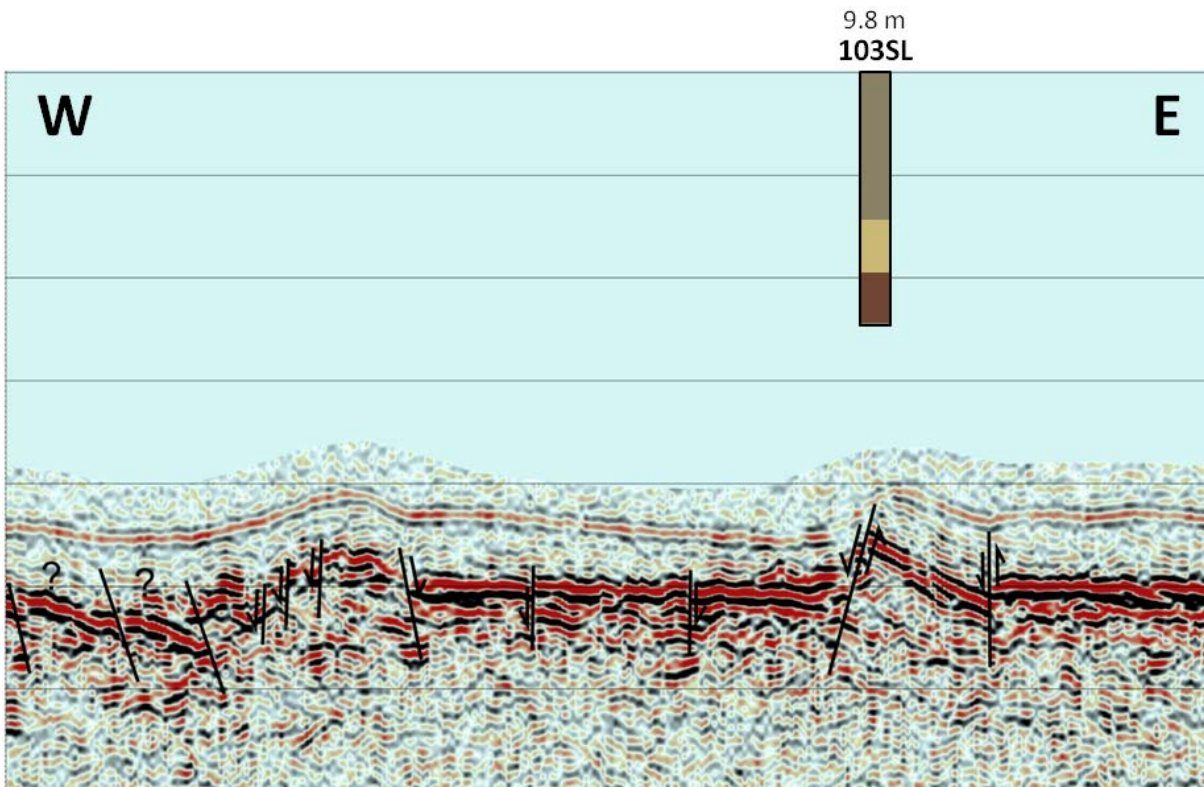


Fig. 7.3.21. West-East transect along seismic profile 82SCS1505_3 in working area 4 (cf. Figs. 6.21 and 6.22 and Chapter 7.1) with schematic representations of sediment core characteristics. The numbers shown above the core labels signify the total length of each sediment core. The colors represent the average color of the sediment sections and the numbers inside the cores reflect the manganese contents of the sediments.

7.4 PORE WATER AND SEDIMENT GEOCHEMISTRY

Ingrid Dohrmann, Christoph Filmsmair, Julia Fronzek, Jan F. Hartmann, Sabine Kasten, Charlotte Kleint, Inken Preuss and Simon Ritter

7.4.1 Research objectives

In the framework of the BMBF project FLUM “**FLU**id fluxes and **Mn** nodules” and during RV SONNE cruise SO-240, geochemical investigations focused on the analysis of element fluxes and biogeochemical processes in sediments overlying seamount basaltic crust in the German license area “East” for the exploration of polymetallic nodules (Rühlemann et al., 2011). As postulated by Fisher and Wheat (2010), slight temperature and pressure gradients in permeable basaltic basement can induce low-temperature fluid/seawater circulation between seamounts acting as recharge and discharge sites. The study by Ziebis et al. (2012) at the so-called “North Pond” site – a sediment-filled basin of the Mid-Atlantic Ridge – demonstrated for the first time that the migration of oxygen-rich seawater in basaltic oceanic crust produces an upward diffusive flux of oxygen and other dissolved seawater constituents into the overlying sediments. Similar increases in pore-water oxygen concentrations at sediment depth had also been detected at three sites located at the flank/foot of a small seamount located in the northern part of the German License area “East” during RV SONNE cruise SO-205 in 2010 and RV L’ATALANTE cruise BIONOD in 2012 (Mewes et al., in review).

Pore-water data can verify the mobilization potential of such fluid circulation for many solutes including chloride, silica, Ca, Sr, Ba, B, Mn and Fe (Wheat and Fisher, 2010). To date, no information is available on the mobility of dissolved trace metals in such systems. The low-temperature circulation system in particular may have an important influence on global geochemical budgets as the fluid discharge can be immense, even when the fluids themselves are only slightly altered compared to seawater. One aim of the FLUM project is to search for chemical indicators of possible fluid fluxes with a focus on elements that may be easily mobilizable from the basaltic rock at low temperatures. In addition, we will also focus on Mn(III) as a metastable form of manganese in the redox transition between Mn(IV) in oxic and Mn(II) in anoxic sediment layers; this soluble species has been shown to play an important role in the mobility and fluxes of trace metals in shallower waters (Madison et al., 2013). Recent work by Abbott et al. (2015) has shown that rare earth element (REE) cycling within the upper ten centimeters of deep-sea marine sediments, as opposed to shallower continental shelf and slope sediments, plays a significant role in controlling the integrated global REE flux from the pore fluids and consequently the broad-scale REE pattern in seawater. Hence, we will also investigate if and how potential shallow fluid fluxes may contribute to sedimentary REE flux into the ocean.

The objectives and research questions of geochemical investigations during cruise SO-240 were:

- 1) Is low-temperature circulation of seawater in basaltic basement a widespread phenomenon in the study area?
- 2) Can sites of seawater/fluid recharge and discharge be identified based on dissolved pore-water constituents?

- 3) How does the circulation of seawater within the basaltic basement determine solute fluxes across the basement/sediment interface as well as redox zonation, biogeochemical processes and preservation of organic matter in the basal sediments?
- 4) Is the availability and mobility of trace metals influenced by the upward diffusion of oxygen and how is the trace metal composition of Mn nodules affected?
- 5) Is the composition of oxic pore water similar to that of the bottom water?

7.4.2 Methods

Immediately after recovery of the CTD and STROMER as well as sediment core recovery with the different coring devices (SL: gravity corer [Schwerelot]; KL: piston corer [Kolbenlot]; MUC: **m**ultiple corer), all water samples and sediment cores taken for geochemical analyses were transferred into and stored in the cold room of the ship at an *in situ* temperature of approximately 4°C for subsequent sampling, *ex situ* oxygen measurements, pore-water extraction and solid-phase sampling.

Oxygen measurements

Oxygen saturation in the sediment was determined using amperometric Clark-type oxygen sensors with an internal reference and equipped with a guard cathode (Revsbech, 1989). The electrodes (Unisense, Denmark) are made of glass, each with a 6 cm long tip that is inserted into a hyperdermic needle (diameter 1.1 mm, length 50 mm), and have a response time of less than 10 s. Signals were amplified and transformed to mV by a picoamperemeter, digitalized by an analogue/digital converter (ADC 216, Unisense, Denmark) and recorded by a computer using the software PROFIX (Unisense, Denmark). Measurements were recorded at each sampling depth for 2-3 minutes and mean saturation values were obtained when signals were stable in order to calculate the depth profiles of oxygen concentrations. Measurements were performed at least 12 hours after core recovery in order to allow temperature equilibration of the sediments to *in situ* temperatures of about 4°C in the cold room. For the calibration of the oxygen sensors, local bottom water was used.

High-resolution (1 mm depth resolution) vertical profiles of oxygen saturation across the sediment/water interface were obtained for MUC cores by use of a micromanipulator down to a maximum sediment depth of 5-6 cm. For the measurement of oxygen in deeper parts of the MUC cores as well as for all SL and KL cores, holes were drilled through the walls of the core liners for the insertion of the microelectrode, in 1 cm intervals for MUC cores and 5 cm intervals for the SL and KL cores (Fig. 7.4.1).



Figure 7.4.1. Oxygen measurements performed on a gravity core at in situ temperatures of approximately 4°C (Photos: Vincent Ozegowski).

Water-column, bottom-water and pore-water sampling

Water-column, bottom-water and pore-water samples were collected from CTD-rosette and STROMER deployments as well as from MUC, SL and KL cores and stored at 4°C in the cold room of the ship until further analyses were carried out.

Water samples collected from the CTD-rosette, STROMER and MUC were filtered over 0.2 µm cellulose acetate filters (Sartorius) and subsamples were taken for minor and trace elements analyses, Mn II/III speciation and the determination of dissolved organic carbon (DOC) in the home laboratories at the Alfred Wegener Institute Helmholtz Center for Polar and Marine Research (AWI) in Bremerhaven and the Jacobs University Bremen (JUB), Germany. Furthermore, additional samples from the overlying bottom water of the MUC cores were filtered through rhizons for subsequent analyses onboard. The remaining bottom water was carefully removed from the MUC cores by means of a siphon to avoid destruction of the sediment surface.

Pore water from MUC, SL and KL cores was extracted (1) by using rhizon samplers with an average pore size of 0.1 µm according to the procedure described by Seeberg-Elverfeldt et al. (2005) (Fig. 7.4.2), and (2) by transferring sediment subsamples into 50 ml acid-washed centrifuge tubes and centrifuging at 2,800 rpm for > 40 min. The supernatant was filtered through a 0.2 µm acid-washed cellulose acetate (Whatman, FP 30) filter. To maintain the anoxic conditions of the pore water, sediment samples from anoxic parts of the sediment cores were flushed with argon and subsamples were processed in a glove bag under a steady stream of argon. Pore water from SL and KL cores was retrieved at 20 cm depth resolution; from MUC cores at 1 cm depth resolution by rhizon sampling (Fig. 7.4.2) and at 7 cm depth resolution by centrifuge sampling. From each sampling depth, subsamples were taken for minor and trace elements analyses as well as DOC determination in the home laboratory. Further subsamples were taken from the SL and KL cores and pooled from 1 m segments for REE analyses.

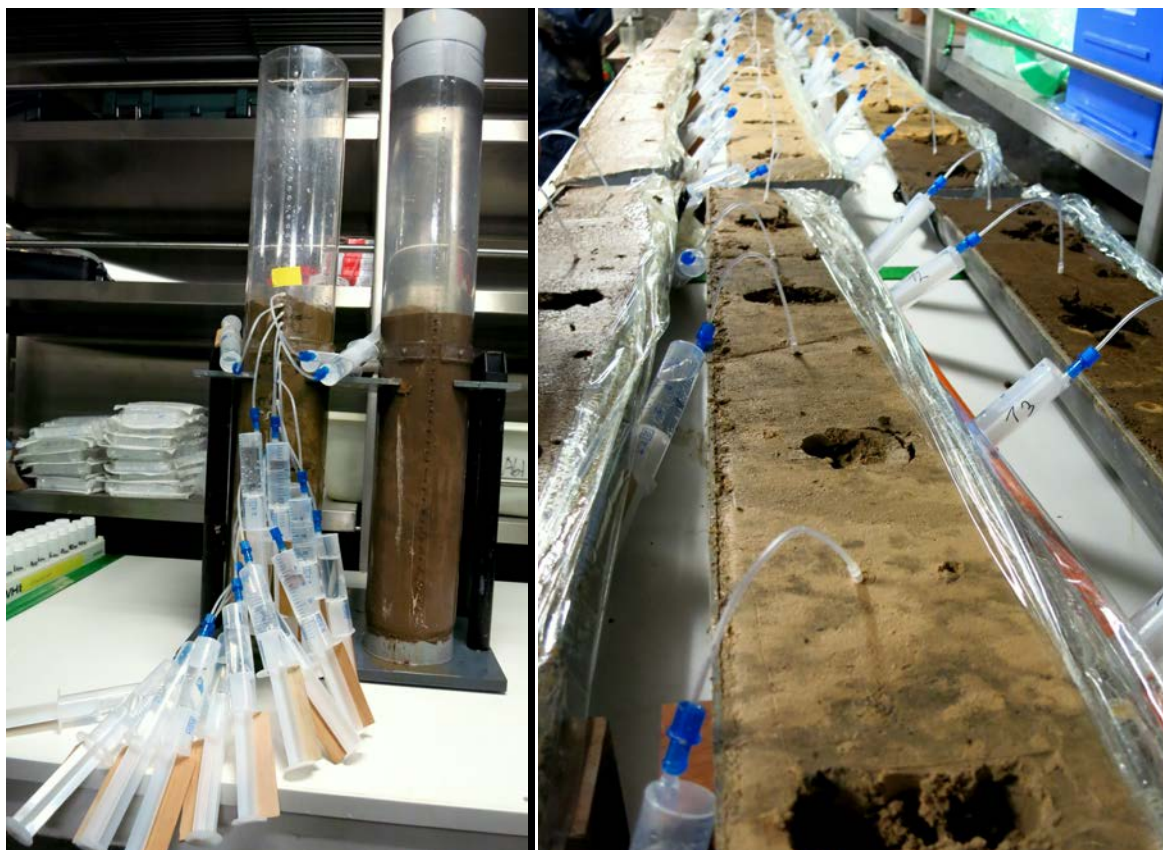


Figure 7.4.2. Pore-water sampling from MUC (left) and gravity/piston (right) cores using rhizon samplers. Sampling was performed at an in situ temperature of approximately 4°C in the cold room of the ship (Photos: Jessica Volz).

Shipboard pore-water analyses

After the supernatant bottom water of a MUC core was taken and filtered through a rhizon for subsequent analyses, the remaining bottom water was carefully removed by means of a siphon to avoid destruction of the sediment surface. Eh and pH were measured by means of punch-in electrodes. In order to avoid any oxidation processes, the first 1 ml of the extracted pore water was disposed of during rhizon sampling. Subsequent to the extraction, analyses were performed onboard including the determination of alkalinity, dissolved iron (Fe^{2+}), phosphate (PO_4^{3-}) and silica. All sites investigated geochemically during this cruise and parameters analyzed on board are shown in table 7.4.1.

Alkalinity

Alkalinity was determined on a 1 ml aliquot of the pore-water sample by titration with 10 mM HCl. The pH measurements were performed using a Hamilton micro-electrode. The samples were titrated with a digital burette to a pH interval of 4.1 - 3.4 and both titration volume as well as the final pH values were recorded. The alkalinity was calculated using a modified equation from Grasshoff et al. (1999).

Dissolved iron (Fe^{2+})

Fe^{2+} was determined photometrically at 565 nm (CECIL 2021 photometer, Lange DR 2800 photometer). 1 ml of sample was added to 50 μl of Ferrospectral solution to complex the Fe^{2+} for colorimetric measurement.

Phosphate (PO₄³⁻)

PO₄³⁻ was determined using the molybdenum blue method (Grasshoff et al., 1999). 50 µl of an ammonium molybdate solution was added to 1 ml of pore-water sample and spiked with 50 µl of an ascorbic acid solution. The phosphomolybdate complex was reduced to molybdenum blue and measured photometrically at 820 nm wavelength (CECIL 2021 photometer, Lange DR 2800 photometer).

Silica

Silica was determined photometrically as silica molybdate complex at 810 nm wavelength (CECIL 2021 photometer, Lange DR 2800 photometer).

Table 7.4.1. Geochemical parameters analyzed on board during the SO-240 cruise.

#	Station SO240-	O ₂ [1 mm]	O ₂ [1 cm]	O ₂ [5 cm]	Rhizon sampling	Centri- fugation	Alk.	Fe ²⁺	PO ₄ ³⁻	Si	Eh pH
1	05 SL	-	-	x	x	x	x	-	x	x	x
2	08 MUC	x	x	-	x	x	x	-	x	x	-
3	09 KL	-	-	x	x	x	x	-	x	x	x
4	14 MUC	every 0.5 mm	x	-	x	x	x	-	x	x	-
5	15 KL	-	-	x	x	-	x	-	x	x	x
6	18 MUC	x	x	-	x	x	x	-	x	x	-
7	22 KL	-	-	x	x	x	x	-	x	x	x
8	23 MUC	-	-	-	x	x	x	-	x	x	-
9	31 KL	-	-	x	x	x	x	-	x	x	x
10	34 MUC	x	x	-	x	x	x	-	x	x	-
11	35 SL	-	-	x	x	x	x	-	x	x	x
12	37 MUC	x	x	-	x	x	x	-	x	x	-
13	42 SL	-	-	x	x	x	x	-	x	x	x
14	43 MUC	x	x	-	x	x	x	-	x	x	-
15	51 SL	-	-	x	x	x	x	-	x	x	x
16	53 SL	-	-	x	x	x	x	-	x	x	x
17	58 SL	-	-	x	x	x	x	-	x	x	x
18	59 MUC	x	x	-	x	x	x	-	x	x	x
19	61 MUC	x	x	-	x	x	x	-	x	x	-
20	65 SL	-	-	x	x	x	x	-	x	x	x
21	69 SL	-	-	x	x	x	x	-	x	x	x
22	70 MUC	x	x	-	x	x	x	-	x	x	x
23	72 SL	-	-	x	x	x	x	-	x	x	x
24	74 MUC	x	x	-	x	x	x	-	x	x	x
25	81 SL	-	-	x	x	x	x	-	x	x	x
26	95 MUC	x	x	-	x	x	x	-	x	x	-
27	96 SL	-	-	x	x	x	x	-	x	x	x
28	106 MUC	x	x	-	x	x	x	-	x	x	-
29	108 SL	-	-	x	x	x	x	-	x	x	x
30	109 MUC	x	x	-	x	x	x	-	x	x	-
31	116 MUC	x	x	-	x	x	x	-	x	x	-
32	117 SL	-	-	x	x	x	x	-	x	x	x

Sample aliquots

Sample aliquots of ideally 2 ml for NH_4^+ and nitrate (NO_3^-) were stored in amber vials sealed with a PTFE septum-bearing lid at -20°C until analyses by means of a continuous flow analyzer at the AWI in Bremerhaven can proceed. About 2 ml of pore water were transferred into an amber vial filled with $10\ \mu\text{l}$ of HgCl_2 , sealed with a PTFE septum-bearing lid and stored at 4°C for the later analysis of dissolved inorganic carbon (DIC). For the analyses of further dissolved pore-water constituents, aliquots of the remaining pore-water samples were diluted 1:10 and acidified with suprapure 1 M HNO_3 in Zinsser vials for the determination of cations (Ca, Mg, Sr, K, Ba, S, Mn, Si, B, Li) by optical emission spectrometry. Subsamples for the determination of sulphate and chloride (anions) were stored at 4°C in Zinsser vials for ion chromatography (HPLC) analyses. All aliquots of pore-water and sediment samples taken and stored for further analyses in the home lab at AWI are listed in table 7.4.2.

Table 7.4.2. List of samples taken and stored for further geochemical analyses in the home lab at the AWI in Bremerhaven.

#	Station SO240-	NH_4^+	NO_3^-	DIC	Cations	Anions	Wet Sediment
1	05 SL	x	x	x	x	x	x
2	08 MUC	x	x	x	x	x	x
3	09 KL	x	x	x	x	x	x
4	14 MUC	x	x	x	x	x	x
5	15 KL	x	x	x	x	x	x
6	18 MUC	x	x	x	x	x	x
7	22 KL	x	x	x	x	x	x
8	23 MUC	x	x	x	x	x	x
9	31 KL	x	x	x	x	x	x
10	34 MUC	x	x	x	x	x	x
11	35 SL	x	x	x	x	x	x
12	37 MUC	x	x	x	x	x	x
13	42 SL	x	x	x	x	x	x
14	43 MUC	x	x	x	x	x	x
15	51 SL	x	x	x	x	x	x
16	53 SL	x	x	x	x	x	x
17	58 SL	x	x	x	x	x	x
18	59 MUC	x	x	x	x	x	x
19	61 MUC	x	x	x	x	x	x
20	65 SL	x	x	x	x	x	x
21	69 SL	x	x	x	x	x	x
22	70 MUC	x	x	x	x	x	x
23	72 SL	x	x	x	x	x	x
24	74 MUC	x	x	x	x	x	x
25	81 SL	x	x	x	x	x	x
26	95 MUC	x	x	x	x	x	x
27	96 SL	x	x	x	x	x	x
28	106 MUC	x	x	x	x	x	x
29	108 SL	x	x	x	x	x	x
30	109 MUC	x	x	x	x	x	x
31	116 MUC	x	x	x	x	x	x
32	117 SL	x	x	x	x	x	x

At one station, centrifuged pore water was filtered over a sterile 0.2 µm filter and stored at -20°C for the analysis/detection of heavy metal resistance genes to be carried out by the group of Prof. Dr. Matthias Ullrich at JUB (SO240-72SL: 35 ml from 35 cm depth and 17 ml from 535 cm depth).

In addition, water-column, bottom-water and pore-water samples were taken and stored at 4°C or at -20°C for home lab analyses of major and trace metals, REEs, DOC and Mn(II)/(III) at JUB, Germany (Tab. 7.4.3). First samples were shipped back by airfreight right after the cruise, and all remaining samples will be shipped back after the last JPI-Oceans cruise (SO242-2) in the beginning of October 2015.

Table 7.4.3 List of subsamples taken and stored for further analyses of major and trace metals, REEs, Mn(II)/(III) and DOC in the home lab at JUB in Bremen.

#	Station SO240-	Position		Water depth [m]	subsamples taken for home analyses			
		Lat. (N)	Long. (W)		major and trace metals	REEs	Mn	DOC
1	01CTD	13°10.52'	118° 12.19'	4262	x	-	-	x
2	05SL	13° 10.525'	118° 06.705'	4287	x	x	-	x
3	08MUC	13° 10.524'	118° 06.708'	4289	x	x	-	x
4	09KL	13° 10.524'	118° 10.104'	4335	x	x	-	x
5	13STR	13° 09.441'	118° 12.985'	3725	x	x	-	x
		13° 10.519'	118° 09.751'	4313				
6	14MUC	13° 10.528'	118° 10.108'	4332	x	x	-	x
7	18MUC	13° 07.109'	118° 07.657'	4318	x	x	-	x
8	22KL	13° 10.527'	118° 08.184'	4288	x	x	x	x
9	23MUC	13° 10.526'	118° 08.186'	4305	x	-	-	x
10	28STR	13° 10.007'	118° 04.869'	4035	x	x	-	x
		13° 10.527'	118° 08.936'	4298				
11	31KL	12° 53.355'	118° 24.572'	4289	x	x	x	x
12	34MUC	12° 53.358'	118° 24.569'	4287	x	x	x	x
13	35SL	12° 54.128'	118° 24.791'	4319	x	x	x	x
14	37MUC	12° 54.131'	118° 24.782'	4319	x	x	-	x
15	40STR	13°02.020'	118° 26.744'	3712	x	-	-	x
		13°02.912'	118° 26.515'	3718				
16	42SL	12° 51.249'	118° 23.976'	4290	x	x	x	x
17	43MUC	12° 51.247'	118° 23.980'	4289	x	x	-	x
18	49STR	12° 51.980'	118° 24.170'	4273	x	x	-	x
		12° 49.056'	118° 23.374'	4292				
19	50CTD	13° 10.020'	118° 04.949'	4026	x	x	-	x
20	51SL	13° 10.526'	118° 06.584'	4286	x	x	-	x
21	53SL	13° 10.508'	118° 06.110'	4273	x	x	-	x
22	58SL	12° 53.216'	119° 08.351'	4309	x	x	-	x
23	59MUC	12° 53.216'	119° 08.344'	4306	x	x	-	x
24	61MUC	12° 56.109'	119° 08.871'	4293	x	x	-	x
25	69SL	12° 39.855'	119° 13.374'	4275	x	x	-	x
26	70MUC	12° 39.857'	119° 13.385'	4270	x	x	-	x
27	72SL	12° 55.597'	119° 08.833'	4295	x	x	x	x
28	74MUC	12° 55.601'	119° 08.830'	4295	x	x	-	x
29	81SL	11° 50.064'	116° 32.890'	4355	x	x	x	x
30	95MUC	11° 49.262'	117° 13.197'	4150	x	x	-	x
31	96SL	11° 49.260'	117° 13.195'	4145	x	x	-	x
32	106MUC	11° 50.079'	116° 32.900'	4351	x	x	-	x
33	108SL	11° 48.796'	116° 31.767'	4326	x	x	x	x
34	109MUC	11° 48.791'	116° 31.760'	4327	x	x	-	x
35	113STR	13° 11.453'	118° 05.231'	4222	x	x	-	x
36	116MUC	13° 11.098'	118° 06.003'	4161	x	x	-	x
37	117SL	13° 11.103'	118° 05.992'	4271	x	x	-	x

Further water-column, bottom-water and pore-water samples were taken and stored in gas-tight copper tubes for the analysis of helium isotopes at the Institute of Environmental Physics (IEP) at the University of Heidelberg (Tab. 7.4.4).

Table 7.4.4. Compilation of water-column, bottom-water and pore-water samples taken for the determination of helium isotopes to be analyzed at the IEP in Heidelberg.

#	Station SO240-	Position		sample type	water depth [m]	sediment depth [m]
		Lat. (N)	Long. (W)			
1	72SL			Pore water	-	5.53–8.53
2	74MUC			Bottom water	4295	-
3	74MUC			Pore water	-	0.10–0.15
4	74MUC			Pore water	-	0.23–0.28
5	79CTD			Intermediate water	2000	-
6	81SL			Pore water	-	9.46–11.46
7	81SL			Pore water	-	11.46–13.46
8	108SL			Pore water	-	8.00–10.00
9	116MUC			Bottom water	4270	-
10	116MUC			Pore water	-	0.10–0.20
11	117SL			Pore water	-	0–4
12	121MUC			Bottom water	4268	-
13	121MUC			Pore water	-	0.10–0.20
14	no official station	13°14.139′	117°57.186′	Surface water	0–1	-

Solid-phase sampling

After oxygen profiles had been measured, sediment samples from each MUC core were taken in 1 cm resolution for solid-phase analysis. For every SL and KL core, the solid phase was sampled every 20 cm. All solid phase samples were taken using either cut-off syringes with a volume of about 12 ml or with a ceramic knife and stored at 4°C in plastic vials for the determination of the bulk sediment composition, sequential extractions and mineralogical analyses (Tab. 7.4.2).

In addition, sediment samples were taken for microbiological and molecular biological investigations to be performed by the group of Prof. Dr. Michael Friedrich at the University of Bremen and for Dr. Walter Geibert at AWI Bremerhaven with the aim of extracting micro-meteorites for the analysis of natural radionuclides (Tab. 7.4.5).

Table 7.4.5. Sediment samples taken and stored at 4°C for microbiology/molecular biological investigations and the extraction of micro-meteorites.

#	Station SO240-	Sediment depth [cm]	Remarks/Purpose
1	22-KL	5 – 1285	every 20 cm, for microbiology
2	35-SL	5 – 965	every 20 cm, for microbiology
3	04-KG	10-11	for micro-meteorites
4		11-12	for micro-meteorites
5	25-KG	0-42	MUC tube 1; for micro-meteorites
6		8-42	MUC tube 2; for micro-meteorites
7		13-14	for micro-meteorites
8		14-15	for micro-meteorites
9		15-20	for micro-meteorites
10		20-21	for micro-meteorites

7.4.3 Preliminary/Shipboard results

During cruise SO-240, 3 CTD, 5 STROMER, 15 MUC, 13 SL, 4 KL and 2 box corer (KG, Kastengreifer) stations were sampled for water-column, bottom-water, pore-water and solid-phase investigations (see figures in chapter 6 for detailed maps). Table 7.4.1 shows the sites sampled for geochemical investigations during this cruise and provides a listing of parameters analyzed onboard. All aliquots of water-column, pore-water and solid-phase samples taken and stored for further analyses at the Alfred Wegener Institute Helmholtz Centre for Polar and Marine Research (AWI) in Bremerhaven, at the Jacobs University Bremen (JUB) or elsewhere are listed in tables 7.4.2, 7.4.3, 7.4.4 and 7.4.5.

One of the major tasks of this cruise was to elucidate whether the distinct shapes of the oxygen depth profiles showing re-increasing oxygen concentrations with depth as found at one seamount (Teddy Bare seamount) during RV SONNE cruise SO-205 and RV L'ATALANTE cruise BIONOD (Mewes et al., in review) represent a widespread phenomenon in the study area. For this purpose, we collected SL and KL cores along several transects and at sampling sites located on the flanks and at the feet of seamounts as well as sites more distal to the seamounts in the four working areas (see Chapter 6). One particular focus of our work was the Teddy Bare Seamount in working area 1, for which oxygen and pore-water profiles for three sites were already available from the two previous cruises mentioned above (Mewes et al., in review).

Our on-board oxygen measurements revealed that all sites located close to and at the foot of seamounts showed oxygen concentrations that first decreased with sediment depth and then re-increased again towards the basaltic basement. Sites located at a greater distance to seamounts did not show this type of oxygen concentration-depth profile, but rather the typical oxygen penetration depth of 1 to 3 m which has been reported for non-seamount settings in the German license area “East” by Mewes et al. (2014). It is possible that sites which are more distant from seamounts also receive a diffusive input of oxygen from the underlying oceanic crust. However, the gravity corer and piston corer only reach down to a maximum depth of about 13.5 m – and thus any potential impact of oxygen supply from below could not be captured in areas characterized by greater sediment thickness.

An example of the above-mentioned trend in oxygen concentration profiles is given in figure 7.4.3, which shows a transect west of the Teddy Bare seamount reaching from the most remote site SO240-09KL in the west to the most proximal site SO240-53SL in the east (see also Fig. 6.4). The sampling locations SO240-05SL, SO240-51SL and SO240-53SL - being located at the foot of the Teddy Bare seamount - all display re-increasing oxygen concentrations with sediment depth. Of these three sites, only site SO240-53SL is characterized by slumping in the lower part of the core (Tab. 7.4.6), which is a typical feature of sediments that deposit at the foot of seamounts. This finding is evidence that oxygen indeed diffuses up into the basal sediments from the underlying crust rather than being an artefact caused by trapping of oxygen-rich bottom water during mass wasting of sediments from the flank down to the foot of the seamount.

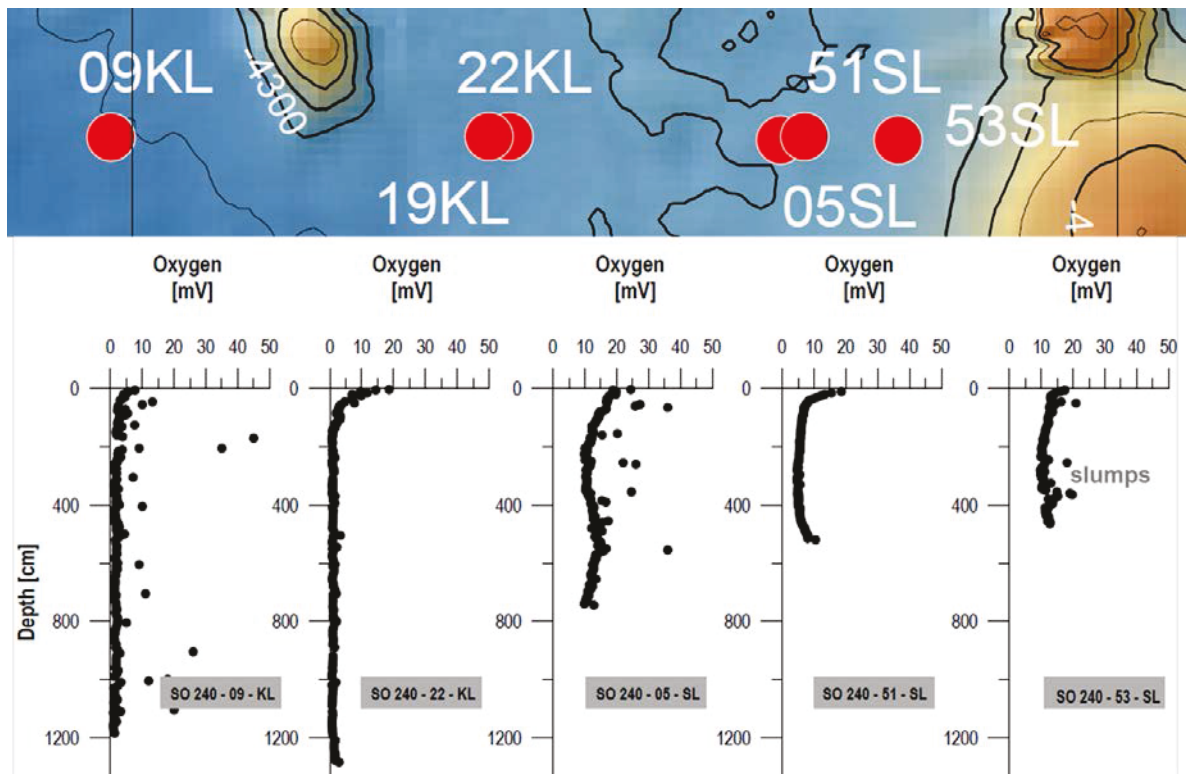


Figure 7.4.3. Oxygen concentration-depth profiles for sites located along a transect west of the Teddy Bare seamount in working area 1.

It was striking to see that all sites which showed increased oxygen concentrations at the base of the cores were also characterized by chocolate-brown sediments either over the whole length of the cores or in the lower part of the cores (Tab. 7.4.6; Chapter 7.3 and Appendix A2 on core descriptions). It is possible that this brown color is produced by Mn oxide mineral phases that might either (1) result from the weathering of the underlying basalt, or (2) form due to the oxidation of Mn^{2+} - previously present in pore-water – when oxygen starts to diffuse upward from seawater circulating within the permeable seamount crust.

In addition to the oxygen and other pore-water data collected on board during RV SONNE cruise SO-240, the analyses of further pore-water constituents and the determination of the elemental and mineralogical composition of the sediments in the home labs of AWI and JUB will help to contribute further to answering the research questions formulated at the beginning of this chapter. Our onboard results already demonstrate that element fluxes across the basalt/sediment interface induced by low-

temperature fluid circulation within the oceanic crust represent a widespread phenomenon in the study area and most likely in other similar deep-sea environments as well.

Table 7.4.6. Characteristics of gravity cores (SL) and piston cores (KL) with respect to oxygen concentration profile, sediment color and the presence of slumping.

#	Station SO240-	Oxygen at base	Chocolate-brown at base	Slump	Core length [m]
1	05SL	yes	yes	no	7.56
2	09KL	no	no	no	11.87
3	15KL	no	no	no	11.61
4	22 KL	no	no	no	13.01
5	31 KL	no	no	yes	11.74
6	35SL	yes	yes	yes	8.82
7	42SL	yes	yes	no	10.36
8	51SL	yes	yes	no	5.37
9	53SL	yes	yes	yes	4.82
10	58SL	no	no	no	12.44
11	65SL	no	no	no	12.75
12	69SL	yes	yes	no	12.65
13	72SL	no	no	no	8.53
14	81SL	yes	yes	no	13.47
15	96SL	yes	yes	no	9.7
16	108SL	no	no	no	10.38
17	117SL	yes	yes?	yes	~6 m, core bent

As typical examples of pore-water nutrient and alkalinity concentration profiles in the study area, pore-water concentration profiles for silica, phosphate and alkalinity are shown for 4 stations sampled in working areas 1 and 2 (Figs. 7.4.4, 7.4.5, 7.4.6 and 7.4.7) – each one with an oxygen penetration depth of a few meters (SO240-22KL and SO240-31KL) and one with oxygen re-increasing towards the basaltic basement (SO240-51SL and SO240-35). Silica generally displays concentrations in the range of 300 (SO240-51SL; Fig. 7.4.5) to 500 (SO240-22KL; Fig. 7.4.4) $\mu\text{mol/l}$ and often shows a typical increase with depth within the uppermost sediments. Phosphate concentrations are low and fluctuate within a narrow concentration range reaching from 1 to about 3 $\mu\text{mol/l}$. At almost all sites sampled during this cruise phosphate concentrations show a decrease with increasing sediment depth. Alkalinity values are similarly low and show very similar and uniform values over depth of about 2.5 $\text{mmol}(\text{eq})/\text{l}$ at all stations. Significant differences in concentration levels or in the shapes of pore-water concentration profiles could not be detected between the sites showing upward diffusion of oxygen from the basement (SO240-51SL, Fig. 7.4.5, and SO240-35, Fig. 7.4.7) and those being characterized by oxygen penetration found at a few meters sediment depth (SO240-22KL, Fig. 7.4.4, and SO240-31KL, Fig. 7.4.6).

SO 240 - 22 - KL

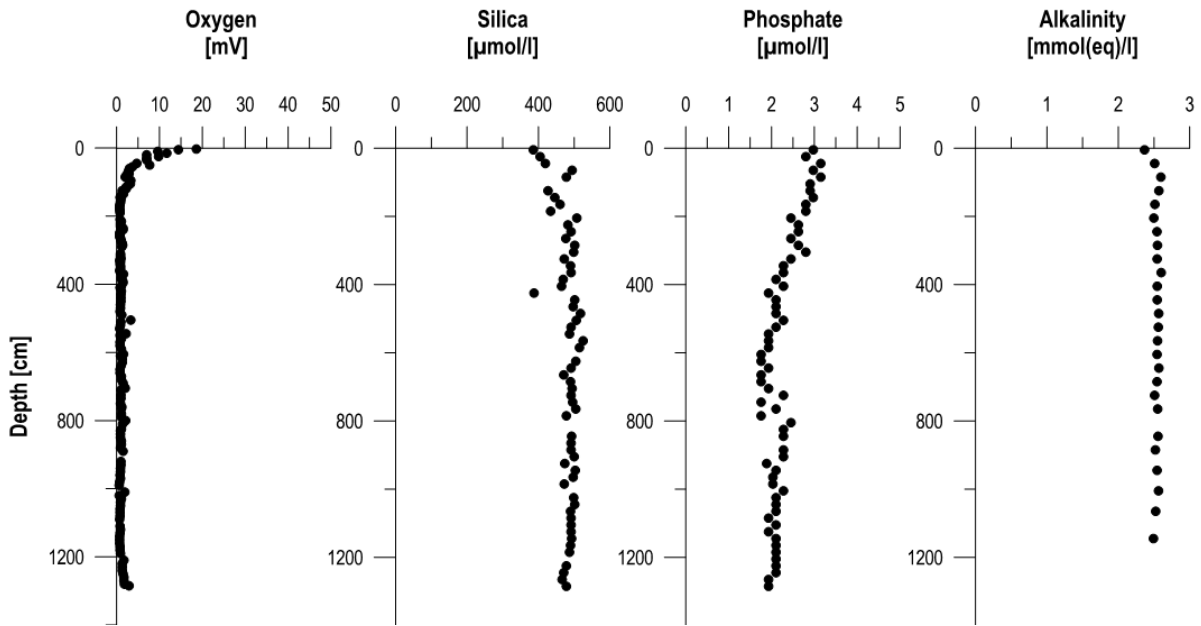


Fig. 7.4.4. Pore-water concentration profiles of oxygen, silica, phosphate and alkalinity for site SO240-22KL.

SO 240 - 51 - SL

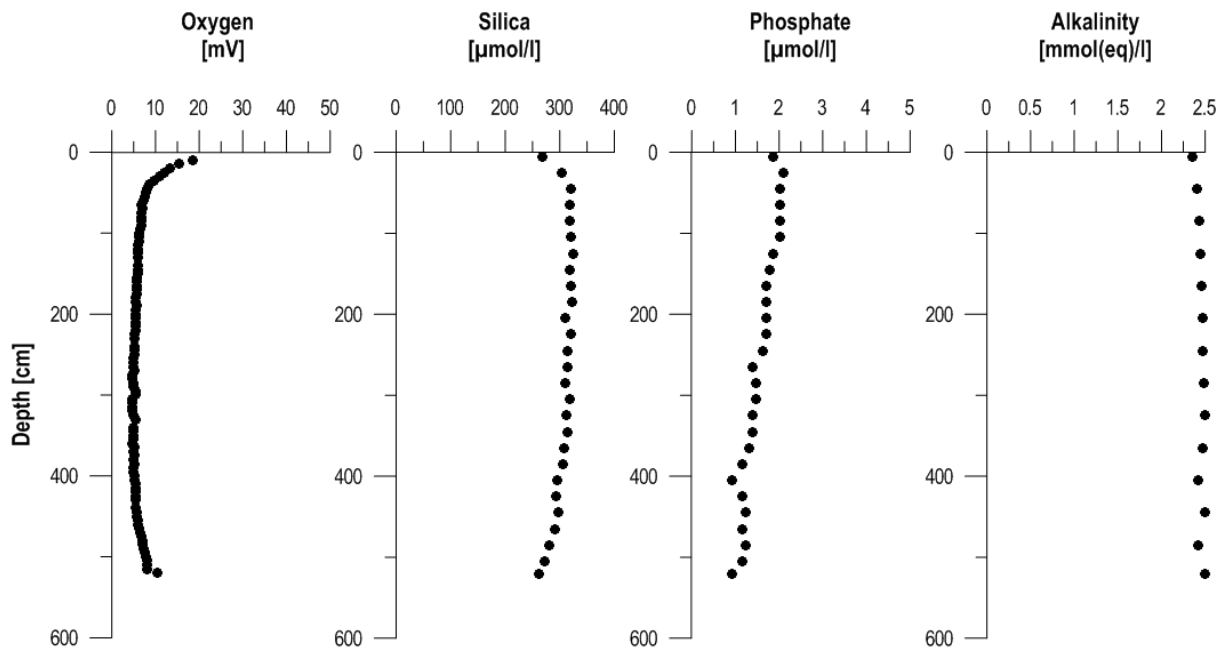


Fig. 7.4.5. Pore-water concentration profiles of oxygen, silica, phosphate and alkalinity for site SO240-51SL.

SO 240 - 31 - KL

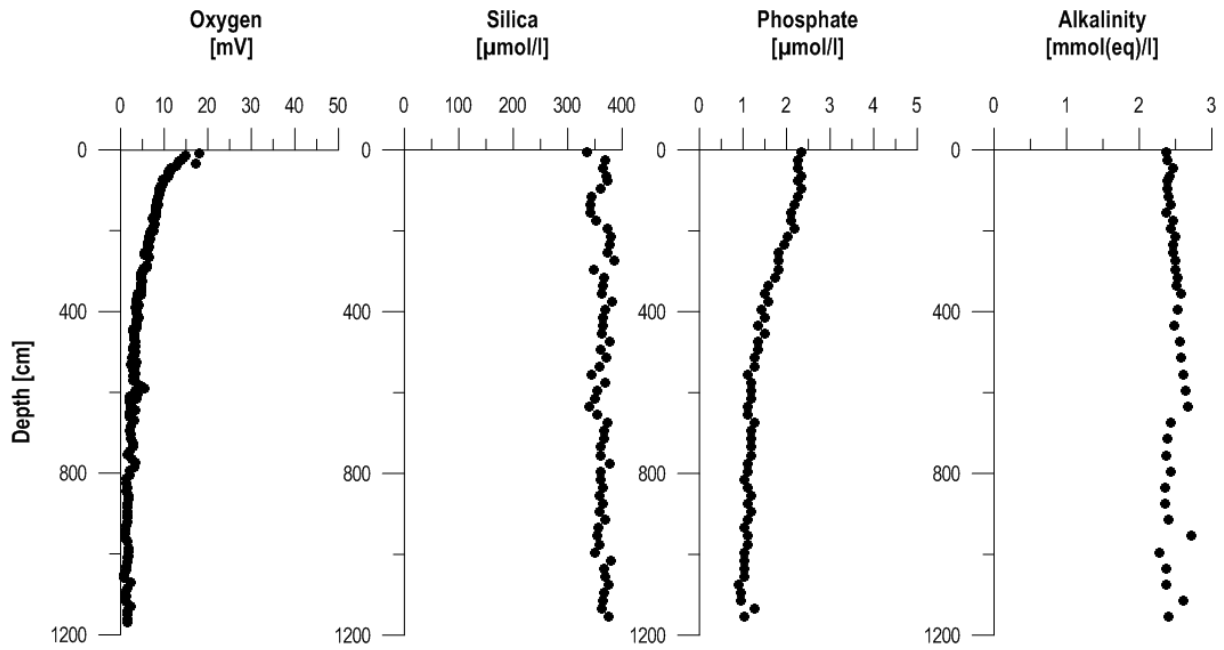


Fig. 7.4.6. Pore-water concentration profiles of oxygen, silica, phosphate and alkalinity for site SO240-31KL.

SO 240 - 35 - SL

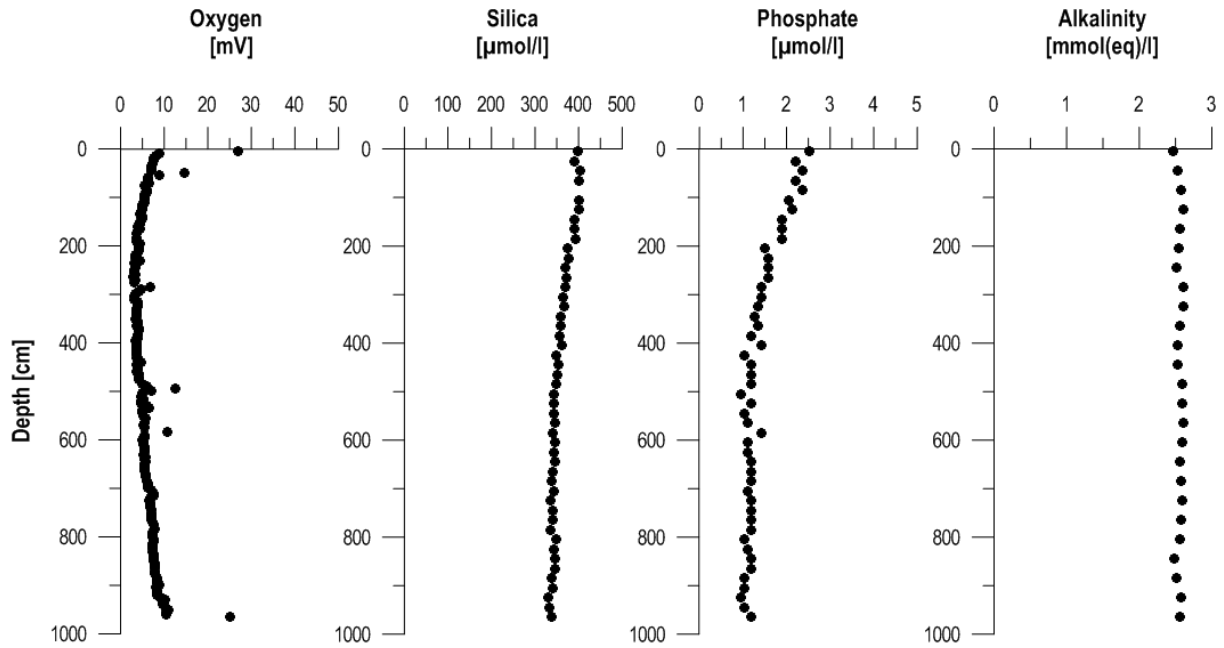


Fig. 7.4.7. Pore-water concentration profiles of oxygen, silica, phosphate and alkalinity for site SO240-35SL.

7.5 OCEAN FLOOR VIDEO AND PHOTO MAPPING

T. Kuhn, H. Wedemeyer

7.5.1 Introduction and research objectives

The BGR-owned video sled STROMER (STR) was deployed for online visual mapping of the seafloor, video and photo documentation as well as near-bottom water and rock sampling. The STROMER was only used in working areas 1 and 2 (cf. Figs. 6.7 and 6.13).

One objective of the STROMER deployment in both working areas was to investigate the manganese nodule size distribution and the nodule density in the immediate surroundings of seamounts. A second task was to map the slopes of seamounts according to sediment cover, rock types, slope angles, and the occurrence of ferromanganese crusts and/or manganese nodules. Moreover, the transition from the lower, sediment-free seamount slopes to the sediment-covered abyssal plains was explored, especially in areas of suspected fluid recharge or discharge. Last but not least, the determination of the characteristics of the sediments and their associated benthic megafauna formed an important part of the visual inspection of the seafloor.

As the new video-sled also has three built-in Niskin bottles for water sampling and a 5-function manipulator at its disposal, it was possible to take respective near-bottom water and rock samples at sites of interest.

7.5.2 Technical layout of the video sled STROMER

Survey tool BGR STROMER

The BGR STROMER (abbr. for German: “Simpler TauchROboter, Multifunktional ERweiterbar”; Fig. 7.5.1) is a simple, towed robotic underwater vehicle, which offers HD video, photo and various sensor survey capabilities as well as basic sampling capabilities, using a small 5-function manipulator arm. Although mainly being a towed vehicle, STROMER is equipped with a propulsion system, which allows a movement within a limited radius, e. g. to reach probably interesting areas close to the tow track or to position the vehicle for sampling. System components can be easily added, replaced or removed according to the actual research cruise requirements.

STROMER is designed to have modest research vessel and tow cable requirements. It is a small vehicle, 1.9 m long, 1.3 m wide and 1.3 m high, about 2.3 m with crow’s foot. Also the weight is modest, around 750 kg in air. The tow cable must, beside a sufficient working load, provide two electrical wires with less than 80 Ohm loop resistance (even higher, with reduced lighting power or without propulsion) and one single-mode optical-fibre. STROMER can also be operated via a coax-only/electrical-only tow cable not being too long, but just the basic data available online.

STROMER was completed just prior to SO-240. Station SO240-006STR was STROMER’s first deployment.

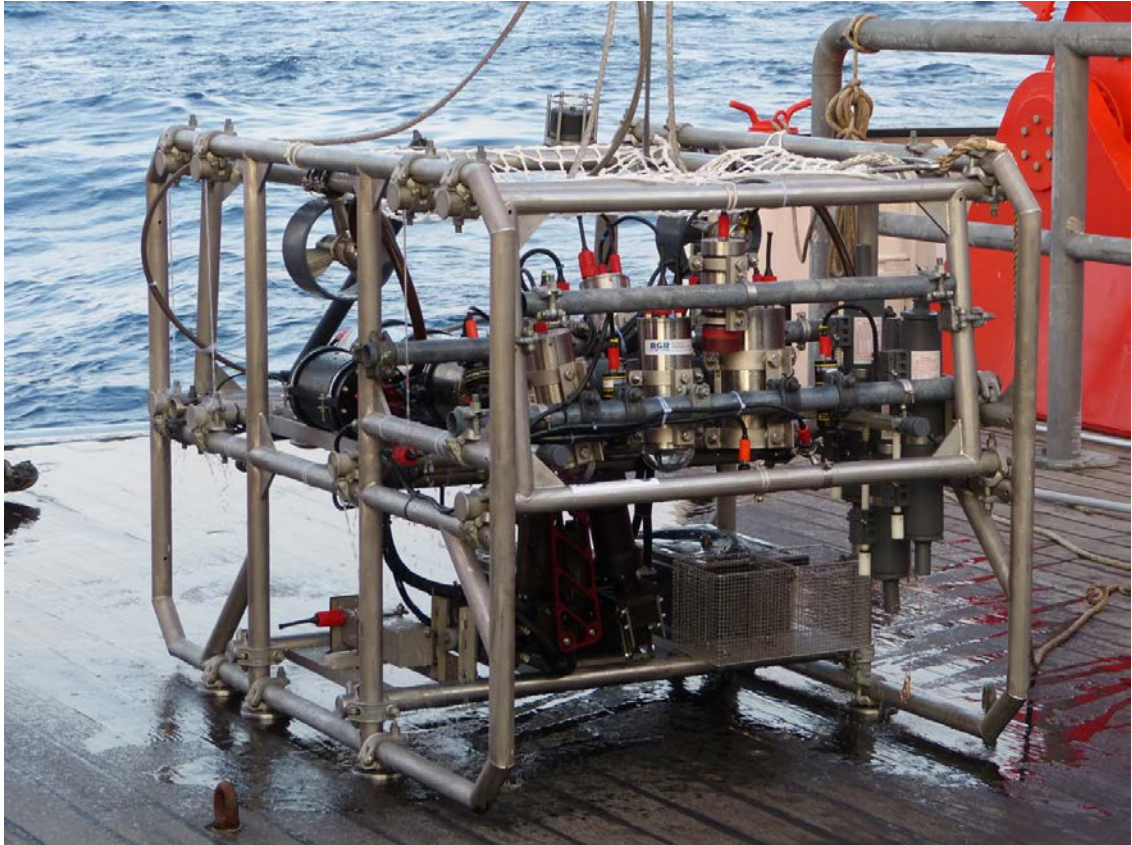


Figure 7.5.1. Simple, towed robotic underwater vehicle BGR STROMER (photo S. Sturm).

STROMER's setup and use experiences during SO-240

The following simplified block diagram shows STROMER's main components and setup during SO-240:

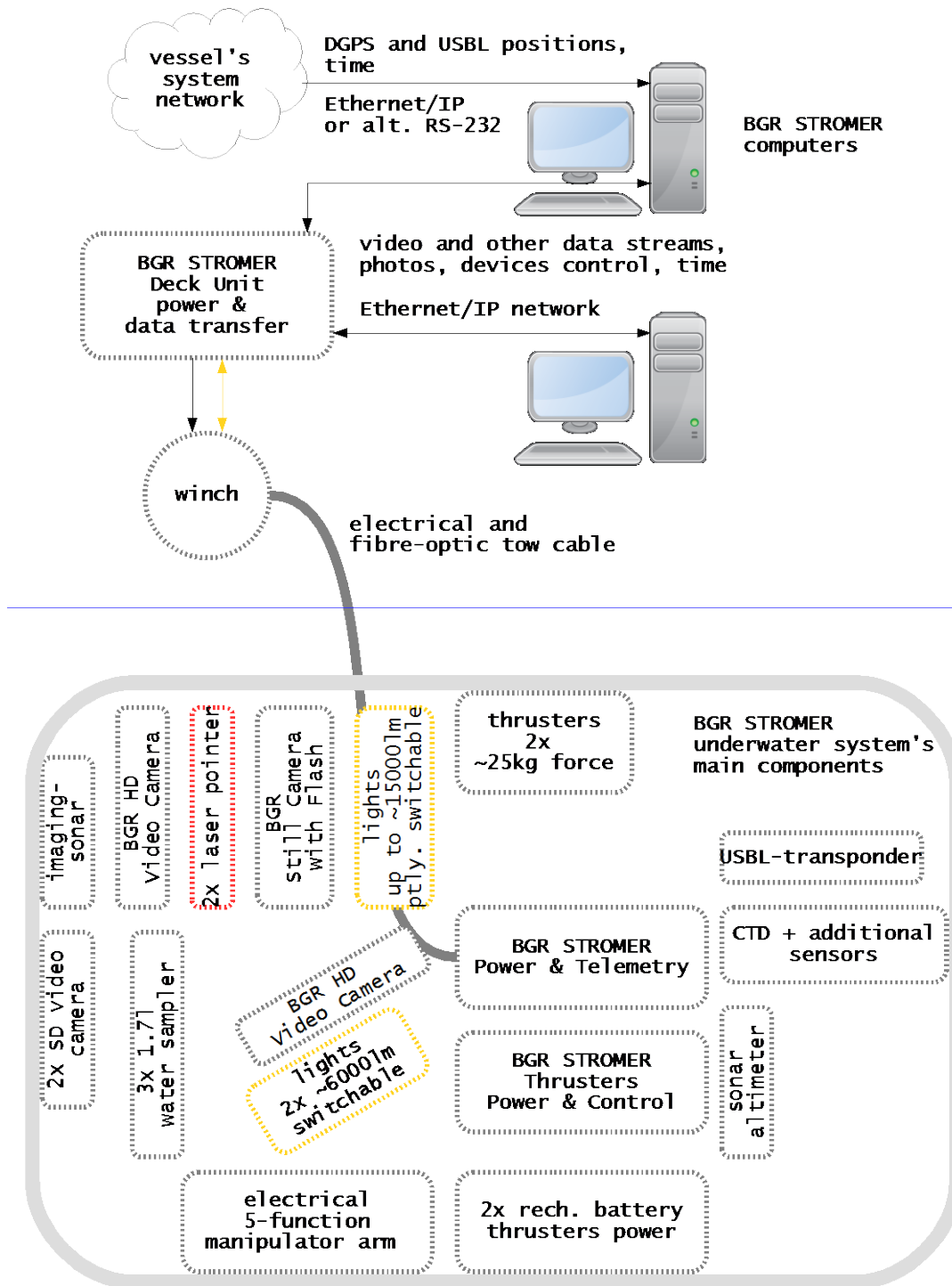


Figure 7.5.2. STROMER's main components and setup during SO-240, simplified block diagram.

HD videos and photos were taken with two new BGR HD video cameras, one BGR online HD-video camera 1.3 MPx, showing the forward direction and manipulator arm sampling area with a ~60° down angle, and one BGR online HD-video camera 3 MPx, showing the ocean floor. Both cameras have a very similar design. Main interface is Ethernet/IP, used for video streaming, data transfer and remote control. Videos can be sent as MPEG4 or MJPEG streams, photo format is JPEG. MJPEG was used for video during SO-240. Videos and photos can also be stored on local flash memory. Both cameras offer one

trigger input and one trigger output. An analogue Composite PAL interface is also offered. The BGR HD-video camera 1,3 MPx was set to a horizontal view angle of 70° (in air and water), the 3 MPx was set to 90°.

The BGR STROMER telemetry is able to trigger one camera according to the height over the ocean floor, given by a Teledyne Benthos PSA-916 sonar altimeter. This function was used with the BGR online HD-video camera 3 MPx, which has no flash, but is very light-sensitive and has an acceptable max. photo resolution of 3 MPx. Photos were taken in different intervals, down to 3sec, in a range between ~1.5 m and ~4 m above the ocean floor, and were directly transferred to one STROMER computer. With that lighting and camera, the shutter speed can be reduced to (1/50) seconds. At STROMER's tow speed, in-motion unsharpness is visible, as well as unsharpness due to the low light condition (camera gain and image compression), but the image quality is still usable, at least to be analyzed by human. At shutter speeds that low, the whole transect can be covered with overlapping photos.

The performance of the BGR online HD-video camera 3 MPx was not as good as expected. Under those conditions, the camera is not able/fast enough to stream a high resolution and quality video and to take and send triggered high resolution photos at a short interval at the same time. Video frame rate drops down. In that case, resolutions and/or photo interval have to be reduced.

Two analogue colour video cameras DeepSea Power & Light Nano SeaCam were installed. One was showing the ocean floor for the winch operator and on the vessel's bridge. Another one was showing the water samplers mounted in the front, left side of STROMER. This video was necessary to release the water samplers with STROMER's manipulator arm. The Nano SeaCam has a horizontal view angle of 59° (in water). The video out signal is analogue Composite, according to PAL standards. The video signals were converted and sent as MPEG4 video streams.

Photos were also taken in a 15 to 20 seconds interval using the BGR Fotokamera mit Blitz, a still camera with flash. The camera can be fully remote operated via an Ethernet/IP interface, using the according control software. The camera display may be put out to an analogue Composite PAL interface or to the according control software. The photo resolution is up to 12 MPx. Photos can be stored as JPEG or RAW on a local SD memory card and/or can be uploaded directly to a computer. At the smallest focal length, the horizontal view angle is 41° (in water). Zoom is up to 6x. The flash is mounted in a separate pressure housing. It is controlled by the camera via E-TTL interface. The flash's Guide Number is 43 (in air). With that flash, the photo shutter speed of the camera can be reduced to (1/250) seconds, which, at STROMER's tow speed, is fast enough to avoid in-motion unsharpness. Photos were directly transferred to one STROMER computer during SO-240 and could be reviewed directly. Due to the higher resolution and better sharpness, these photos contain much more details than HD video or photos taken by a video camera without flash.

STROMER was equipped with different LED (Light-Emitting Diode) lights during SO-240, altogether providing up to 27000 lm luminous flux. Two Deepsea Power & Light SeaLite Sphere spotlights with 6000 lm each and a light angle of 40° were used in forward direction. Four Deepsea Power & Light Sealite Six lights with 1500 lm luminous flux and a light angle of 85°, as well as one BGR LED tube with

7000 lm, ~100° and two BGR light tubes with 1200 lm, ~100° were used in downward direction. The colour temperature of the lighting is between 5000 K and 6500 K. Some of the lights are switchable.

Due to the high electrical resistance of the 11 km long coax and fibre-optic tow cable on new RV Sonne, STROMER's full lighting could not be used, to reduce the vehicle's power consumption. That gets necessary at tow cable resistances above ~80 Ohm, to keep the electrical current and voltage drop on the tow cable within STROMER's system limits.

Two red laser pointers Kule Type 2 with 10 mW light power provided a scale at the ocean floor. The distance between both light dots is 0.33 m.

STROMER is equipped with three electrical Tecnydyne thrusters. Two model 1040 thrusters provide up to 50 kg thrust in forward/backward direction. One model 540 thruster provides 10 kg to turn STROMER. The thrusters can be operated from a STROMER computer. According software was provided by Tecnydyne. Controller is a joystick. Monitoring of the thrusters subsystem is also possible. Power and the control interface for the thrusters is provided by a BGR Thrusters Power and Control unit, which integrates Tecnydyne control components and an own power supply. The power supply is buffered by two deep sea batteries, providing power for about half an hour operation at full thrust. The batteries are recharged via STROMER's Deck Unit power supply. Control interface is RS-232. Only two thrusters could be used during SO-240. One thruster electronics got damaged due to a wrong wiring given in the documentation provided by Tecnydyne and limited testing possibilities on the vessel. Some wiring had to be done during the cruise, since most of the thrusters subsystem components came late for SO-240 shipping. Therefore, only both 1040 thrusters were used. The thrusters control setup was changed to also allow turning STROMER with the 1040 thrusters.

Moving STROMER worked as expected, but turning worked slightly coarse due to the two-thruster setup. STROMER can be turned while being towed on transect, enabling a better overview over the area using the forward direction camera. It is also possible to leave the tow track for a few 10 meters or to inspect a small area below the vessel being on station. If an interesting area is found, STROMER can be moved to that area and be holding on position, e. g. to take a photo or while it is settled down by the winch operator, e. g. to take a sample.

STROMER is equipped with an ECA HYTEC ARM 5E Mini manipulator arm, which enables basic sampling. It can be used to take small, solid objects, or also other materials, using a special tool. The arm's reach is 85 cm, the max. jaw opening is 16 cm. Lifting force is 25kg at full extension, jaw closing force is up to 50 kg. Sampling area is in STROMER's front. STORMER has to be settled at the ocean floor to take samples from the ocean floor. STROMER was not equipped with adequate sample containers for solid objects during SO-240. As best available sample containers, two gabions were installed. Light objects, such as manganese nodules, were flushed out of these gabions when STROMER moved down fast. Sampling itself worked well. But lifting STROMER from the ocean floor after sampling is a critical situation. The horizontal distance between vessel and STROMER has to be kept low, to avoid a horizontal movement of STROMER on/close to the ocean floor, which could result in a collision with an obstacle. It should not exceed 5 % of the vertical distance

During SO-240, STROMER was required to take water samples. Three 1.7 l Niskin “free flow” water collectors were installed in STROMER’s front, left side, in reach of the manipulator arm, which was used to release the water samplers. Water sampling worked very well, in the water column as well as settled at the floor.

To get the distance between STROMER and the ocean floor, a Teledyne Benthos PSA-916 sonar altimeter was installed. The PSA-916 has a maximum range of 100 m. Its RS-232 output was used, providing a resolution of 0.01m and a repetition rate of 5pps. An Imagenex 881A imaging sonar was installed for collision avoidance. The range was set to 60 m or 80 m. The 881A works at 675 kHz frequency at both ranges by default. The sector angle was set to 180°. The 881A has no attitude sensor, the sonar data is not attitude corrected.

The CTD (conductivity, temperature, depth) was a Sea-Bird SBE 19plus V2 with an additional oxygen sensor Sea-Bird SBE 43 and a WetLabs ECO FL(RT)D fluorometer installed. Both sensors are connected to analogue CTD inputs. The conductivity sensor has 0 to 9 S/m measurement range, 0.00005 S/m resolution in most oceanic waters and an accuracy of ~0.005 S/m. The temperature range is -5 to 35 °C with 0.0001 °C resolution and 0.0075 °C accuracy. The strain gauge pressure sensor has 7000 m range, 0.002 % of full scale resolution and should have ~0.2 % of full scale accuracy. The SBE 43 has a range of 120 % of surface saturation; the initial accuracy is 2 % of saturation. The ECO FL(RT)D has 0 to 125 µg/l range, the resolution is 0.0075 µg/l. A WetLabs ECO NTU(RT)D turbidity meter was also installed, connected to the CTD's RS-232 input. The measurement range is 0 to 125 NTU, the resolution is 0.0077 NTU.

During SO-240, three high-performance computers with additional interfaces and a special/according software setup were used to control STROMER’s components, to show and record video streams and other data as well as to record the deployment protocols. Additionally, a 40” television was used to show video streams. Video streams were shown and recorded using the Open Source software VLC media player (version 2.1.3). Videos were (re-)compressed using the efficient H.264/MPEG4 video codec, video container is AVI or Matroska (MKV).

The software Ocean Floor Observation Protocol (OFOP, version 3.3.4a) was used to record the station protocols. Beside the station protocol, OFOP also recorded the vessel DGPS (Differential Global Positioning System) positions and heading, the USBL data (STROMER’s positions and depths) as well as STROMER’s sonar altimeter and attitude data. Vessel positions, heading and time as well as the USBL data were provided through the vessel's Ethernet/IP system network. The vessel’s DGPS time was used as STROMER’s system time. It is UTC (Coordinated Universal Time). One STROMER computer is a NTP (Network Time Protocol) time server and shares this time through STROMER’s Ethernet/IP system network with NTP compatible components (e. g. the BGR online HD video cameras and SD video cameras). On the BGR Fotokamera mit Blitz still camera, the time has to be set manually, resulting in a slight deviation from STROMER’s system time.

The CTD data were displayed and recorded using the Sea-Bird software SeasaveV7 (version 7.21k), not covering the first/last few 10 metres when STROMER was not powered. The CTD data were also recorded to the CTD's internal storage. The CTD-recorded data also includes the first/last few meters.

Underwater positioning system

During all transects, except SO240-113STR, RV Sonne's iXBlue Posidonia 2 USBL (Ultra-Short BaseLine) acoustic positioning system was used. Transponder was a BGR's own, fully compatible iXBlue MT861S Posidonia transponder. The transponder was triggered acoustically, in Posidonia "transponder mode". According to the specifications, the Posidonia 2 system has a range of 10 km and an accuracy of 0.2 % of the slant distance. RV Sonne's Posidonia 2 did not work as well as expected. A high count of wrong distances and thus wrong positions were determined. The issue is under investigation by iXBlue. During SO240-113STR, BGR's own, portable iXBlue Posidonia 1 USBL system was used, to compare the performance between both Posidonia systems. It has 10 km range and 0.3 % of slant distance accuracy. An iXBlue Octans motion sensor is integrated in an assembly with the antenna, which can be used on different vessels without re-calibration. The antenna assembly was mounted in RV Sonne's port side moon pool, using an adapter plate brought by BGR. BGR's Posidonia 1 did not accept RV Sonne's DGPS messages as originally sent via RS-232. But it accepted these DGPS messages when re-framed using according software, matching the framing of the Octans messages, also sent via RS-232. That is most likely an iXBlue Posidonia Abyss software issue, under investigation by iXBlue. Except that issue, BGR's Posidonia 1 worked according to its specifications.

Vehicle connection and deployment on RV Sonne

STROMER was towed using RV Sonne's astern A-frame, due to the higher heave a disadvantageous tow point compared to midships. But RV Sonne's heave compensation worked very well, reducing the heave reaching STROMER via the tow cable to a few decimeters. Connecting STROMER to RV Sonne's tow cable worked well. Mechanical tow cable termination was a PMI Evergrip, STROMER's crow's foot could be connected directly. Electrical and fibre-optic termination was the same GISMA series 40, size 3, 6 receptacle as used by STROMER's telemetry, according connection cables were available on RV Sonne.

On-deck handling of STROMER worked well. RV Sonne provides a lot of working deck space as well as the necessary handling equipment. The A-frame is high enough to lift STROMER and buoyancy sufficient for a few meters tow cable and termination, mounted close to the tow cable termination. RV Sonne's crew is well trained to handle devices such as STROMER. RV Sonne's Data Center lab provides just enough space for STROMER's on-vessel components and the personnel necessary to operate STROMER. The winch's radio remote control used in the lab was battery powered. The winch operator lost winch control due to an empty or dropped out battery two times. That issue was improved by the vessel's crew providing a remote control power cable during the cruise.

7.5.3 General deployment strategy

The vessel sailed with a speed of about 1 kn along a pre-defined line, with the video sled being towed behind the vessel and held at about 3-4 m above the seafloor. The underwater positions of the video sled were calculated using a Posidonia USBL transponder installed on the sled. The accuracy of the underwater positioning is in the range of 1% of the water depth, i.e. around 30–50 m.

All data, including the photographs, were transmitted on-line via a fiber-optical cable to the onboard units and recorded there. The photographs could be inspected immediately after their recording which

considerably increased the quality of the on-line interpretation of the video survey. Due to the good functioning of the heave compensation of the new R/V Sonne, the video sled could be held at a constant distance of about 3 m to 4 m above the seafloor. Therefore, it was possible to automatically trigger the image recording to every 15 seconds. The image view and illumination remained relatively constant, thus considerably increasing the quality and the comparability of the images, which in turn are important prerequisites for the automatic analysis of each image using special software.

During each video transect, on-line monitoring of the seafloor was carried out by a geology and a biology expert. For this purpose, a number of pre-defined buttons representing different nodule sizes (< 4 cm long axis = small; > 4 cm = medium to large), different nodule abundances, areas without nodules, rock outcrops, pillow lavas, etc. as well as all major megafaunal groups such as brittle stars, sponges, holothurians, corals, etc., were installed using the software OFOP. For the characterization of the seafloor, the respective button had to be hit and a record was made into a data file containing UTC date and time, STROMER underwater position and the respective record. In addition to the description itself (i.e., the occurrence of rock outcrops, large nodules, brittle stars, sponges etc.), a numerical number was assigned to each record (1 for large nodules, 2 for medium nodules, etc.) which enabled plotting these records along the video transect using ArcGIS. Nodule fields are differentiated into fields with predominantly small nodules when their longest axis is smaller than ca. 4 cm and large nodules when the longest axis is larger than 4 cm (Fig. 7.5.3). This division is based on the general nodule size distribution in about 76 box cores from previous cruises (Rühlemann et al., 2014). Apart from the focus on Mn nodule fields, special attention was paid on the geology of seamount slopes, i.e., to focus on questions such as: (i) are these slopes characterized by bare-rocks free of sediments, (ii) is it possible to detect pathways for seawater entrance or discharge on seamount slopes, (iii) what are the characteristics of the transition zone from the base of seamount slopes to the sediment-covered abyssal plains, etc.

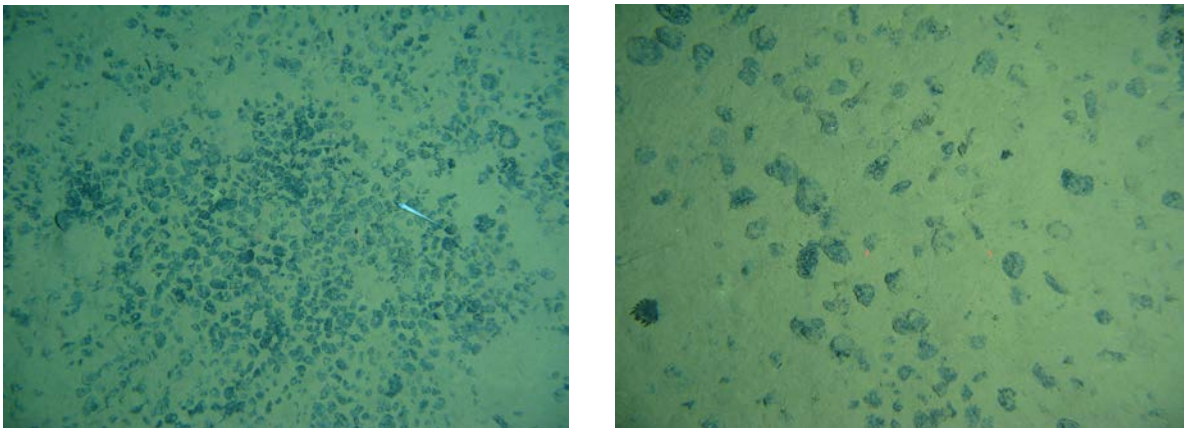


Figure 7.5.3. Seafloor images with predominantly small-sized (left; image 49STR-0824.jpg) and large-sized nodules (right; image 49STR-0676.jpg). The red laser dots are 30 cm apart and serve as scale. The images cover an area of approx. 3 m² (2 m x 1.5 m). They derive from station 49STR.

Table 7.5.1 summarizes all video tracks carried out during SO-240.

Table 7.5.1. Statistics of the MFT transects carried out during SO-240.

#	Station SO240-	Position on bottom		Water depth [m]	Duration ¹ (hrs: min)	Length ² (m)	Number of pictures ³
		Latitude (N)	Longitude (W)				
1	06STR						
	Start	13° 10.060'	118° 04.858'	4024	1:30	--	System Test
	End	13° 10.060	118° 04.560'	4075			
2	13STR						
	Start	13° 09.441'	118° 12.985'	3725	8:36	6500	1553
	End	13° 10.519'	118°09.751'	4313			
3	28STR						
	Start	13° 10.007'	118° 04.869'	4035	8:48	7100	1496
	End	13° 10.527'	118° 08.936'	4298			
4	40STR						
	Start	13° 02.020'	118° 26.744	3712	2:54	1500	460
	End	13° 02.912'	118° 26.515'	3718			
5	41STR						
	Start	12° 56.018'	118° 26.157'	3884	9:00	8400	1431
	End	12° 51.978'	118° 24.180'	4275			
6	49STR						
	Start	12° 51.980'	118° 24.170'	4273	8:24	5200	1440
	End	12° 49.056'	118° 23.374'	4292			
7	113STR						
	Start	13° 11.453'	118° 05.231'	4222	4:08	2100	687
	End	13° 10.723	118° 05.216'	4161			
Total					43:20	30800	7067

¹: From the start to the end of bottom view; ²: length of straight line along transect; ³: all seafloor images taken manually with the HD still camera during bottom view

7.5.4 Shipboard results

7.5.4.1 Working area 1: Transects SO240-13STR, SO240-28STR, and SO240-113STR

Transects 13STR, 28STR and 113STR were carried out in working area 1 (WA-1). During stations 13STR and 28STR, seamount slopes and their immediate vicinity were investigated, whereas station 113STR was designed to especially analyze the transition from the lower seamount flank to the sediment-covered abyssal plain (Fig. 7.5.4). The latter station was close to the location where the highest heat flow values ($>180 \text{ mW/m}^2$) were measured during this cruise (see Figs. 6.3 and 6.7). In order to calibrate the seafloor images with respect to Mn nodule size distribution and coverage, box core deployments were carried out along some of the video transects (Fig. 7.5.4).

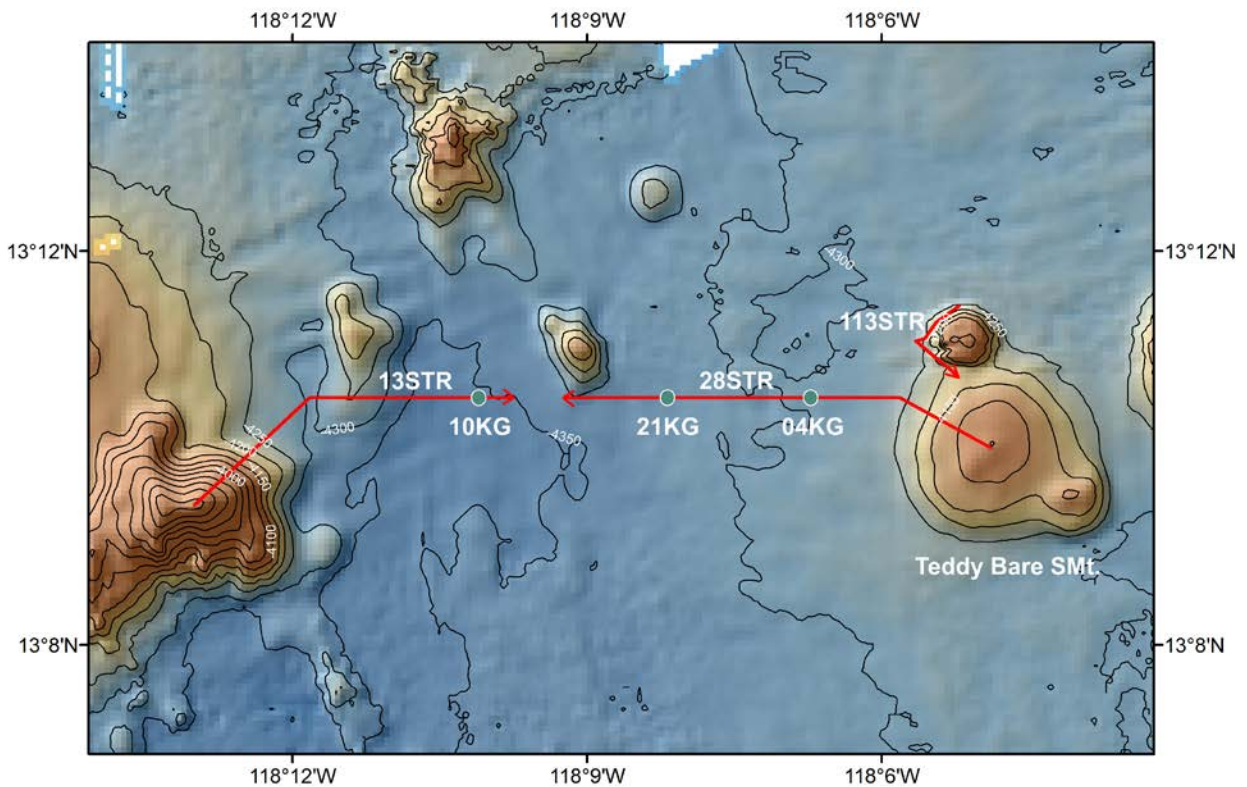


Figure 7.5.4. Location of video stations in working area 1. The abbreviation STR stands for STROMER (simple diving robot modularly extendable). The arrows mark the direction of movement during each station. The box core stations (04, 10, 21KG) were used for the calibration of the underwater images with respect to the Mn nodule size distribution and nodule coverage. Teddy Bare Seamount was named due to its topographic features.

Station SO240-13STR

This transect started on top of a prominent seamount in WA-1 (“western seamount”) in 3725 m water depth, followed the seamount slope to the northeast until it reached the sediment-covered abyssal plain, where it turned eastwards into a large basin. The station ended in the western part of this basin in 4313 m water depth (Fig. 7.5.4).

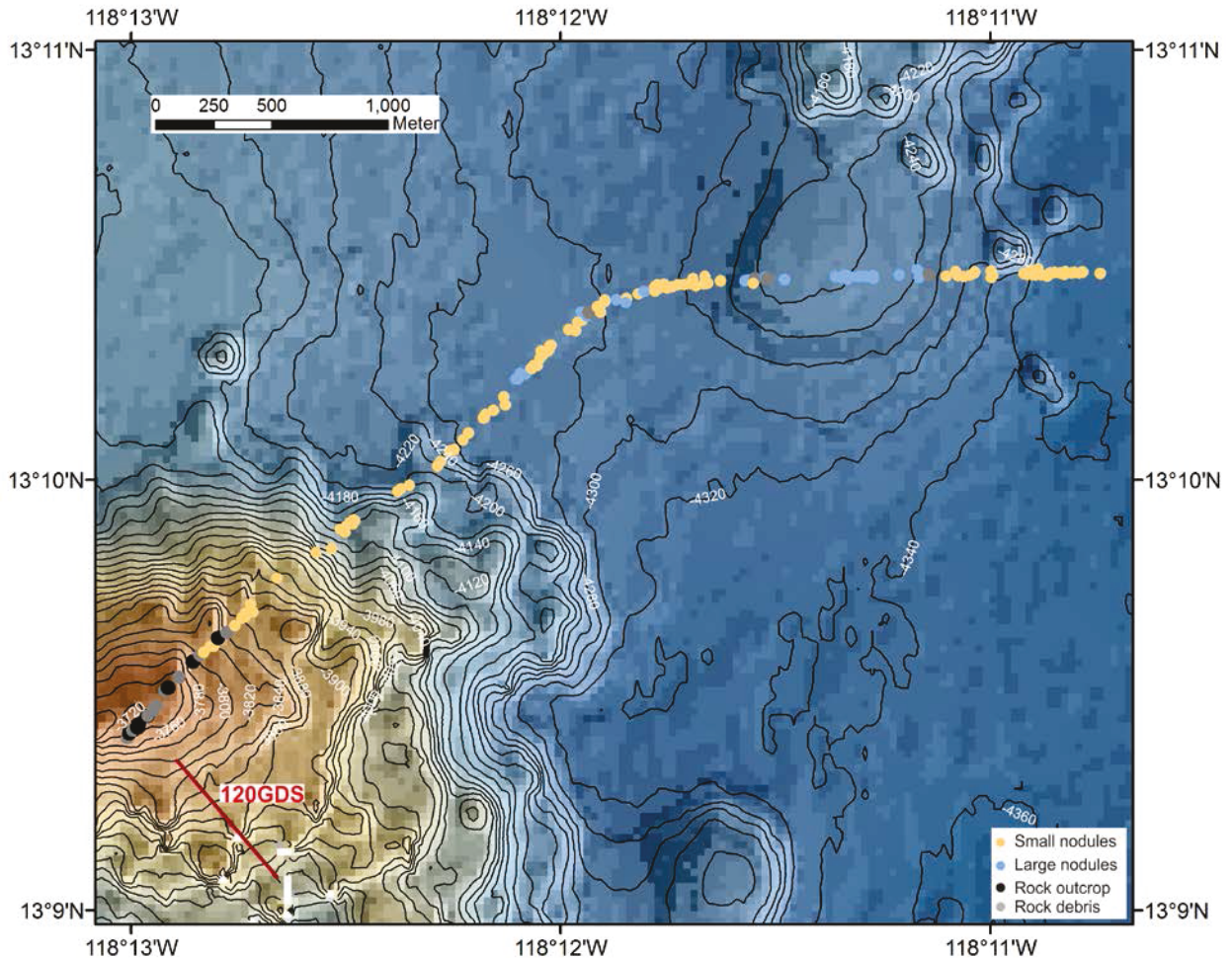


Figure 7.5.5. “En route” interpretation of the seafloor geology during station 13STR plotted onto the 30 m-gridded bathymetric data recorded during SO-240. Note the high resolution of the bathymetry revealing many more details compared to previous data (see Fig. 7.5.4). Station 120GDS is a dredge station.

The “Western Seamount” rises more than 600 m above the central basin of WA-1 (Fig. 7.5.5). The seamount slopes consist of steep cliffs and terraces. The cliffs are made up of massive pillow flows, whereas pillow debris gathers at the base of each cliff. The terraces are sediment-covered and small-sized Mn nodules with high coverage are found on the sediment surface (Fig. 7.5.5 and 7.5.6). A dredge station on the southwest slope of this seamount revealed that massive ferromanganese crusts cover the pillow flows.

Thicker sediment cover is only found in regions where the seamount slope reduces to about 10°, which is in about 4200 m water depth. The transition from the almost sediment-free steep slope to the flat, sediment-covered abyssal plain with its typical Mn nodule coverage is only a narrow zone without special

characteristics. The sediment-covered plain in the immediate surroundings of the seamount is characterized by the occurrence of many small-sized nodules. About 700 m to the northeast of the lower base of the seamount slope, some very large Mn nodules (up to 15 cm in diameter; Fig. 7.5.8) occur, but small-sized nodules predominate until the track crosses a N-S oriented ridge. Outcropping rocks form cliffs at the edges of the ridge. The top of the ridge is flat and about 80 m higher than the surrounding seafloor. Large-sized Mn nodules occur on top of the ridge. The ridge itself is the southern prolongation of a larger seamount rising about 200 m above the surrounding seafloor (Fig. 7.5.4).

The final eastern part of this video profile ends in a basin which forms the central part of WA-1 (Figs. 7.5.4 and 6.2). Small-sized nodules with high coverage lie on top of the sediments just east of the ridge, followed by a several hundreds of meters wide zone which is almost devoid of nodules (Fig. 7.5.5). Large-sized nodules with low coverage start to dominate the seafloor towards the end of the track. In this part of the transect, box core station SO240-10KG shows that 80% of the nodules are larger than 4 cm in diameter (Fig. 7.5.5; Appendix). This is in good agreement with the optical observations of the seafloor.

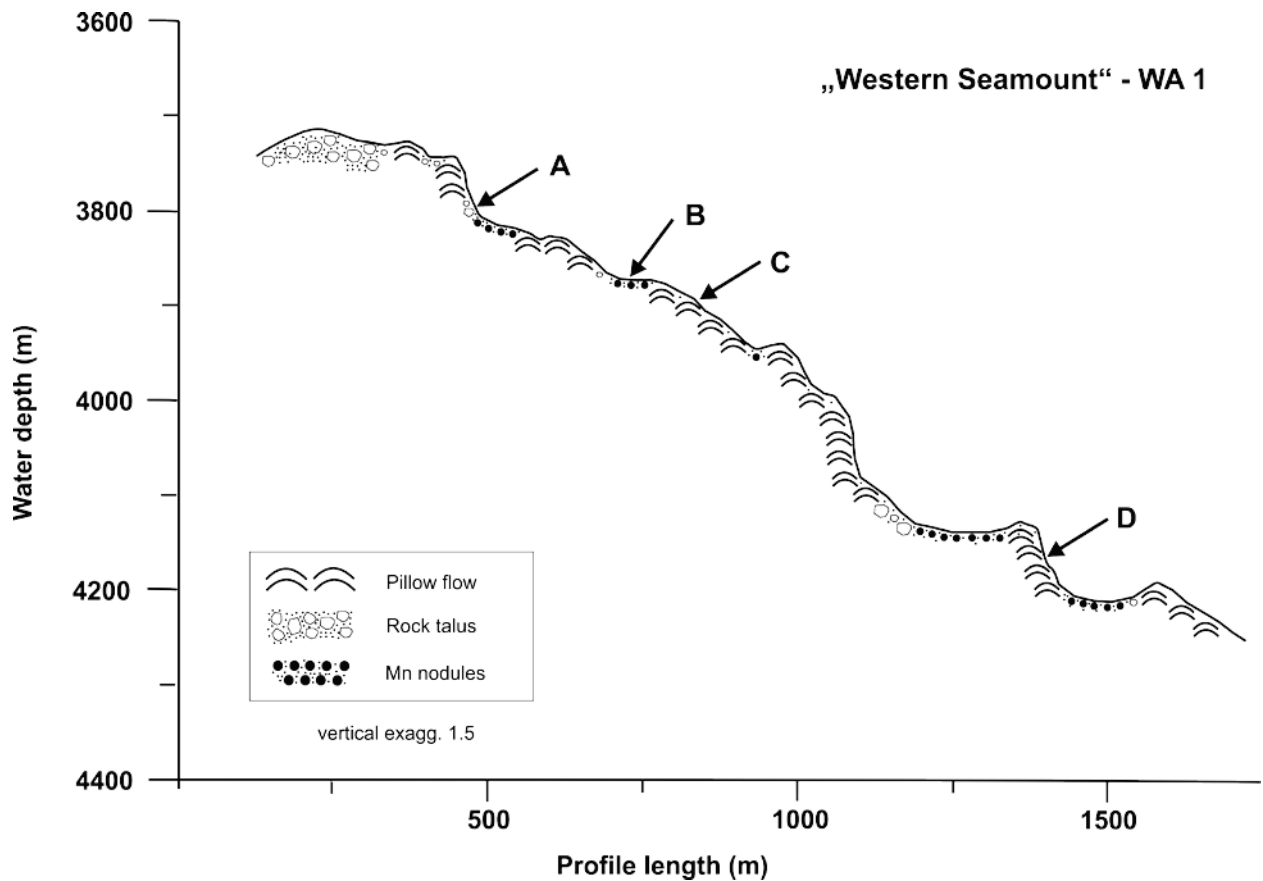


Figure 7.5.6. Profile along the northeastern seamount slope along station 13STR (see Fig. 7.5.5) and its geological interpretation based on seafloor images. Vertical exaggeration: 1.5×. The letters indicate the positions of seafloor pictures as presented in Fig. 7.5.7.

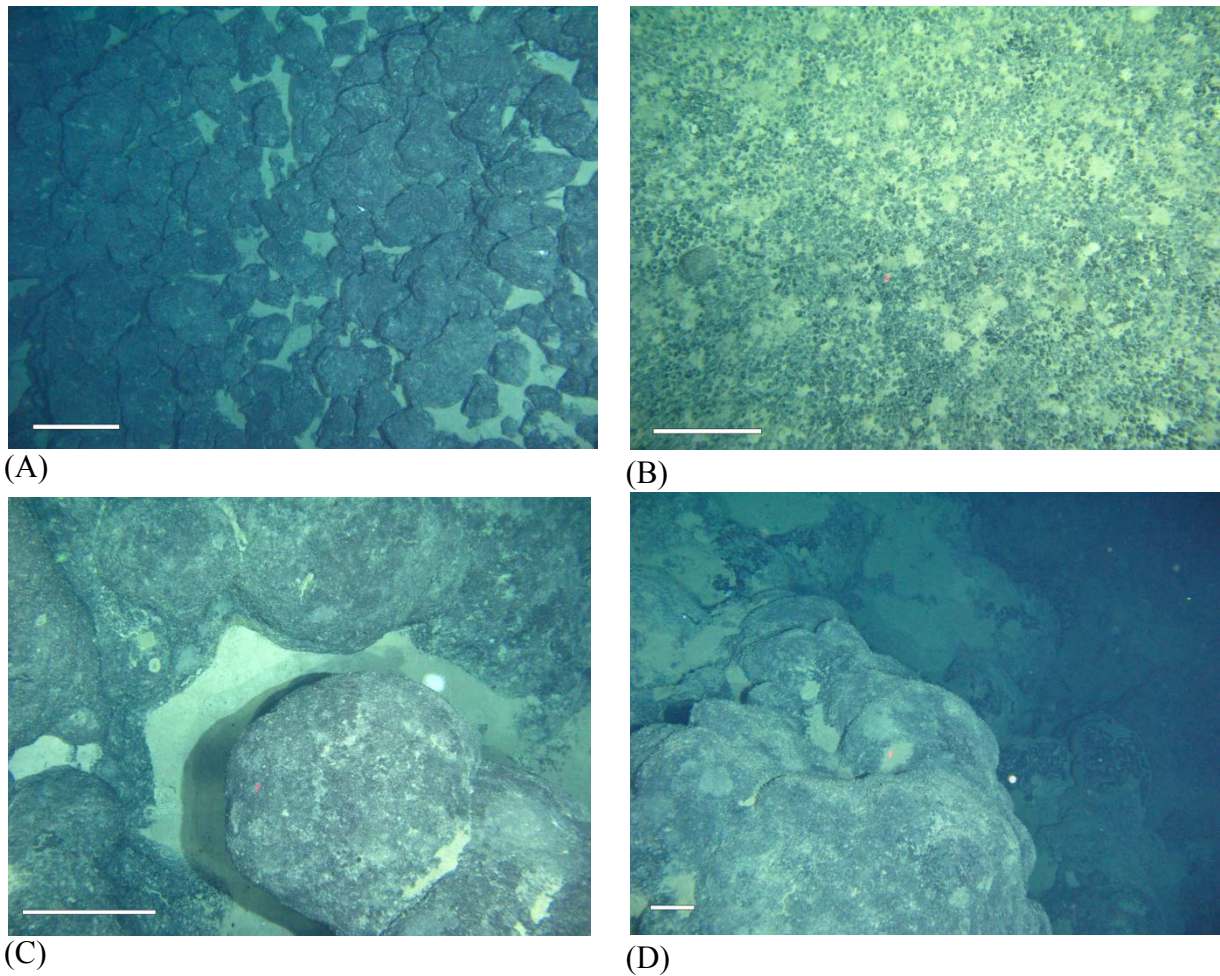


Figure 7.5.7. Underwater images from the slope of the „Western Seamount”(station 13STR) of working area 1: (A) rock talus at the foot of a cliff, (B) small-sized Mn nodules on plateaus, (C) large pillows, (D) massive pillow flows forming a cliff. Scale bar: 30 cm. Positions of the images in relation to seamount topography are shown in figure 7.5.6.

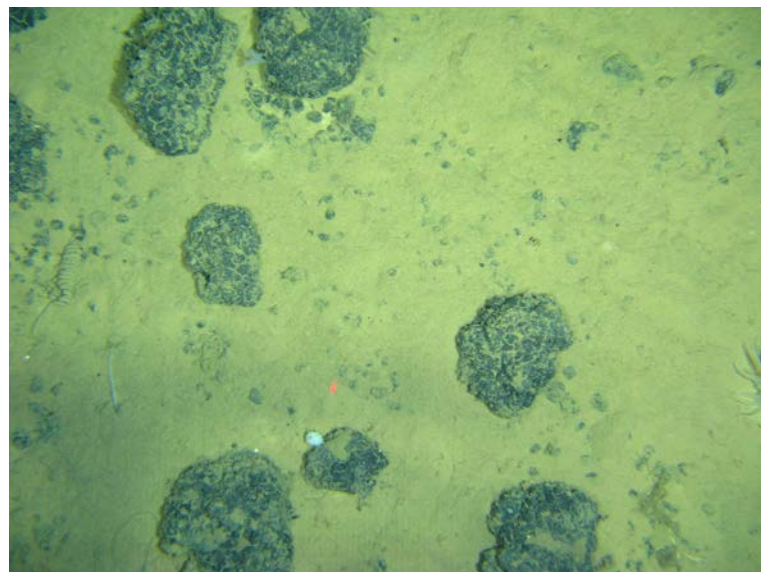


Figure 7.5.8. Large manganese nodules occur about 700 m northeast of the base of the seamount slope along station 13STR (see Fig. 7.5.5). The length of the image represents about 1 m.

Station SO240-28STR

Station 28STR started on top of the so-called Teddy Bare Seamount in 4035 m water depth, following a northwest direction down the slope of the seamount and turning westwards at the base of the slope. The transect ended about 5 km west of the Teddy Bare Seamount in the middle of the basin forming WA-1 (Figs. 7.5.4 and 7.5.9).

Teddy Bare Seamount rises about 220 m above its surroundings from 4260 m to 4040 m and has an almost circular base with a diameter of ca. 3.5 km. On the northwest, west and southwest seamount slopes there is a terrace between 4140 m and 4120 m. A SW-NE oriented ridge forms the top 80 m of the seamount (Fig. 7.5.9).

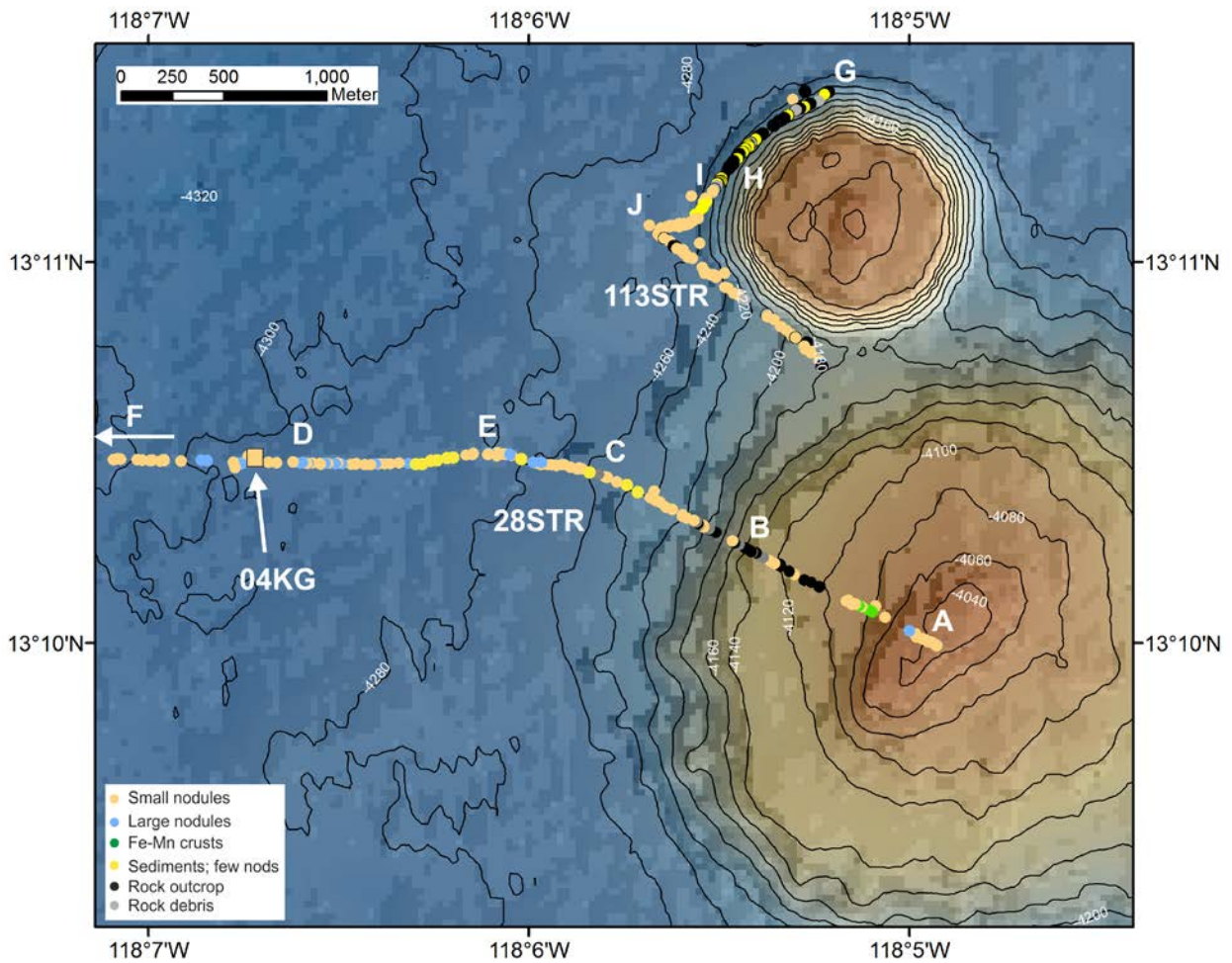


Figure 7.5.9. “En route” interpretation of the seafloor geology during stations 28STR and 113STR plotted onto the 30-m-gridded bathymetric data recorded during SO-240. Station 04KG is a box core station. The yellow color indicates that small-sized nodules dominate in this box core, which is consistent with the seafloor observations at this position. Letters mark the positions of the images presented in Figs. 7.5.10 and 7.5.12. The large seamount is the Teddy Bare Smt.

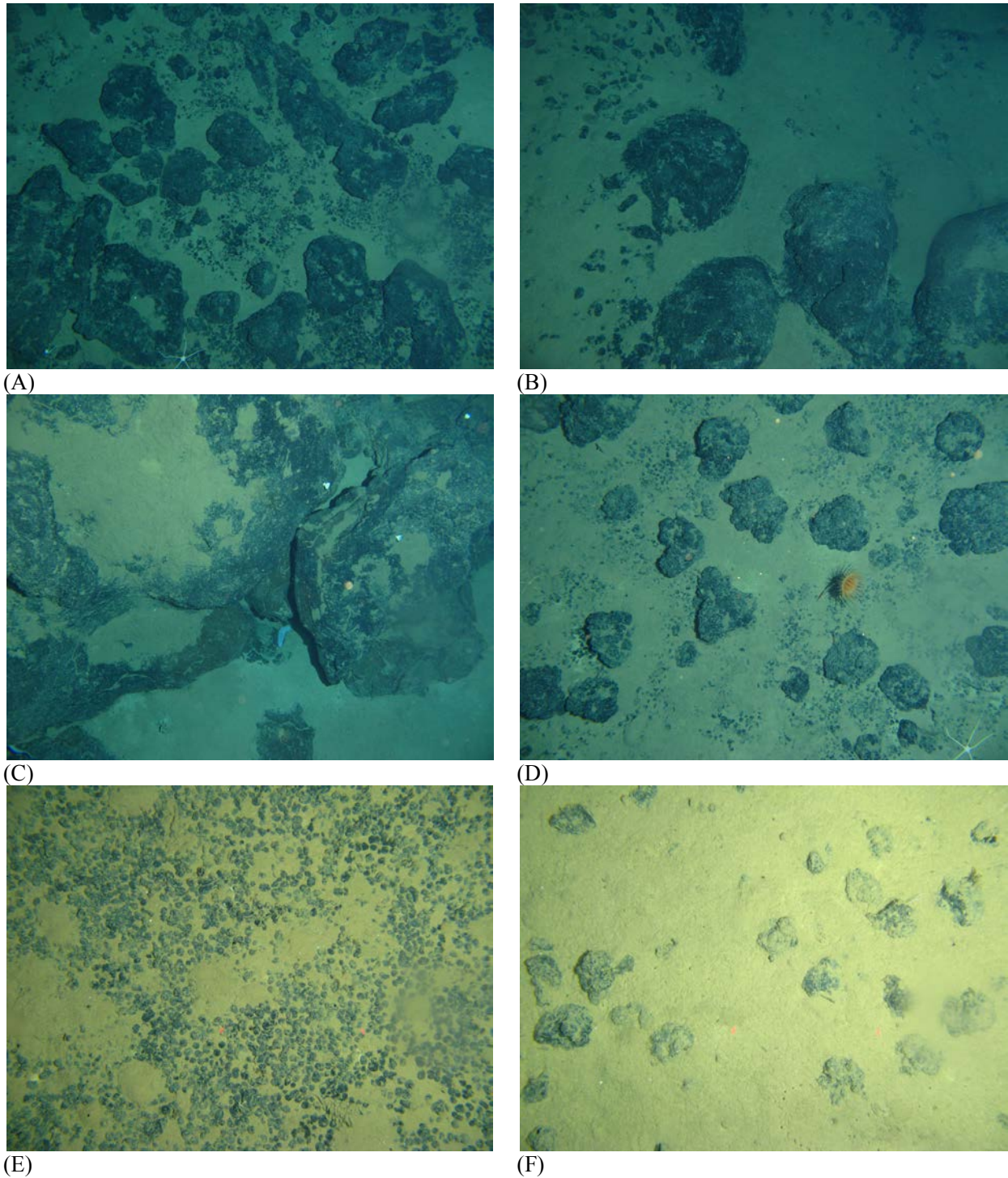


Figure 7.5.10. Underwater images along video transect SO240-28STR. For the positions of the images, see figure 7.5.9. A: Rock pieces covered with Fe-Mn crusts on top of Teddy Bare Seamount; B: Pillow basalts on steep slopes; C: Transition from the seamount slope to the surrounding sediment-covered plain, rocks seem to have an alteration rim (brownish color); D: unusual large Mn nodules; E: typical small-sized nodules; F: typical large-sized nodules at the end of this transect (Fig. 7.5.4). Lengths of images represent about 1 m.

The steeper slopes of Teddy Bare Smt. are comprised of outcropping flows of pillow basalts (Fig. 7.5.10B). The terrace is sediment-covered with a high abundance of small-sized nodules. Outcropping rocks at the transition from the seamount base to the flat sediment-covered plain seem to show some alteration rims (Fig. 7.5.10C). The sediments of the immediate surroundings are characterized by a high coverage with small-sized Mn nodules (Fig. 7.5.10E). However, there are at least three zones within the

first 2000 m off the seamount in which very large Mn nodules (up to approx. 15 cm diameter) occur together with small-sized nodules. These zones are some tens of meters wide and they do not appear further to the west of the seamount. We suspect that these large nodules may be rock pieces covered by Fe-Mn crusts, and that the sediment cover in these zones is very thin. Parasound records indicate that this area might be affected by slumping from Teddy Bare Smt. (see Chapter 7.1; Rühlemann et al., 2012).

Further to the west of station 04KG, the small-sized nodules are replaced by medium to large-sized nodules (Fig. 7.5.8E, F) as are typical for this part of the CCZ (Kuhn et al., 2012). There is consistency between the visual observation of the seafloor and the results from box core sampling with respect to nodule size distribution and nodule coverage (Fig. 7.5.9).

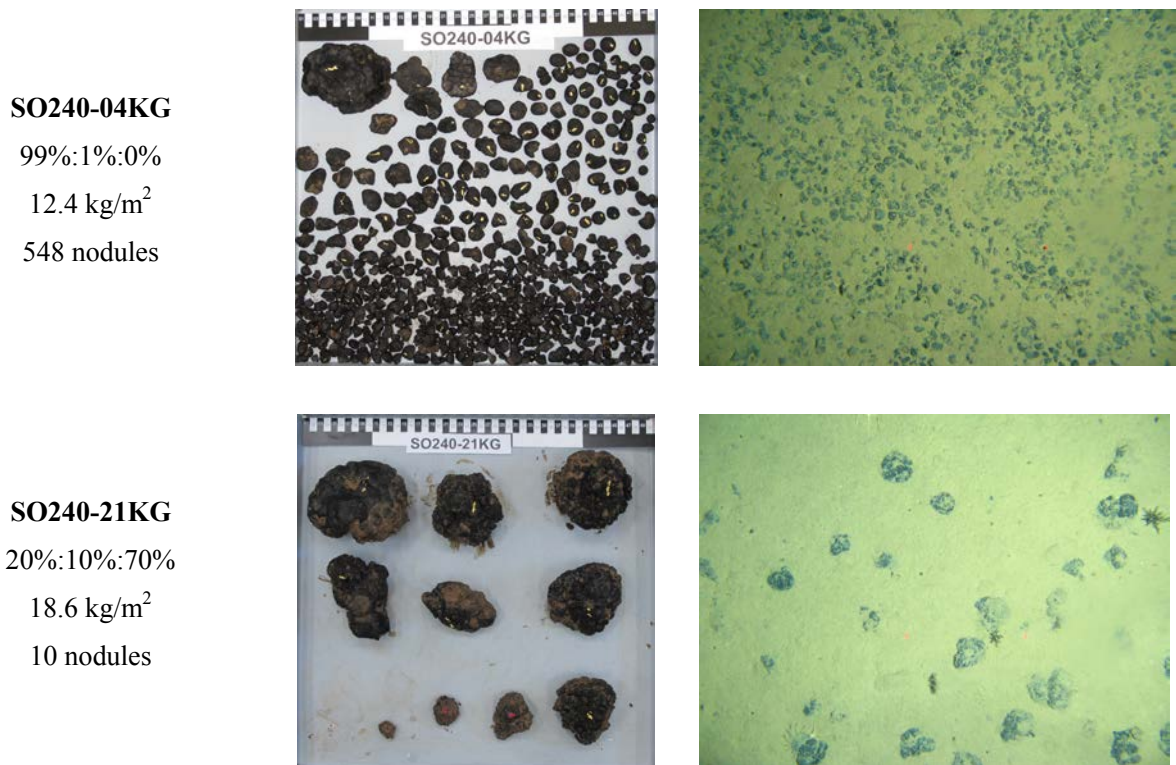


Figure 7.5.11. Comparison between nodules from box core stations and seafloor images taken close to the box core stations along 28STR. The percentage numbers on the left side reflect the frequency ratio between small (< 4 cm), medium (4-8 cm), and large (> 8 cm) nodules. The total number of nodules refers to the box core surface (upper 10 cm) as does the nodule abundance (wet weight). Laser points in seafloor images are ~ 30 cm apart.

Station SO240-113STR

Video transect 113STR was obtained along the western slope base of a small seamount satellite to the north of Teddy Bare Smt. (Figs. 7.5.4, 7.5.5, 7.5.9). This area was chosen as the highest heat flow values measured during this cruise were obtained here (see Chapter 7.1, heat flow results). The station started on the northern slope, followed the 4200 m contour line along the western slope, moved 280 m to the west of this contour line to the westernmost point of this transect, and then turned to the southeast towards the saddle between the satellite and Teddy Bare Smt., where the station ended in 4161 m water depth. Three near-bottom water samples and one rock sample were taken at the end of the station (at 118°05.22'W; 13°10.73'N; 4160 m).

Outcropping rocks (lava flows) were encountered on the NW side of the seamount (Fig. 7.5.12G, H). The transition to the sediment-covered plain occurring on the 4240 m contour line was unremarkable. The sediment-covered plain has a high coverage with small-sized Mn nodules. Towards the saddle between the satellite and Teddy Bare Smt., a combination of rock debris, outcropping rocks and sediments appeared. There was no indication of any fluid recharge or discharge or any other unusual characteristic.

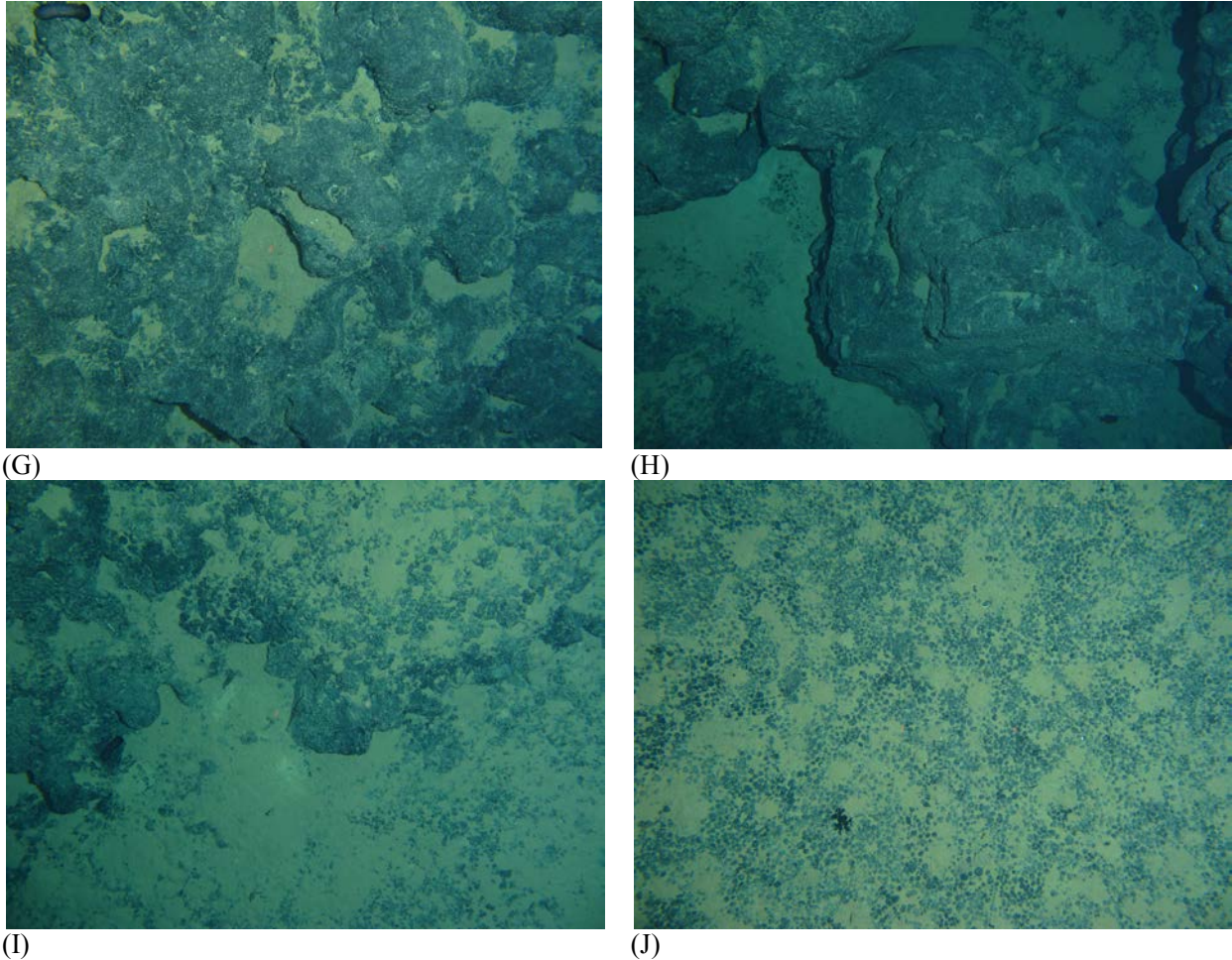


Figure 7.5.12. Underwater images along video transect SO240-113STR. For the positions of the images see figure 7.5.9. G: Rock outcrop probably covered with Fe-Mn crusts; H: Massive block lava; I: Transition between seamount slope and surrounding sediment-covered plain; J: typical small-sized nodules. The length of each image represents about 1.5 m.

7.5.4.2 Working area 2: Transects SO240-40STR, SO240-41STR, and SO240-49STR

Transects 40STR, 41STR and 49STR were carried out in working area 2 (WA-2; Fig. 7.5.13). The objective of station 40STR was to investigate a seamount crater/caldera, as these structures typically characterize many small-sized seamounts in the working area and may act as recharge sites for seawater. Station 41STR started on a seamount top and followed the slope to the south into the sediment-covered plain surrounding the seamount. Transect 49STR is the continuation of 41STR. Small basins with increased heat flow were crossed and investigated during this station. In contrast to the situation at Teddy Bare Smt. in WA-1, where heat flow increased towards the seamount, heat flow significantly decreased towards the seamount where station 41STR started, indicating that recharge of seawater may occur at the seamount. Special attention was therefore, paid to the transition between the seamount and the abyssal plain during transect 41STR.

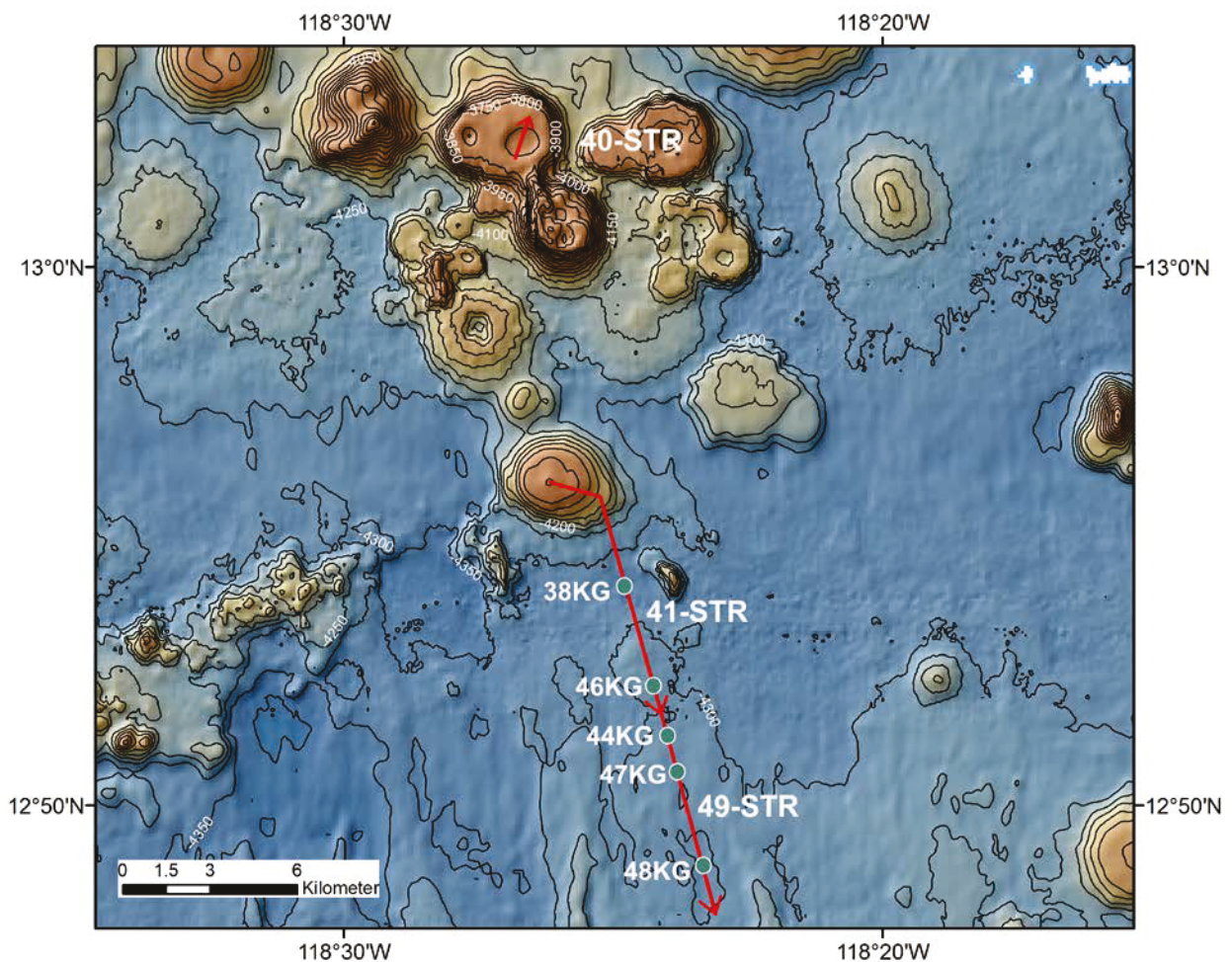


Figure 7.5.13. Locations of video stations in working area 2. The abbreviation STR stands for STROMER (simple diving robot modularly extendable). The arrows mark the direction of movement during each station. The box core stations (38, 44, 46, 47, 48KG) were used for the calibration of the underwater images with respect to the Mn nodule size distribution and nodule coverage. Bathymetry is from previous cruises (120 m grid; Rühlemann et al., 2011).

Station SO240-40STR

This station started on the flat edge of a typical small-sized seamount in the working area. The seamount has an elliptically-shaped base with a diameter of 4.6 km (E-W) and 3.5 km (N-S), rising steeply about 300 m above the surrounding seafloor with slope angles between 25° and 45° . The top is formed by a plateau between 3740 m and 3720 m water depth. This plateau is flat with slope angles between 0° and about 5° . There are two crater-like structures: one larger one in the east with a diameter of 1.1 – 1.3 km and a depth of 80 m, and one smaller one in the west, with a diameter of ca. 500 m and a similar depth (Fig. 7.5.14). The walls of these craters are just as steep as the outer flanks of the seamount, and the crater foot is as flat as the seamount top. There are more than 100 seamounts of the same size in the eastern German license area, having the same crater-like depressions surrounded by the same “rasor-cut” plateau. It is not clear how these structures formed. One possible explanation is that the magma chamber was emptied during eruption and the walls of the submarine volcano collapsed, forming the crater. However, why do most of these seamounts possess a “rasor-cut” plateau and why do they almost have the same dimensions?

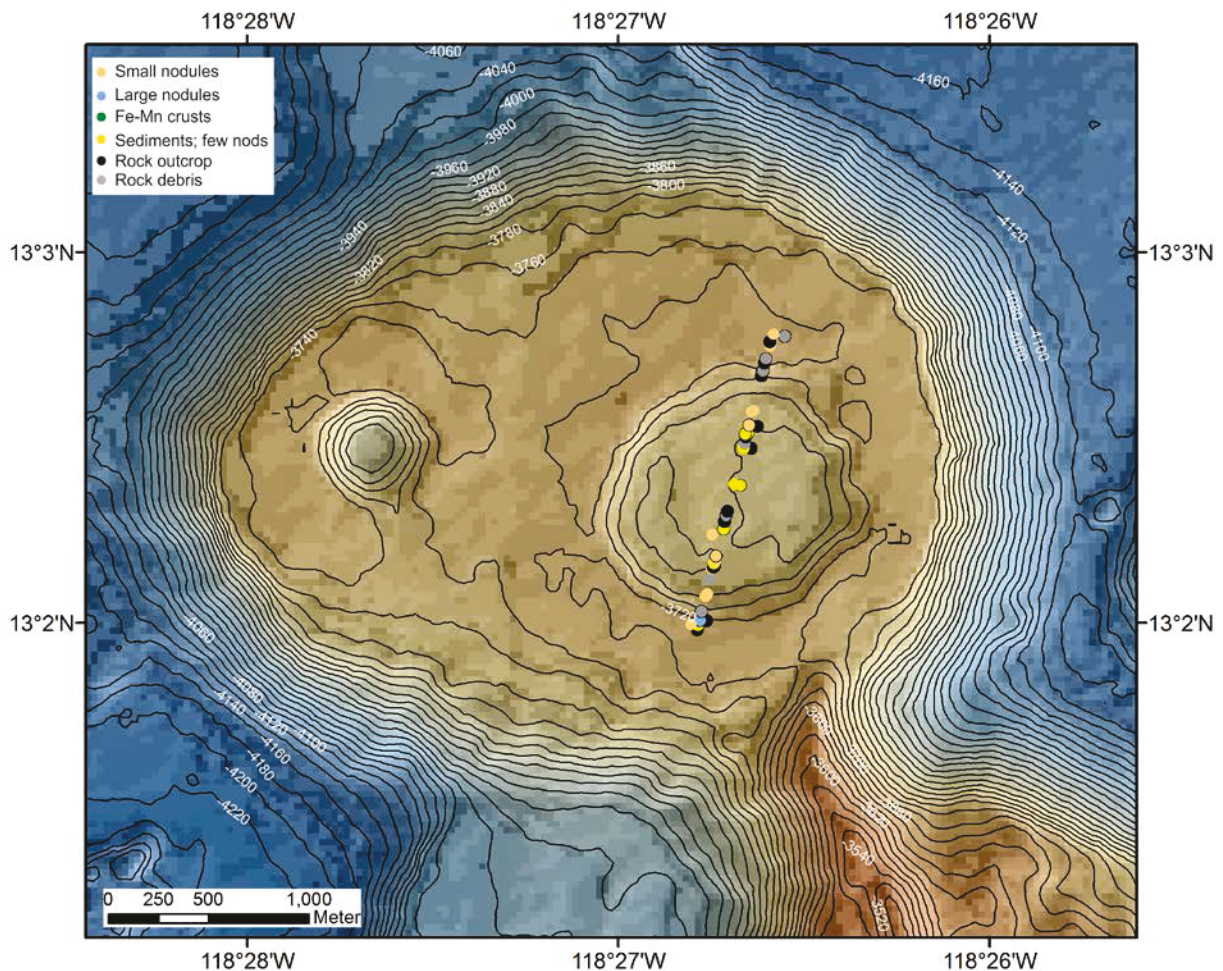


Figure 7.5.14. “En route” interpretation of the seafloor geology of the “Donut Seamount” during station 40STR plotted onto the 30 m-gridded bathymetric data recorded during SO-240.

In order to try to shed some light on this question, a video station was taken over this structure. Strikingly, there is not much talus (coarse-grained rock debris) in the crater/caldera. The southern wall consists of a succession of pillow flows and some talus at the bases of almost vertical cliffs where the slope decreases slightly. At the lower part of the southern wall, the seafloor is covered by small-sized Mn nodules of large coverage (Fig. 7.5.15, 7.5.16A). The crater/caldera floor is densely covered by Mn nodules in this southern part, followed by outcropping lava flow (Fig. 7.5.16B). Further to the north, sediments and fine-grained talus material dominate, and Mn nodules occur with variable coverage. These nodules are always small-sized and probably of hydrogenetic origin. Unfortunately it was not possible to sample them.

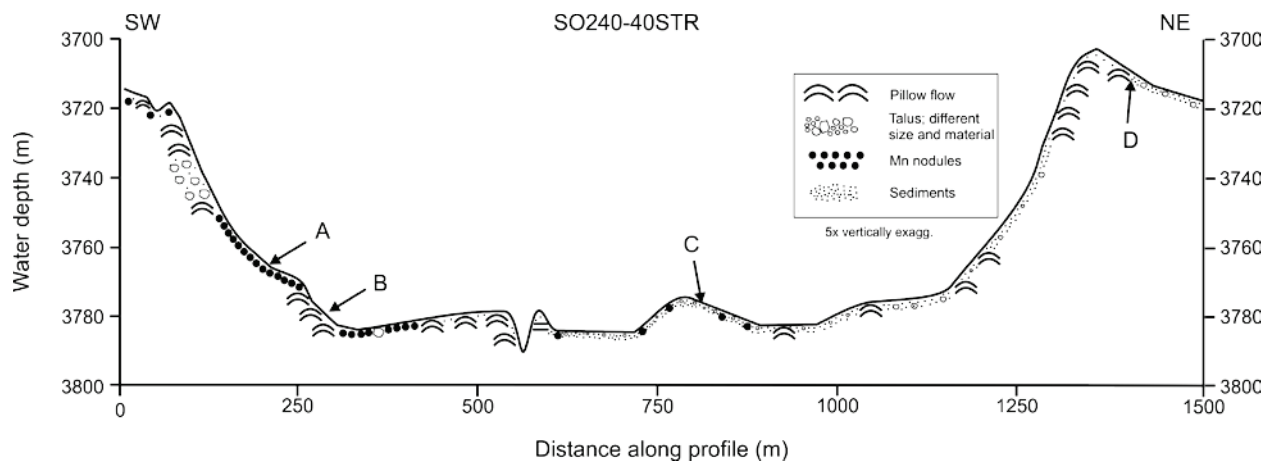


Figure 7.5.15. Profile over the crater/caldera structure of the “Donut Seamount” along station 40STR (see Fig. 7.5.14 for location) and its geological interpretation based on seafloor images. Vertical exaggeration: 5×. The letters indicate the positions of the seafloor images presented in figure 7.5.16.

The northern wall is less steep and mainly consists of fine-grained talus. Outcropping, massive lava flows were only mapped on the upper wall where it becomes steeper and sediment-free. Almost no Mn nodules occur on the northern wall. We suspect that a massive land slide occurred on this northern wall, reducing the lower slope angle and the increasing the amount of fine-grained talus material. Almost perfect circular structures were observed in large numbers on the seafloor within the crater (Fig. 7.5.16C). They may have been caused by the activity of benthic organisms.

The fact that there is no coarse-grained rock talus but abundant fine-grained talus may either indicate that the coarse material has already been eroded (the volcanoes were assumedly formed on the East Pacific Rise, i.e. are about 20 Mio. years old) or suggests that there never has been much talus in the crater, which contradicts the theory that the crater formed as a collapse structure. Unfortunately, it was not possible to obtain good Parasound data (for sediment thickness) from inside the crater, as the structure appears to be too small and there are too many side echoes from the crater walls.

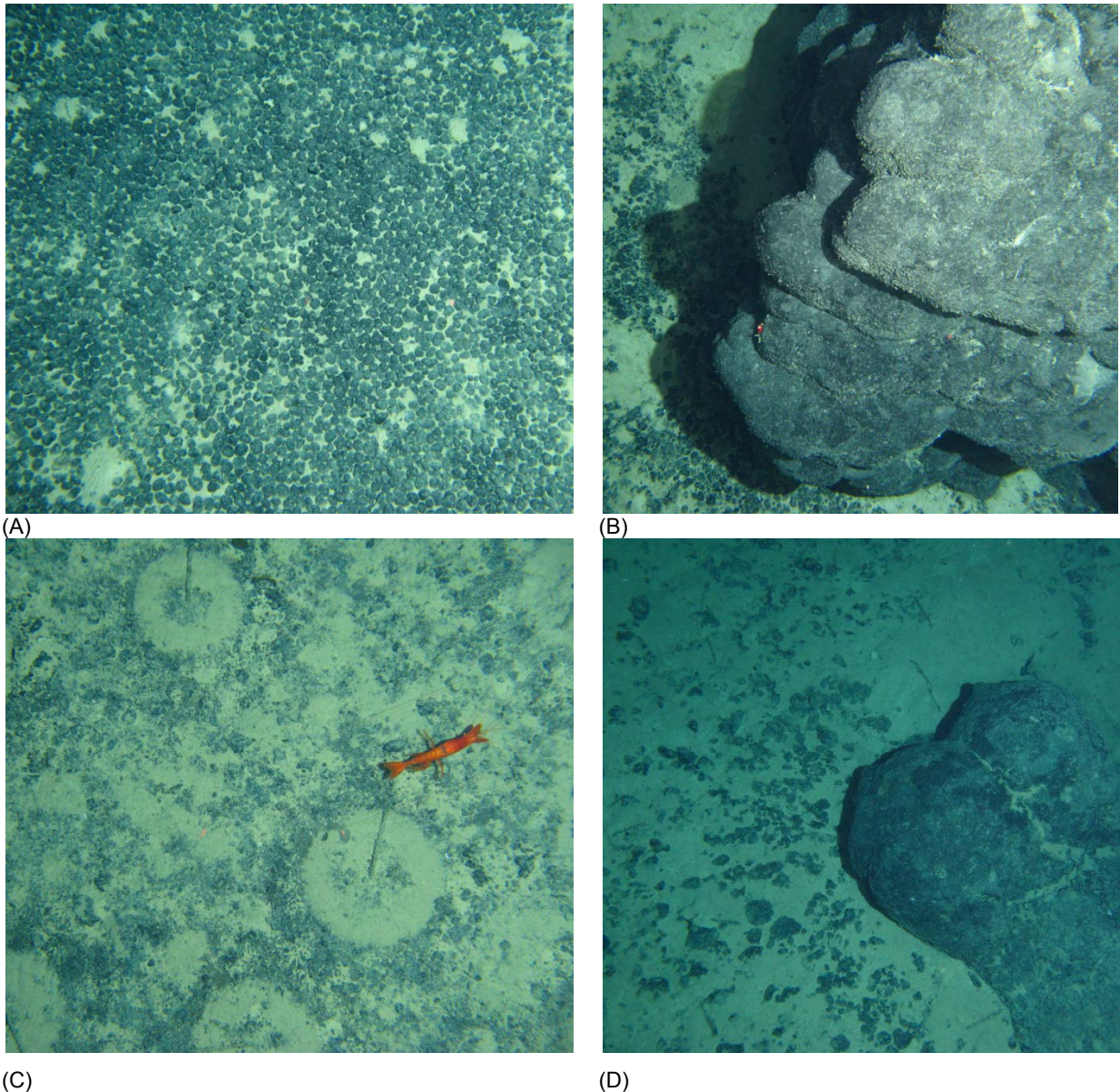


Figure 7.5.16. Seafloor photographs taken from inside the crater during station SO240-40STR. (A) Mn nodule field with high coverage. (B) Massive lava flows on crater floor. (C) Fine-grained talus, sediment, few small Mn nodules, and a shrimp. The circular structures may be caused by benthic organisms. (D) crust-like talus material close to pillow flow. Laser points as scale (approx. 30 cm).

Stations SO240 -41STR and 49STR

Video transects 41STR and 49STR were combined as station 49STR represents the southern prolongation of station 41STR (Figs. 7.5.13, 7.5.17). The former started in 3900 m water depth on top of a seamount that marks the southern edge of a group of seamounts (Fig. 7.5.13). The transect followed the east-southeast slope of this seamount down to about 4050 m water depth, where it turned south-southeastwards. The station ended in about 4300 m water depth about 14 km SSE of the foot of the seamount.

This area was chosen for detailed inspection for several reasons: (1) The seamount could be a typical recharge area, supported by heat flow data from areas close to the seamount; (2) The transect runs parallel to the main structural features of the sediment-covered basin. If fluid flow takes place in the basaltic crust

then it should follow this structural orientation; (3) The video profile covers at least three small basins which were assumed to be hydrothermal pits, i.e., formed by dissolution of carbonate layers at depth by hydrothermal solutions. (4) Last but not least, the backscatter data from the EM 120 swath echosounder suggest that both small-sized and large sized manganese nodules occur along this transect.

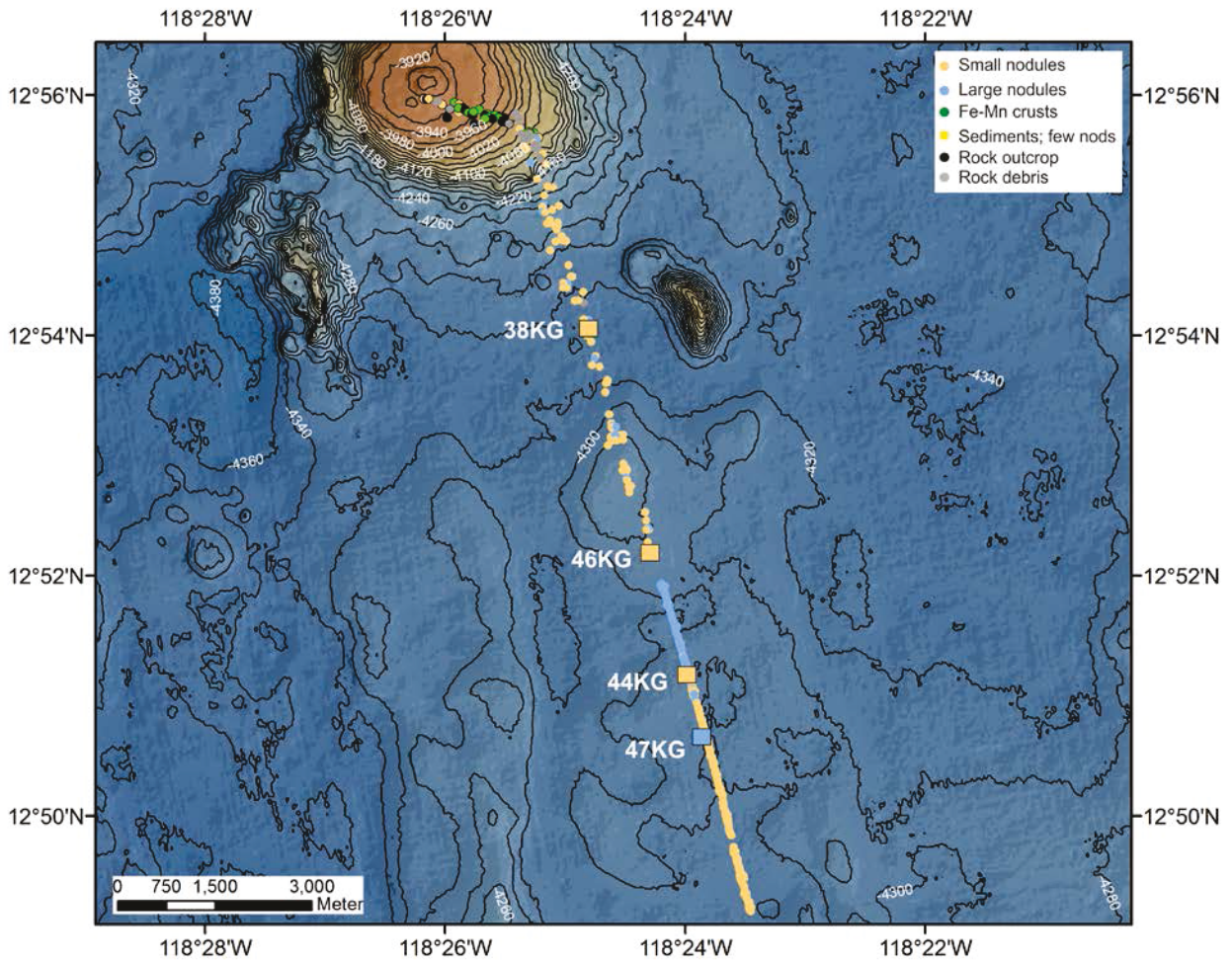


Figure 7.5.17. “En route” interpretation of the seafloor geology along stations 41STR and 49STR plotted onto the 30 m-gridded bathymetric data recorded during SO-240. Box core stations obtained along these video profiles are also shown. Yellow color indicates the dominance of small-sized nodules (< 4 cm diameter) and blue color indicates the dominance of large-sized nodules (> 4 cm).

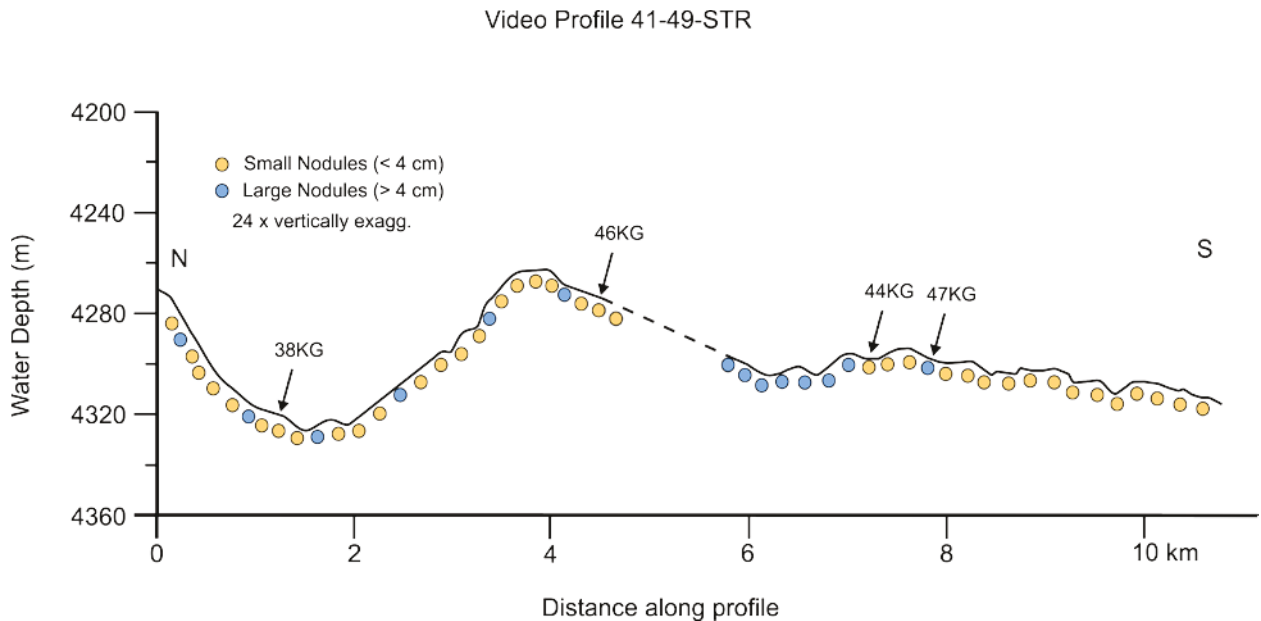


Figure 7.5.18. Profile along stations 41STR and 49STR (see Fig. 7.5.17 for location) and its geological interpretation based on seafloor images. Vertical exaggeration: 24 \times .

The seamount is a flat-topped cone rising about 250 m above its surroundings. The flat top is about 1.5 km in diameter and is composed of outcropping rocks, pillow flows and rock debris (Fig. 7.5.19). Close to the edge, Fe-Mn crusts cover the rocks (Fig. 7.5.19A). Small-sized manganese nodules occur at some sites on the flat top. The flank of the seamount is mainly composed of pillow flows of different thickness and degree of erosion (Fig. 7.5.19B). At some locations, sheet flows with distinct flow textures also occur. A giant sponge was found at one site (Fig. 7.5.19C). Manganese nodules start to dominate in the southern turn of the transect at about 4050 m water depth (Fig. 7.5.19D). Small-sized nodules mainly cover the basin which surrounds the southern flank of the seamount. This basin is about 4 km wide (in N-S direction) and 50 m deep (Fig. 7.5.18) and may have been formed by the erosion of sediments due to increased activity of near-bottom currents. Medium to large-sized nodules irregularly occur in the basin, outcropping pillow lavas appear at one site (Fig. 7.5.18).

A slight elevation occurs further to the south which is mainly covered by small-sized nodules. The northern boundary of this elevation is marked by rather steep faults reaching from the basaltic crust to the sediment-covered seafloor (see Chapter 7.1). Further south there is a succession of small basins of different size (a few hundreds to ~2000 m in N-S direction) and 10 – 20 m depth. These basins have higher heat flow values compared to their surroundings and, therefore, may have been sites of upwelling fluids in the past (see Chapter 7.1). The northernmost basin contains medium to large-sized nodules (Figs. 7.5.17, 7.5.20) whereas further to the south, small-sized and medium-sized nodules appear in similar amounts (Figs. 7.5.17, 7.5.20).

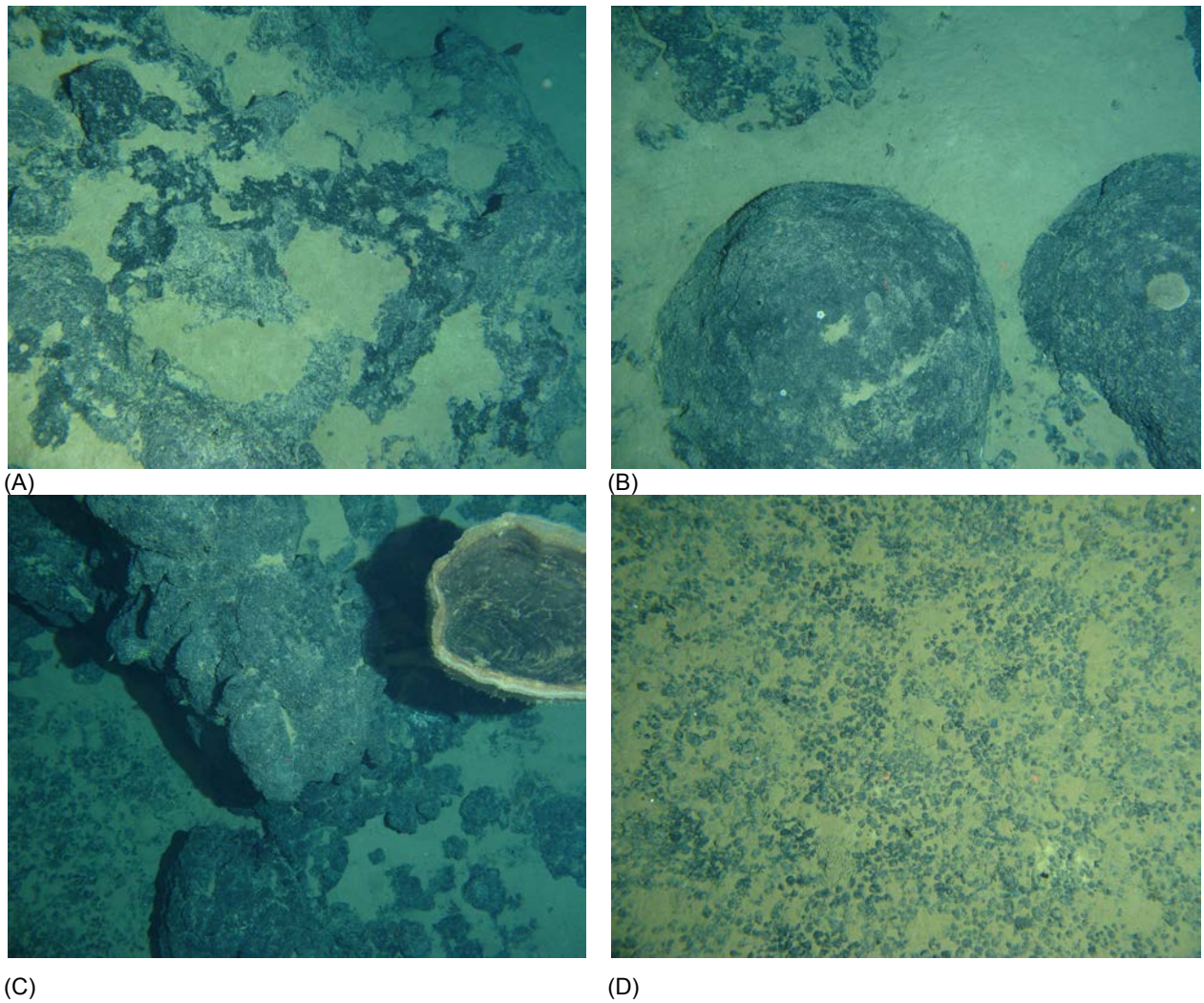


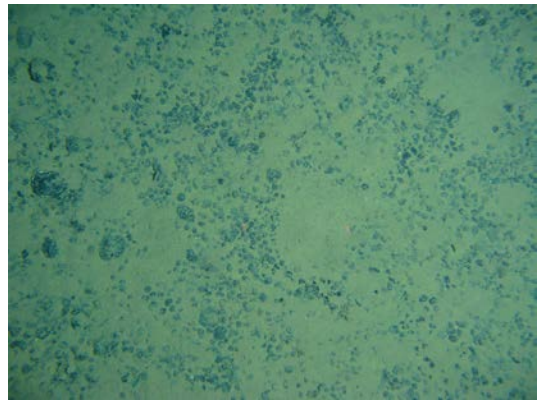
Figure 7.5.19. Seafloor photographs obtained along station SO240-41STR. (A) Outcropping rocks, partly with Fe-Mn crust coverage, at edge of flat seamount top. (B) Pillow lava forming the seamount flank. (C) Giant sponge on rock substrate. (D) Small-sized Mn nodules at turning point of the transect. The lengths of the images represent about 1.50 m.

SO240-38KG

85%:15%:0%

15.8 kg/m²

285 nodules

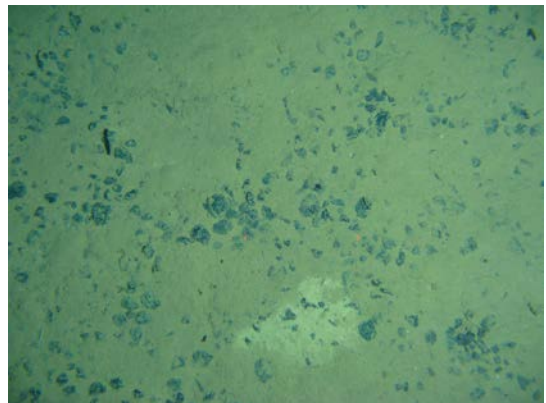


SO240-44KG

53%:47%:0%

17.8 kg/m²

137 nodules

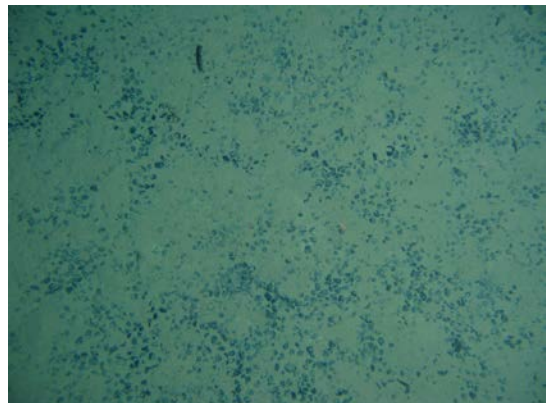


SO240-46KG

67%:33%:0%

18.4 kg/m²

225 nodules



SO240-47KG

24%:64%:12%

23.4 kg/m²

75 nodules

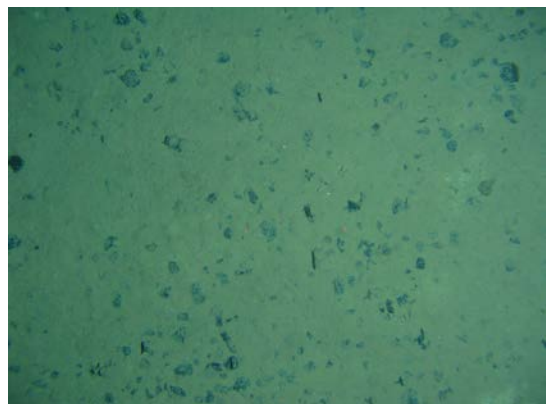


Figure 7.5.20 Comparison between nodules from box core stations and seafloor images deriving from seafloor areas close to the box core stations along 41STR and 49STR. The percentage numbers on the left side reflect the frequency ratio between small (< 4 cm), medium (4-8 cm), and large (> 8 cm) nodules. The total number of nodules refers to the box core surface (upper 10 cm), as does the nodule abundance (wet weight). Laser points are ~ 30 cm apart in seafloor images. Note that fields dominated by small-sized nodules have a different appearance in the underwater images than fields dominated by medium to large-sized nodules.

7.6 BENTHIC BIODIVERSITY

Annika Janssen, Katja Uhlenkott

The aim of the biodiversity studies carried out during the FLUM S0-240 cruise was to analyze the influence of the processes of fluid fluxes between seamounts on benthic fauna (i.e. the endemic fauna around recharge/discharge sites). Furthermore, the analyses of the samples taken during the cruise will complement ongoing investigations in the eastern part of the German license area for manganese nodules in terms of community structure, standing crops and biodiversity.

7.6.1 Methods

Several devices were used for these biological investigations: the multicorer for studying the meiofauna, the box corer for macrofauna (specifically infauna) and photographs taken by the STROMER for megafauna.

Megafauna

The megafaunal composition and richness was examined through the comprehensive analysis of *in situ* still and video images of the seafloor taken by the HD camera installed on the video-sledge STROMER (see chapter 7.5 for details on STROMER functions and transects). Videos and photographic images of the sea floor were collected during all 6 STROMER deployments. While the video recorded non-stop, photographs were taken automatically every 20 seconds. Although specimens were identified and counted during the deployment in real time, a detailed identification on the lowest possible taxonomic level will take place after the cruise.

Macrofauna

Samples for the investigation of macrofaunal organisms were obtained from the box corer (especially infauna). Upon recovery of a box corer (see Chapter 7.3 for details on box corer deployment), the supernatant water was removed using flexible plastic tubes, passed through a 300 µm mesh sieve to sample the macrobenthic fauna and fixed separately in pre-cooled (4°C) 96% Ethanol (Fig. 7.6.1). Photographs were taken to document the distribution and original position of the nodules on top of the sediment. Subsequently, sessile organisms were picked out and fixed separately in pre-cooled (4°C) 96% Ethanol (Fig. 7.6.1). After the removal of the nodules and sediment subsamples, the remaining upper 10 cm of the sediment (separated in three layers, i.e. 0-3 cm, 3-5 cm and 5-10 cm) were sieved through a 300 µm mesh using filtered (100 µm) seawater, thus retaining nearly all individuals of taxa generally regarded as macrofauna (standard box core washing method as used by Hessler and Jumars, 1974). Samples were preserved in pre-cooled (-20°C) 96% ethanol which was renewed after 24 h and sorted to higher taxonomic level on board using *Leica* binocular microscopes. The detailed taxonomic and genetic analyses of samples will be carried out in the home laboratory (DZMB).



Figure 7.6.1. Removal of surface water and picking out the sessile animals on nodules from box corer.

Meiofauna

Samples for the investigation of metazoan meiofauna were obtained from the Multicorer (MUC). The 12-tube multiple corer from the DZMB was used (Fig. 7.6.2), which allows the sampling of an intact column (core) of sediment together with its overlying water and the transitional thick fluffy layer. The outer diameter of a tube is 100 mm and its length is about 60 cm. Its inner diameter is 96 mm, and covers an area of 55cm². The distances between the single tubes mounted on the multicorer are not the same. This has to be considered when analysing the differences between the various samples collected from the same multicorer deployment. Therefore, the tubes were numbered and the position of each tube was recorded in the deployment protocol. The device was lowered at a speed of 0.8 m/sec until it reached a position ~50 m above the seafloor. The corer was stopped for about 1 min and then lowered with a speed of 0.5 m/sec until contact with the seafloor was monitored through the decrease in wire tension. The corer remained on the seafloor for ca. 1 minute, and was then pulled out at a speed of 0.3 m/sec and finally heaved onboard at 0.8 m/sec.

At least 4 cores per deployment were taken by AWI and JUB for geochemical analyses and pore-water analyses, and one core was sampled by the BGR for sedimentological analyses. All remaining cores were taken for faunal analyses by DZMB. At least five cores were used for quantitative community analyses and the remaining cores were used for qualitative genetic analyses. The overlying water was removed from every core through a sieve with a mesh size of 32 µm. Nodules were fixed separately (Fig. 7.6.3). The upper 5 cm of sediment was sampled and fixed in ~4% formaldehyde (for quantitative analyses) and DESS, a solution containing dimethyl sulphoxide EDTA, desodium EDTA and saturated NaCl (Yoder *et al.*, 2006) (for qualitative analysis). Meiofauna for qualitative analysis was already extracted by centrifugation on board, using the colloidal gel Levasil®. Centrifugation was carried out 3 times with 4000 rpm for 6 minutes. In the home laboratory, the meiofauna for quantitative analysis will be extracted in the same way. The separated meiofauna for quantitative as well as qualitative analysis will be sorted out by hand under a stereo microscope, and sorted into major taxa. The material will be used for genetic, systematic, chorologic, and faunistic investigation, e.g. using similarity and diversity analyses.

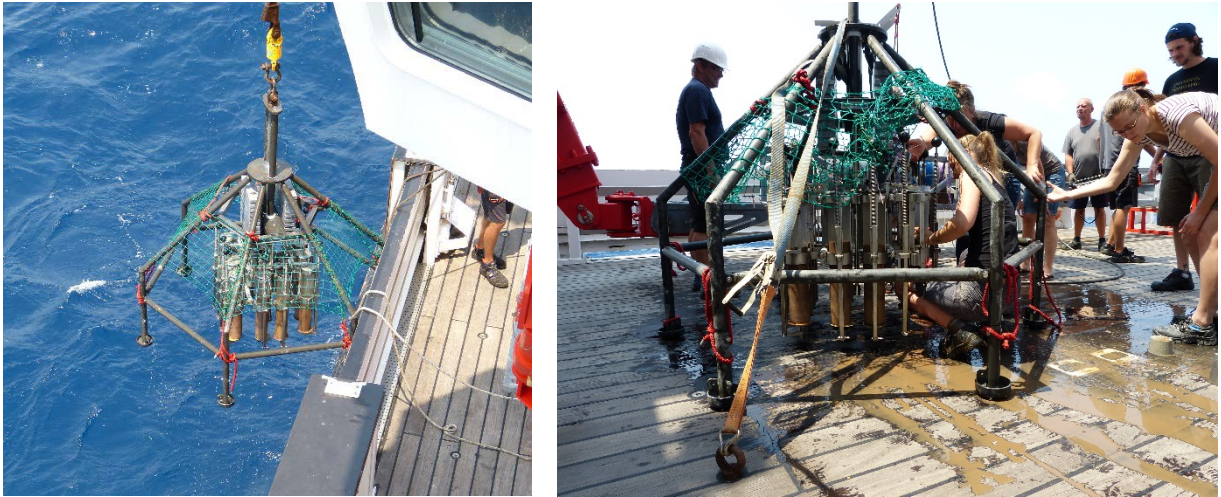


Figure 7.62. Multicorer with filled tubes and recovery of samples.

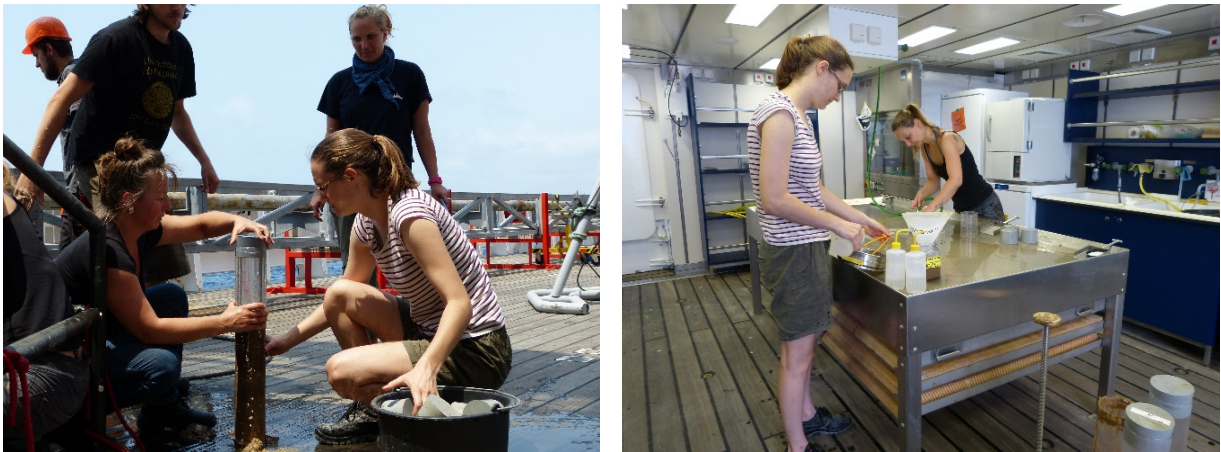


Figure 7.6.3. Multicorer sample processing on board.

7.6.2 Preliminary results

Megafauna

A high variety of different megafaunal organisms was observed on the seafloor during the six transects of the video-sledge STROMER. A total of 7069 photographs were obtained. From the photographs at least 7 different phyla and at least 10 different classes could be recognized (Tab. 7.6.1 and Fig. 7.6.4).

Table 7.6.1. Observed phyla and classes during 6 STROMER transects.

Phylum	Class
Foraminifera (protists)	Komokiacea
	Xenophyophora
Cnidaria	Anthozoa
Echinodermata	Asteroidea
	Echinoidea
	Holothuroidea
	Ophiuroidea
	Echinodermata indet.
Crustacea	
Porifera	
Mollusca	Bivalvia
	Gastropoda
Chordata	Pisces
	Indet.

First impressions from the video observations reveal a different fauna on seamounts compared to that of the abyssal plains. Echinoderms and poriferans are most abundant in the deep sea plains, whereas the anthozoans are most abundant at the seamounts and on their slopes.

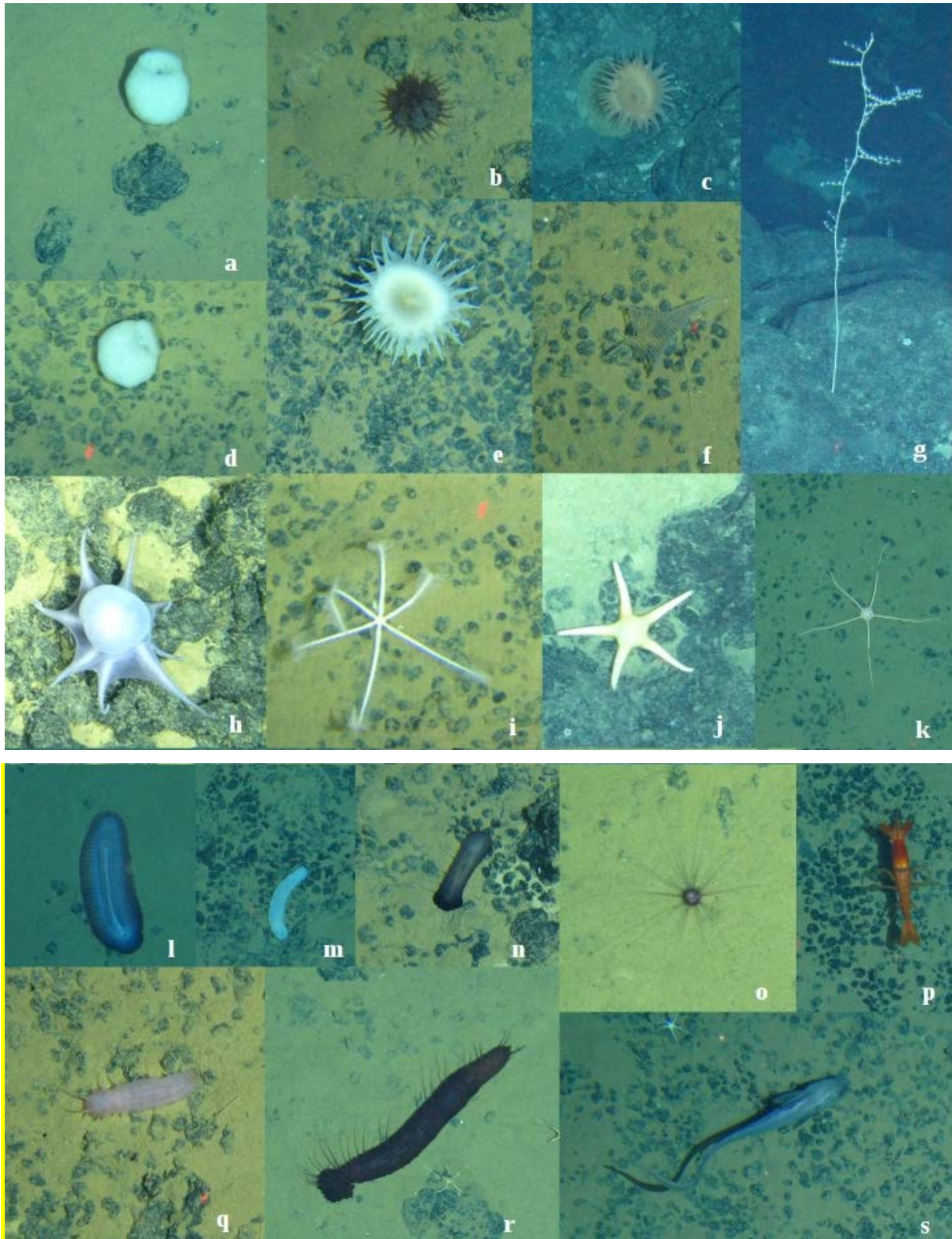


Figure 7.6.4. Megafaunal organisms observed with the video-sledge STROMER; a,d: Porifera; b-c, e-f: Cnidaria, Hexacorallia; g: Cnidaria, Octocorallia; h: Mollusca, Cephalopoda; i, j: Echinodermata, Asteroidea; k: Echinodermata, Ophiuroidea, l-n, q-r: Echinodermata, Holothuridea; o: Echinodermata, Echinoidea; p: Crustacea, Mysida; s: Pisces, Actinopterygii.

Macrofauna

The box corer was deployed at 20 locations, of which 18 were used for macrofaunal sampling. Of these 18 locations, seven were located in WA#1, six in WA#2, four in WA#3 and one in WA#4. The two additional box cores that were not sampled for biology were located (1) in a reserved manganese nodule area that was visited during the weathering of hurricane Andres, and (2) in WA#4 and used for the mass sampling of surface sediment for sedimentological and geochemical purposes. Nonetheless, the supernatant waters of these two box cores were sieved and fixed as qualitative samples for biological investigations.

Preliminary analyses carried out on board are based on the box cores of WA#1 (excluding 118KG), WA#2 and WA#3 only. For a detailed list of sampling stations and maps of sampling positions, see Chapter 6.

The following sessile macrofauna organisms were found on the nodules: calcareous tube-building polychaetes (Serpulidae), Octocorallia (Primnoida), Porifera, Bryozoa, Xenophyophora (especially large forms) - animals that are definitely or possibly suspension feeders. Other taxa such as Bivalvia, Ophiuroidea and chain-aggregated Foraminifera were found as well. Figure 7.6.5 gives an overview of the most abundant taxa that were sampled from nodules in the box corer.

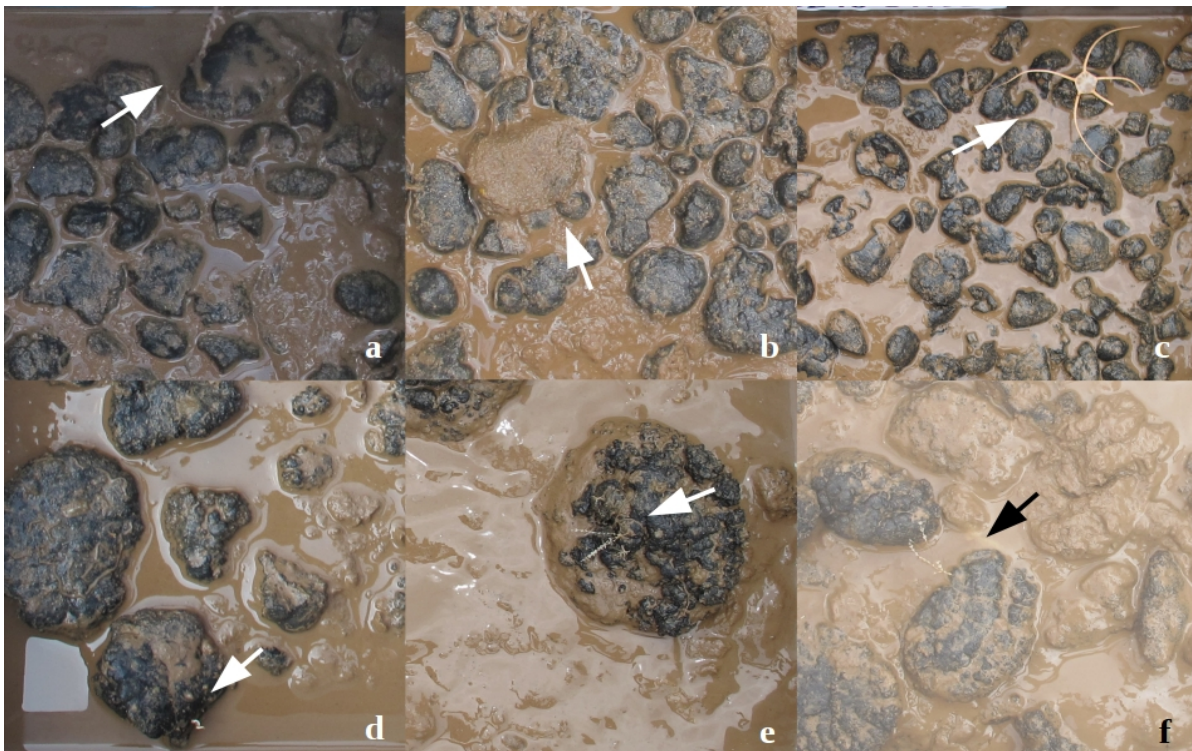


Figure 7.6.5. Selected sessile macrofaunal taxa collected by the box corer during the FLUM SO-240 cruise: a, e-f: Octocorallia (Primnoida); b: Porifera; c: Echinodermata, Ophiuroidea; d: Polychaeta (Serpulidae).

In total, the box corer was successful in collecting several different taxonomic groups in the supernatant water and the first, second and third horizon (Tab. 7.6.2). A total of twelve phyla and twenty four classes are represented in the sediment samples of the box corer. The most common taxa

were Polychaeta, Peracarida (Isopoda and Tanaidacea) and Copepoda. All other taxa listed in Table 7.6.2 are represented by a few specimens only (Figs. 7.6.6 and 7.6.7).

Table 7.6.2. Observed taxonomic groups in the supernatant water and first, second and third sediment horizons of the analyzed box cores

<i>Protozoa</i>	
	Foraminifera
	Komokiacea
	Xenophyophora
<i>Porifera</i>	
	Hexactinellida
<i>Nematoda</i>	
<i>Crustaceans</i>	
	Peracarida
	Isopoda
	Amphipoda
	Cumacea
	Tanaidacea
	(formerly) Maxillopoda
	Copepoda
	Ostracoda
<i>Mollusca</i>	
	Polyplacophora
	Bivalvia
	Gastropoda
	Scaphopoda
<i>Bryozoa</i>	
<i>Cnidaria</i>	
	Hydrozoa
<i>Annelida</i>	
	Polychaeta
<i>Echinodermata</i>	
	Asteroidea
	Ophiuroidea
<i>Sipunculida</i>	
<i>Chaetognatha</i>	
<i>Chelicerata</i>	
	Pantopoda



Figure 7.6.6. Selected macrofaunal crustaceans collected by the box corer during the FLUM cruise: a: Isopoda; b: harpacticoid copepods; c: Tanaidacea; d: calanoid copepod; e: Amphipoda; f: Ostracoda. Note that different scales have been used.

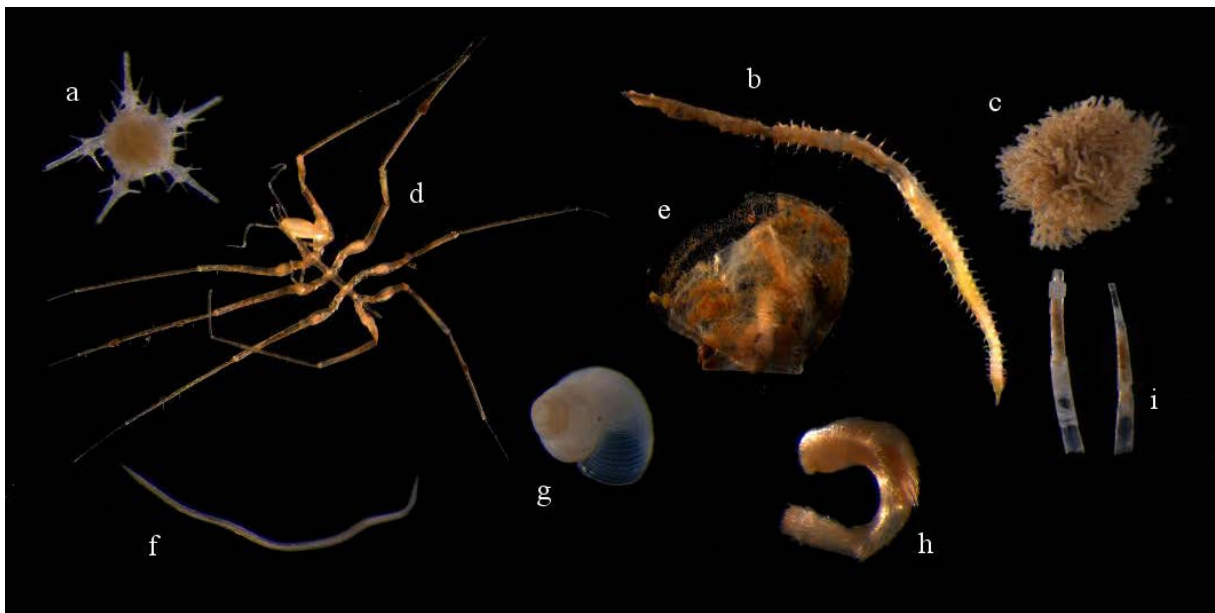


Figure 7.6.7. Various selected macrofaunal specimens collected by the box corer during the FLUM cruise: a: Ophiuroidea; b: Polychaeta; c: Komokiacea; d: Pantopoda; e: Bivalvia; f: Nematoda; g: Gastropoda; h: Caudofoveata. Note that different scales have been used.

Our first observations show that the majority of individuals were usually found in the uppermost 5 cm layer (Fig.7.6.8). The sediment of the uppermost 0-10 cm was mainly fluffy and of dark brown color, containing manganese nodule fragments, sponge spicules, radiolarians and foraminiferans. The macrofauna of this sediment layer was clearly dominated by polychaetes, followed by tanaids, copepods, nematods and isopods (Fig. 7.6.9).

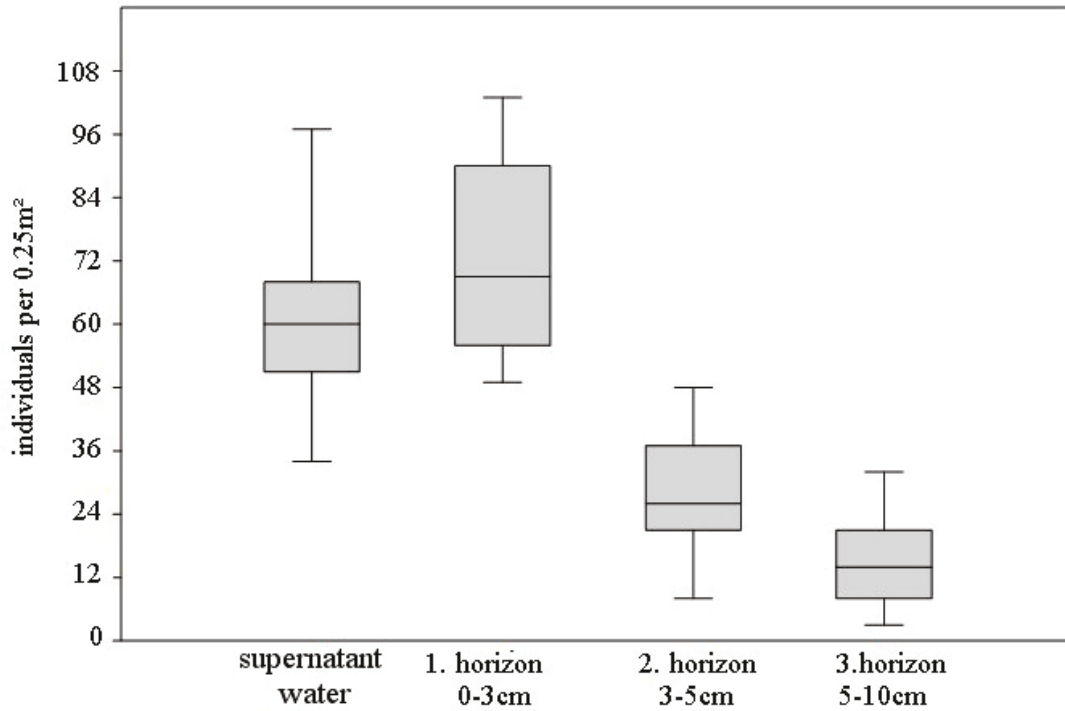


Figure 7.6.8. Macrofaunal abundance within the box core sub-samples.

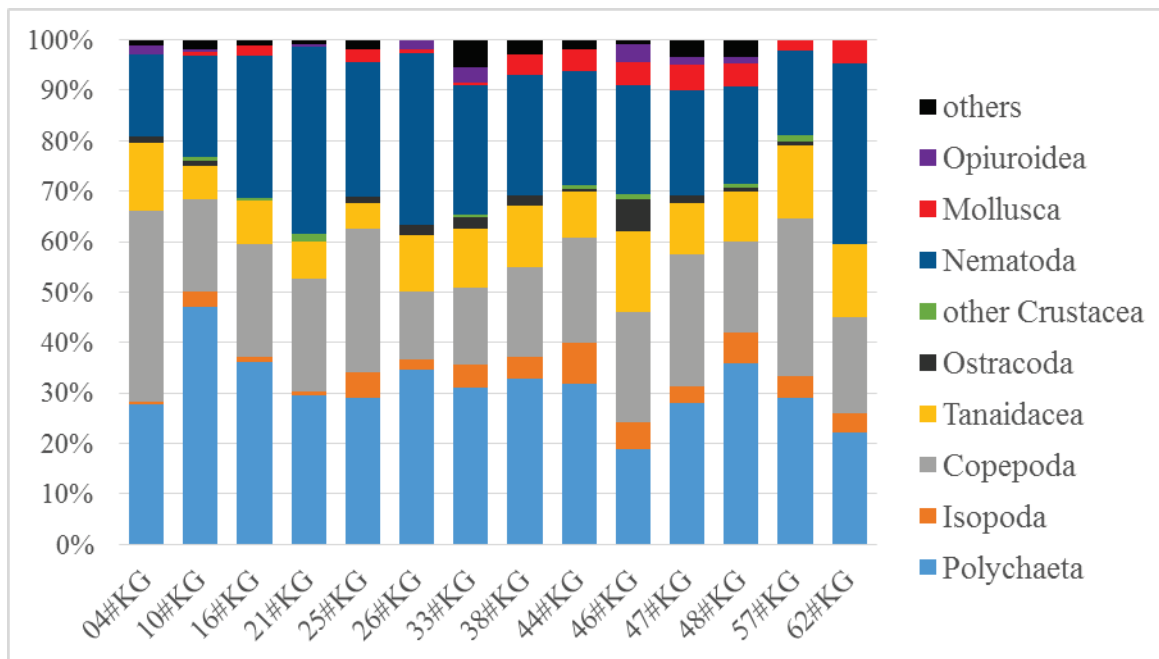


Figure 7.6.9. Relative abundance of macrofaunal taxa in the sediment samples of 14 box cores.

For preliminary results, non-metric, multi-dimensional scaling (nMDS) plots were created to reflect similarities between the stations at community level in relation to nodule size, working area and distance to seamounts. Furthermore, multivariate analysis was conducted using ANOSIM (Analysis of Similarity) in order to test for significant differences in community composition in relation to a priori defined factors.

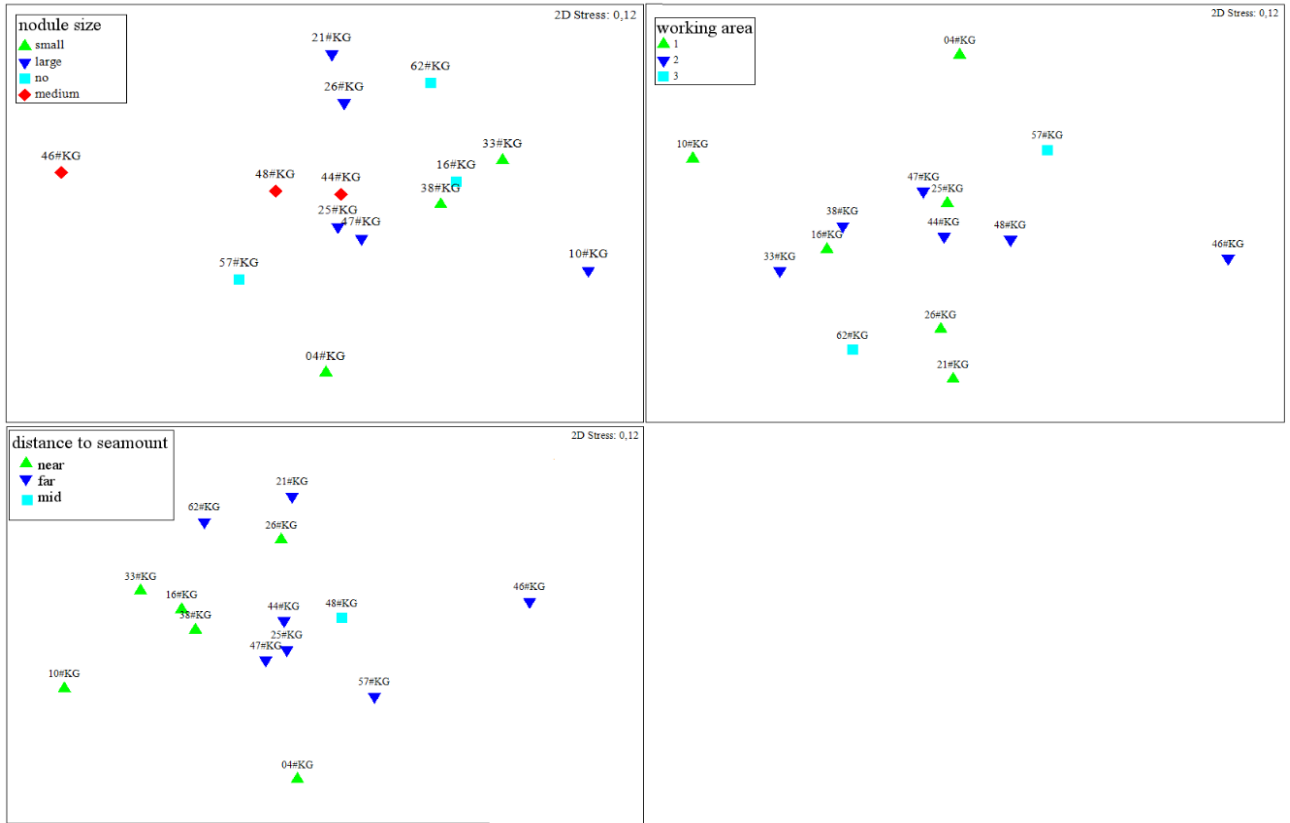


Figure 7.6.10. Non-metric, multi-dimensional scaling (nMDS) plots of total abundances to test for similarity of macrobenthic communities in relation to three factors: nodule size, working area and distance to seamounts, based on Bray-Curtis Similarity.

The nMDS plots (Fig.7.6.10) showed no obvious grouping between samples with respect to the factors nodule size and working area. ANOSIM confirmed that there are no significant differences between the compositions of macrobenthic communities living in the different working areas or areas of different nodule size (Tab. 7.6.3). However, ANOSIM did reveal significant differences between macrobenthic communities living close to and far away from a seamount (Tab. 7.6.3). Figure 7.6.11 shows that the significant difference is mainly caused by a higher abundance of macrofaunal organisms in box cores that were located near to a seamount in comparison to those box cores that were located further away from a seamount.

Table 7.6.3. Multivariate analysis (ANOSIM) reflecting the relationship between composition of macrobenthic communities and (1) areas with different nodule size, (2) different working areas, and (3) areas with varying distances to a seamount.

(1) nodule size	small	no	large
medium	--	--	--
large	--	--	
no	--		
(2) working area	1	2	
2	--		
3	--	--	
(3) distance to seamount	near	mid	
mid	--		
far	*	--	

* p < 0.05 significance level, -- p > 0.05 significance level

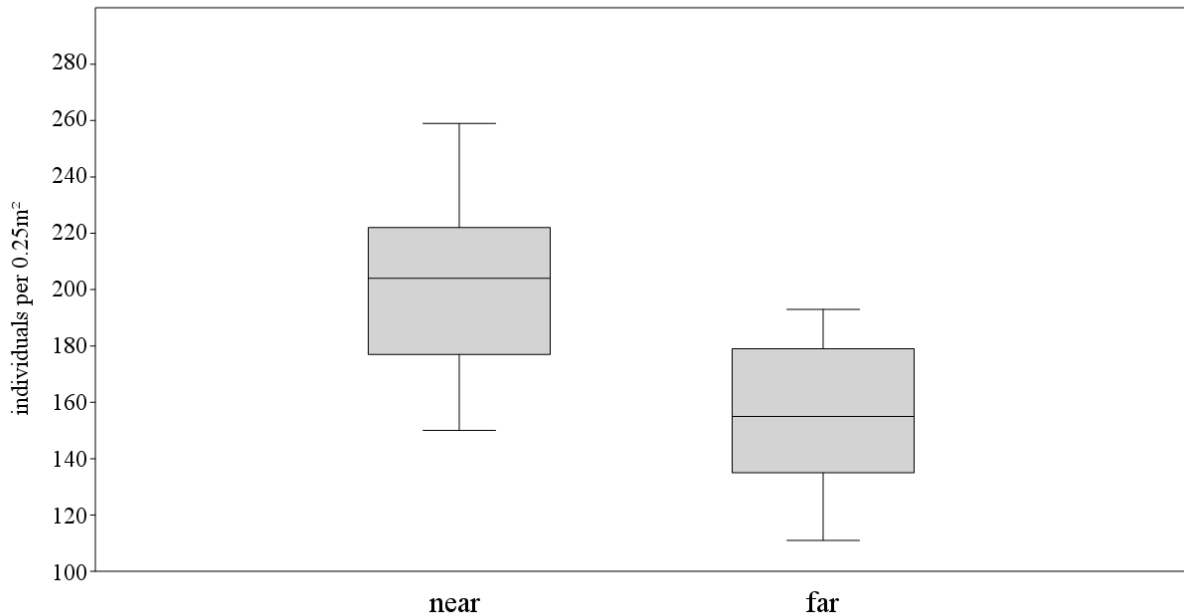


Figure 7.6.11. Abundance of macrofaunal organisms in box cores located near to and far off from a seamount.

Meiofauna

The MUC was successful in all 17 hauls and recovered 10-12 completely filled cores per station. Table 7.6.4 shows the distribution of cores according to the aims of the different working groups. For faunal analyses, cores with the most undisturbed sediment surfaces were taken as quantitative samples for meiofaunal community analyses, whereas the remaining cores will be used for genetic analyses as qualitative samples.

Table 7.6.4. List of multicorer stations with the distribution of cores according to purpose (total amount of cores used and exact positions of cores in brackets).

Station SO240-	Meiofauna communities (quantitative analyses)	Genetic analyses (qualitative analyses)	Sedimentological analyses (BGR)	Pore-water and geo-chemical analyses (AWI/JUB)	Lat (N)	Long (W)	Depth (m)	Notes
08 MUC	5 (2, 3, 8, 11, 12)	1 (9)	1 (7)	5 (1, 4, 5, 6, 10)	13°10.524'	118°06.780'	4289	
14 MUC	5 (2, 3, 5, 11, 12)	1 (10)	1 (9)	4 (1, 4, 6, 8)	13°10.528'	118°10.108'	4333	1 corer empty
18 MUC	5 (4, 5, 9, 11, 12)	1 (7)	1 (8)	5 (1, 2, 3, 6, 10)	13°07.109'	118°07.657'	4318	
23 MUC	5 (2, 3, 5, 11, 12)	1 (9)	1 (8)	3 (1, 6, 10)	13°10.526'	118°08.186'	4305	2 corers empty
34 MUC	5 (2, 4, 9, 11, 12)	1 (10)	1 (8)	4 (1, 3, 5, 6)	12°53.354'	118°24.569'	4287	1 corer empty
37 MUC	4 (2, 3, 5, 11)	2 (4, 12)	0	4 (1, 6, 8, 9)	12°54.127'	118°24.782'	4319	2 corers empty
43 MUC	5 (4, 5, 9, 11, 12)	2 (7, 8)	0	5 (1, 2, 3, 6, 10)	12°51.247'	118°23.980'	4289	
59 MUC	5 (3, 4, 5, 11, 12)	2 (2, 9)	0	5 (1, 6, 7, 8, 10)	12°53.216'	119°08.349'	4306	
61 MUC	5 (2, 4, 5, 11, 12)	1 (8)	1 (7)	5 (1, 3, 6, 9, 10)	12°56.109'	119°08.871'	4293	
68 MUC	5 (2, 3, 6, 11, 12)	6 (4, 5, 7, 8, 9, 10)	1 (1)	0	12°40.370'	119°11.514'	4408	
70 MUC	5 (4, 5, 8, 11, 12)	2 (2, 7)	0	5 (1, 3, 6, 9, 10)	12°39.857'	119°13.385'	4270	
74 MUC	5 (3, 4, 9, 11, 12)	2 (7, 8)	0	5 (1, 2, 5, 6, 10)	12°55.601'	119°08.830'	4295	
95 MUC	5 (2, 3, 4, 11, 12)	1 (9)	1 (8)	5 (1, 5, 6, 7, 10)	11°49.262'	117°13.197'	4150	
106 MUC	5 (2, 3, 5, 11, 12)	2 (8, 9)	1 (7)	4 (1, 4, 6, 10)	11°50.079'	116°32.900'	4351	
109 MUC	5 (2, 3, 7, 11, 12)	3 (4, 5, 9)	0	4 (1, 6, 8, 10)	11°48.791'	116°31.760'	4327	
116 MUC	5 (2, 4, 5, 11, 12)	2 (8, 9)	0	5 (1, 3, 6, 7, 10)	13°11.098'	118°06.003'	4270	
121 MUC	8 (2, 3, 5, 6, 9, 10, 11, 12)	3 (4, 7, 8)	0	1 (1)	13°11.235'	118°03.623'	4268	

7.7 PHYSICAL OCEANOGRAPHY

J. Gerken, K. Purkiani, A. Vink

7.7.1 Introduction and research objectives

During cruise SO-240, four working days were dedicated to oceanographic investigations that form part of the “EcoResponse” project within the framework of the European Program “Joint Programming Initiative – Oceans” (JPI-O), which deals with the potential ecological impacts of future Manganese nodule mining. The use of seabed (test-)mining equipment will create operational and discharge plumes of particulate material, potentially at different levels in the water column depending on the depth of discharge. Physical oceanographic data are required to (i) analyze the natural spatial and temporal variability of the current regime at potential mining sites; and (ii) predict and model the behavior and environmental impact of potential sediment plumes.

For these purposes, full-depth, high resolution vertical profiles of temperature, stratification and turbidity have been obtained from the entire water column using the onboard CTD/rosette in normal, yoyo and tow-yo modus. Furthermore, similar data were obtained during deployments of the video sledge STROMER, which was equipped with a CTD and a turbidity sensor as well as one or more **Miniature Autonomous Plume Recorders** (MAPRs) attached to the cable above the STROMER. CTD deployments above the “Teddy Bare” seamount in working area 1 (WA-1) revealed a temperature anomaly in the water column directly above the seamount that was investigated in detail in order to determine whether this phenomenon has an oceanographic origin or whether external hydrothermal sources could be responsible.

Long-term data on current speed and direction as well as background turbidity should be collected at the depths that will be influenced by the operational and discharge plumes arising from the testing of collector systems and equipment, i.e. in particular near the seafloor. Seven previously moored systems (four long-term **Ocean Bottom Moorings** (OBMs) of the BGR, two lander systems (BoBo of NIOZ and DOS of GEOMAR) and one thermistor chain of NIOZ), all equipped with oceanographic instrumentation to obtain high resolution data from close to the seafloor, had to be retrieved during this cruise and data were downloaded and analyzed. Furthermore, the four OBMs were redeployed at exactly the same locations for another year. Special focus was set on working area 4 (WA-4) as this is a prospective future mining area (“Impact Reference Area”, see Rühlemann et al., 2014) that has been chosen for hydrodynamic modeling exercises in the framework of the JPI-O project.

Ultimately, the measured high-resolution temperature, current and turbidity data will be used for (i) assessing the hydrographic conditions that are characteristic of the area (e.g. background mean flow velocities, tidal wave activities, degree of local stratification/mixing, etc.), and (ii) configuring, implementing and calibrating existing and specifically adapted deep-sea 3D ocean circulation-sediment transport models that will provide information on the probable fate of mining-induced discharged sediments under varying discharge scenarios at both the local (near-field) and the regional (far-field) scale in and beyond the (test-)mining area.

7.7.2 Sea water properties

Methods

During the SO-240 cruise, temperature and salinity profiles of the entire water column were recorded at eight locations using an onboard CTD/rosette (Fig. 7.7.1; Tab. 7.7.1), including one tow-yo and two yoyo deployments in WA-4. The equipment consists of a Seabird SBE 19 plus V2 CTD profiler with an additional oxygen sensor Sea-Bird SBE 43 and a seapoint turbidity meter mounted externally to the CTD. The latter detects light scattered by particles suspended in water, thus generating an output voltage proportional to the turbidity caused by suspended particles. During tow-yo deployment (SO240-93CTD), the CTD was heaved and hoisted at 0.5 m/s between 50 and 500 m above the seafloor over a previously defined transect at a ship speed of ca. 0.5 kn for 17 h. During yoyo deployment (SO240-97CTD, SO240-111CTD), the CTD was heaved and hoisted throughout the complete water column at one location at 0.7 m/s until 4 complete cycles had been obtained (14 h). For the locations of tow-yo and yoyo deployments, see figure 6.27.

Furthermore, CTD and turbidity profiles were obtained during the vertical and horizontal deployment (close to the seafloor) of the video sledge STROMER (Fig. 7.7.1) at another seven stations (Tab.7.7.2), using a Seabird SBE 19 plus V2 CTD profiler with an additional oxygen sensor Sea-Bird SBE 43 and a WetLabs ECO FL(RT)D fluorometer (see Chapter 7.5.2 for technical specifications). In order to collect physical oceanographic information of a wider part of the water column close to the seafloor, four MAPRs were attached to the support cable of the video sledge during five deployments (Tab. 7.7.2). The MAPR is designed to be an inexpensive, lightweight, simple and self-contained instrument for recording water temperature, pressure, and optical data during seagoing operations. The vessel sailed with a speed of about 1 kn along a pre-defined transect, with the video frame being towed behind the vessel and maintained about 3-6 m above the seafloor. The video sledge was only deployed in WA-1 and WA-2.

Table 7.7.1. CTD downcast deployments during SO-240.

Station SO240-	Type of station	Date	Latitude (N)	Longitude (W)	Water depth (m)	Working area
01CTD	Vertical profile	07.05.2015	13° 10.52'	118° 12.19'	4262	WA-1 (Fig. 6.7)
50CTD	Vertical profile	21.05.2015	13° 10.020'	118° 04.949'	4026	WA-1 (Fig. 6.7)
55CTD	Vertical profile	24.05.2015	12° 55.596'	118° 58.433'	3870	WA-3 (Fig. 6.20)
79CTD	to 2000 m: EM122 calibration	01.06.2015	11° 45.997'	116° 32.005'	4327	WA-4 (Fig. 6.27)
93CTD	tow-yo	04.06.2015	11° 53.850'	116° 57.783'	4101	WA-4 (Fig. 6.27)
97CTD	yoyo	06.06.2015	11° 51.490'	117° 00.233'	4118	WA-4 (Fig. 6.27)
111CTD	yoyo	08.06.2015	11° 50.393'	116° 56.673'	4131	WA-4 (Fig. 6.27)
119CTD	Vertical profile	11.06.2015	13° 17.488'	118° 10.806'	3502	WA-1 (Fig. 6.7)



Figure 7.7.1. Left: RV Sonne's CTD with Rosette samplers on top. Right: the multi-functional video sledge STROMER.

Table 7.7.2. STROMER video sledge CTD and MAPR deployments during SO-240.

Station SO240-	Date	Latitude (N)	Longitude (W)	Water depth (m)	MAPRs	Working area
06STR	08.05.2015	13° 10.060'	118° 04.858'	4024		WA-1 (Fig. 6.7)
		13° 10.060	118° 04.560'	4075		
13STR	11.05.2015	13° 09.441'	118° 12.985'	3725		WA-1 (Fig. 6.7)
		13° 10.519'	118° 09.751'	4313		
28STR	15.05.2015	13° 10.007'	118° 04.869'	4035	50, 100, 150, 200 m above sledge	WA-1 (Fig. 6.7)
		13° 10.527'	118° 08.936'	4298		
40STR	18.05.2015	13° 02.020'	118° 26.744	3712	100, 200, 300, 400 m above sledge	WA-2 (Fig. 6.13)
		13° 02.912'	118° 26.515'	3718		
41STR	19.05.2015	12° 56.018'	118° 26.157'	3884	100, 200, 300, 400 m above sledge	WA-2 (Fig. 6.13)
		12° 51.978'	118° 24.180'	4275		
49STR	21.05.2015	12° 51.980'	118° 24.170'	4273	100, 200, 300, 400 m above sledge	WA-2 (Fig. 6.13)
		12° 49.056'	118° 23.374'	4292		
113STR	09.06.2015	13° 11.453'	118° 05.231'	4222	100, 200, 300, 400 m above sledge	WA-1 (Fig. 6.7)
		13° 10.723	118° 05.216'	4161		

Results

SO240-01CTD

The vertical distribution of sea water properties in cast SO240-01CTD obtained from the western part of WA-1 (Fig. 6.7) is shown in figure 7.7.2. The salinity profile (plot a) shows a sharp halocline at 50 m depth. The halocline layer is extended down to 170 m depth. Within this layer, salinity increases by 0.8 psu, which in turn causes an excess of seawater density. Below the halocline layer, the salinity profile does not show significant changes all the way down to the seafloor.

The vertical distribution of temperature is depicted in figure 7.7.2b. A strong thermocline layer appears at a depth of 70 m and extends to 150 m depth. The temperature difference between the top and the bottom of the thermocline layer is 16°C. The profiles of temperature and salinity reflect the vertical distribution of water masses. Most of the density stratification is due to a vertical salinity gradient, but is reinforced by the thermocline.

Eastern tropical Pacific sub-pycnocline waters are characterized by very low concentrations of oxygen (Fiedler and Talley, 2006). This is clearly depicted by the very low concentrations of oxygen below 100 m depth (Fig. 7.7.2c). The **Oxygen Minimum Zone (OMZ)** is the zone in which oxygen saturation in seawater is at its lowest. Extremely low oxygen concentrations in the water column are mainly attributed to the fact that the sharp permanent pycnocline prevents local ventilation of subsurface waters, but are also caused by bacterial metabolic processes that lower the oxygen concentrations within this layer. Below 1000 m, where water temperature drops below 5°C, the concentration of oxygen in the water column increases constantly to the seafloor. The oxygen concentrations at the seafloor reach almost similar values to those of the surface water, indicating that huge amounts of oxygen are advected by deep ocean currents. This oxygen increase occurs due to the fact that the rates of oxygen consumption in deep water are low in cold, oxygen-rich deep waters deriving from the polar region. Oxygen concentrations observed in all CTD casts obtained during this cruise are generally higher than those obtained during the BGR cruise MANGAN2014 at similar locations.

Turbidity values are very low below 100 m down to the seafloor at 4260 m water depth, indicating clear deep and bottom waters without any measurable suspension load, see figure 7.7.2d. Higher values of turbidity above 100 m water depth are probably due to high concentrations of organisms living in this photic zone. The peak in Chl a concentrations to a maximum at ca. 75 m water depth coincides with the depth where oxygen concentrations drop sharply to values of 0.1-0.2 ml l⁻¹, indicating that primary production and subsequent remineralisation of particulate organic matter under oxygen consumption is an important factor for the formation of the OMZ, see figure 7.7.2e.

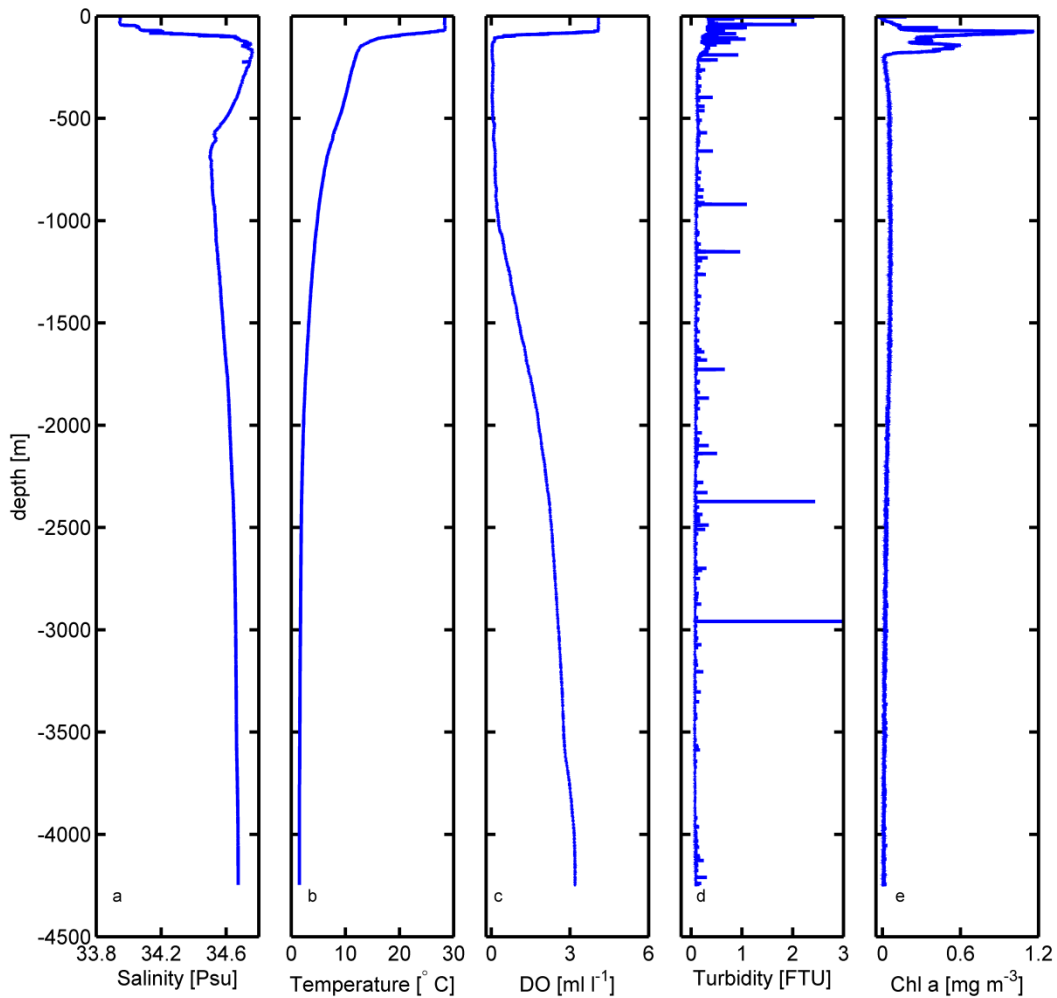


Figure 7.7.2. Exemplified sea water properties obtained by the downcast profile of SO240-01CTD in May 2015 in WA-1. The vertical distribution of salinity, temperature, dissolved oxygen, turbidity and chlorophyll a are shown in subfigures a to e.

SO240-50CTD

The vertical distribution of sea water properties in cast SO240-50CTD obtained from the top of the Teddy Bare seamount in WA-1 (Fig. 6.7) is shown in figure 7.7.3. Water column properties are very similar to those in station SO240-01CTD.

Sea surface salinity is 33.6 psu, which is 0.35 psu less than observed at the SO240-01CTD site. This relatively low surface salinity value is the result of precipitation exceeding evaporation due to a period of heavy rainfall at the time of deployment. Below the halocline, 01CTD and 50CTD show identical values in their vertical salinity profiles. The vertical distribution of temperature in the upper 150 m shows a slightly cooler upper water mass at the 50CTD site (0.3°C at the surface and reaching to 2.5°C). Below 150 m water depth, the temperature profile is identical to that of 01CTD.

The amount of oxygen dissolved in the water column also shows a small deviation to that observed at the 01CTD site. Due to increased wind velocity during the 50CTD cast, more oxygen could pass into surface waters. In contrast to the lower concentrations of oxygen in the mixed layer, 50CTD shows higher oxygen concentrations at redoxcline depth.

Surface turbidity at the 50CTD site does not show such a strong peak in subsurface waters compared to the 01CTD site. Also, the weaker surface peak in Chl a concentration reflects a lower penetration of sun light due to cloudiness during the 50CTD cast, and thus a lower primary production in subsurface waters (Fig. 7.7.3d,e).

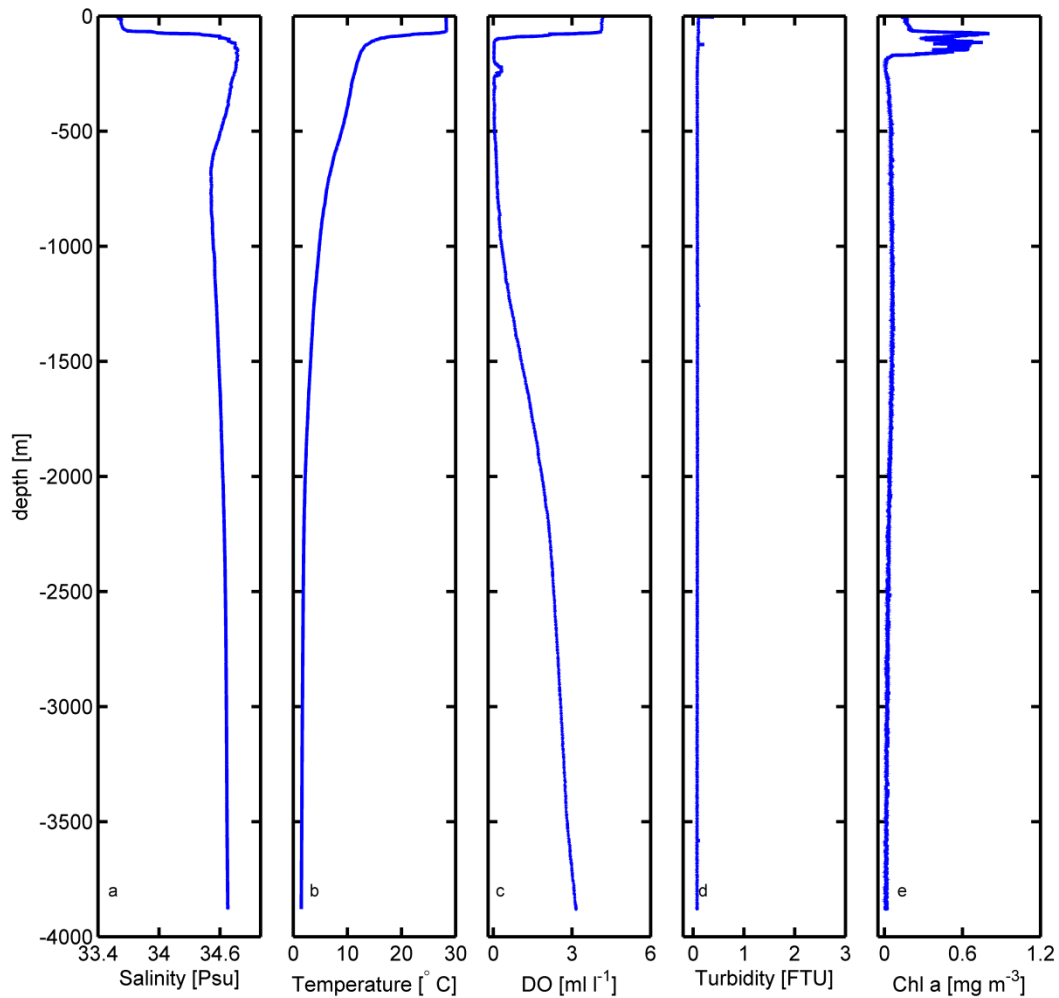


Figure 7.7.3. Exemplified sea water properties obtained by the downcast profile of SO240-50CTD in May 2015 in WA-1. The vertical distribution of salinity, temperature, dissolved oxygen, turbidity and chlorophyll a are shown in subfigures a to e.

SO240-28STR

The STROMER deployment SO240-28STR took place in WA-1 (Fig. 6.7), starting on top of the Teddy Bare seamount and then moving into the abyssal plain to the west of the seamount. Two MAPRs placed at 50 and 150 m above the mounted CTD on video frame recorded reliable data. Thus, temperature records of the last 150 m of the water column above the seafloor could be obtained with a sufficient vertical resolution during the towing process (Fig. 7.7.4). Surprisingly, water column temperature showed a significant increase of up to 0.02°C compared to the ambient water on top of the Teddy Bare seamount. This spectacular water temperature anomaly phenomenon was not observed at any of the other 6 video sledge stations.

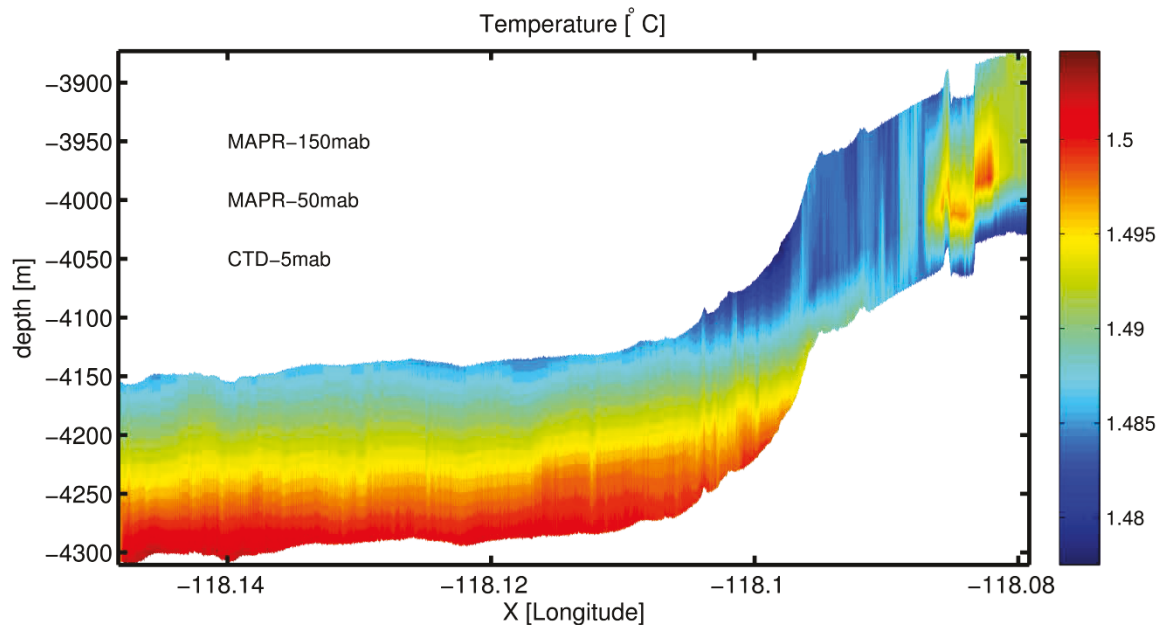


Figure 7.7.4. Vertical profile of water temperature along station SO240-28STR (WA-1) of the last 150 m of the water column above the seafloor. A sledge-mounted CTD was towed at 5 m above the seafloor. Two MAPRs have been attached 50 m and 150 m above the CTD. For location of transect, see figure 6.7. A 0.02°C temperature anomaly was found on top of the Teddy Bare seamount (topographic high shown on right-hand side of transect) whose origin is questionable. In contrast, the temperature increase close to the seafloor is attributed to adiabatic processes.

SO240-41STR

The STROMER deployment SO240-41STR took place in WA-2 (Fig. 6.13), also starting on top of a seamount and then moving into the abyssal plain to the south of the seamount. Four MAPRs were attached at 100, 200, 300 and 400 m above the mounted CTD on the video frame. Thus, temperature profiles of last 400 m of the water column above the seafloor could be obtained with a sufficient vertical resolution during the towing process (Fig. 7.7.5). In contrast to the results obtained during the SO240-28STR deployment showing a temperature anomaly on top of the seamount (Fig. 7.7.4), no unexpected temperature phenomenon was found on top of the seamount at this location. Temperature simply decreases with an increase of water depth.

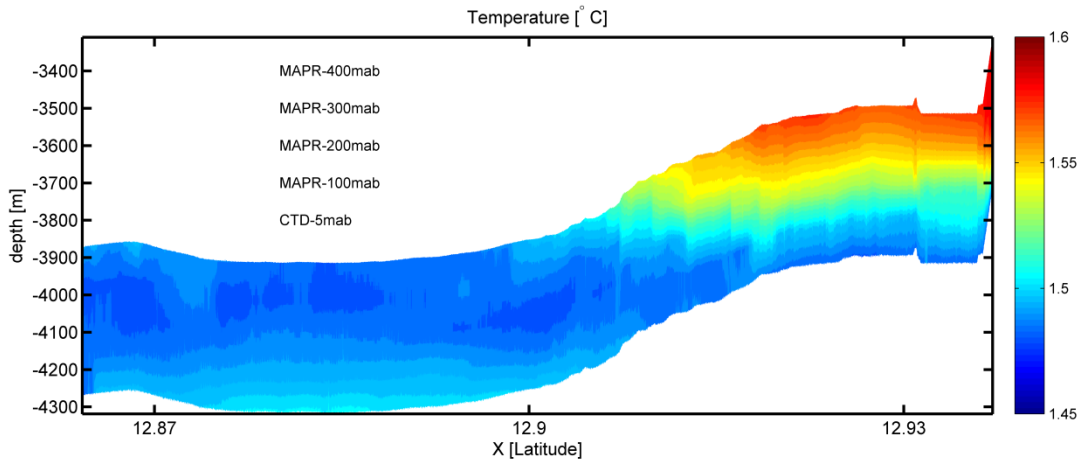


Figure 7.7.5. Vertical profile of water temperature along station SO240-41STR (WA-2) of the last 400 m of the water column above the seafloor. A sledge-mounted CTD was towed at 5 m above the sea floor. Four MAPRs have been attached with 100 m vertical resolution above the CTD. For location of transect, see figure 6.13.

Warm water anomaly on top of the Teddy Bare seamount

The vertical profiles of water column temperature of the last 1000 m of the water column above the sea floor at stations SO240-01CTD and -50CTD are shown in figures 7.7.2 and 7.7.3, respectively. A more precise investigation shows that both profiles deviate from the classical vertical profile of water column temperature expected for the deep ocean, where a linear decrease of temperature with increasing depth is expected. Figure 7.7.6 elucidates this sudden increase of temperature of up to 0.02°C at a depth of 3400 m.

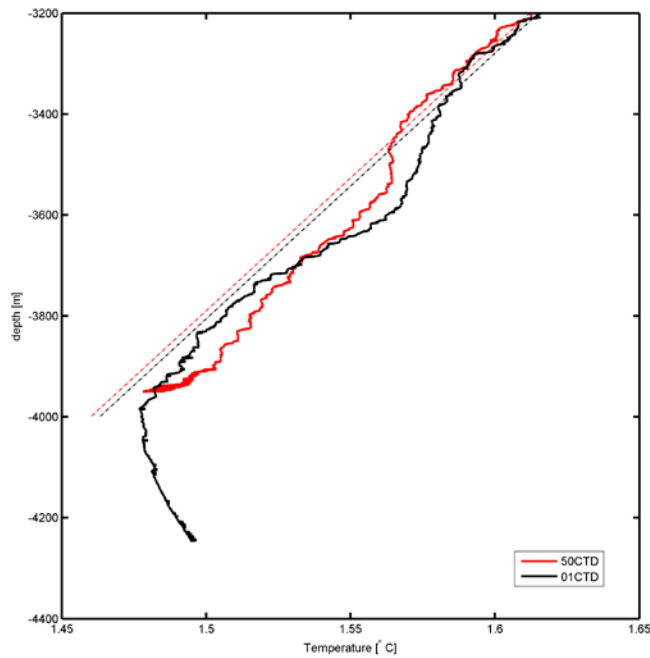


Figure 7.7.6. Vertical profiles of water temperature in the last 1000 m of the water column above the seafloor: black line = SO240-01CTD, red line = SO240-50CTD. Linear fits for each station are shown in corresponding colors.

The following questions arise: Why does the vertical profile of water temperature show such deviation from linear expected conditions? Is this due to an external source of heat flow such as a hydrothermal plume, or due to a small-scale eddy causing an impinging downward flow and pushing the warmer water from upper layers downwards toward the seafloor?

In order to answer to these questions, we examined whether the Teddy Bare seamount would be able to generate such eddies that are capable of disturbing the water column temperature. Next, we investigated the secondary effects of potential eddies, such as water column mixing, on the currents over the Teddy Bare seamount.

Chapman and Haidvogel (1992) show that rotating fluids in geostrophic balance cannot cross isobaths. On encountering a topographic irregularity such as a seamount, such a flow moves around the seamount and cannot pass over it. The isolated region of flow situated above the seamount with limited height is called the Taylor cap/column. This idealized Taylor cap phenomenon remains as long as the currents are in geostrophic balance. Any ageostrophic process in nature breaks the Taylor cap region down, allowing the flow to cross the topography. This Taylor cap trapping phenomenon at a seamount has remarkable effects on ocean circulation, mixing, water properties and biological properties at a local scale. Chapman and Haidvogel (1992) could show that the flow passing over a seamount results in two counter-rotating eddies that rotate clockwise until one vanishes, causing the other eddy trapped over the seamount to generate a Taylor cap. The likelihood that Taylor cap eddies develop depends on five principal parameters: the morphological shape of the seamount including fractional height and horizontal scale, and the strength of Coriolis force, determined by latitude, local density stratification and the strength of the geostrophic current.

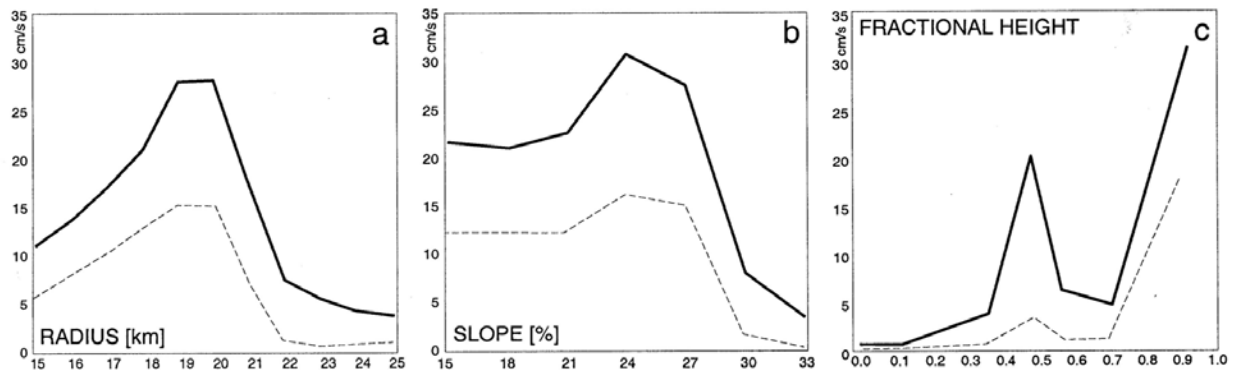


Figure 7.7.7. Resonant amplification and mean flow over different seamounts as a function of seamount radius (a), slope (b) and fractional height (c) adopted from Beckmann (1999).

Studies carried out by Chapman and Haidvogel (1992) and Beckmann (1999) show that the seamount radius and height are the critical factors affecting Taylor cap development (Fig. 7.7.7). It is shown that the maximum resonance of the mean flow occurs at a radius of 20 km and a fractional height of 0.4. Seamounts with a radius less than 15 km and shorter than 0.1 (at fractional height) do not show any mean flow rectification. Hence, the morphological features of the Teddy Bare seamount, with 1.5 km radius and

250 m height above the seafloor, present a far-off situation from the above-mentioned critical conditions for Taylor cap formation.

Apart from these morphological characteristics that are a strong argument against Taylor cap formation, we assume that in the case of occurrence of a Taylor Cap, the amount of water column mixing would also have to change. We therefore determined the amount of mixing occurring on top of the seamount to verify the origin of the temperature anomaly. The vertical flux of heat carried by turbulent motion is often expressed as:

$$1) \langle \rho c_p w T \rangle = -\rho c_p K_T \frac{dT}{dz}$$

This can be written approximately as:

$$2) \langle w T \rangle = -K_T \frac{dT}{dz}$$

where K_T is the vertical heat diffusivity and assumed to be in order of $10^{-5} \frac{m^2}{s}$ in the deep ocean. Based on equation (2), the amount of mixing in the last 1000 m of the water column above the seafloor can be estimated (Fig. 7.7.8). The comparison of vertical mixing at SO240-01CTD on the abyssal plain and SO240-50CTD at Teddy Bare seamount demonstrates that the amount of mixing does not vary significantly between these two topographically different sites. Therefore, we conclude that the Taylor Cap phenomenon did not occur at the top of the Teddy Bare seamount, and that external thermal sources must be the cause for the observed temperature anomaly.

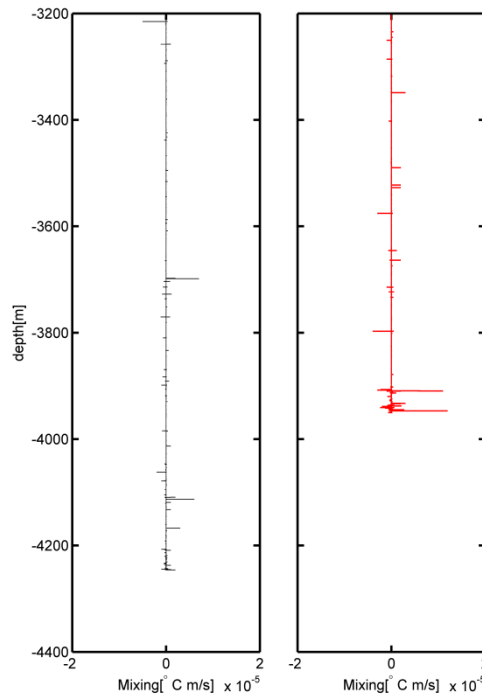


Figure 7.7.8. Vertical profile of water column mixing in last 1000 m of the water column above the seafloor. Black line = SO240-01CTD; red line = SO240-50CTD. For locations of CTD stations, see figure 6.7.

7.7.3 Long-term current profiling

Instrumentation and methods

Current profilers

During cruise SO-240, four Ocean Bottom Moorings (OBMs) measuring current strengths and directions close to the seafloor were recovered from WA-4 after a year of deployment and were redeployed at exactly the same positions for a further year of measurement (these will be recovered during the 2016 BGR exploration cruise to the area). Three of the four OBMs are equipped with two different current profilers: an upward-oriented Teledyne RDI ADCP (Acoustic Doppler Current Profiler) Workhorse Sentinel with a frequency of 600 kHz, and a sideward-oriented Aanderaa Seaguard Recording Current Meter (RCM) with a frequency of 2 MHz (both rated to 6000 m water depth). The fourth OBM was equipped with an upward-oriented Teledyne RDI ADCP Workhorse Quartermaster (four battery packs) with a frequency of 150 kHz. All current profilers are self-recording instruments equipped with alkaline batteries and internal data storage capacity. Each profiler is equipped with 4 transducers (Fig. 7.7.9), which transmit short pulses (pings) of acoustic energy along narrow beams. The same transducers receive backscattered signals from scatterers in the water column (such as particles or air bubbles), making use of the Doppler Effect to calculate the vector averaged speed and direction of ocean currents.

The ADCPs make use of broadband signal processing to improve data precision through the reduction of noise in the data and to allow for lower power consumption, thus extending the potential deployment time. The 600 kHz Workhorse Sentinel has a maximum measurement range of 50 m, the range being reduced when the concentration of scatterers in the water column is low (e.g. in deep-sea environments such as our working area, where the maximum range in the 2013-2014 deployment was found to be 15 m). The ADCPs in our deployed OBMs were configured to sample in 45 minute intervals with 170 pings per interval, pre-defining 12 bins with a cell size of 1.5 m (Tab. 7.7.3). The battery consumption using this configuration for a 365-day deployment period was estimated to be ca. 80%. The 150 kHz Workhorse Quartermaster has a maximum measurement range of 235 m, but was configured to sample every 45 minutes in 12 pre-defined bins with a cell size of 8 m only due to the low particle concentrations and assumed lower attainable range in the lower water column (Tab. 7.7.3). The battery consumption using this configuration and a ping rate of 180 pings per interval for a 400-day deployment period was estimated to be 95%.

The Seaguard RCM is equipped with a Z-pulse™ Doppler Current Sensor (DCS). To minimise effects of marine fouling and local disturbance, the DCS measures horizontal currents at least 0.4 m away from the instrument. The Seaguard has a maximum range of 4 m and measurements are made within one bin only. The RCMs in our deployed OBMs were configured to sample in hourly intervals with 170 pings per interval, through 1 bin located between 0.5 and 2 m from the instrument (Tab. 7.7.3). Pings were configured to be distributed during the last minute of the hourly recording interval ("burst mode"), as the sleep mode between measurements reduces power consumption significantly. The possible deployment time based on the available battery and storage capacity and this configuration was calculated to be 441

days. One RCM was equipped with a turbidity sensor 4112 (0–25 FTU range) and, for the new deployment, a temperature sensor 4060/4880 (–4–36°C range; resolution 0.001°C).

Table 7.7.3. Specifications and configurations of the ADCPs and Seaguard RCMs deployed during cruise SO-240.

	ADCP Workhorse Sentinel 150 kHz	ADCP Workhorse Sentinel 600 kHz	AADI Seaguard RCM 2MHz
Max. measuring range (m)	235 m vertical	50 m vertical	4 m horizontal
Sampling interval (mins)	45	45	60
No. of pings	180	170	170 (in bursts)
No. of bins	12	12	1
Blanking length (m)	12.8	2.73	0.5
Cell size (m)	8	1.5	1.5
Current range (cm/s)	0 - 500	0 - 500	0 - 300
Resolution (cm/s)	0.1	0.1	0.01
Mean accuracy (cm/s)	± 0.44	± 0.3	± 0.15



Figure 7.7.9. Left: Teledyne RDI Workhorse Sentinel (600 kHz) clamped into a buoy of syntactic foam, equipped with a MetOcean WABO iridium beacon (upper left) and a Novatech MMF-7500 miniflasher (lower right) for exact location purposes. Right: Teledyne RDI Workhorse Quartermaster (150 kHz).

Mooring configurations

The mooring configuration of each 600 kHz ADCP OBM is illustrated as sketch and photograph in figure 7.6.10. Each ADCP was clamped into the top of a syntactic foam buoy for the upward vertical measurement of currents. The buoys were manufactured by Flotation Technologies (model AF40-6000), whereas the titanium frames were produced by K.U.M. Umwelt- und Meerestechnik GmbH (Kiel). Buoys have a 40" diameter, a buoyancy of 170 kg, a nominal weight of 342 kg in air and a depth rating of 6000 m. Two additional smaller mooring clamps in the buoy allow for the fixation of locator instruments (Figs. 7.7.9 and 7.7.10).

As the minimal height of the ADCP above the seafloor would amount to ca. 3.5 meters due to the interconnection of an acoustic releaser and a weight below the buoy, and due to a minimal blanking length of at least 1.5 m, but more likely 3 m, above the ADCP transducers, good current data can only be expected from ca. 7 m above the seafloor and upwards in the shortest possible version of such a mooring. As our primary aim is to determine current variability starting from as close as possible to the seafloor, an AADI Seaguard RCM was placed in between the buoy and the releaser in order to at least obtain some horizontal current data from a height of ca. 2 m above the seafloor (Fig. 7.7.10).

Each OBM has been equipped with an IXSEA OCEANO oceanographic acoustic releaser of the type AR 661 - CT (titanium housing). A time release was not installed. A Novatech MMF-7500 miniflasher and a MetOcean WABO iridium beacon were installed onto each buoy for asset recovery purposes. The WABO iridium beacon is equipped with iridium satellite telemetry for real-time data transmission (iridium 9601 SBD modem; GPS Navman Jupiter 32). Its transmission interval is 3 h when submersed (at 0:00, 03:00, 06:00, 09:00 GMT, etc.) and 15 min for 6 h upon surfacing. After this, the beacon transmits every 12 h for life (at 08:00 and 20:00 GMT). Joubeh Technologies is the service provider for the beacons, offering a back office package as an Asset Management System to keep track of assets (e.g. through mapping). Automated SBD messages with GPS positions are sent per email when assets surface.

As with the three 600 kHz ADCP moorings, the heavy-weight 150 kHz ADCP was clamped into the top of a syntactic foam buoy for the upward vertical measurement of currents. The minimal height of the ADCP above the seafloor amounts to ca. 7 meters due to the interconnection of 2 extra VITRONEX glass flotation housings (46 kg buoyancy), an acoustic releaser and a weight below the buoy (Fig. 7.7.11). Taking account of a minimal blanking length of at least 12.8 m above the ADCP transducers, good current data can only be expected from ca. 20 m above the seafloor and upwards. This OBM was equipped with an IXBLUE OCEANO dual acoustic releaser of the type RT861B2S (steel housings). A time release was not installed. A Novatech MMF-7500 miniflasher and a MetOcean WABO iridium beacon were installed into the buoy for asset recovery purposes.

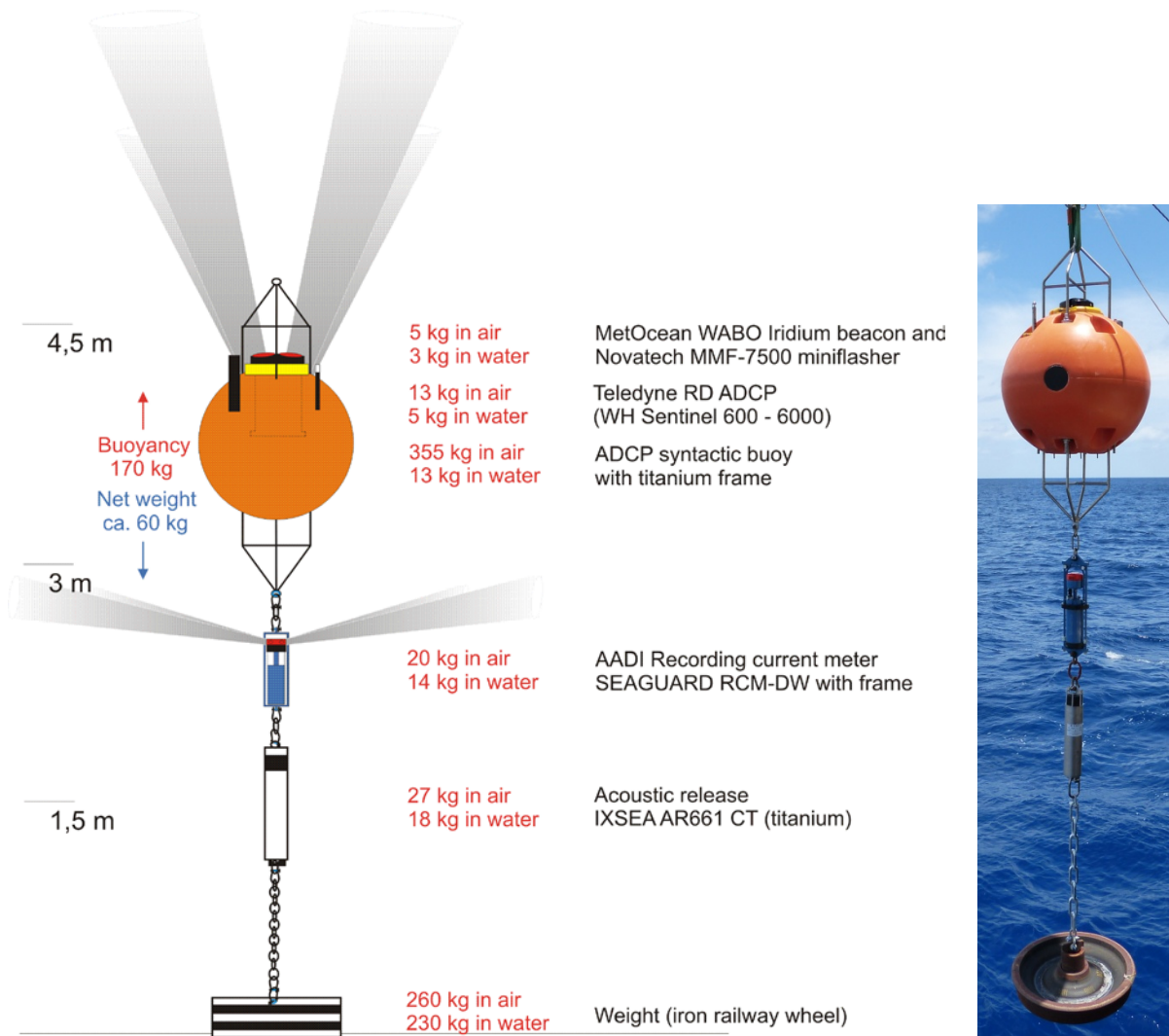


Figure 7.7.10. OBM configuration for the 600 kHz ADCPs and RCMs.

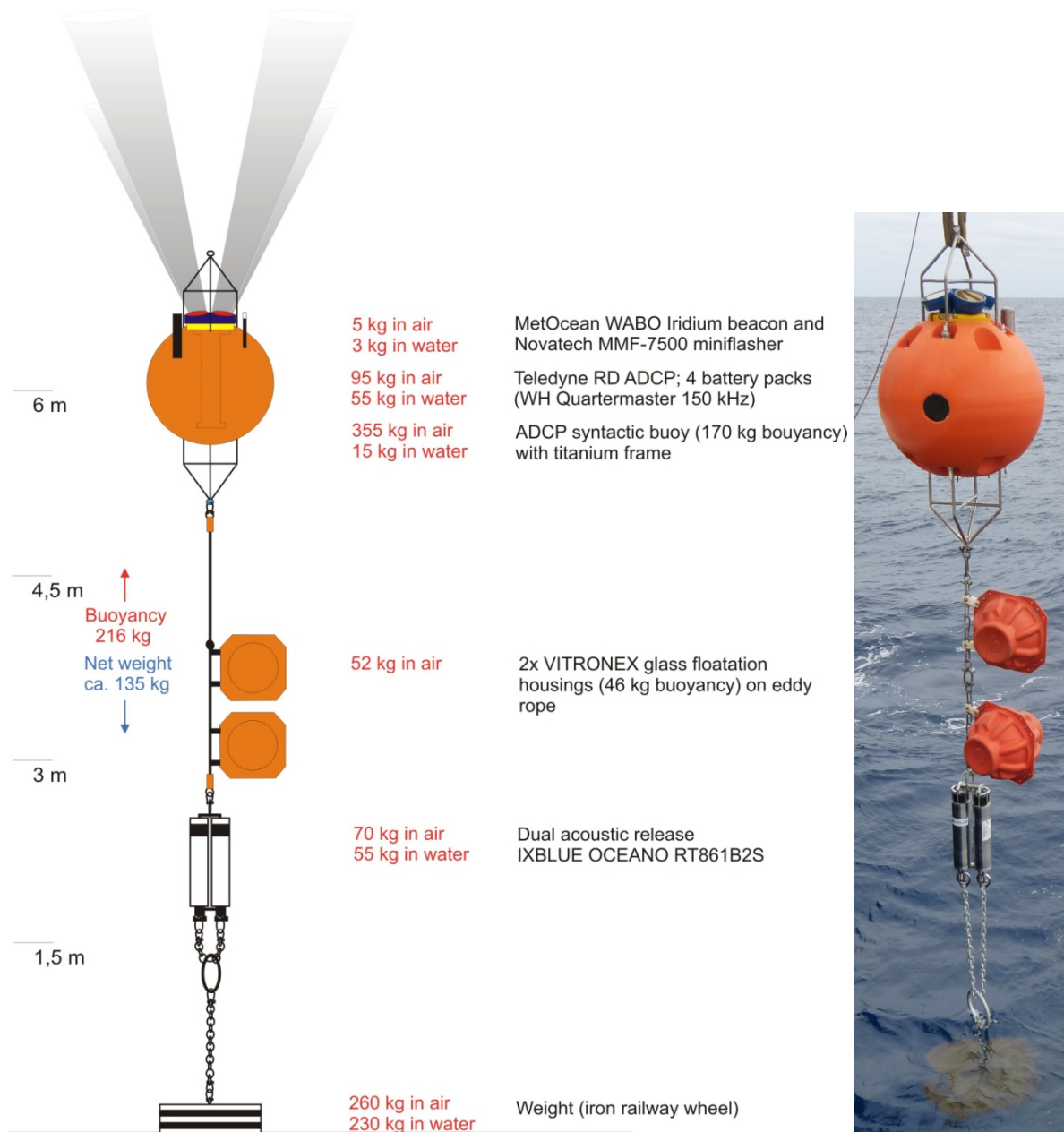


Figure 7.7.11. OBM configuration for the 150 kHz ADCP.

Mooring recovery

As part of the JPI-O “EcoResponse” working program for SO-240, the four above-mentioned BGR OBMs as well as a GEOMAR lander system (DOS) and a 400-m-long thermistor chain and lander system (BoBo) from NIOZ, were recovered on the 2nd and 3rd June 2015 after 13 months and 10 weeks of deployment, respectively. The BGR moorings had been deployed ca. 5–8 km apart in Prospective Area 1 in the eastern German license area (i.e. within SO-240 WA-4; see Fig. 6.28) on May 12th, 2014 (see Rühlemann et al., 2015 for details). The time between the acoustic release of the IXSEA OCEANO releaser and the surfacing of the OBM constituted ca. 30 minutes at a water depth of ~4100 m and with an upward

buoyancy of ca. 110 kg. Hardly any displacement of the OBMs compared to their original mooring positions was registered. After surfacing, R/V SONNE sided up with the floating OBM and retrieval directly onto the ship's deck over the starboard side occurred with relative ease under calm sea state conditions.

The GEOMAR DOS lander, equipped with an upward-looking 300 kHz ADCP, a Seabird 16plus CTD with a Wetlabs ECO-FLNTURTD fluorometer-turbidity sensor, a KUM sediment trap with 10 bottles (filled with DESS), an Ocean Imaging Systems stereographic camera system (photo interval 15 minutes), and a small temperature logger (Fig. 7.7.12; Tab. 7.7.4), was deployed on March 26th, 2015 about 2 km to the northeast of KM14-036OBM (Fig. 7.6.13). Surfacing of the DOS lander took ca. 60 minutes after releasing. The NIOZ BoBo lander is equipped with an upward-looking 300 kHz ADCP, a downward-looking 1200 kHz ADCP, a Seabird 16 CT with a Wetlabs ECO-FLNTURTD fluorometer-turbidity sensor, and a Technicap sediment trap with 12 sample bottles (poisoned with AgCl₂). BoBo was deployed on March 19th, 2015 about 1.5 km southeastwards of the DOS lander position (Tab. 7.7.4; Fig. 7.7.13). Surfacing of the BoBo lander took at least 90 minutes after releasing. The NIOZ thermistor chain was equipped with 201 NIOZ-4 thermistors as well as 3 Aquadopp acoustic current meters and was deployed close to the position of KM14-037OBM on March 19th, 2015 (Tab. 7.7.4; Fig. 7.7.13). All data from the landers, thermistor chain and moorings were downloaded and secured for further analysis in the framework of the JPI-O “EcoResponse” project. Instrumentation generally recorded data up to recovery according to the pre-programmed configurations. Only the 150 kHz ADCP of BGR mooring KM14-037OBM stopped measuring on December 5th, 2014; probably due to insufficient battery power.

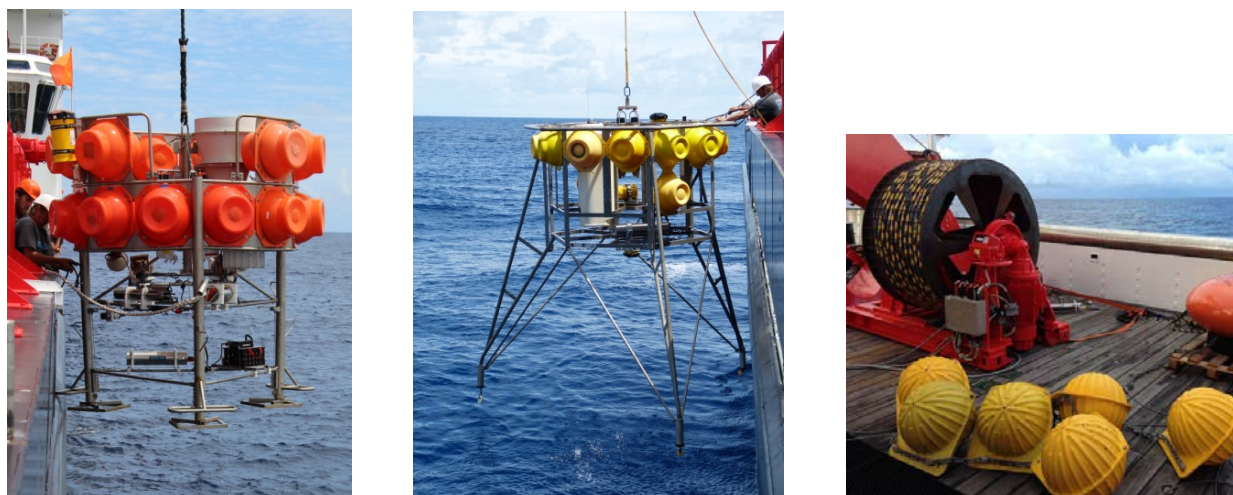


Figure 7.7.12. Left: DOS lander (GEOMAR); middle: BoBo lander (NIOZ); right: thermistor chain and floats (NIOZ).

Table 7.7.4. Mooring station characteristics for lander and thermistor chain deployment and recovery.

	DOS-2 (SO239 #44)	BoBo-1 (SO239 #4)	T. chain (SO239 #2)
Instrumentation	- 300 kHz upward-looking ADCP	- 300 kHz upward-looking ADCP	- 201 NIOZ-4 thermistors
	- Sediment trap	- 1200 kHz downward-looking ADCP	- 3 aquadopp current meters
	- CTD and ECO-FLNTURTD	- Sediment trap	
	- Stereographic camera system	- CT and ECO-FLNTURTD	
	- Temp. logger		
Deployment date	26.03.2015	19.03.2015	19.03.2015
Deployment time (UTC)	15:16	20:48	15:30
Position latitude (N)	11°51.47'N	11°51.28'N	11°50.65'N
Position longitude (W)	117°00.19'W	116°59.67'W	116°57.77'W
Water depth (m)	4115	4117	4101
Recovery date	03.06.2015	03.06.2015	02.06.2015

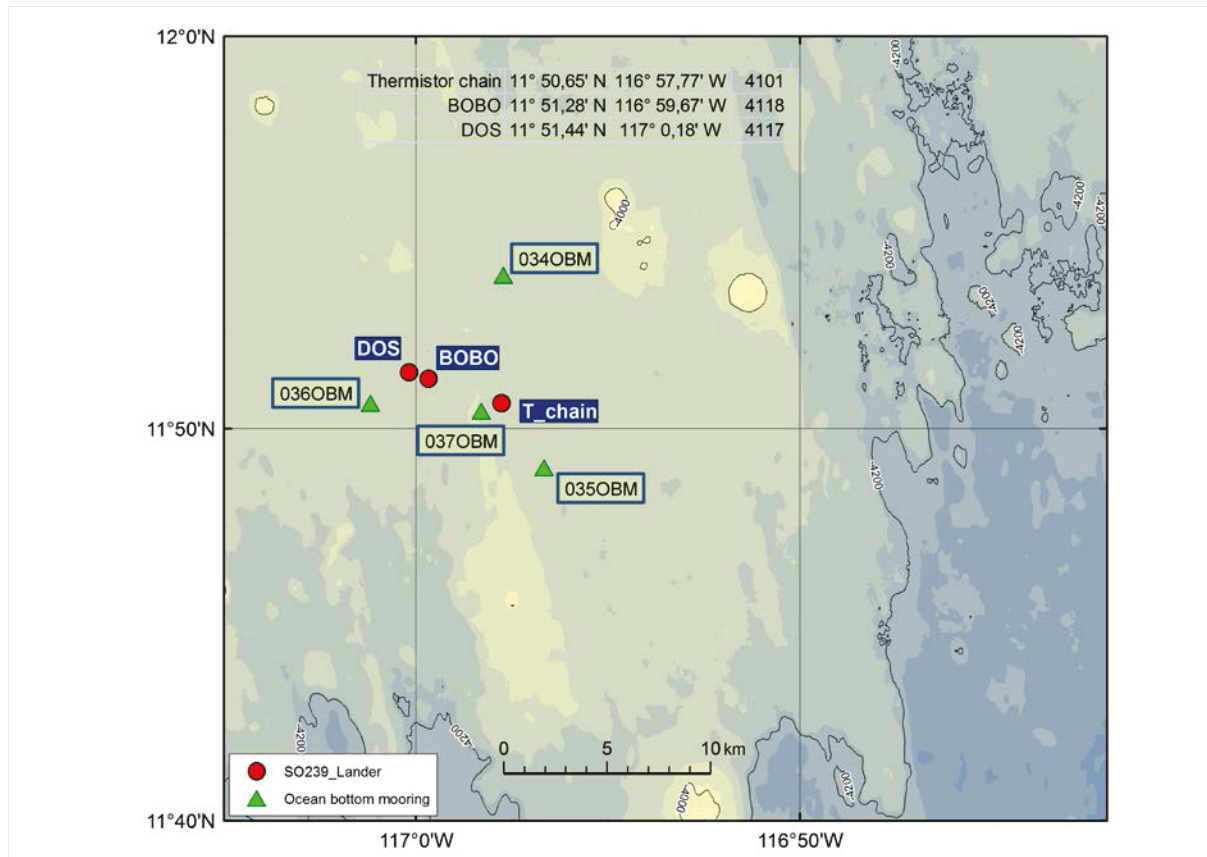


Figure 7.7.13. OBM (green triangles) and lander and thermistor chain (red dots) deployment positions in WA-4.

Redeployment of Ocean Bottom Moorings

As the OBMs of 2013 and 2014 were successful and all instruments provided reliable and good data, we decided to redeploy them at exactly the same positions and in the same mooring configurations as last year in order to retrieve more information on interannual variability at these sites (Tab. 7.7.5; Fig. 6.28). The OBMs were redeployed on June 6th, 2015. Due to the short length of the moorings, each complete mooring was picked up by crane from the deck (starboard side), put overboard and released slightly below the water surface.

Table 7.7.5. Mooring station characteristics for 2015 (deployed instruments; OBM positions).

SO-240 mooring station number	SO240-98OBM	SO240-99OBM	SO240-100OBM	SO240-101OBM
Old mooring station number (MANGAN 2013)	KM13-02OBM	KM13-03OBM	KM13-01OBM	
Old mooring station number (MANGAN 2014)	KM14-034OBM (recovery: SO240-86OBM)	KM14-035OBM (recovery: SO240-85OBM)	KM14-036OBM (recovery: SO240-88OBM)	KM14-037OBM (recovery: SO240-84OBM)
IXSEA AR 661 CT Releaser SN	833	834	832	
IXSEA Tandem RT 861B2S Releaser SN				856 + 857
Teledyne RD ADCP WH600 SN	17271	17270	17177	14908
AADI Seaguard RCM SN	333	336	331	
NOVATECH MMF-7500 miniflasher	A11-019	A11-020	C01-076	A11-020
MetOcean WABO iridium beacon	D063HQ; IMEI 300234011094850	DO5HFJ; IMEI 300234011095850	DO619W; IMEI 300234011099850	J00TXR; IMEI 300234060046030
Deployment date	06.06.2015	06.06.2015	06.06.2015	06.06.2015
Deployment time (UTC)	15:16	16:04	17:16	18:32
Position latitude (N)	11°53.915'N	11°48.987'N	11°50.619'N	11°50.447'N
Position longitude (W)	116°57.733'W	116°56.669'W	117°01.184'W	116°58.317'W
Water depth (m)	4108	4120	4122	4088

With an approximate sinking speed of 0.6 m/s, we assume that the deployment positions reflect the actual mooring positions with an acceptable degree of accuracy (~2 h sinking time). A triangulation exercise was carried out in order to verify mooring positions. Using the acoustic telecommand unit IXSEA TT801, the releasers of the OBMs were ranged for distance from 4 positions located between the OBMs approximately 2 h after the last OBM had been deployed (see Fig. 6.28). The ranged distances confirm that the OBMs did not drift much during their descent to the ocean floor (Tab. 7.7.6). Recalculating back to horizontal distances between each mooring position and ranging position, 98OBM shows a slight north-eastward drift of maximally 100 m, 99OBM a slight westward shift of maximally 50 m, and 100OBM a

slight north-westward drift of maximally 120 m, whereas 101OBM drifted north-westwards by about 300 m.

Table 7.7.6. Ranging values (triangulation) of OBM positions on the seafloor from fixed ranging positions at the sea surface (see Fig. 6.28).

Pos.	Latitude (N)	Longitude (W)	Distance to SO240-98OBM (m)	Distance to SO240-99OBM (m)	Distance to SO240-100OBM (m)	Distance to SO240-101OBM (m)
1	11°51.11'N	116°58.43'W	6649	6500	6583	4270
2	11°51.75'N	116°55.76'W	6752	6676	10933	6577
3	11°48.30'N	116°59.36'W		6574	6740	6023
4	11°53.19'N	117°00.48'W	6727		6434	7619

7.7.4 Shipboard results: Preliminary analysis of long-term current and turbidity data

ADCP Data

The very low particle concentrations in the water column close to the seafloor could endanger the functionality of the ADCPs, as measurements are based on the backscatter of acoustic signals sent out by the instrument. Fortunately there was no serious problem in data recording in the period of mooring deployment. Current velocities and directions obtained from bins 4 to 8 have been averaged to obtain more reliable results, translating to current velocity and direction between 10 and 18 m above the seafloor.

KM14-035OBM

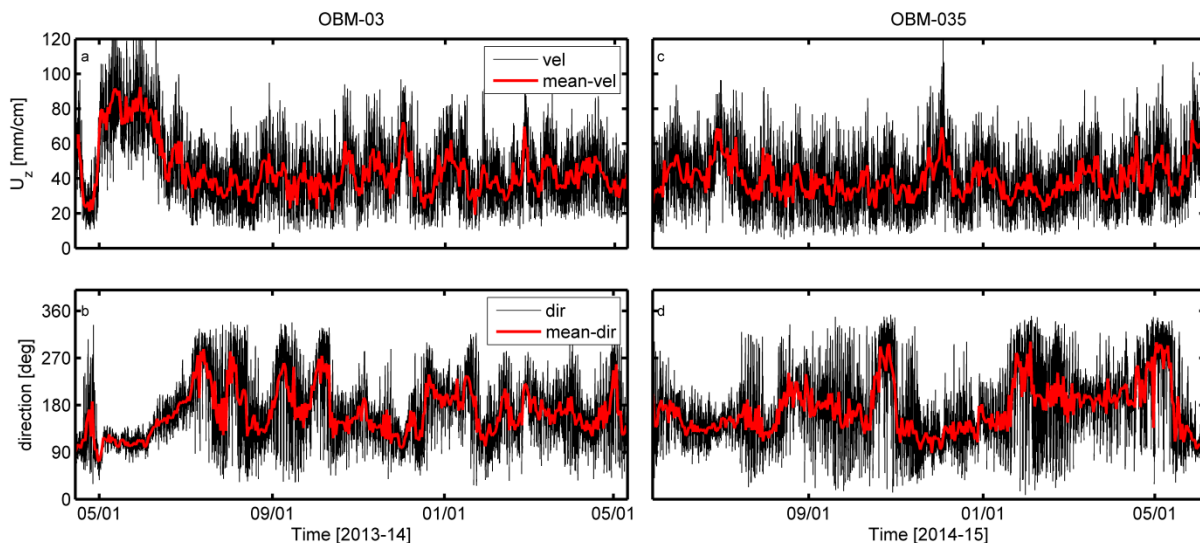


Figure 7.7.14. Current properties recorded by a 600 kHz ADCP at the site of KM13-03OBM/KM14-035OBM from April 2013 to June 2015 (see Fig. 7.7.13 for exact location). Black: averaged current velocity (a,c) and direction (b,d) in the water layer 10–18 m above the seafloor; Red: daily-averaged current velocity (a,c) and direction (b,d) in the water layer 10–18 m above the seafloor. Left (a,b): Current properties from April 2013 to May 2014; Right (c,d): same plots from May 2014 to June 2015.

Figure 7.7.14 shows a comparison of the current velocities and directions that have been registered by the 600 kHz ADCP at the site of KM14-035OBM (SO240-99OBM during this cruise) from April 2013 to June 2015. Current velocities vary between 5 mm/sec and 119 mm/sec, with an average of 39.1 mm/sec. A statistical comparison of the 2 years of data is shown in figure 7.7.15. The relative abundance is calculated based on the normalized values of each current magnitude and direction of the two datasets. Average current velocities were slightly higher in the second deployment year, showing a value of 39.9 mm/sec in comparison to 37.7 mm/sec during 2013-2014. Nevertheless, a higher relative abundance of greater current velocities (> 80 mm/sec) is found in the 2013-2014 dataset (Fig. 7.7.15) and is associated with the passing over of a large eddy at this site during May/June 2013 (Inall et al., 2015). Current velocities greater than 80 mm/sec are very rare during 2014-2015.

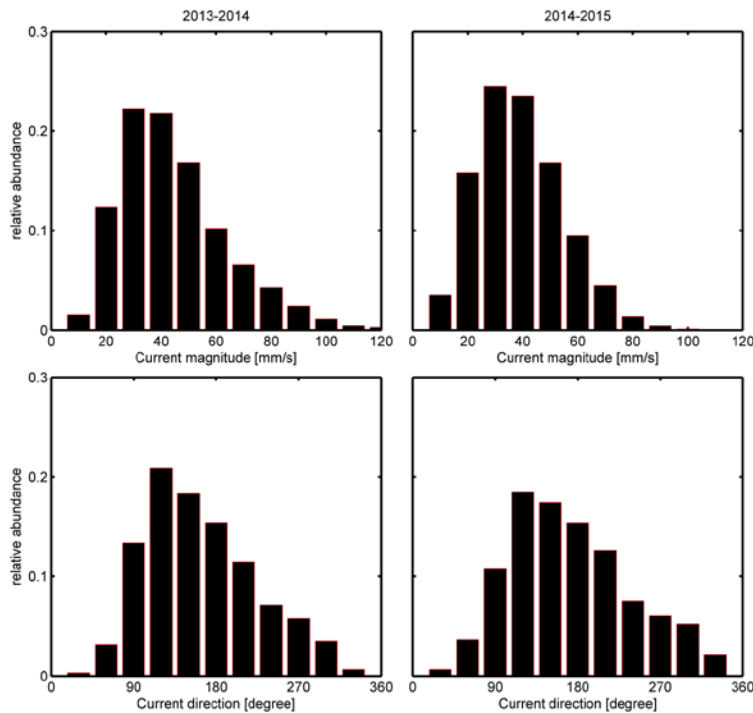


Figure 7.7.15. Statistical comparison of current velocities (upper panels) and directions (lower panels) as measured by a 600 kHz ADCP during the first (KM13-03OBM) and second (KM14-035OBM) year of OBM deployment at the same site.

KM14-034OBM

A similar current velocity and direction analysis was carried out for the 600 kHz ADCP data collected at the site of KM14-034OBM (SO240-98OBM during this cruise). Figure 7.7.16 illustrates the current velocities and directions at this site during the two observation periods. Averaged current velocities were 38.9 mm/sec and 37.8 mm/sec during 2013-2014 and 2014-2015, respectively. Again, the noticeably higher current velocity event during May and June 2013, with current speeds up to 100 mm/sec, deviates significantly from the rest of the current velocity pattern during the following two years. Although some individual peaks are observed in the current pattern of 2014-2015, they are not longer than 4-5 days. The averaged current directions show a southeast to southward dominant current direction during both periods of measurement.

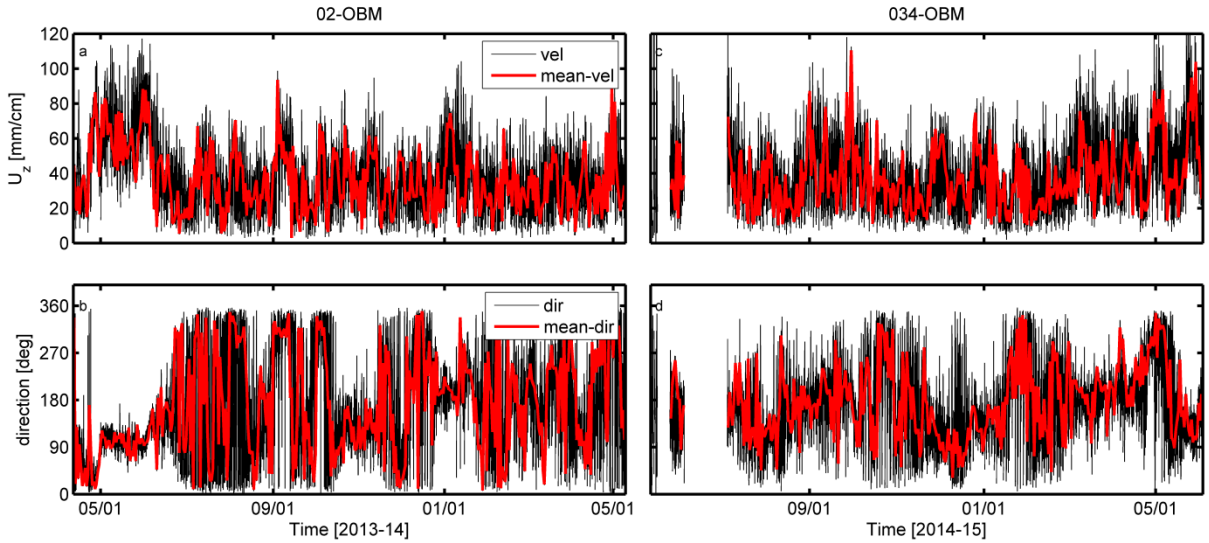


Figure 7.7.16. Current properties recorded by a 600 kHz ADCP at the site of KM13-02OBM/KM14-034OBM from April 2013 to June 2015 (see Fig. 7.7.13 for exact location). Black: averaged current velocity (a,c) and direction (b,d) in the water layer 10–18 m above the seafloor; Red: daily-averaged current velocity (a,c) and direction (b,d) in the water layer 10–18 m above the seafloor. Left (a,b): Current properties from April 2013 to May 2014; Right (c,d): same plots from May 2014 to June 2015.

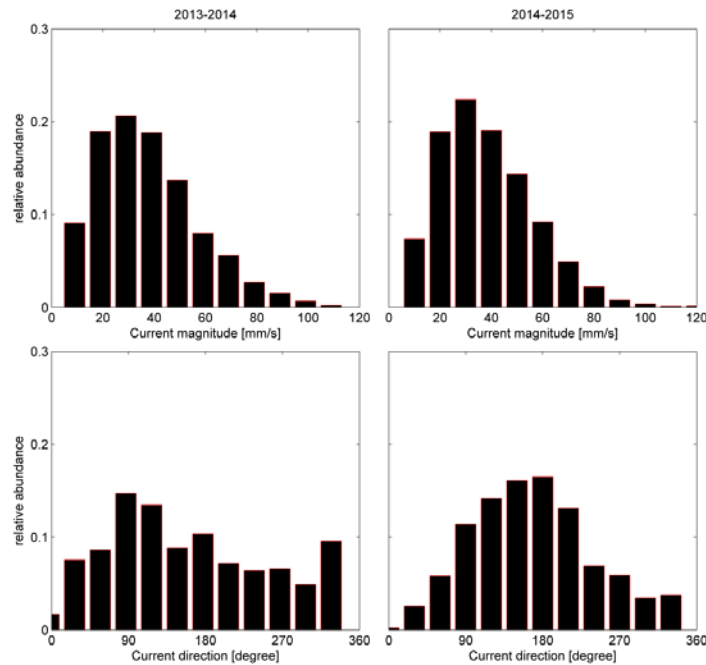


Figure 7.7.17. Statistical comparison of current velocities (upper panels) and directions (lower panels) as measured by a 600 kHz ADCP during the first (KM13-02OBM) and second (KM14-034OBM) year of OBM deployment at the same site.

Figure 7.7.17 shows that current velocities mainly vary between 20 mm/sec and 50 mm/sec in both datasets. The analysis of current direction shows different results. A multi-directional current was registered in the 2013-2014 dataset. In contrast, current directions show a more robust behavior during 2014-2015, with a clear eastward and southward current direction.

KM14-036OBM

Figure 7.7.18 illustrates the current velocities and directions measured by the 600 kHz ADCP at site KM14-036OBM (SO240-100OBM during this cruise) during the two observation periods. Averaged current velocity values show 42.8 mm/sec and 35.5 mm/sec during 2013-2014 and 2014-2015, respectively. The larger averaged current velocity value during 2013-2014 is probably due to the higher current velocity period associated with eddy formation in the early part of the first dataset, which deviates significantly from the rest of the current velocity pattern during the following two years. The averaged current directions show southeast to southward dominant current directions, with a deflection towards southwestward in the second year at this site (Fig. 7.7.19).

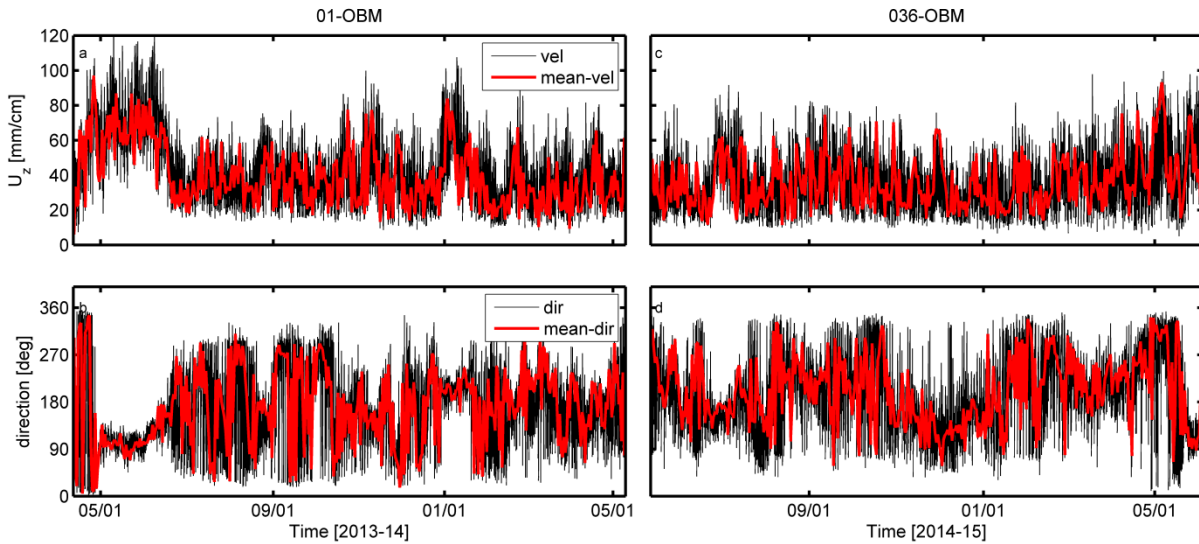


Figure 7.7.18. Current properties recorded by a 600 kHz ADCP at the site of KM13-01OBM/KM14-036OBM from April 2013 to June 2015 (see Fig. 7.7.13 for exact location). Black: averaged current velocity (a,c) and direction (b,d) in the water layer 10–18 m above the seafloor; Red: daily-averaged current velocity (a,c) and direction (b,d) in the water layer 10–18 m above the seafloor. Left (a,b): Current properties from April 2013 to May 2014; Right (c,d): same plots from May 2014 to June 2015.

Summarizing the results of all three OBM positions:

- currents have a predominant southeast to southwestward direction at the observed sites (see Fig. 7.7.20 for a comparison of 2014-2015 data);
- an extreme event with significantly higher current velocities was captured by the OBM data in May/June 2013;
- despite this fact, average current velocities in the 2013-2014 dataset do not deviate significantly from the average current velocities during 2014-2015;
- a northward current direction was not registered at any of the OBM sites.

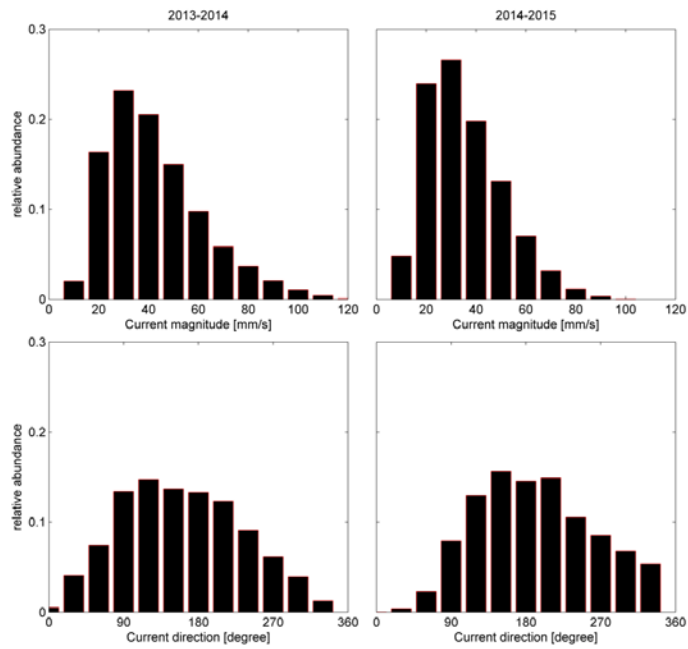


Figure 7.7.19. Statistical comparison of current velocities (upper panels) and directions (lower panels) as measured by a 600 kHz ADCP during the first (KM13-01OBM) and second (KM14-036OBM) year of OBM deployment at the same site.

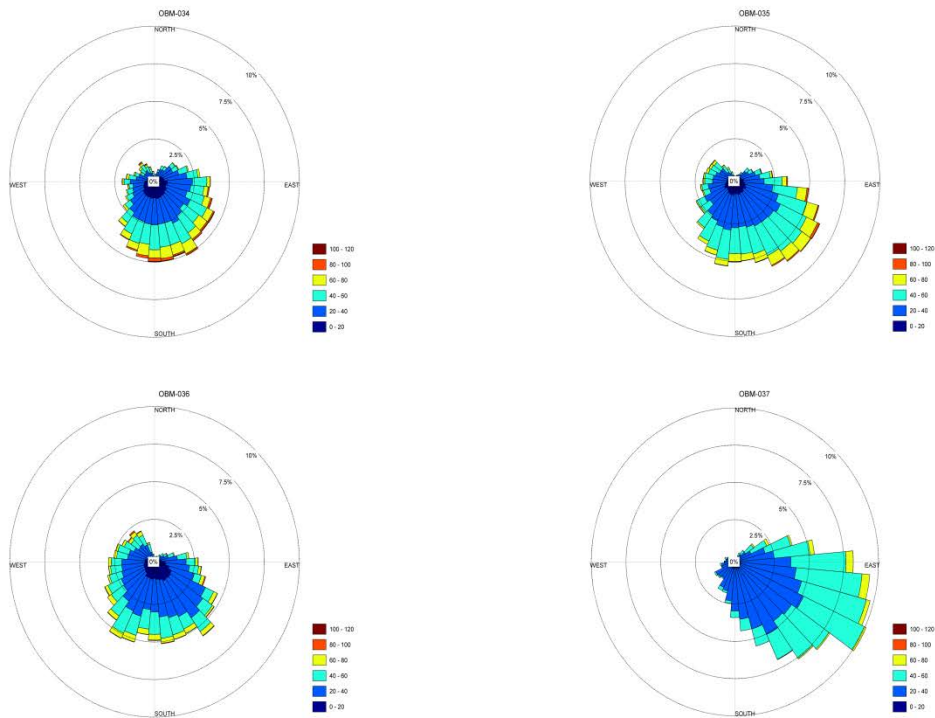


Figure 7.7.20. Current rose diagrams based on ADCP data from the water layer 10-18 m above the seafloor at the four OBM sites from May 2014 to June 2015.

RCM Data

Current velocities measured by the RCMs generally show lower values (on average 20 – 25 mm/sec) than those measured by the ADCPs (Figs. 7.7.21 – 7.7.24). This probably reflects reduced current speed close to the seafloor due to bottom friction, i.e. the logarithmic decay of flow velocity towards the bottom as is typical for the bottom boundary or Ekman layer. Despite the relatively low absolute velocities, the fluctuations of current speed with time mimic those of the corresponding ADCPs during the first year of measurement and increased current speeds in May/June 2013 as shown by the ADCPs are also reflected in two of the three RCM records (Figs. 7.7.22 and 7.7.23). Current directions delivered by RCMs during 2013-2014 show no distinctive preference at site KM13-02OBM, whereas there is a clear westward and southwestward predominance in the records of the other two RCMs.

The RCM records of 2014-2015 are more variable. Surprisingly, the current velocities measured during 2014-2015 at site KM14-034OBM indicate a periodic variation of approximately 45 days (Fig. 7.7.21). This oscillation in current speed is completely different from the current velocity pattern observed at this site one year earlier. Current directions oscillate correspondingly with eastward and westward components. The mean current velocity is 8 mm/sec higher than during the previous year. However, figures 7.7.22 and 7.7.23 show that such oscillations in current velocity are not a typical phenomenon for 2014-2015. The origin of the oscillations is unclear at the moment but may point to defect instrumentation. Current directions during 2014-2015 show a clear westward and northwestward predominance in the records of the other two RCMs (Fig. 7.7.24).

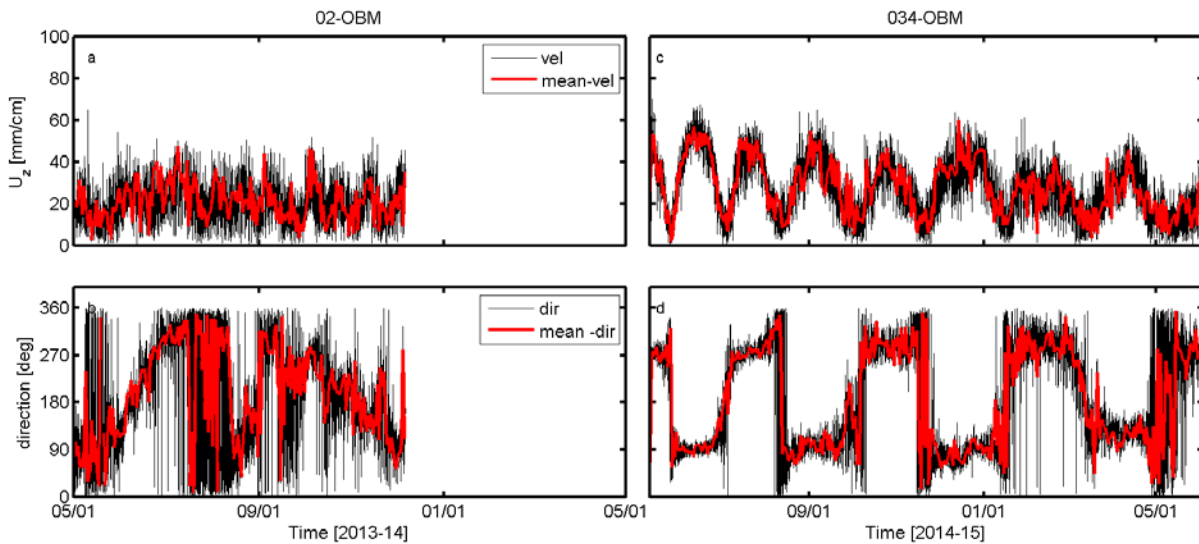


Figure 7.7.21. Current properties recorded by an RCM at the site of KM13-02OBM/KM14-034OBM from April 2013 to June 2015 (see Fig. 7.7.13 for exact location). Black: averaged current velocity (a,c) and direction (b,d) in the water layer 2 m above the seafloor; Red: daily-averaged current velocity (a,c) and direction (b,d) in the water layer 2 m above the seafloor. Left (a,b): Current properties from April 2013 to May 2014; Right (c,d): same plots from May 2014 to June 2015.

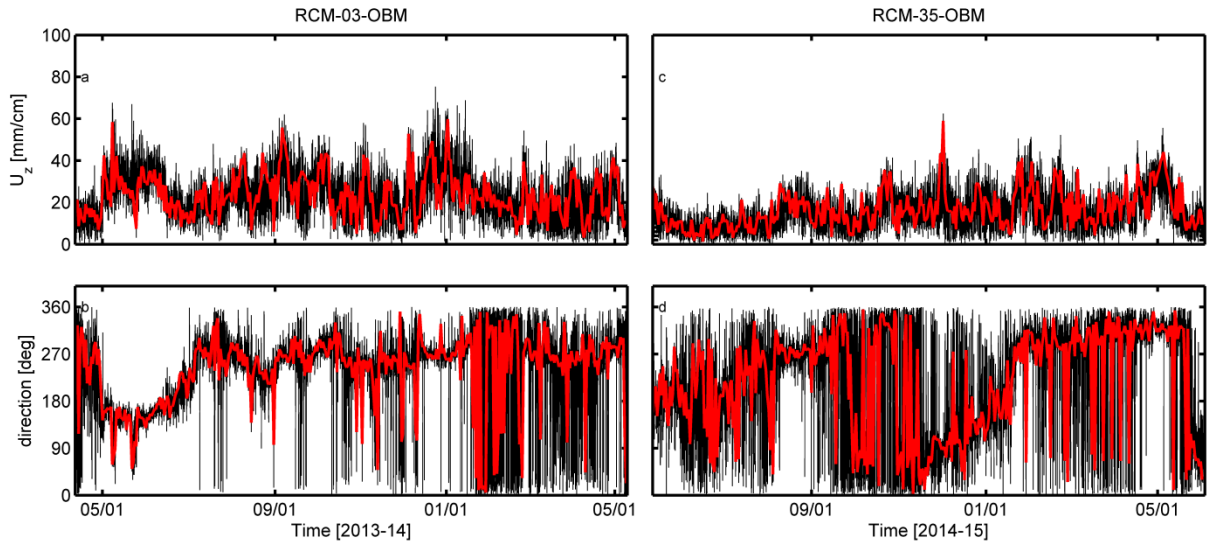


Figure 7.7.22. Current properties recorded by an RCM at the site of KM13-03OBM/KM14-035OBM from April 2013 to June 2015 (see Fig. 7.7.13 for exact location). Black: averaged current velocity (a,c) and direction (b,d) in the water layer 2 m above the seafloor; Red: daily-averaged current velocity (a,c) and direction (b,d) in the water layer 2 m above the seafloor. Left (a,b): Current properties from April 2013 to May 2014; Right (c,d): same plots from May 2014 to June 2015.

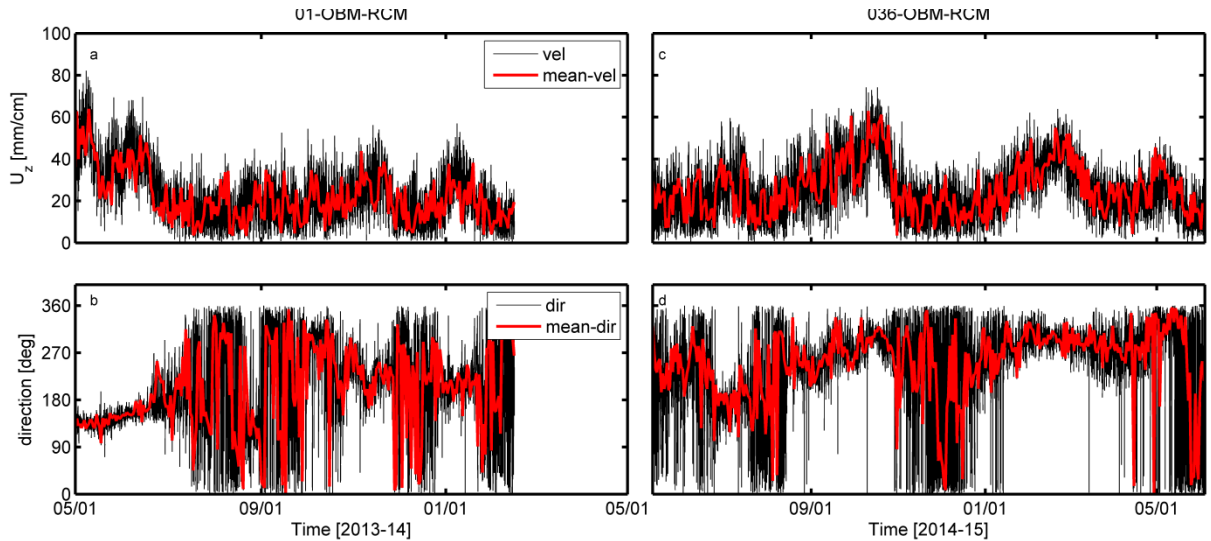


Figure 7.7.23. Current properties recorded by an RCM at the site of KM13-01OBM/KM14-036OBM from April 2013 to June 2015 (see Fig. 7.7.13 for exact location). Black: averaged current velocity (a,c) and direction (b,d) in the water layer 2 m above the seafloor; Red: daily-averaged current velocity (a,c) and direction (b,d) in the water layer 2 m above the seafloor. Left (a,b): Current properties from April 2013 to May 2014; Right (c,d): same plots from May 2014 to June 2015.

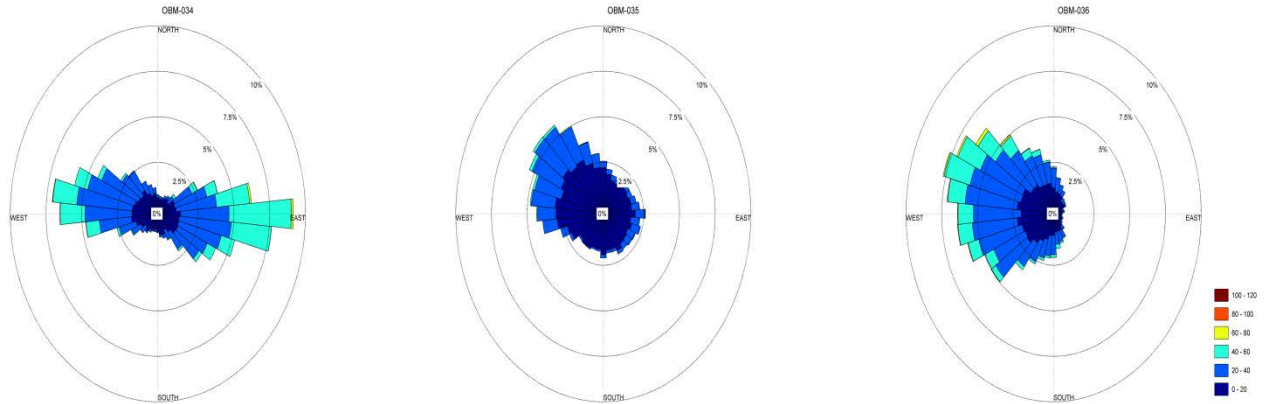


Figure 7.7.24. Current rose diagrams based on RCM data from the water layer 2 m above the seafloor at the three OBM sites from May 2014 to June 2015.

Turbidity

The comparison of turbidity values obtained by the RCM turbidity sensor at site KM13-02OBM/KM14-034OBM from a height of 2 m above the seafloor throughout 2013-2015 is shown in figure 7.7.25. Averaged background turbidity values of 0.1 FTU were measured for most of the time during both periods. The increased current speeds in May/June 2013 do not relate to any changes in turbidity during this event. A phase of greatly increased turbidity with maximum values of 4.18 FTU (i.e. an approximate 40-fold increase compared to background values) followed in September and October 2013, dropping to average values of 0.27 FTU from 08.11.2013 onwards. This increase in turbidity may be explained by the increase in surface water chlorophyll concentrations in the upper water column as registered by satellite imagery (see Rühlemann et al., 2015), and the consequent increase in particle fluxes to the seafloor. Although the measured turbidity values during 2014-2015 do not show such significant increases, turbidity did increase slightly in November 2014 and remained higher than background turbidity until March 2015. Again, there is no noticeable increase in current magnitude during this period of greater turbidity.

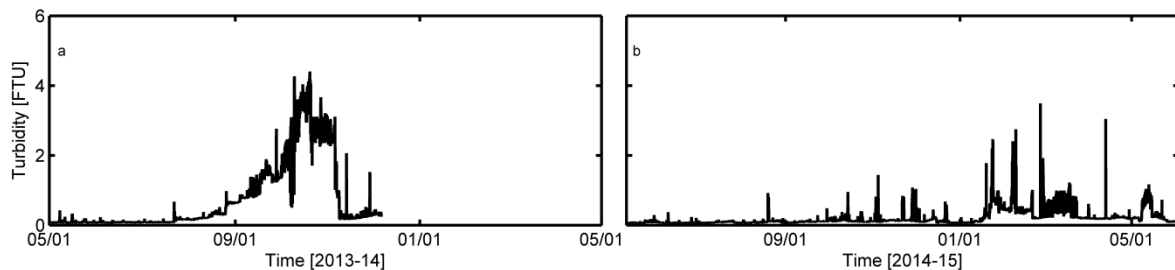


Figure 7.7.25. Turbidity data obtained by the moored RCM turbidity sensor at site KM13-02OBM/KM14-034OBM at a height of 2 m above the seafloor between (a) April 2013 and December 2013, and (b) May 2014 and June 2015.

Thermistor chain and DOS lander current data

The 400-m long thermistor chain of the NIOZ was equipped with 3 Aquadopp current meters at the top, middle and bottom of the chain. The pressure sensors of the Aquadopps showed deployment positions at 3788, 3971 and 4180 m water depth, respectively. The results obtained from a preliminary analysis of the current velocities recorded by these Aquadopps are shown in figure 7.7.26. Averaged current velocities from the bottom to the top of the chain between March 19th, 2015 and June 2nd, 2015 are 41 mm/sec, 44 mm/sec and 50.6 mm/sec, respectively. A greater distance from the seafloor thus leads to an increase in current magnitude. The current directions registered by all three Aquadopps are consistent and show a predominant southward current direction with hardly any deviation. The measurements of the thermistors themselves will only be read out and analyzed after the end of the SO-242 cruise at the end of the year.

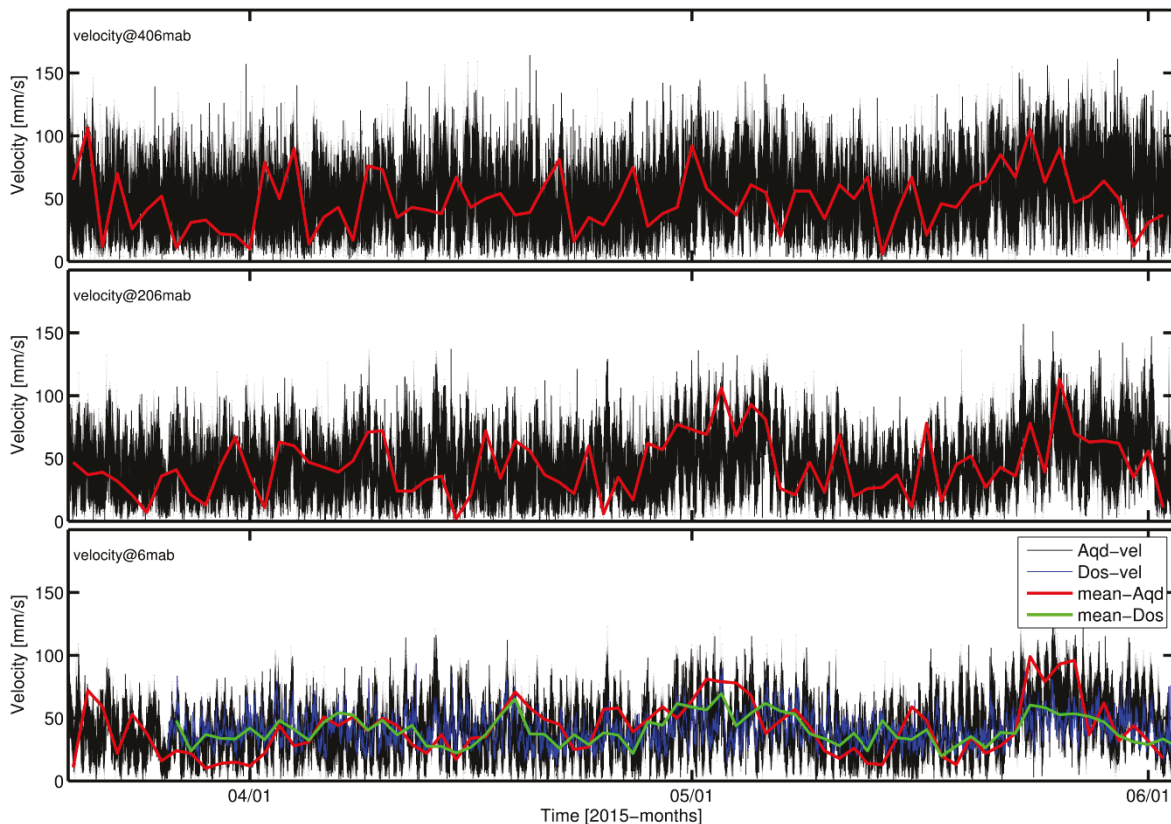


Figure 7.7.26. Current velocities obtained by the Aquadopp current meters installed on Thermistor Chain deployment SO239 #2 at 6 masf, 206 masf and 406 masf (meter above seafloor) between March 19th, 2015 and June 2nd, 2015 in WA-4 (see Fig. 7.7.13 for exact location). Daily averaged current velocities are shown by the red lines. Current velocities recorded by the upward-looking 300 kHz DOS-ADCP in bins 4 and 5 (comparable depth to the bottommost Aquadopp) are shown by the blue line; daily averages by the green line.

The current velocities recorded by the upward-looking 300 kHz ADCP mounted on the DOS lander during the same time interval were analyzed and are shown in the lower subplot of figure 7.7.26 (blue line). Current velocities obtained in the 4th and 5th bins were averaged in order to obtain comparative current velocities for the depth level of the lowest Aquadopp on the thermistor chain. Current velocities obtained

by the ADCP follow the current velocities recorded by the Aquadoppe very well (Fig. 7.7.26). The different geographic positions of the thermistor chain and the DOS lander cause small deviations in the averaged current velocities. Therefore, it can be concluded that the current velocities recorded by Aquadoppe and DOS-ADCP are highly consistent with one another.

8 Acknowledgements

We thank Capt. Lutz Mallon and his crew for the excellent support during the SO-240 cruise - we really enjoyed working with them. The cruise was financed through BMBF grant 03G0240.

9 References

- Abbott, A.N., Haley, B.A., McManus, J. and Reimers, C.E., 2015. The sedimentary flux of dissolved rare earth elements to the ocean. *Geochimica et Cosmochimica Acta* 154, 186-200.
- Anderson, O.B., 2010. The DTU10 Gravity field and Mean sea surface. *Second international symposium of the gravity field of the Earth (IGFS2)*, Fairbanks, Alaska.
- Beckmann, A., 1999. Dynamic processes at isolated seamounts. *Habilitation thesis*, Carl-von-Ossietzky University Oldenburg.
- Bekins, B.A., Spivack, A.J., Davis, E.E. and Mayer, L.A., 2012. Dissolution of biogenic ooze over basement edifices in the equatorial Pacific with implications for hydrothermal ventilation of the oceanic crust. *Geology* 35 (8), 679-682.
- Bullard, E., 1954. The Flow of Heat through the Floor of the Atlantic Ocean. *Proceedings of the Royal Society A: Mathematical, Physical and Engineering Sciences* 222 (1150), 408–429.
- Caress, D. W., Chayes, D. N., 2009. *MB-System: Mapping the Seafloor*. URL <http://www.mbari.org/data/mbsystem>.
- Chapman, D.C., Haidvogel, D.B., 1992. Formation of Taylor caps over a tall isolated seamount in a stratified ocean. *Geophysical & Astrophysical Fluid Dynamics* 64, 31-65.
- Fiedler, P.C., Talley, L.D., 2006. Hydrography of the eastern tropical Pacific: A review. *Progress in Oceanography* 69, 143-180.
- Fisher, A. T., 2005. Marine hydrogeology: recent accomplishments and future opportunities. *Hydrogeology Journal* 13 (1), 69–97.
- Fisher, A. T. and Wheat, C. G., 2010. Seamounts as conduits for massive fluid, heat, and solute fluxes on ridge flanks. *Oceanography* 23 (1), 74-100.
- Grasshoff, K., Kremling, K. and Ehrhardt, M., 1999. *Methods of seawater analysis*. 3 ed. Wiley, Weinheim, 600 pp.
- Hansbo, S., 1957. A new approach to the determination of shear strength of clay by the fall-cone test, Proc. Royal Swed. Geotech. Inst., 14, 5-47. Halbach, P., Friedrich, G., von Stackelberg, U. (Eds.), 1988. *The Manganese Nodule Belt of the Pacific Ocean*. Ferdinand Enke Verlag, Stuttgart, 358 pp.
- Harris, R. N., Fisher, A. T., Chapman, D. S., 2004. Fluid flow through seamounts and implications for global mass fluxes. *Geology* 32 (8), 725–728.
- Hartmann, A., Villinger, H., 2002. Inversion of marine heat flow measurements by expansion of the temperature decay function. *Geophysical Journal International* 148 (3), 628–636.
- Hasterok, D., 2013. A heat flow based cooling model for tectonic plates. *Earth and Planetary Science Letters* 361, 34–43.
- Hessler, R.R., Jumars, P.A., 1974. Abyssal community analysis from replicate cores in the central North Pacific. *Deep Sea Research and Oceanographic Abstracts* 21, 185-209.
- Houlsby, G.T., 1982. Theoretical analysis of the fall cone test. *Géotechnique* 32, 111-119.
- Hutnak, M., Fisher, A. T., 2007. Influence of sedimentation, local and regional hydrothermal circulation, and thermal rebound on measurements of seafloor heat flux. *Journal of Geophysical Research* 112 (B12101), 1–19.
- Hutnak, M., Fisher, A. T., Harris, R., Stein, C., Wang, K., Spinelli, G., Schindler, M., Villinger, H., Silver, E., 2008. Large heat and fluid fluxes driven through mid-plate outcrops on ocean crust. *Nature Geoscience* 1 (9), 611–614.

- Hyndman, R., Davis, E., Wright, J., 1979. The measurements of marine geothermal heat flow by a multipenetration probe with digital acoustic telemetry and in-situ thermal conductivity. *Marine Geophysical Researches* 4 (2), 181–205.
- Inall, M., Aleynik, D., Dale, A., Vink, A., 2015. Central American gap winds and abyssal CCZ plumes. *MIDAS Newsletter Issue 4*, Spring 2015, 6-7.
- Isezaki, N., 1986. A new shipboard three-component magnetometer. *Geophysics* 51, 1992–1998.
- König, M., 2006. Processing of shipborne magnetometer data and revision of the timing and geometry of the Mesozoic break-up of Gondwana. *Berichte zur Polar- und Meeresforschung* 52/5, 137p.
- Kriete, C.; 2011. An Evaluation of the Inter-Method Discrepancies in Ferromanganese Nodule Proficiency Test GeoPT 23A. *Geostandards and Geoanalytical Research* 35-3, 319 – 340.
- Kuhn, T., Rühlemann, C., Wiedicke-Hombach, M., Barckhausen, U., Schwarz-Schampera, U., Rutkowski, J., Lehmann, S., 2010. New insights of Mn nodule exploration from the German license area in the Pacific manganese nodule belt. In: Cherkashev, G., Morgan, C.L. (Eds.). *Underwater Mining Institute 2010: Towards the Sustainable Development of Marine Minerals: Geological, Technological, and Economic Aspects*. Gelendzhik, Russia, 1-11.
- Kuhn, T., Rühlemann, C., Wiedicke-Hombach, M., 2012. Developing a Strategy for the Exploration of Vast Seafloor Areas for Prospective Manganese Nodule Fields. In Zhou, H. & Morgan, C.L. (eds) *Marine Minerals: Finding the Right Balance of Sustainable Development and Environmental Protection*. The Underwater Mining Institute 2012, Shanghai, K1-9.
- Landrø, M., 1992. Modelling of Gi Gun Signatures. *Geophysical Prospecting* 40, 721–747. URL <http://doi.wiley.com/10.1111/j.1365-2478.1992.tb00549.x>
- Lister, C. R. B., 1970. Measurement of in situ sediment conductivity by means of a Bullard-type probe. *Geophysical Journal of the Royal Astronomical Society* 19, 521–532.
- Lister, C. R. B., 1979. The pulse-probe method of conductivity measurement. *Geophysical Journal of the Royal Astronomical Society* 57, 451–461.
- Madison, A.S., Tebo, B.M., Mucci, A., Sundby, B. and Luther III, G.W., 2013. Abundant porewater Mn(III) is a major component of the sedimentary redox system. *Science* 341, 875-878.
- Mewes, K., Mogollón, J.M., Picard, A., Rühlemann, C., Kuhn, T., Nöthen, K. and Kasten, S., 2014. Impact of depositional and biogeochemical processes on small scale variations in nodule abundance in the Clarion-Clipperton Fracture Zone. *Deep-Sea Research I*, 91, 125-141.
- Mewes, K., Mogollón, J.M., Picard, A., Rühlemann, C., Eisenhauer, A., Kuhn, T., Ziebis, W. and Kasten, S., in review. Diffusive transfer of oxygen from seamount basaltic crust into overlying sediments: an example from the Clarion-Clipperton Fracture Zone. *Earth and Planetary Science Letters*.
- Morelli, C., 1974. The International Standardization Net 1971. *International Association of Geodesy Special Publication* 4, 194.
- Ratcliffe, E. H., 1960. The Thermal Conductivities of Ocean Sediments. *Journal of Geophysical Research* 65 (5), 1535.
- Revsbech, N.P., 1989. An oxygen microsensor with a guard cathode. *Limnology and Oceanography* 34, 474-478.
- Rühlemann, C, Barckhausen, U, Ladage, S, Reinhardt, L, and Wiedicke, M., 2009. “Exploration for Polymetallic Nodules in the German License Area”, *Proceedings of The Eight (2009) ISOPE Ocean Mining Symposium*, Chennai, 8-14.

- Rühlemann, C., Kuhn, T., Wiedicke, M., Kasten, S., Mewes, K. and Picard, A., 2011. Current status of manganese nodule exploration in the German license area. *Proceedings of the Ninth (2011) ISOPE Ocean Mining Symposium*, Maui, Hawaii, USA, June 19-24, 2011, 168-173.
- Rühlemann, C. and Shipboard Scientific Party, 2012. Biodiversity, Geology, and Geochemistry of the German and French License Areas for the Exploration of Polymetallic Nodules in the Equatorial NE Pacific. *BIONOD Cruise Report of R/V L'Atalante, BGR, Hannover* 302 pp.
- Rühlemann, C. and Shipboard Scientific Party, 2014. Geology and biodiversity of the German License Area for the exploration of polymetallic nodules in the Equatorial NE Pacific. *MANGAN-2013 Cruise Report of R/V Kilo Moana, BGR, Hannover*, 354 pp.
- Rühlemann, C., and Shipboard Scientific Party (2015). Geology, biodiversity and environment of the German License Area for the exploration of polymetallic nodules in the Equatorial NE Pacific. *MANGAN-2014 Cruise Report of R/V Kilo Moana, BGR, Hannover*, 349 pp.
- Sandwell, D. T., and W. H. F. Smith, 2009: Global marine gravity from retracked Geosat and ERS-1 altimetry: Ridge segmentation versus spreading rate. *Journal of Geophysical Research* 114, B01411.
- Seeberg-Elverfeldt, J., Schlüter, M., Feseker, T. and Kölling, M., 2005. Rhizon sampling of porewaters near the sediment-water interface of aquatic systems. *Limnology and Oceanography Methods* 3, 361-371.
- Spinelli, G. A., Giambalvo, E. R. and Fisher, A. T., 2004. Sediment permeability, distribution, and influence on fluxes in oceanic basement. In: *Hydrogeology of the Oceanic Lithosphere*, eds. E. E. Davis and H. Elderfield. Cambridge University Press, Cambridge
- Villinger, H., Davis, E. E., 1987. A New Reduction Algorithm for Marine Heat Flow Measurements. *Journal of Geophysical Research* 92 (B12), 12846–12856.
- Wessel, P., Smith, W., 2010. The Generic Mapping Tools (GMT), Version 4.5.2. *Technical Reference and Cookbook*. URL <http://gmt.soest.hawaii.edu/>
- Wheat, C.G. and Fisher, A.T., 2010. Massive, low-temperature hydrothermal flow from a basaltic outcrop on 23 Ma seafloor of the Cocos Plate: Chemical constraints and implications. *Geochemistry, Geophysics, Geosystems* 9 (12) doi: 10.1029/2008gc002136.
- Wiedicke-Hombach, M. and Shipboard Scientific Party (2009). Cruise Report “Mangan 2008”, RV Kilo Moana, 13 Oct. – 22 Nov. 2008. *Bundesanstalt für Geowissenschaften und Rohstoffe, Hannover*, 89 pp.
- Wiedicke-Hombach, M. and Shipboard Scientific Party (2010). Cruise Report “Mangan 2009”, RV Kilo Moana, 20 Oct. – 27 Nov. 2009. *Bundesanstalt für Geowissenschaften und Rohstoffe, Hannover*, 64 pp.
- Whittaker, J., Goncharov, A., Williams, S., Dietmar Müller, R., Leitchenkov G., 2013. Global sediment thickness dataset updated for the Australian-Antarctic Southern Ocean, *Geochemistry, Geophysics, Geosystems*. <http://onlinelibrary.wiley.com/doi/10.1002/ggge.20181>
- Yoder, M., Tandigan, De Ly I., King, I.W., Mundo-Ocampo, M., Mann, J., Blaxter, M., Poiras, L., De Ley, P., 2006. DESS: A versatile solution for preserving morphology and extractable DNA of nematodes. *Journal of Nematology* 8, 367-376.
- Ziebis, W., McManus, J., Ferdelman, T., Schmidt-Schierhorn, F., Bach, W., Muratli, J., Edwards, K.J. and Villinger, H., 2012. Interstitial fluid chemistry of sediments underlying the North Atlantic gyre and the influence of subsurface fluid flow. *Earth and Planetary Science Letters* 323, 79-91.

10 Abbreviations

ADCP	Acoustic Doppler Current Profiler
ANOSIM	Analysis of Similarity
AWI	Alfred Wegener Institute Helmholtz Center for Polar and Marine Research
BGR	Bundesanstalt für Geowissenschaften und Rohstoffe
BoBo	Benthic Boundary Observatory
CTD	Conductivity, Temperature, Depth
DCS	Doppler Current Sensor
DOS	Deep Sea Observatory System
DZMB	Deutsches Zentrum für Marine Biodiversitätsforschung, Wilhelmshaven
EDTA	Ethylenediaminetetraacetic acid
EM	Multibeam echosounder
EPR	East Pacific Rise
FLUM	FL uid Fluxes and Mn nodules in the equatorial eastern Pacific
FTU	Formazine turbidity units
GDS	Chain bag dredge (German: Gesteinsdredge)
GEOB	Geowissenschaften, Universität Bremen
HF	Heat Flow
ISM	Intelligent sensor modules
IUP	Institut für Umweltphysik, Ozeanographie, Universität Bremen
JPI-O	Joint Programming Initiative - Oceans
JUB	Jacobs Universität Bremen
KG	Box Corer (Kastengreifer)
KL	Piston corer (Kolbenlot)
LIR	Lance Insertion Retardation meter
MAPRs	Miniature Autonomous Plume Recorders
MFT	Multi-Functional Tool
MUC	Multiple Corer
mW	Milliwatt
nMDS plots	Non-metric, multi-dimensional scaling plots
NTU	Nephelometric Turbidity Unit
OBM	Ocean Bottom Mooring
OFOP	Ocean Floor Observation Protocol
OMZ	Oxygen Minimum Zone
PS	Parasound
Psu	Practical Salinity Unit
RCM	Recording Current Meter
RV	Research Vessel
SCS	Seismic survey
SL	Gravity Corer (Schwerelot)
STR	STROMER
STROMER	S impler T auch r oboter M ultifunktional E rweiterbar
USBL	Ultra-Short Baseline
UTC	Universal Time Coordinated
WA	Working Area
WP	Way point
XRF	X-ray fluorescence analyzer

11 Appendix

A1 Geophysics

Documentation of bathymetry, parasound and seismic profiles and heat flow profiles for the different working areas of the SO240 cruise

A2 Box core descriptions

Photo documentation of nodules and sediments, depth profiles of shear strength, and statistical analyses on manganese nodules size and mass distribution and metal composition for each box core station

A3 Nodule sample descriptions

Photo documentation and sample description of selected nodules from SO-240 box core stations

A4 Long sediment core descriptions

Photo documentation and sediment description of the sediments from SO-240 gravity and piston core stations